

# Fatigue Behaviour of Axially Loaded Grouted Connections in Jacket Structures

Von der Fakultät für Bauingenieurwesen und Geodäsie der  
Gottfried Wilhelm Leibniz Universität Hannover

zur Erlangung des akademischen Grades

Doktor der Ingenieurwissenschaften

- Dr.-Ing. -

genehmigte Dissertation von  
Dipl.-Ing. Anne Christine Bechtel  
geboren am 1. November 1984 in Alsfeld

---

**Promotionskommission**

Referent: Prof. Dr.-Ing. Peter Schaumann  
1. Korreferent: Prof. Dr.-Ing. Ludger Lohaus  
2. Korreferent: Prof. Milan Veljković  
Vorsitzender: Prof. Dr.-Ing. Martin Achmus

Tag der Promotion: 24. Juni 2016

---

## Preface

The future expansion of offshore wind farms will be related to the installation of offshore support structures in deeper waters. For that purpose latticed substructures like jackets represent a favourable and cost-effective solution. Nevertheless, constructional details such as the grouted connection, joining the substructure to the driven foundation piles, exceed current knowledge and experience with regard to governing loading situations and dimensions. In order to close the current lack of knowledge and to allow for a design transfer from previous experience, the fatigue behaviour of axially loaded grouted connections with increased dimensions have been set in the focus of this thesis.

The conducted research investigation was performed as partly in the framework of a national research project, while I was working as scientific staff member at the Institute for Steel Construction at the Gottfried Wilhelm Leibniz Universität Hannover. In this context I cordially thank Prof. Dr.-Ing. Peter Schaumann, my supervisor and first reviewer of this thesis, for giving me the possibility to intensify and pursue my scientific curiosity, especially in the area of grouted connections. I am grateful for the scope for individual development, the trust for initiating, developing and managing research projects. Apart from the research related work and supporting advice, I am thankful for having the opportunity to experience expert related work for legal and normative procedures.

I specially thank Prof. Milan Veljkovic, who has served as second reviewer, for the detailed analysis of my research work, the constructive discussions and for taking the journey to Hannover for the examination. I sincerely thank Prof. Dr.-Ing. Ludger Lohaus for undertaking the third review. I appreciate the fruitful discussions during the entire research project, but especially the purposeful conversation at the end of the thesis. I thank Prof. Dr.-Ing. Martin Achmus for undertaking the chair of the examination committee and supporting the framework of the procedure.

I express my appreciation to the German Federal Ministry for Economic Affairs and Energy for the financial support of the research project “GROWup – Grouted Joints for Offshore Wind Energy Converters under reversed axial loading and upscaled thicknesses” (funding sign 0325290). In that regard, I am grateful for the material supply and support during the grouting procedure by BASF Masterflow and Densit. Great thanks convey to the technical and scientific staff of the Institute for Steel Construction and the Institute for Building Material Science, who assisted to realize the experimental investigations.

Cordial thanks to my colleagues at the Institute for Steel Construction for the positive climate during and after work time. I appreciate especially the sportive discussions as well as the focused review of my thesis by Dr.-Ing. Stephan Lochte-Holtgreven.

Finally I would like to express great thanks to my family and best friends for supporting and motivating me from the beginning to the end of this doctoral phase. Eminently, I thank you, Klaus, for all your unconditional motivation, support and patience throughout this time, especially in the final year of the thesis. You kept me going and being motivated to finalize the thesis in an appreciate manner. I thank you with all my heart for all you have done for me.

---

## Abstract

For the wind energy expansion a significant amount of offshore wind turbines (OWTs) have to be installed in comparable large water depths by use of latticed substructures like jackets or tripods. These framework-like substructures are linked to the driven foundation piles by grouted connections being composed of two steel tubes with different diameters. By filling the annulus with a high performance grout, driving induced pile inclinations can be compensated. At multi-pile substructures, this feature requires for considerable large grout annuli, which exceed present design experience. The design rules account for a load transfer between the steel tubes and the grout being predominantly characterised by shear keys, which are placed as weld beads diagonally opposite to each other on the facing steel surfaces.

While current design approaches originate from investigations for grouted connections with smaller grout thickness and deviating loading conditions, their applicability for grouted connections in latticed structures at OWTs is currently unsecure. In particular, the fatigue behaviour of this connection with up-scaled grout thickness being exposed to predominant cyclic reversal axial loads has not been investigated. Therefore, the objective of this thesis was to identify and evaluate the fatigue behaviour of cyclic axially loaded grouted connections with large grout thicknesses by using experimental and numerical investigations.

Large-scale tests were performed considering dimensions adapted from offshore grouted connections at jacket and tripod substructures. Four test specimens representing two different grout thicknesses being filled with two high strength grout materials were subjected to a stepwise increased loading covering alternating and pulsating compression loads. Apart from displacement and strain measurements, surface roughnesses and damage characteristics were determined to evaluate the fatigue behaviour of the connection.

A three-dimensional numerical model using a multiaxial grout material model was developed to describe the bearing behaviour of grouted connections with high strength grouts. The model was validated on the results of experimental tests. Enhancement of the numerical model was achieved by incorporating the cyclic fatigue degradation. For this purpose, a calculation procedure was implemented accounting for stress-dependent cyclic grout strength and stiffness degradation based on uniaxial S-N curves. Moreover, the validated numerical models were used to describe the impact of main influencing parameters on the load bearing and fatigue behaviour.

The achieved experimental and numerical results indicate that the fatigue behaviour is particularly influenced by the grout thickness and shear key configuration. The results further demonstrate the detrimental impact of alternating loading compared to pulsating compression loading. Although the grout material behaves quite brittle, the grouted connection represents a ductile behaviour with large fatigue strength. The failure mechanism is characterised by compression strut cracking especially at the external shear keys. Comparison of the results with offshore design codes reveals that the fatigue strength of the specimens is larger than predicted. Based on the investigations, present design approaches are applicable for axially loaded grouted connections with increased grout thicknesses.

**Key words:** offshore wind energy, grouted connection, large-scale tests, fatigue

---

## Kurzfassung

Für den Ausbau der Windenergie ist eine Vielzahl von Offshore-Windenergieanlagen (OWTs) mit aufgelösten Unterstrukturen wie Jackets oder Tripods in vergleichsweise großen Wassertiefen zu errichten. Diese fachwerkartigen Unterstrukturen werden mit den Gründungspfählen durch Grout-Verbindungen bestehend aus zwei ineinander geführten Stahlrohren verbunden. Rammbedingte Pfahlschiefstellungen können durch die Verfüllung des Ringspalts mit hochfestem Vergussmörtel kompensiert werden. Diese Eigenschaft führt bei Multi-Pfahlgründungen zu Spaltdicken, welche den abgesicherten Bemessungsbereich überschreiten. Der bemessungsrelevante Lastabtrag ist vorwiegend durch Shear Keys gekennzeichnet, welche als Schweißwülste auf den zugewandten Stahlrohroberflächen positioniert sind.

Aufgrund der bisherigen Untersuchungen von Grout-Verbindungen mit geringen Spaltdicken und abweichenden Belastungsbedingungen ist die Anwendung dieser Verbindungsart für aufgelöste OWT Strukturen derzeit nicht abgesichert. Insbesondere das Ermüdungsverhalten von Grout-Verbindungen mit großen Spaltdicken infolge zyklischer axialer Wechsellasten ist nicht hinreichend untersucht. Das Ziel dieser Dissertation ist daher die Identifikation und Bewertung des Ermüdungsverhaltens von zyklisch axial belasteten Grout-Verbindungen mit großen Spaltdicken durch Anwendung experimenteller und numerischer Untersuchungen.

Unter Berücksichtigung adaptierter Abmessungen von Grout-Verbindungen in Jackets und Tripods wurden großmaßstäbliche Versuche durchgeführt. Vier Versuchskörper mit zwei unterschiedlichen Grout-Spaltdicken verfüllt mit zwei hochfesten Vergussmörteln wurden durch eine schrittweise gesteigerte Wechsel- und Druckschwellbelastung beansprucht. Neben Verschiebungen und Dehnungen wurden Oberflächenrauigkeiten und Schadenscharakteristika zur Bewertung des Ermüdungsverhaltens bestimmt.

Zur Beschreibung des Tragverhaltens von Grout-Verbindungen mit hochfesten Vergussmörteln wurde ein dreidimensionales numerisches Modell unter Verwendung eines mehraxialen Materialmodells entwickelt. Die Validierung des Modells wurde anhand der experimentellen Versuchsergebnisse vollzogen. Zur Berücksichtigung der zyklischen Degradation wurde eine Modellerweiterung vorgenommen, welche die spannungsabhängige Festigkeits- und Steifigkeitsdegradation gemäß einaxialer Beton-Wöhlerlinien berücksichtigt. Mittels der validierten numerischen Modelle konnte der Einfluss der maßgebenden Parameter auf das Trag- und Ermüdungsverhalten beschrieben werden.

Die erreichten experimentellen und numerischen Ergebnisse zeigen die Maßgeblichkeit der Grout-Spaltdicke und der Schubrippenausbildung auf das Ermüdungsverhalten sowie den negativen Einfluss von Wechsellasten im Vergleich zu Druckschwelllasten. Die Verbindung weist trotz des spröden Verfüllmaterials ein stark duktileres Verhalten auf, wobei sich ein Versagen vor allem durch Druckstrebenbrüche an den äußeren Schubrippen kennzeichnet. Vergleichende Darstellungen der Versuchsergebnisse mit den Regelwerken ergeben eine höhere Ermüdungsfestigkeit für die Versuchskörper als prognostiziert. Zusammenfassend wird auf Grundlage der Untersuchungen festgestellt, dass die Bemessungsansätze auch für axial-beanspruchte Grout-Verbindungen mit großen Grout-Spaltdicken anwendbar sind.

**Schlagnworte:** Offshore-Windenergie, Grout-Verbindung, großskalige Versuche, Ermüdung



---

## Contents

1	Introduction.....	1
1.1	Motivation .....	1
1.2	Objective.....	3
1.3	Structure.....	4
2	State of the Art.....	6
2.1	Grouted Connections in Offshore Support Structures.....	6
2.1.1	Offshore support structures .....	6
2.1.2	Constructions and dimensions.....	7
2.1.3	Materials.....	10
2.1.4	Loads and load effects.....	15
2.2	Load Bearing Behaviour.....	17
2.2.1	Chronological research overview.....	17
2.2.2	Load transfer and failure modes.....	19
2.2.3	Impact of geometrical parameters .....	23
2.2.4	Impact of material characteristics .....	26
2.2.5	Impact of load states.....	28
2.3	Current Design Approaches.....	31
2.3.1	Standards and guidelines .....	31
2.3.2	Ultimate limit state .....	32
2.3.3	Fatigue limit state .....	36
2.3.4	Numerical approaches .....	38
2.4	Material Specific Fatigue Behaviour.....	40
2.4.1	Steel.....	40
2.4.2	High performance grout .....	42
2.5	Conclusion.....	48
3	Experimental Investigations.....	51
3.1	Test Concept.....	51
3.2	Test Specimen.....	52
3.2.1	Geometry and reference structures.....	52
3.2.2	Materials.....	56

---

3.2.3	Specimen preparation.....	57
3.3	Test Procedure.....	58
3.3.1	Test set-up.....	58
3.3.2	Test load scenario and reference loads.....	59
3.3.3	Measurements and test documentation.....	64
3.4	Fatigue Test Results.....	66
3.4.1	Global deformation behaviour.....	66
3.4.2	Relative displacements.....	69
3.4.3	Stiffness development.....	77
3.4.4	Strain development.....	84
3.4.5	Damage process.....	91
3.4.6	Steel surface changes.....	95
3.4.7	Damage characteristics.....	97
3.5	Conclusion.....	103
4	Numerical Investigations.....	106
4.1	Purpose.....	106
4.2	Model and Method Configuration.....	107
4.2.1	Finite element model.....	107
4.2.2	Material models and characteristics.....	108
4.2.3	Calculation procedure.....	114
4.3	Validation of the Numerical Model.....	118
4.3.1	Global deformation behaviour.....	118
4.3.2	Relative displacements.....	119
4.3.3	Strain development.....	121
4.3.4	Damage and cyclic degradation.....	122
4.4	Parametric Studies.....	130
4.4.1	Model configuration.....	130
4.4.2	Grout thickness.....	130
4.4.3	Material strength.....	131
4.4.4	Surface conditions.....	133
4.4.5	Load sequence.....	135
4.5	Conclusion.....	138



---

5	Design Considerations .....	140
5.1	Intention.....	140
5.2	Transferability of Test Conditions.....	140
5.3	Comparison with Existing Design S-N curves .....	145
5.4	Derivation of Design Recommendations.....	148
5.5	Conclusion.....	153
6	Summary and Outlook .....	155
6.1	Summary.....	155
6.2	Outlook.....	158
7	List of References .....	161
7.1	Standards, Codes of Practice and Laws.....	161
7.2	Book, Articles and Handbooks.....	165
7.3	Product Information and Data Sources.....	175
8	Lists.....	176
8.1	List of Figures.....	176
8.2	List of Tables.....	181
	Curriculum Vitae.....	210

## List of Abbreviations and Symbols

### Latin symbols

$e_{gp}, e_{gs}$	[mm]	grout end pile, grout end sleeve in the test specimens
$f_a$	[MPa]	interface transfer stress
$f_{bk}$	[MPa]	interface shear capacity
$f_{bu}$	[MPa]	ultimate bond strength
$f_c$	[MPa]	uniaxial concrete compressive strength
$f_{c,cube,75}$	[MPa]	uniaxial concrete compressive cube strength with an edge length of 75 mm
$f_{c,cyl}$	[MPa]	uniaxial concrete compressive cylinder strength
$f_{c,prism}$	[MPa]	uniaxial concrete compressive prism strength
$f_{cc}$	[MPa]	biaxial concrete compressive strength
$f_{ck}$	[MPa]	characteristic concrete cylinder compressive strength
$f_{ck}$	[MPa]	fatigue concrete compressive strength
$f_{ct}$	[MPa]	uniaxial tensile concrete strength
$f_{ct,fl}$	[MPa]	bending tensile concrete strength
$f_{cu}$	[MPa]	compressive concrete strength
$f_d$	[MPa]	design interface strength
$f_g$	[MPa]	characteristic interface transfer strength
$f_{g, shear}$	[MPa]	interface transfer strength for grout matrix failure
$f_{g, sliding}$	[MPa]	interface transfer strength for sliding between grout and steel
$f_{uk}$	[MPa]	steel tensile strength
$f_{yk}$	[MPa]	steel yield strength
$h$	[mm]	shear key height
$h_{a,fl} h_{p,fl} h_{s,fl}$	[mm]	flange height (a = adapter, p = pile, s = sleeve)
$k$	[N/mm]	stiffness
$k_{LiV}$	[N/mm]	stiffness based on vertical laser (i = 1 or 7)
$k_{rel, LiV}$	[N/mm]	related stiffness development based on vertical laser (i = 1 or 7)
$n$	[-]	number of shear keys
$n'$	[-]	cyclic hardening exponent
$s$	[mm]	shear key distance
$t, t_a, t_{a,pl}, t_g,$ $t_p, t_{pl}, t_s$	[mm]	thickness (a=adapter, a,pl = adapter plate, g = grout, p = pile, pl = plate, s = sleeve)
$u$	[mm]	vertical relative displacement
$u_c, u_t$	[mm]	vertical relative displacement (c = compression; t = tension)
$u_{c,max}, u_{t,max}$	[mm]	maximum displacement (c = compression; t = tension)
$u_{IST}$	[mm]	displacement by load cylinder of Instron (IST) testing rig
$w$	[m]	water depth

---

w	[mm]	shear key width
w/c	[-]	water/cement ratio
$W_{a, fl}, W_{p, fl}, W_{s, fl}$	[mm]	flange width (a = adapter, p = pile, s = sleeve)
v	[mm]	radial displacement
A	[%]	elongation
A	[MPa]	shear envelope exponential coefficient
B	[1/MPa]	shear envelope exponent
$C_L$	[-]	ratio of overlapping length to pile diameter Eq. 2-2
$C_p$	[-]	scale parameter accounting for the pile diameter Eq. 2-7
$C_s$	[-]	surface condition parameter
D	[-]	damage according to Palmgren-Miner
$D_a, D_{a,pl}, D_g, D_p, D_{pl}, D_s$	[mm]	diameter ( a = adapter, g = grout, p = pile, pl = plate, s = sleeve)
$D_m$	[-]	damage at each node m
E	[MPa]	elasticity modulus or Young's modulus
$E_c$	[MPa]	elasticity modulus of concrete
$E_{cm}$	[MPa]	mean elasticity modulus of concrete
$E_D$	[MPa]	reduced stiffness depending on the material damage $D_s$
$F_{bu}$	[-]	bond strength parameter
$F_c, F_t$	[MN]	axial load (c = compression, t = tension)
$F_{c,max}, F_{t,max}$	[MN]	maximum axial load (c = compression, t = tension)
$F_{IST}$	[MN]	load induced by the load cylinder of the Instron testing rig
$F_{ULS}$	[MN]	ultimate load capacity
$I_1$	[MPa]	stress invariant
$J_2, J_3$	[MPa]	stress invariants
K	[-]	radial stiffness
K	[-]	coefficient of hardening
K	[-]	strength related parameter for the Drucker-Prager criterion
$L_a$	[mm]	adapter length
$L_e$	[mm]	effective grouted connection length
$L_g$	[mm]	grouted connection length
M	[Nmm]	bending moment
N	[-]	endurable number of load cycles
N	[N]	normal load
$N_{eq}$	[-]	equivalent endurable number of load cycles
$N_i$	[-]	number of load cycles
$N_{ref}$	[-]	reference number of load cycles

---

$P_d$	[MN]	axial design load
$R$	[-]	stress ratio according to Figure 2-5
$R_a$	[ $\mu\text{m}$ ]	arithmetic roughness surface
$R_c$	[-]	compaction cap parameter
$R_{eH}$	[MPa]	yield point
$R_{em}$	[MPa]	tensile yield strength
$R_p, R_s$	[mm]	radius (p = pile, s = sleeve)
$R_q$	[ $\mu\text{m}$ ]	root mean square roughness
$R_t$	[ $\mu\text{m}$ ]	maximal roughness height
$R_t$	[-]	expansion cap parameter
$R_z$	[ $\mu\text{m}$ ]	surface roughness
$S$	[-]	stress level
$S_{\text{amplitude}}$	[MPa]	stress amplitude
$S_{c,\text{max}}, S_{c,\text{min}}$	[MPa]	maximum and minimum compressive stress level
$W_t$	[ $\mu\text{m}$ ]	total waviness
$X_i$	[MPa]	compaction cap yield pressure
$Z$	[ $\mu\text{m}$ ]	profile height

### Greek symbols

$\alpha$	[ $^\circ$ ]	compression strut angle
$\alpha$	[-]	parameter for the Drucker-Prager criterion Eq. 2-20
$\alpha$	[-]	shear envelope linear coefficient for Extended Drucker-Prager
$\alpha_{c,i}$	[ $^\circ$ ]	compression induced compression strut angle $i = 1$ to $3$
$\alpha_{t,i}$	[ $^\circ$ ]	tensile induced compression strut angle $i = 1$ to $3$
$\beta_{cc}(t)$	[-]	function to describe the development with time
$\gamma$	[-]	partial safety factor
$\delta$	[-]	surface irregularities
$\varepsilon_a$	[ $\mu\text{m}/\text{m}$ ]	strain amplitude
$\varepsilon_{el}, \varepsilon_{pl}$	[ $\mu\text{m}/\text{m}$ ]	elastic and plastic strain part
$\varepsilon^{\text{fat}}$	[‰]	irreversible strain
$\varepsilon_z$	[ $\mu\text{m}/\text{m}$ ]	longitudinal strain
$\varepsilon_\theta$	[ $\mu\text{m}/\text{m}$ ]	hoop strain
$\theta$	[ $^\circ$ ]	lode angle
$\mu$	[-]	coefficient of friction
$\nu$	[-]	poisson's ratio
$\xi$	[-]	hydrostatic axis
$\rho$	[ $\text{kg}/\text{m}^3$ ]	density
$\sigma$	[MPa]	stress

---

$\sigma_a$	[MPa]	stress amplitude
$\sigma_c$	[MPa]	cohesion yield parameter for the Extended Drucker-Prager model
$\sigma_{lat}$	[MPa]	lateral stress
$\sigma_{max}$	[MPa]	maximum stress
$\sigma_{mean}$	[MPa]	mean stress
$\sigma_{min}$	[MPa]	minimum stress
$\tau$	[MPa]	shear stress
$\psi$	[-]	ratio of extension to compression strength

### Abbreviations

ALS	Accidental limit state
API	American Petroleum Institute
BSH	Bundesamt für Seeschifffahrt und Hydrographie
DLC	Design load case
DNV	Det Norske Veritas
EEZ	Exclusive Economic Zone
FAT	Fatigue design detail category
FEM	Finite Element Method
FLS	Fatigue Limit State
GL	Germanischer Lloyd
HAC	High-Alumina Cements
HPC	High Performance Concrete
HSC	High Strength Concrete
HSE	Health & Safety Executive
ISO	International Organization for Standardization
JIP	Joint Industry Project
LRFD.	Load and Resistance Factor Design
LS	Load Stages
MSL	Mean Sea Level
NSC	Normal Strength Concrete
OPC	Ordinary Portland Cements
OWT	Offshore Wind Turbine
O & G	Oil and Gas
SLS	Serviceability Limit State
TS	Test Specimen
UHPC	Ultra High Performance Concrete
ULS	Ultimate Limit State



# 1 Introduction

## 1.1 Motivation

Animated by the climate change and the growing environmental sensibility, a sustainable development using renewable energy resources is pursued. This is manifested by several international agreements and national targets. For instance, the European Commission (2010) aspires to increase the share of regenerative electrical energy consumption by 2020 to 20%. Even more ambitious aims are set by the German government (2013) intending to achieve a 40 to 45% renewable electrical energy use by 2025. Consequently, renewable technologies need to be extensively expanded within the next decades. Due to the limitations for biomass, water power, solar energy, and locations for onshore wind energy converters, the largest contribution to electricity from renewable energy sources in Germany has to be provided by the offshore wind energy. The first offshore wind farm alpha ventus, cf. Figure 1-1, was erected in 2010 consisting of 12 offshore wind turbines (OWT) with a nominal power of 5 MW per turbine. By the end of 2015, 3.3 GW nominal offshore wind capacity were installed, cf. German Windguard (2015). In view of the targeted 6.5 GW in 2020 and 15 GW in 2030, cf. EEG (2014), numerous offshore wind farms with thousands of OWTs have to be erected in the German North and Baltic Sea.



**Figure 1-1. Offshore wind energy turbines at the wind farm alpha ventus (photo: Bechtel).**

Although at offshore locations the energy generation is - due to less wind turbulences and higher wind speeds - more efficient, the offshore specific conditions provoke severe technical and logistical challenges. Beside the weather dependent transport, installation, and monitoring issues, the salinity and cyclic character of the environmental and operational impacts are highly demanding for the durability of offshore constructions. As a result, complex loading situation consisting of cyclic axial and lateral loads as well as bending and torsional moments from wind, wave and turbine operation have to be transferred by the support structure to the subsoil.

In principle, support structures of offshore wind energy converters consist of the tower, the substructure and the foundation being commonly realised by piles driven into to the subsoil.

For the connection of foundation and tower different substructure concepts have been developed in dependence on the water depth. Within the last years, the monopile foundation, consisting of a single driven pile being connected by a transition piece to the tower, became the preferred solution for water depths up to ~30 m. Notwithstanding, its application is limited at present for economic and installation reasons to these water depths. Thus, entering deeper waters for the offshore wind energy expansion provoked the establishment of latticed substructures like jackets or tripods. While tripods are composed by a three-legged steel construction with the central node below sea level, jackets represent a spatial framework consisting of numerous steel tubes bracing usually four main legs. Compared to monopiles, latticed substructures generally comprise less steel related to their substructure stiffness.

For the conjunction of substructure and foundation piles the well-known grouted connection was adopted from offshore oil & gas (O&G) platforms, as it entails the advantage to overcome driving induced pile inclinations. Grouted connections are composed of two cylindrical steel tubes with different diameter overlapping each other and having the annulus filled with high strength grout. As multiple pile inclinations have to be compensated considerable large grout annuli are required at latticed substructures. For an adequate load transfer so-called shear keys as weld beads are placed circumferentially on the opposing surfaces of the steel tubes. These shear keys increase the interlocking of the cylindrical steel tubes with the grout layer.

While for monopile substructures alternative solutions like ring flange or conical grouted connections are discussed, these options are not applicable to latticed structures. The ring flange connection is not suitable, because a set of pile inclinations have to be compensated exceeding the tolerances of bolted connections. Additionally, the use of bolts far below sea level represent not a reasonable option regarding installation and maintenance. The conical grouted connection as second alternative is limited to the monopile being exposed merely to axial compression and predominant bending moments. In contrast, connections in jackets and tripods are prevalently exposed to cyclic axial alternating loads due to the push-pull mechanism of the framework-like structure.

Recommendations for the design of grouted connections are presented in DIN EN ISO 19902 (2014), DNV-OS-J101 (2014), GL Guideline (2012), GL Technical Note (2013) and Norsok Standard N-004 (2013). Even though these design codes were to some extent amended recently due to failure of grouted connections at monopiles for offshore wind turbines, the current procedure emphasises the complexity and existing uncertainty with regard to the design. Currently, an approval in the individual case for the type of construction grouted connection and for the material grout has to be obtained for every German offshore wind farm and offshore substation. Reason for this is that neither the mentioned guidelines are listed in the "List of Technical Building Rules", DIBt Technische Baubestimmungen (2015), nor the material is listed in the "Construction Products Lists", DIBt Bauregellisten (2015), of the German Institute for Structural Engineering (DIBt).

As the axially loaded grouted connection was originally used for O&G platforms, corresponding testing in the 1970's and 1980's essentially constituted the basis for present design formulations. Notwithstanding, unlike prevalent static loading induced by the heavy



O&G platforms, additional, more demanding cyclic loads arise at grouted connections of OWTs. Thus, former design formulations were adapted within the last decade to account for the dominating environmental and operational induced cyclic load situations at offshore wind turbines. However, the conducted investigations primarily focussed on the load bearing behaviour and fatigue performance of grouted connections in monopile substructures being predominantly subjected to cyclic bending moments. For instance, research activities by Schaumann et al. (2011b) dealt with the optimisation of this type of connection by considering the impact of a reduced overlapping length, the strength of different grout materials and the application of shear keys by using large-scale tests.

As the majority of future wind farms in Germany will be installed in deeper waters, the latticed substructure concept will become a more common solution. The impact of the large grout thickness on the fatigue behaviour of grouted connections being subjected to cyclic reversal loading conditions exceed the present range of design limitations and experience, and is thus associated with great uncertainties. With the intention to determine the fatigue behaviour and to evaluate the applicability of current design approaches for grouted connections in latticed substructures, the joint research project "GROWup - Grouted Joints for Offshore Wind Energy Converters under reversed axial loadings" was initiated constituting the basis of this thesis.

## 1.2 Objective

The objective of this thesis is to determine and evaluate the fatigue behaviour of predominantly cyclic axially loaded grouted connections with large grout thicknesses in latticed substructures of offshore wind turbines.

While former investigations addressed geometrical configurations and load conditions for monopiles and O&G related grouted connections, experimental tests covering present dimensions and cyclic loading situations of grouted connections in latticed substructures for OWTs are required. Thus, the focus of investigations has to be set on the impact of increased grout thicknesses on the fatigue behaviour for identifying relevant failure mechanisms. Moreover, material and geometric related impacts on the fatigue behaviour need to be identified. Within these tests, a cyclic axial alternating and pulsating compression loading has to be considered representing the dominating load conditions occurring at framework-like constructions. While current design approaches originate from former investigations, their applicability for grouted connections in latticed structures at OWTs is currently insecure, because these do not cover present dimensions in any case. Consequently, on the basis of new and more reliable experimental tests and their results a comparison with current design approaches is necessary to clarify their appropriateness.

For further design purposes, numerical investigations become essential, as the finite element method represents a common tool for assessing the complex and highly non-linear bearing behaviour of grouted connections. In order to consider the confined grout layer, multiaxial stress states need to be considered with regard to the material behaviour of high strength grouts. In view of the fatigue behaviour, it would be further beneficial to account for material

strength and stiffness degradation induced by repeated loading to determine the fatigue strength of the connection by numerical simulations. By validation of the numerical model and the cyclic degradation calculation procedure, extended parametric studies are possible allowing to evaluate the main influencing parameters. Finally, achieved results need to be transferred to offshore conditions with the target to derive adequate design recommendations for grouted connections with large grout annulus in latticed substructures.

Based on previous outlined demands for scientific investigations, the following leading questions for axially loaded grouted connections with increased grout thicknesses at offshore wind turbine structures can be summarised:

- What effect do large grout thicknesses have to the load bearing and fatigue behaviour?
- What are the specific failure mechanisms with respect to the grout thickness?
- Which material and geometrical related parameters influence the fatigue behaviour?
- What impact have alternating and pulsating compression loads to the load bearing and fatigue behaviour?
- Are current analytical design recommendations applicable for grouted connections with increased grout layers?
- Which available numerical material models describe the multiaxial stress states of high strength grout sufficiently?
- How can the cyclic degradation be considered by numerical methods?
- Does the load sequence have an impact on the fatigue behaviour?

These questions shall be investigated and answered based on experimental and numerical investigations as outlined subsequently.

### 1.3 Structure

Initially the current state of the art and state of the scientific knowledge for axially loaded grouted connections is presented in **chapter 2**. Earlier research investigations and experimental tests obtained for monopiles and O&G platforms are set in contrast to the present dimensions and load situations at grouted connections in lattice substructures in order to identify unresolved issues and to clarify the background of current design recommendations. Moreover, the load bearing behaviour as well as the material specific fatigue behaviour are outlined, as these significantly influence the fatigue behaviour of grouted connections.

With reference to the pending questions and tasks, experimental investigations are introduced in **chapter 3**. The test adaptation and test load scenarios are developed in reference to dimensions and load cases at offshore substructures. Moreover, the fatigue test results are presented and assessed by focusing on the most important questions about the fatigue behaviour of grouted connections with increased grout thickness.

**Chapter 4** contributes to extend the knowledge by use of numerical investigations. Finite element models are validated and used for parametric studies. As present design concepts rely on numerical calculations, the focus is set on identification and adaptation of reliable material

models accounting for multiaxial stress states in the high strength grout. In addition, it is pursued to account for cyclic induced material strength and stiffness degradation, which enables to cover the fatigue behaviour of grouted connections by finite element simulations.

Achieved findings of the experimental and numerical investigations are combined in **chapter 5**. In order to derive design recommendations based on the observed results, used test conditions are set in contrast to the actual offshore conditions. Moreover, test results are compared to current design approaches. In consequence, these considerations on test results, offshore conditions and design concepts allow the derivation of design recommendations for grouted connections in latticed substructures.

Finally, performed investigations and achieved results are summarised in **chapter 6**. Apart from that, an outlook on future investigations is given.

## 2 State of the Art

### 2.1 Grouted Connections in Offshore Support Structures

#### 2.1.1 Offshore support structures

Support structures at offshore locations require a stable foundation to resist the environmental loads, especially from wind and wave actions. Bottom-fixed offshore constructions, such as oil and gas (O&G) platforms, substations or offshore wind turbines (OWT), can be realised by a piled, gravity based or suction bucket foundation. Currently, the preferred solution for offshore support structures in the North and Baltic Sea represents the pile foundation, whereby piles are driven into the subsoil. For the conjunction of the support structure to the piles, grouted connections have been widely used in the O&G industry. Because O&G platforms are located in large water depths, the platform deck is welded to leg piles of a steel framework, which is connected by a set of legs to the driven piles by the grouted connection, cf. Figure 2-1 left. Each grouted connection is composed of two steel tubes with varied diameter overlapping each other and having the annulus filled with a cementitious material.

During the last decade, this type of constructional detail became a favourable solution for offshore support structures of wind turbines and transformer platforms, as it entails the advantage to overcome driving induced pile inclinations. The first offshore wind project that was built with a grouted connection, although with additional load transfer mechanism, was the Utgrunden wind farm, installed in Sweden in 2000. A monopile substructure was used due to the comparably shallow water depth of  $\sim 10$  m. Even though the monopile foundation, cf. Figure 2-1, became the preferred solution for water depths up to  $\sim 30$  m within the last years, its application to larger water depths is limited due to installation techniques and economic reasons.

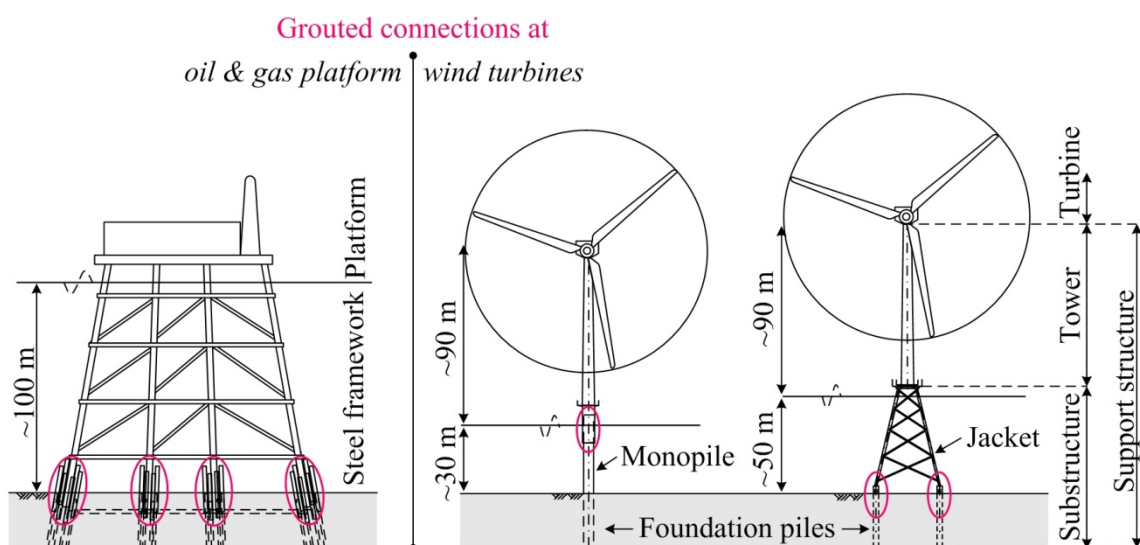


Figure 2-1. Grouted connections at offshore oil & gas platforms (left) and offshore wind turbines with monopile and jacket (right) based on Lamport (1988) and Schaumann et al. (2010b).

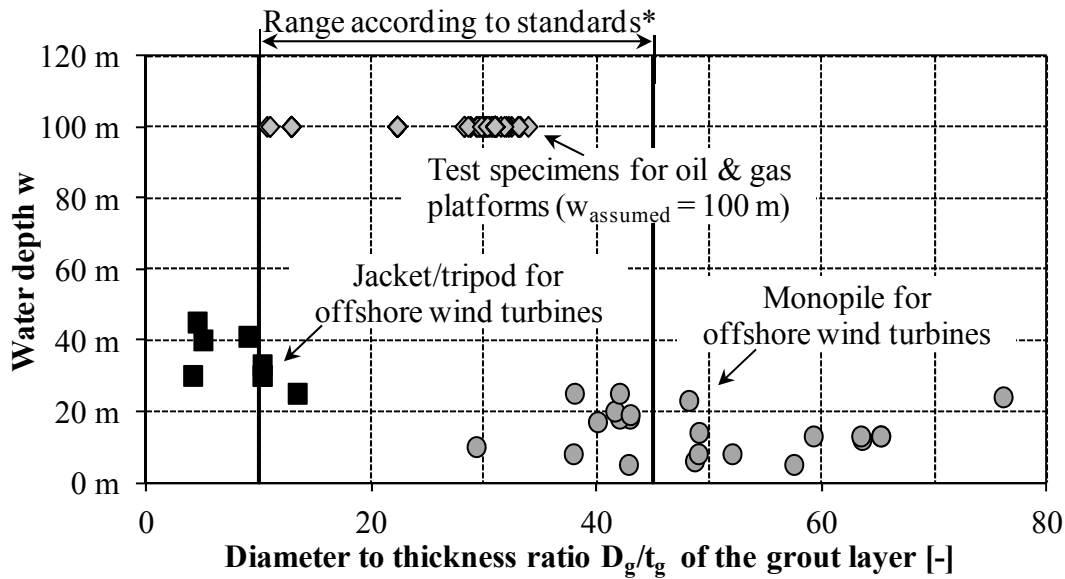
Entering larger water depth for the expansion of the offshore wind energy provoked the establishment of latticed structures, such as jackets or tripods, cf. Schaumann et al. (2011a). The latest statistical survey by the European Wind Energy Association (2016) reflects that apart from the monopile, the jacket is preferably installed in Germany and in Europe by the end of 2015. The spatial framework comprises less steel related to the overall bearing resistance. However, as latticed substructures consist of a set of legs, a set of pile inclinations have to be compensated simultaneously by the grouted connections. For this purpose, a large annulus between leg and driven pile is required, especially in cases of pre-piled installation methods, where the pile is driven prior to the erection of the substructure. Moreover, in contrast to monopiles, which are predominantly exposed to bending moments, grouted connections in lattice structures experience prevalingly axial loads. The connection dimensions and occurring load conditions vary significantly to grouted connections in monopile substructures of offshore wind turbines and to grouted connections at O&G platforms. The latter are subjected to dominating static from the heavy platform and less cyclic loads. Hence, the construction of today's grouted connections in latticed substructures, its dimension, used materials, occurring loads and load effects are introduced in the following by setting them in contrast to connections used for monopiles and O&G platforms regarding the chronological development.

### 2.1.2 Constructions and dimensions

The majority of offshore O&G platforms in the North Sea are fixed by tubular steel piles, which are commonly arranged as a set of piles at each leg of the lattice structure. The piles are driven through a set of sleeves being attached by shear plates at the lower part of the main legs. The annulus between pile and sleeve is filled with cement slurries, such as portland or high alumina cements. The pile diameter varies from 1'000 to 2'000 mm having a diameter to thickness ratio  $D_p/t_p$  between 20 and 45, cf. Elnashai & Dowling (1991).

Because the sleeves at the main legs are used as driving template for the piles, the grout annulus is small compared to current grouted connections in latticed wind turbines. The diameter to thickness ratio for the grout annulus  $D_g/t_g$  for these types of connections is commonly not smaller than 10. Test specimens used to analyse the load bearing behaviour of grouted connections of O&G platforms have a diameter to thickness ratio of 10 to 40, cf. Figure 2-2. Even though these tests, which are not representative for wind turbines, have been published in the 1970's and 1980's by authors such as Billington (1978) or Elnashai et al. (1986), their geometrical validity limits still constitute the basis of today's offshore guidelines.

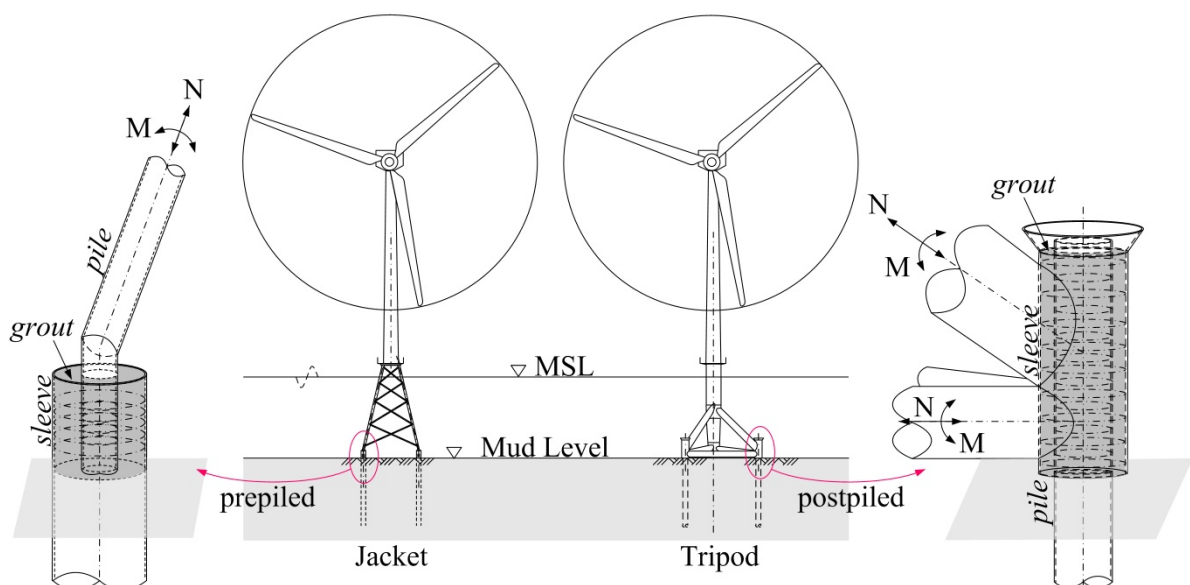
By using the grouted connection for mono-founded offshore wind turbines, the geometrical dimensions were scaled up significantly. The monopile, which is driven into the seabed, has nowadays a diameter of up to 8'000 mm in water depths of  $\sim 30$  m. According to Lochte-Holtgreven (2013), the pile diameter to thickness ratio  $D_p/t_p$  of executed offshore wind turbines is in the range of 60 to 110, which is far beyond limits known from the oil and gas platforms. Nevertheless, the grout thickness for monopiles is relatively small with thicknesses of up to 120 mm and a related diameter to thickness ratio  $D_g/t_g$  of 30 to 80, cf. Figure 2-2.



\* Norsok (2014), DNV-OS-J101 (2014), DIN EN ISO 19902 (2014)

**Figure 2-2.** Comparison of diameter to thickness ratios  $D_g/t_g$  and water depths for varied grouted connections in accordance with 4coffshore-database (2015), Lochte-Holtgreven (2013), alpha ventus (2012), Ingebrigtsen et al. (1990), Sele & Kjoey (1989), Boswell & D'Mello (1986) and Elnashai et al. (1986).

The compensation of more than one inclined pile at multi-pile foundations requires a larger grout annulus. Grout thicknesses of modern jacket and tripod structures amount to 300 to 500 mm. Hence, the  $D_g/t_g$  ratio results to values lower than 10. Unlike for monopiles, where the pile is driven prior to the installation of the remaining support structure, for latticed structures it can be chosen between pre- or post-piled installation procedures. That means that the piles are either installed prior or subsequent to the substructure erection. Figure 2-3 shows exemplarily a pre-piled grouted connection (left) for the jacket substructure and a post-piled grouted connection (right) for the tripod substructure.



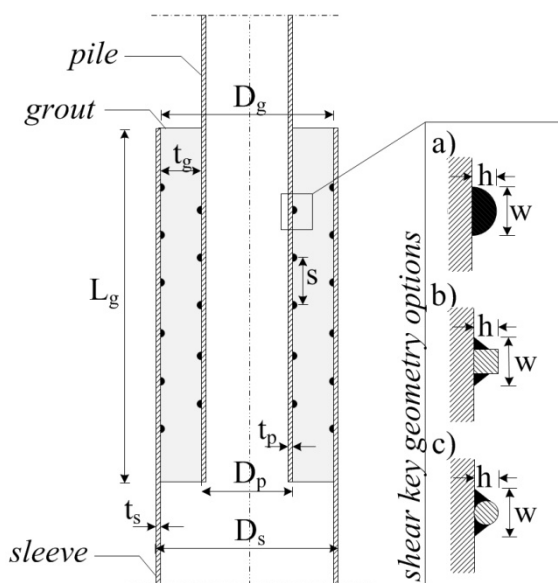
**Figure 2-3.** A jacket with a pre-piled grouted connection (left) and a tripod (right) with a post-piled grouted connection at offshore wind turbines adapted from Schaumann et al. (2012a).

The piles for the pre-piled jacket structure are driven by using a template. After pile driving, the jacket is positioned and levelled. Hereby, the driven pile acts as sleeve and the jacket leg as inner steel tube, being officially called grout-pin. At post-piled structures, the substructure is used as driving template. For that purpose, tubular steel sleeves as pile guides are arranged at the bottom of the substructure. Even though the prepiled grouted connection usually consists of the pile being driven into the seabed and a grout pin placed inside the pile, hereafter for pre- as well as for post-piled connections uniform terms shall be used. The inner steel tube is named the pile (p) and the outer steel tube is denoted as the sleeve (s), irrespective of the installation type, cf. Figure 2-3.

Independent of the installation procedure, after positioning and adjusting the substructure by hydraulic jacks, the annulus is filled from bottom-up with cementitious based grout. With regard to connections at tripod or jacket substructures, the grout is mixed above the water level at the installation vessel. Hence, the material has to be pumped over a long distance through the hose to the filler neck at the bottom of the grouted connection. The installation process requires the material to have sufficient flowability and an adequate consistency to be fluid and unmixed until the grouted connection is totally filled up with the material. Because the initial layer will be impaired by sea water and binder, the filling process ends by a predefined overflow of the disturbed material. Nevertheless, for the design a reduced overlap length is taken into account.

Depending on the installation type and the overall design of the support structure, the tubular steel sleeves have diameters in the range of  $D_s = 2'000 - 3'500$  mm. The steel pile diameter varies between  $D_p = 1'000 - 2'500$  mm. The steel tubes have thicknesses of approximately  $t_s = t_p = 50 - 70$  mm. In addition to the diameter and thickness, the grouted connection is described by the overlapping length  $L_g$  which represents the load transferring grouted length.

For an adequate load transfer and bearing capacity, additional weld beads are commonly arranged at both steel tubes. These so-called shear keys are placed diagonally opposite to each other on the facing surfaces of the steel tubes in the grouted section. The geometry of shear keys can either be a) a weld bead, b) a square bar or c) a round bar welded to the steel tubes, cf. Figure 2-4. The dimensions are described by the shear key height  $h$ , the shear key width  $w$  and the shear key distance  $s$ , cf. Figure 2-4. Schaumann & Wilke (2006) recommend applying the shear keys in the centre of the grouted connection at constructions which are exposed predominantly to bending moments, e.g. monopiles. As grouted connections in



**Figure 2-4. Geometric parameters and shear key geometry options: a) weld bead, b) square bar, c) round bar, for grouted connections referring to DIN EN ISO 19902 (2014).**

latticed structures are prevalingly exposed to axial loads, shear keys are applied equidistant over the connection length. Nonetheless, any material inconsistencies and misalignments from the perfect location in the upper and lower region have to be taken into account while locating the shear keys. Therefore, current standards, such as DIN EN ISO 19902 (2014) recommend to reduce the total length  $L_g$  by the larger value of either two times the grout thickness ( $2 \cdot t_g$ ) or the shear key distance  $s$  to an effective length  $L_e$ . Apart from that, in the GL Technical Note (2013) the application of horizontal and vertical shear keys is recommended. However, the impact of both, vertical and horizontal shear keys on the load bearing behaviour, and especially the fatigue resistance of crossing weld beads is not known. The former construction of cylindrical grouted connections without shear keys, transferring the loads only by friction in the intersection of grout and steel, are not any more installed, as slippage has occurred at some locations, cf. Schaumann et al. (2010a). As alternative to cylindrical grouted connections with shear keys, conical solutions were developed for monopiles.

Moreover, the position of the grouted connection with respect to the water level has a substantial effect. As grouted connections in monopile structures are located in the splash zone, grouted connections in latticed structures are totally submerged. The position depicts a technical challenge with regard to the installation process and has a considerable influence to the load bearing behaviour. Initial research results for the latter task are published by Schaumann et al. (2014a) and Schaumann et al. (2016). However, the influence of water to the fatigue behaviour is subject of ongoing research and not in the focus of this thesis.

### 2.1.3 Materials

Grouted connections represent a hybrid connection consisting of two different materials, the tubular steel and the cementitious based filling material. The load bearing behaviour is influenced by both material characteristics and their interrelation being reflected by contact properties. The used materials have to meet offshore specific requirements. Not only during operation, but also during installation, specific material characteristics are requested to constitute the basis for an adequate load bearing behaviour. In the following the applied materials and their specific properties and requirements are outlined.

#### *Steel*

Offshore wind turbines are exposed to extreme climate and cyclic loading conditions. Therefore, high demands concerning the structural safety and reliability of the steel components in the support structure have to be considered. Offshore specific requirements such as strength, toughness especially at low temperatures, suitability for welding and cold deformability are defined by current standards, e.g. BSH Standard (2015), DNV-OS-J101 (2014), GL Guideline (2012), DIN EN 10225 (2009) and DIN EN 10025 (2011). For the choice of the steel material, the structural component category being defined by the importance of the structural member, the occurring loads and stress levels, the offshore specific material characteristics and the structural properties need to be considered. According to the GL Guideline (2012), three different categories for steel components are defined: special, primary and secondary structural steel members. For each of these categories the



strength classifications, either high ( $f_{yk} > 380$  MPa), higher ( $f_{yk} = 285 - 380$  MPa) or normal yield strength  $f_{yk}$  ( $f_{yk} < 285$  MPa), as well as relevant codes and the designation of the material are stated. The ranking of the structural component categories represents the importance of the steel member to the overall integrity of the structure. Special structural members are exposed to complex conditions, e.g. stress concentrations, and are essential to the overall integrity, i.e. a failure of these members leads to an overall failure of the structure. Primary structural members are important for the operational safety, but are not as sensitive as special structural members. That means the load situation is comparable to special structural members, but small irregularities such as cracks or local dimples do not have the consequence of an overall failure. The last category is reflected by secondary steel members which are less relevant for the overall integrity. Accordingly, these members are not required for the operation of the structure. The steel tubes of grouted connections are exposed to cyclic loads and are important for the load bearing capacity. But, local damages do not lead to a subsequent overall failure of the structure. Therefore, the steel tubes of grouted connections can be classified as primary structural members according to GL Guideline (2012).

Depending on the structural component category, the choice of structural steel strength is defined. For steel tubes of grouted connections, which are exposed to fatigue loads, it is recommended to use steel structures not exceeding a yield strength of 355 MPa, cf. GL Guideline (2012). Commonly, the steel grades S235 or S355 are used. In addition to the material strength being defined by the yield strength  $f_{yk}$  and tensile strength  $f_{uk}$ , the through thickness properties, related carbon equivalent, the yield strength ratio and the impact energy are of significance for the steel of offshore structures. Specific material characteristic values and chemical compositions are outlined in detail in DIN EN 10025-4 (2005) and DIN EN 10225 (2009). For additional information reference is made to the offshore specific codes, BSH Standard (2015), DNV-OS-J101 (2014) and GL Guideline (2012).

With regard to the environmental offshore conditions, steel structures have to be equipped with several corrosion protection systems. Different systems are available such as coatings, sacrificial anodes, cathodic protection and corrosion allowance. In most cases a combination of previously named systems is applied to offshore steel structures. For the application of corrosion protection systems, the component location presents a decisive factor. Here, it is distinguished between the splash zone and components being permanent below or above the water level. Typical passive corrosion systems such as coatings are defined by DIN EN ISO 12944 (2008). DIN EN 12495 (2000) contains guidance on active corrosion systems such as sacrificial anodes. Grouted connections at latticed structures are located in a uniform circumference being fully submerged close to the sea ground. A coating is only applied on the outside of the steel tubes in the upper half of the substructure. Commonly, submerged parts are equipped with anodes. Surfaces which are in contact with the cementitious material shall be free of any coating, free of loose material, mill scale, grease or any other material that may influence the friction coefficient leading to unknown friction conditions. Moreover, coatings may react to some extent with cementitious materials provoking discontinuities, cf. Domone & Jefferis (1994).

### ***Cementitious material***

Different cementitious materials can be used to fill the gap between the steel tubes of the driven pile and the substructure. Grouted connections in O&G platforms are usually filled with normal and higher strength cementitious grouts based on different cements without any extra application of aggregates. Common materials used for O&G platforms were ordinary portland cements (OPC), high-alumina cements (HAC) and oilwell cements, cf. for instance Billington & Tebbett (1980), Lamport (1988).

For the highly cyclic loaded offshore support structures of wind turbines specialised high strength materials having self-compacting properties are applied nowadays. Contrary to former cement-slurries, today's high strength grouts include aggregates with a grain size up to 6 mm. High strength materials were improved especially with regard to an increased compressive strength being accompanied by sufficient workability and reduced shrinkage. As an alternative, additional supplements as steel fibres can be added to the material to enhance the connection's bearing resistance. Despite a possible resistance increase and a modified crack behaviour of the grout by steel fibres, their influence to the workability is detrimental, cf. Anders (2007). Due to this contradicting effects, an explicit enhanced load bearing behaviour by steel fibres is not finally proven, cf. Lohaus et al. (2012).

Recently, the research investigations of the research project GROWup were extended to investigate the applicability of OPC materials to grouted connections of offshore support structures for wind turbines, as these represent a cost-effective alternative to common high performance grouts. Nevertheless, during hardening of ordinary portland cements high temperatures are expected to develop causing significant cracks in particular for large grout annuli. Therefore, the applicability of cement-slurries like OPC's has to be proven and analysed carefully by experimental testing and intensive evaluation especially for large grout sizes as used in jacket structures.

A prerequisite for the material choice is that the material meets the requirements for the installation process and reliably fulfils the demands during the operation. Particularly with regard to grouted connections in latticed structures being located at the sea bottom, high demands are exposed to the grout material as post repair works and monitoring of the annulus is difficult and expensive to be realised. Consequently, specific material properties for the fresh and for the hardened condition need to be considered and addressed while choosing the material. An extensive overview of grouts and their properties, composition and application is presented by Domone & Jefferis (1994). Complementary, explanations and statements for modern high strength grouts used in offshore turbines are addressed by Lohaus et al. (2012).

For the grouting procedure at jackets and tripods, the ambient temperature and the distance between vessel and grouted connection at the sea bottom requires a material having a good workability for different temperatures and for a long pumping distance. As the material gets in contact with water, it needs to have a high sedimentation stability. Furthermore, the hardening process should be characterised by a low hydration temperature and low autogenous shrinkage. Earlier cement slurries were mixed by a comparable low water cement ratio to obtain a good unmixing stability (segregation stability) and higher density leading to

increased compressive strengths and reduced crack behaviour, cf. Lamport (1988). To achieve a low water cement ratio, concrete plasticizer and liquefier were added to the cement slurries. Today's offshore grouts contain an increased binder and powder amount compared to common concretes, which has a significant influence on the shrinkage behaviour of the material. High autogenous and drying shrinkage may reduce the load bearing strength as it entails a volumetric change which may be accompanied by cracking and adhesive bond loss. The choice of material and the testing prior to application have to account and ensure a low shrinkage behaviour of the grout. The shrinkage behaviour of high performance grout is subject of latest research by Lohaus & Weicken (2014). In addition, an early strength development is essential for the bearing capacity to reduce any early-age cycling effects. Unforeseen interruptions leading to a stop of the filling process may cause an inhomogeneous material or layering of the material, cf. Lohaus & Werner (2014), and thus need to be taken into consideration. Sufficient compressive and tensile strength as well as elasticity and transverse deformation strength needs to be fulfilled by the cementitious material. Finally, the material has to withstand cyclic loads appearing over the entire lifetime of the construction. Therefore, special attention has to be paid to the fatigue related and multiaxial material characteristics being addressed in chapter 2.4.2. The essential material characteristics for offshore structures being exposed to cyclic loads can be summed up as follows:

- strength development in particular time-, load- and temperature-dependent,
- fatigue strength, elasticity, shrinkage and creeping behaviour,
- flowability, pumpability, sedimentation / segregation stability in particular for submerged conditions,
- low hydration heat development and autogenous shrinkage.

The strength is substantial for the design and the evaluation of the fatigue performance of offshore grouts. Commonly, the uniaxial compressive strength of a cube with the edge length of 75 mm after 28 days is used. Cement slurries like OPC, HAC and oilwell cements have medium compressive strengths up to 80 MPa. Whereas high strength grouts have compressive strengths in the range of 80 to 200 MPa. Table 2-1 presents an overview of used filling materials and to some extent their essential properties. Beside the design relevant grout strength value, the strength development for different temperatures shall be considered. With regard to the strength development after curing, Model Code 2010 (2012) recommends an approximation function which is representative for the strength growth of high strength grouts.

To ensure and monitor the quality of the material, specific characteristics are controlled by testing fresh material and hardened reference specimens. Current requirements for grouts in offshore support structures are recommended by Lohaus et al. (2012) addressing the execution-, material- and strength-related demands.

**Table 2-1. Cementitious materials and relevant properties for offshore applications.**

Application	Materials*	Uniaxial compressive cube strength	Young's modulus	Water/powder ratio	Density	Aggregates/Grain size	Shrinkage classification**	Application thickness
		$f_c$ [MPa]	$E_c$ [Gpa]	w/c [-]	$\rho$ [kg/m <sup>3</sup> ]	[-]/ [mm]	[-]	[mm]
O&G	HAC	> 70	> 20	~ 0.4	1'990	no	n.a.	n.a.
	Oilwell B	> 60	> 10	0.3 - 0.4	2'040	no	n.a.	n.a.
	OPC (e.g. CEMI 52.5R)	> 52.5	> 10	0.4 - 0.5	1'980	no	n.a.	n.a.
OWT	Densit Ducorit <sup>®</sup> S5	> 120	~ 55	~ 0.06	2'440	0 - 5	SKVB I	n.a.
	Densit Ducorit <sup>®</sup> S2	> 90	~ 40	~ 0.06	2'385	yes	SKVB I	n.a.
	Densit Ducorit <sup>®</sup> D4	> 200	~ 70	~ 0.06	2'740	yes	SKVB I	n.a.
	BASF Masterflow <sup>®</sup> 9500	> 135	~ 50	~ 0.075	2'400	yes	n.a.	25 - 600
	BASF Masterflow <sup>®</sup> 9800	> 95	~ 30	~ 0.14	2'250	yes	SKVM 0	20 - 600
	Pagel <sup>®</sup> V1/30 HF	> 120	~ 41	~ 0.09	2'450	0 - 3	SKVM 0	30 - 300
	Pagel <sup>®</sup> V1/60 HF	> 110	~ 43	~ 0.09	2'450	0 - 6	SKVB 0	40 - 600
*Lamport (1988), Densit Ducorit <sup>®</sup> (2013), BASF Masterflow <sup>®</sup> (2015), Pagel <sup>®</sup> Data Sheet (2014 )								
**DAfStb cast concrete guideline (2006)								
n.a. = not available								

The application of available filling materials for grouted connections in offshore wind turbines erected in the EEZ are subjected to the permission by the Federal Maritime and Hydrographic Agency (Bundesamt für Seeschifffahrt und Hydrographie - BSH). For the material and the construction, a site specific approval in the individual case has to be granted by the agency, because neither the material nor the type of construction are listed in the List of Technical Building Rules, DIBt Technische Baubestimmungen (2015), or the Construction Products Lists, DIBt Bauregellisten (2015), of the German Institute for Structural Engineering (DIBt). The procedure as well as requirements to achieve the approval for the individual case are outlined by Lohaus et al. (2013) and Schaumann et al. (2013b). The applicability of high performance grout has to be assessed by considering the composition, properties and preparation according to the following national and international standards:

- DAfStb cast concrete guideline (2006),
- DIN EN 206-1 (2001),
- DIN EN 1992-1-1 (2011), and
- Model Code 2010 (2012).

### 2.1.4 Loads and load effects

Offshore support structures including the grouted connections have to be designed for loads which can be classified into the following categories:

- self-weight loads,
- environmental loads,
- operating loads,
- accidental loads, and
- installation loads.

In general, the structural resistance has to be verified by four different limit states, which are the ultimate limit state (ULS), the serviceability limit state (SLS), the fatigue limit state (FLS) and the accidental limit state (ALS), e.g. DNV-OS-C101 (2011). The limit state design is also called the load and resistance factor design (LRFD). In order to account for different load combinations and their probability of occurrence, so called design load cases are defined in offshore codes such as DIN EN 61400-1 (2011), DIN EN 61400-3 (2010), DNV-OS-J101 (2014), and GL Guideline (2012).

Offshore wind turbines are comparable slender structures which are only slightly affected by loads from the structure's self weight but are more influenced by environmental and operational loads. The environmental loads originate from wind, wave, current and, depending on the location, ice and seismic impacts. However, the loads cannot be directly superimposed to loads acting on the grouted connection due to the non-static characteristic and occurrence probability of the individual load components. Furthermore, the tower-like wind turbines are susceptible for dynamic excitation and thus, dynamic amplification of the loads has to be taken into account. Hence, integrated models incorporating the structural and mechatronical characteristics of the OWT are used to comprise the respective load actions with the corresponding time-dependent characteristic and occurrence probability cf. Böker (2009). The environmental loads are modelled based on related parameters such as the mean wave height, mean wind speed or turbulences intensity which are derived from met masts, measuring buoys and long-term statistics. By realistically accounting for the turbine's operation status, the model also enables to include the impact of harmonic excitations associated with the turbine's revolution speed as well as impacts from the start- or stop operation.

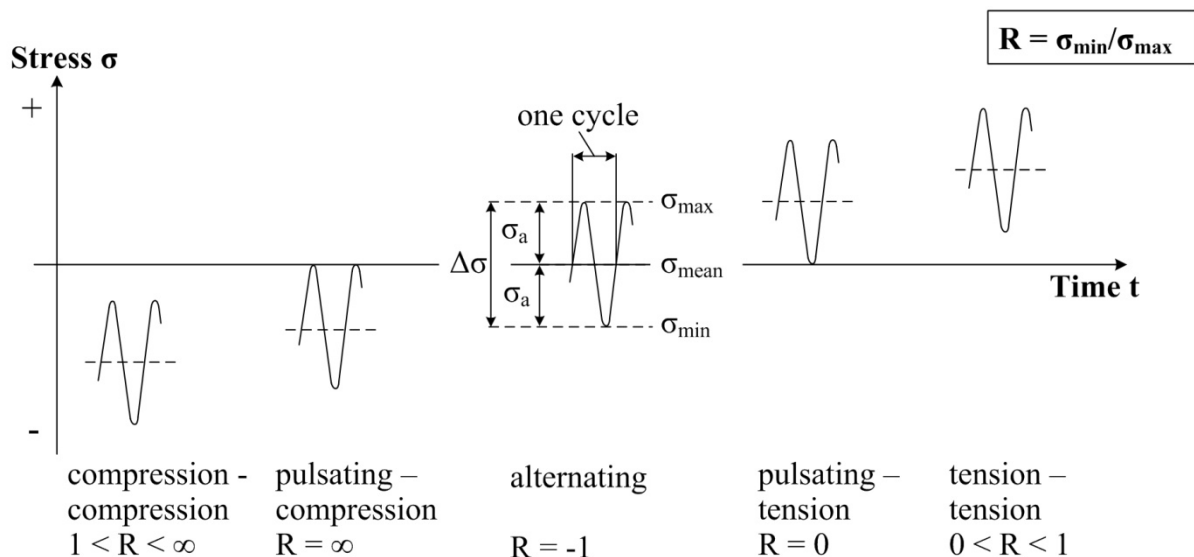
For the design of grouted connections, the ultimate limit state (ULS) and fatigue limit state (FLS) are of particular relevance. The ULS design accounts for extreme load scenarios caused by extreme manoeuvres of the turbine or by extreme wind and wave actions appearing in a certain time period, e.g. the 50 year gust or 50 year wave, cf. BSH Standard (2015).

The fatigue loading originates from the cumulative effect of all impacts occurring during the structural lifetime which is normally set to 20 to 25 years. Thus, smaller environmental loads which are temporally fluctuating and frequently occurring mainly contribute to the fatigue loading. Hence, the most fatigue load cases constitute normal operation of the turbine with associated environmental loadings by wind, wave and current. According to DNV-OS-J101 (2014), the load distribution shall, however, also be contributed by effects from turbine

operation and non-operation (idling and standing still), start, normal stop, control, protection and system faults, assembly and transport, maintenance and repair. Similar load cases have to be accounted for according to DIN EN 61400-3 (2010) and GL Guideline (2012).

For the determination of the fatigue loading, load time series originating from the integrated load simulations are analysed and multiplied by the respective frequency of occurrence. The number of load cycles within a load time series can be determined by counting the cycles between the peak values. Different counting methods exist, whereas the rainflow and reservoir method are the most common ones, cf. Almar-Naess (1985). In particular the two parameter rainflow method is favoured for offshore wind turbines, as this method enables to account for the mean stress values. The fatigue loading is usually comprised in so-called Markov matrices.

With regard to fatigue loads, the cyclic nature of these loads is of particular interest for the design and for experimental investigations. The cyclic loading is characterised by a sinusoidal function, whereas the upper peak reflects the maximum stress level  $\sigma_{\max}$  and the lower reverse point represents the minimum stress level  $\sigma_{\min}$ , cf. Figure 2-5.



**Figure 2-5. Stress ratio and cycles based on Almar-Naess (1985) and Radaj & Vormwald (2007).**

Especially for grouted connections, the mean value represented by the mean stress level  $\sigma_{\text{mean}}$ , and the stress amplitude  $\sigma_a$ , representing the difference between mean and maximum stress value, are of relevance, cf. Schaumann et al. (2011b). Anisotropic materials like concrete or grout as well as non-linear load transfer at contact interfaces are sensitive to changes of the mean stress value. With regard to the fatigue design, the stress ratio  $R = \sigma_{\min}/\sigma_{\max}$  is an important value, as it reflects the stress state being either in the range of compression or tension loading or in the intermediate state represented by alternating stresses, cf. Figure 2-5. The stress ratio of  $R = -1$  describes a stress state where the mean stress level is equal to zero and the amplitude in the tension and compression range is identical. Stress ranges where either the upper or the lower peak are equal to zero are called pulsating stresses. The impact of different stress ratios and occurring load situations to the bearing behaviour of grouted connections is outlined in chapter 2.2.5.

Compared to other civil engineering constructions, the support structure of wind turbines are exposed to an extensive number of load cycles. During the operational lifetime of the wind turbine, occurring number of load cycles amount to  $10^9$  load cycles, whereas other high cyclically loaded structures such as airplane runways, bridges and high speed lines experience load cycles of  $10^3$  to  $10^8$ , cf. Gasch & Tvele (2010). Hence, the fatigue limit state design is one of the crucial design aspects and thus the fatigue loads are compared to the resistance of the structure. In the past, so called S-N curves have been developed depicting the endurable number of load cycles corresponding to the stress amplitude. With regard to grouted connections some developments have been performed in the past, but until now no reliable basis for a general applicable S-N curve has been developed. Specific design and load bearing considerations are outlined in the following chapter 2.2.

## 2.2 Load Bearing Behaviour

### 2.2.1 Chronological research overview

Permanent and non-permanent loads provoke bending and torsional moments as well as compression and tension forces which are to be transferred by the grouted connection to the foundation piles. In general, the load transfer mechanism in grouted connections depends on the material characteristics, the connection geometry and the occurring load situations. In contrast to grouted connections in monopile substructures, being predominantly exposed to large bending moments, grouted connections in latticed structures with multiple foundation piles are prevalingly loaded by axial forces.

The research for axially loaded grouted connections at O&G platforms dates back to the 1960's when the oil and gas exploration started. During the period of 1960 to 1980 experimental investigations were carried out to investigate the bearing behaviour of grouted connections by performing small-scale, nearly full-scale and full-scale testing in several research projects. e.g. Billington (1978), Billington & Lewis (1978) and Lewis et al. (1980). These provide the basis for the corresponding earlier offshore standards by Health & Safety Executive (HSE), the International Organization for Standardization (ISO), the American Petroleum Institute (API) and the Det Norske Veritas (DNV). Even though a wide basis of experimental testing was conducted during that period, none of the tested constructions reflect the current geometrical constitution and load situation of grouted connection at offshore wind turbine support structures. Nevertheless, basic mechanism and correlations are supportive for understanding and evaluating the load bearing behaviour and appearing failure mechanism.

The first offshore wind turbines were installed by using the technology known from the O&G platforms. But as the support structure of a wind turbine is rather large and slender compared to the compact construction of an O&G platform, it had to be dealt with additional loads and different, more demanding cyclic load conditions. Thus, the first offshore wind farm Utgrunden, installed in 2000, was accompanied by a research project which had the aim to evaluate the long-term load bearing behaviour and to obtain knowledge about the occurring loads at offshore wind turbines, cf. Kühn (2001) and Cheng et al. (2005). Because the performance of grouted connections in offshore wind turbines was unknown until then,

additional load transferring mechanism were installed at the support structure in the offshore wind farm Utgrunden. However, this initial research investigation was followed by experimental testing conducted at the Aalborg University in 2001 to analyse the load bearing behaviour of grouted connections in monopile substructures for the offshore wind farm Horns Rev 1, cf. Tech-wise (2001). It was the objective of these experimental tests that the appearing loads, especially the bending moments, could be transferred by the grouted connection without severe damage over the lifetime of the structure. In addition to the experimental investigations, numerical calculations in the form of finite element analyses were conducted, cf. Andersen & Petersen (2004). With regard to the load transfer mechanism it was concluded from these investigations that the bending moments were transferred by a force couple occurring at the upper and lower end of the grouted connection and that shear keys can be omitted.

In 2003, the research work on grouted connections at the Leibniz University Hannover started with the objective to improve the design methods used for the fatigue design. As the grouted connection in monopile substructures became a standard solution, the focus of the second research project GROW starting in 2006 was set on the optimisation of this connection. The impact of a reduced overlapping length, the strength of different grout materials and the application of shear keys were investigated in large-scale test specimens being exposed to high cycle bending moments. The main research findings are outlined by Lochte-Holtgreven (2013), Wilke (2014) and the final report of the research project GROW, cf. Schaumann et al. (2011b). After first settlements of grouted connections in monopiles at the offshore wind farm Egmond aan Zee became public in 2009, the DNV initiated a joint industry project (JIP I), cf. Lotsberg et al. (2011), to investigate the cause of defects in detail by experimental and numerical investigations and discussions between experts from the industry, the research community and certification bodies. It became apparent that the axial load bearing capacity of cyclic loaded grouted connections in monopile substructures was overestimated by the design recommendations presented in DNV-OS-J101 (2004). JIP phase I was followed by a second phase of the joint industry project, cf. Lotsberg et al. (2013), focusing on the load bearing behaviour of grouted connections with shear keys. Outcome of these JIP projects were new design equations which are included in the updated standard of the DNV, cf. DNV-OS-J101 (2014). A third joint industry research project was initiated by the end of 2013, named JIP Grouted OPC Connections for Annuli of Large Dimension (JIP GOAL), being lead by RWE Innogy GmbH. This project is still in progress and investigates also grouted connections in jacket substructures for offshore wind turbines. Research findings by JIP GOAL are currently not public. Prior to this industry-related research project the research project GROWup performed by the Institute for Steel Construction and the Institute for Building Material Sciences at the Leibniz Universität Hannover started in 2011. The research project GROWup deals with the fatigue behaviour of grouted connections with large grout annulus and submerged conditions as well as the installation impacts on the grout characteristics. As a result, this research project constitutes the basis of this thesis, whereby parts of the experimental large-scale fatigue testing of grouted connection test specimens were used for the herein presented investigations.



From the historical overview it results that numerous experimental and numerical investigations for axially loaded grouted connection in O&G platforms and for grouted connections in monopiles for offshore wind turbines have been conducted. On the basis of these tests design recommendations in current design codes reflecting the state of the art and research were derived.

Previous research findings are summarised in the following sections by focusing on the decisive aspects of the load bearing behaviour, which are:

- the general load transfer mechanism and failure modes,
- the geometrical dimensions, e.g. overlapping length, slenderness, stiffness, shear keys,
- the material characteristics, e.g. grout strength, surface condition of the steel tubes, and
- the load conditions, e.g. timing and occurrence of permanent and non-permanent loads.

In consideration of the research task dealing with the fatigue behaviour of grouted connections in latticed substructures with large grout annuli, the overview is limited to predominantly axially loaded cylindrical grouted connections with shear keys.

### 2.2.2 Load transfer and failure modes

Axial loads in grouted connections with shear keys are transferred by frictional and interlocking forces arising at the grout steel interface and between the shear keys. The resulting interface strength between grout and steel depends on the surface conditions, radial stiffness, applied shear keys and material strength in the overlapping region. Experimental tests were used to develop design equations allowing to determine the capacity of grouted connections with shear keys.

Billington & Lewis (1978) defined an equivalent bond strength, which can be determined by dividing the ultimate axial force  $F_{\max}$  by the surface area of the pile in the overlapping region. It considers a uniform load distribution at the steel grout interface.

$$f_{\text{bu}} = \frac{F_{\max}}{D_p \cdot \pi \cdot L_g} \quad \text{Eq. 2-1}$$

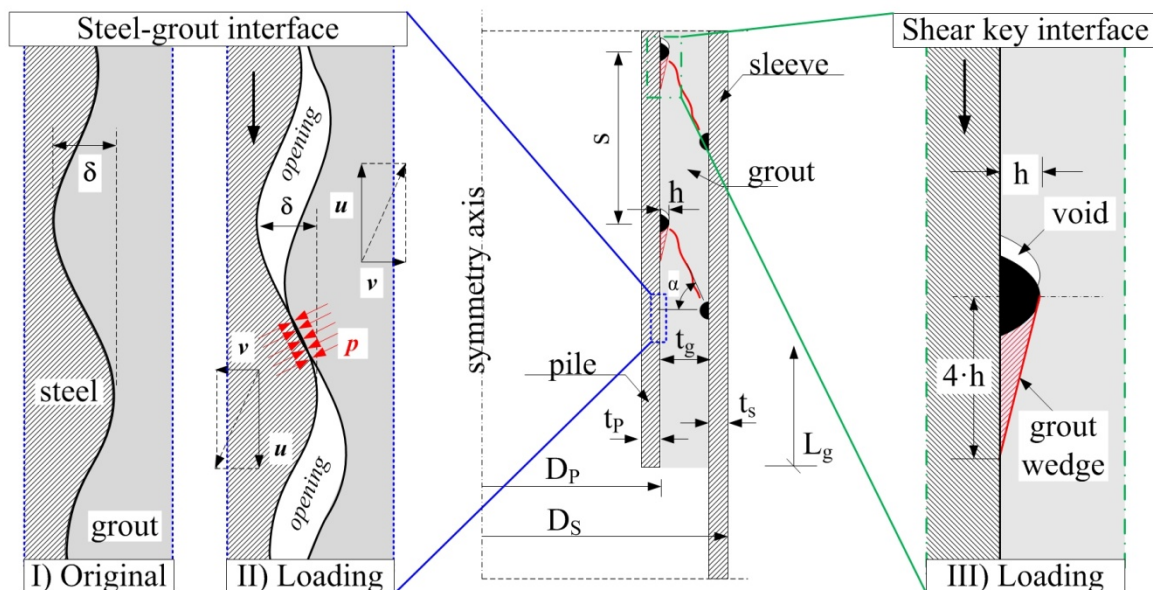
Based on experimental test results and regression analyses Billington & Lewis (1978) concluded that the ultimate bond strength  $f_{\text{bu}}$  depends on the material strength of the grout  $f_{\text{cu}}$ , the radial stiffness of the connection  $K$  and the ratio of overlapping length to pile diameter  $L_g/D_p$  being considered by the parameter  $C_L$ . The application of additional shear keys as weld beads led to an increased bond strength capacity, which was considered by the shear key height to shear key spacing ratio  $h/s$ , cf. Eq. 2-2.

$$f_{\text{bu}} = C_L \cdot K \cdot \frac{h}{s} \cdot f_{\text{cu}}^{0.5} \quad \text{Eq. 2-2}$$

$$\text{with } K = \left( \frac{E_g}{E_s} \right) \cdot \left( \frac{t_g}{D_g} \right) + \left[ \left( \frac{D_s}{t_s} \right) + \left( \frac{D_p}{t_p} \right) \right]^{-1} \quad \text{Eq. 2-3}$$

The radial stiffness  $K$  is determined by considering the modulus of elasticity  $E$  of steel (subscript  $s$ ) and grout (subscript  $g$ ) and the diameter to thickness ratios  $D/t$  of sleeve (subscript  $s$ ), pile (subscript  $p$ ) and grout (subscript  $g$ ), cf. Figure 2-4.

Contrary to the empirical model by Billington & Lewis (1978), Sele et al. (1989) derived from experimental testing and analysis of test results a semi-mechanical model to describe the strength of grouted connections. The formulation is based on the Mohr Coulomb's friction law and takes a coefficient of friction  $\mu$  and the surface irregularities  $\delta$  of the steel surfaces into account. It was assumed that the coefficient of friction results from the surface roughness of the steel tubes. The surface irregularities represent a surface waviness originating from the rolling process of the steel plates including weld misalignments from circumferential and longitudinal welds. In the original state of a grouted connection, full contact between steel and grout can be assumed, which is provided by initial bonding caused by material dependent adhesion strength, cf. Figure 2-6 left status "I) Original". Loading of the structure causes a weakening of the adhesion and a debonding accompanied by a relative displacement  $u$ , cf. Figure 2-6 left status "II) Loading". This relative displacement  $u$  activates frictional forces by provoking a radial pressure  $p$  between steel and grout. Hence, axial loads are transferred by this local contact pressure between grout and steel. According to Sele & Kjeoy (1989), radial displacements  $v$  appear as the grout to steel interface experiences debonding and vertical movements are facilitated at the steel grout interface, cf. Figure 2-6 left status "II) Loading". Radial displacements are caused by the surface irregularities  $\delta$  leading to an opening between steel and grout. Sele & Kjeoy (1989) call this interface sliding process the "wedging" effect, cf. Figure 2-6 left.



**Figure 2-6. Load transfer at grouted connections with shear keys in steel-grout interface (left) acc. to Sele & Kjeoy (1989) and shear key interface (right) acc. to Karsan & Krahl (1984).**

Analogous to the surface irregularities, the effect of surface waviness is significantly enlarged by weld beads like shear keys. Enhanced wedging forces arise to resist the relative axial movement. In consideration of the geometrical parameters and the grout strength  $f_{cu}$ , the shear strength  $\tau$  following Sele & Kjeoy (1989) results to:

$$\tau = \mu \cdot E_s \cdot \frac{\frac{\delta}{R_p} + \frac{h}{16s} \cdot \sqrt{\frac{t_p}{R_p} \cdot f_{cu}^{0.3}}}{\frac{R_p}{t_p} + \frac{E_s}{E_g} \cdot \frac{t_g}{R_p} + \frac{R_s}{t_s + \frac{E_g}{E_s} t_g}} \quad \text{Eq. 2-4}$$

Herein represents R the radius and t the thickness of sleeve (subscript s), pile (subscript p) and grout (subscript g) and E the elasticity modulus of grout (subscript g) and steel (subscript s). The shear key geometry is reflected by the height h and the spacing s.

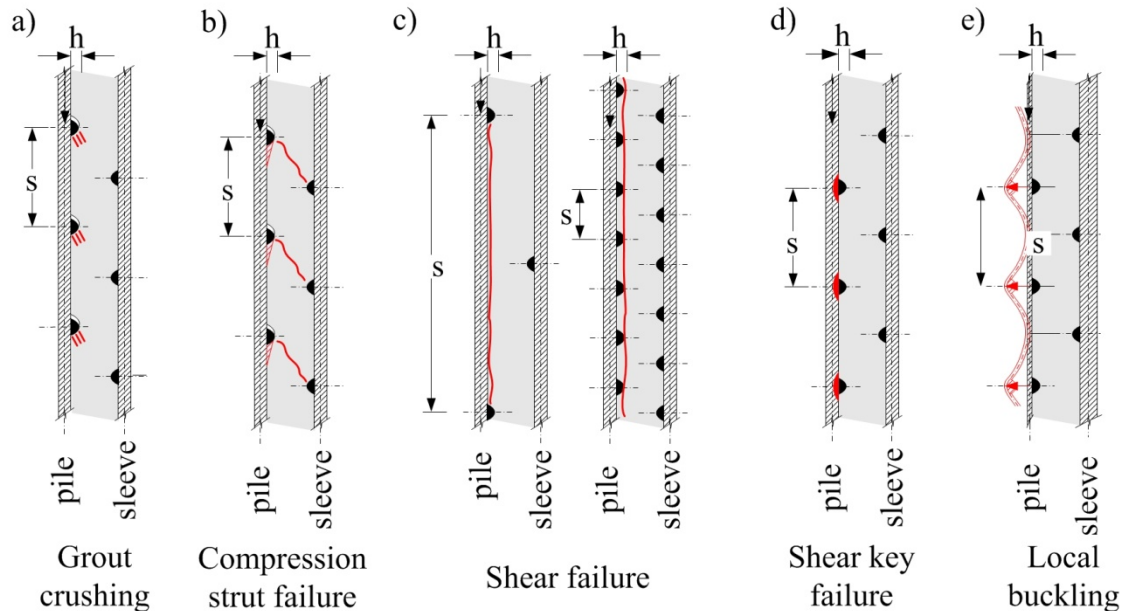
It can be summarised that axial loads are transferred by interlocking effects arising from friction, surface irregularities and an increased wedging by the shear keys. Nevertheless, the surface irregularities and frictional effect by the surface roughness may be reduced due to cyclic loading, cf. Schaumann et al. (2014b). Updated design provision by DNV accounts for these effects. Former values for the coefficient of friction were recently adapted based on the JIP investigations, cf. Lotsberg (2011).

Between diagonal facing shear keys, forces are transmitted by arising compression struts with an angle  $\alpha$ , cf. Figure 2-6. The visualised compression strut angle is influenced by the shear key distance s, the shear key height h and the grout thickness  $t_g$ . Analogue to the wedging effect caused by surface irregularities, an axial relative displacement is required to establish the interlocking effect provoking compression struts. To activate the compression struts, comparable large relative displacements are necessary. These are accompanied by debonding and loss of adhesion, cf. Figure 2-6 right status "III) Loading". As a result of the relative displacement, a void in form of a slippage appears at the load facing side of the shear key, cf. Sele & Kjeoy (1989). Concurrent at the compression side of the shear key a crushed grout wedge appears, which forms a triangle having a length of about four times the shear key height, cf. Figure 2-6 right, according to Krahl & Karsan (1985).

The arising compression struts and crushed grout wedge were observed from opened tested specimens. Numerous axial tests have formed a reliable basis for characterising different failure modes that may appear individually or in combination. Figure 2-7 presents an overview of different failure modes for axially loaded grouted connections with shear keys according to Billington & Lewis (1978), Lewis (1980), Karsan & Krahl (1984), Sele & Kjeoy (1989), Hordyk (1996), Schaumann et al. (2012a) and Schaumann et al. (2013a).

Thus, axial loading may provoke grout crushing at the shear key part under compression, which can be described by a grout wedge, failure mode a) Figure 2-7. Secondly, compression struts appear between opposed shear keys, failure mode b) Figure 2-7, which were observed e.g. by Billington & Lewis (1978), and Sele & Kjeoy (1989) by diagonal cracks. In addition to the compression strut failure mode and arising grout crushing at the shear keys, Krahl & Karsan (1985) as well as later on Forsyth & Tebbett (1988) introduce failure mode c), the shear failure, which depends on the shear key distance s. For closely spaced shear keys, a shear failure may appear from shear key tip to tip forming a cylindrical surface. Contrary, a large distance s between the shear keys may provoke failure at the steel-grout interface between the shear keys. Beside these prevailing grout failure modes, the failure modes d) and

e) represent steel failure modes, cf. Schaumann et al. (2012a). Failure mode d) in Figure 2-7 reflects a shearing off of the weld beads, which may appear due to weld deficiencies reducing the fatigue strength. Secondly local plastic deformations may arise, representing a local buckling failure mode e) in Figure 2-7. The latter can be omitted by considering sufficient steel plate thickness.



**Figure 2-7. Failure modes for axially loaded grouted connections with shear keys: a) grout crushing, b) compression strut failure, c) shear failure, d) shear key failure and e) local buckling according to Schaumann et al. (2012a).**

Complementary to the different failure modes, Aritenang et al. (1990) observed at experimental tests of axially loaded grouted connections with shear keys that the diagonal cracks appear at an angle of approximately  $45^\circ$  and that the maximum stress transfer took place at the outer shear keys. Considering that the compression strut angle depends on the geometrical parameters of the shear key and grout layer, the predominant load transfer at the outer shear keys was confirmed by experimental tests for grouted connections in wind turbines with high strength filling material by Anders (2007) and Schaumann et al. (2009).

From previous presentation of the main load transfer mechanism and occurring failure modes it becomes clear, that numerous parameters have a significant impact on the load bearing behaviour of grouted connections with shear keys. According to Hordyk (1996), the connection strength depends mainly on the shear key characteristics, the grout material strength and the radial stiffness. Because ribbed bars have a significantly stronger bond than smooth bars, Hordyk (1996) supposes that the shear key grout interlocking is comparable to bond strength of rebar embedded in concrete. Beside the geometrical parameters and material strength, the material surface conditions and different load states influence the load bearing behaviour. Therefore, former research results regarding geometrical, material and load related impact factors to the load bearing behaviour are addressed in the following subchapters.

### 2.2.3 Impact of geometrical parameters

Previous explanations of the load transfer mechanism have identified most significant impact factors to the load bearing behaviour. One of these is the grouted connection geometry, whereby the steel tube diameters, the grout annulus, the overlapping length and the shear keys are of relevance.

Resulting important geometrical parameters are

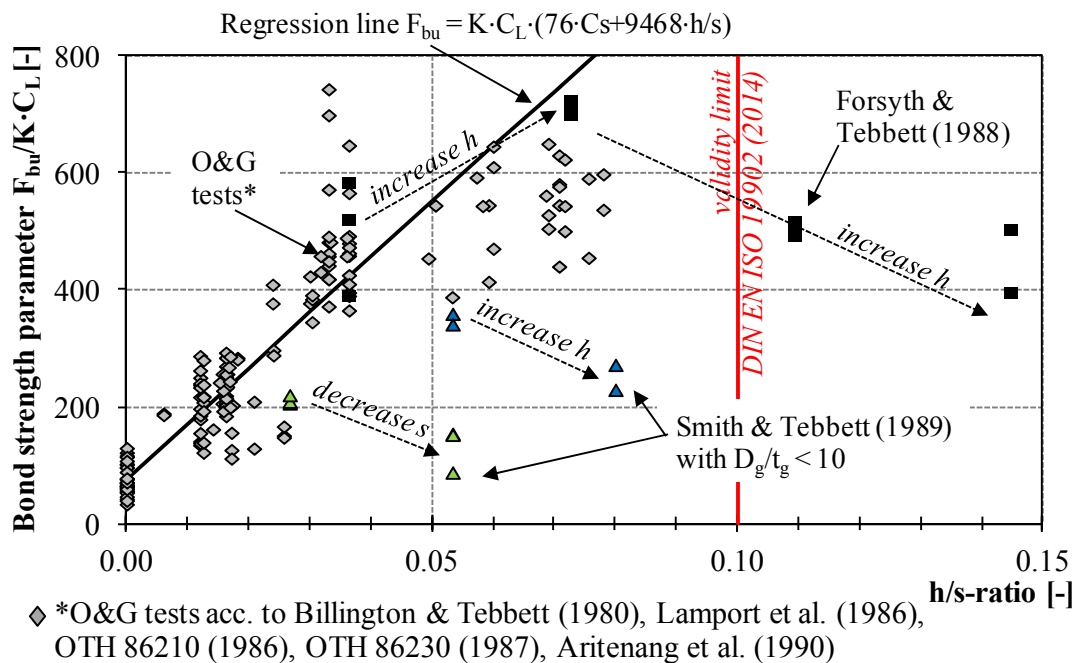
- the shear key height to shear key distance ratio  $h/s$ ,
- the radial stiffness  $K$  and related tube slenderness's  $D_g/t_g$ ,  $D_s/t_s$ ,  $D_p/t_p$ ,
- the overlap length  $L_g$ .

The shear key height to shear key distance ratio  $h/s$  contributes by a significant amount to the capacity, as it reflects the interlocking of the connection. Billington & Tebbett (1980) introduced the bond strength parameter  $F_{bu}$  to evaluate the impact of different geometrical parameters by normalising the experimental test results, cf. Eq. 2-5.

$$F_{bu} = \frac{f_{bu}}{1.105} \cdot \left(\frac{50}{f_{cu}}\right)^{0.5} \tag{Eq. 2-5}$$

This non-dimensional bond strength parameter is based on the parabolic relation between ultimate bond strength  $f_{bu}$  [N/mm<sup>2</sup>] and grout strength  $f_{cu}$  [N/mm<sup>2</sup>] being complemented by a factor of 1.105, which shall reflect multiples of a design bond stress value for extreme conditions according to Billington & Tebbett (1980).

In Figure 2-8 related test results for the bond strength parameter being normalised by stiffness  $K$  and length to diameter parameter  $C_L$ , which were performed for the offshore O&G industry by Billington & Tebbett (1980), Lamport et al. (1986), the Wimpey Laboratories contributing to OTH 86210 (1986) and OTH 86230 (1987) and Aritenang et al. (1990) are summarised.



**Figure 2-8. Relationship of bond strength and shear keys for experimental test results and resulting validity limit according to DIN EN ISO 19902 (2014).**

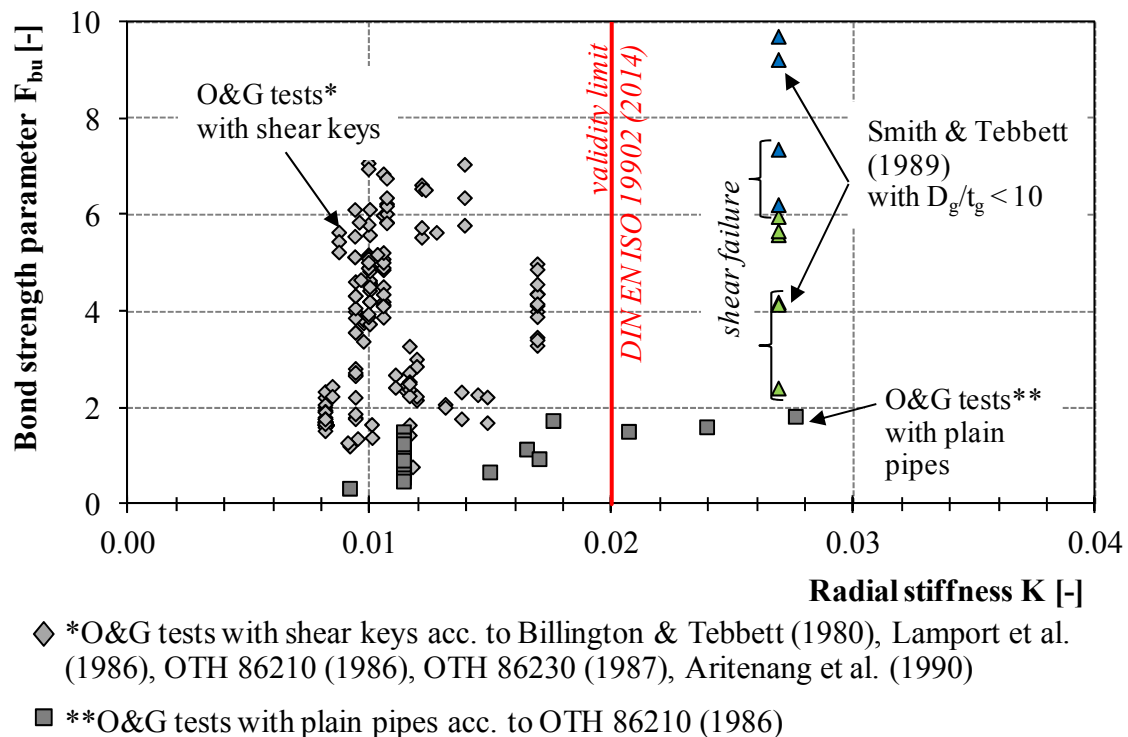
The test results depict that an increased  $h/s$  ratio tendentially causing an increased bond strength. Billington (1978) concluded that the significant strength increase due to shear keys allows a reduction of the overlapping length of sleeve, pile and grout amount. Billington & Tebbett (1980) defined a general equation for the bond strength based on a regression analysis of their test results including a surface condition parameter  $C_s$ , which equals a steel surface with shear keys by a value of 1.0 and a plain steel tube surface being painted by an epoxy coat by a value of 0.3, cf. Figure 2-8. Test results by Forsyth & Tebbett (1988), cf. black squares in Figure 2-8, depict that an increased shear key height with  $h/s > 0.11$ , leads to a reduced strength as it provokes a shear failure at the shear key tips, cf. Figure 2-7. Similar results were achieved by Smith & Tebbett (1989), who increased the height  $h$  and decreased the distance  $s$ , cf. triangles in Figure 2-8. Both variations lead to a reduced axial bearing capacity. In contrast to the test specimens by the remaining authors, these test results were observed at specimens with a rather large grout annulus having a  $D_g/t_g$  ratio less than 10. These considerations to the grout thickness indicate that a very thick grout annulus may cause shear failure for increased  $h/s$  ratios. The  $h/s$  ratio was recommended to be limited to a maximum value of 0.1 by Harwood et al. (1996). In addition, the geometrical dimensions of the test specimens were used to define specific geometrical validity limits for the developed design equations. Mentioned geometrical validity limits are still part of the current code recommendations according to DIN EN ISO 19902 (2014), chapter 2.3.

Even though Aritenang et al. (1990) complied with the general proposal of an increased shear strength capacity by increased  $h/s$  ratio, they concluded that the relationship is not linear over the connection's length, as suggested by Billington & Tebbett (1980). Aritenang et al. (1990) performed measurements of occurring strains and relative displacements at top, middle and bottom shear key that eventuate in a non-linear stress distribution over the shear keys. In consequence of the crack patterns, it was concluded that the load facing shear key transfers the most loads and corresponding compression strut fails due to crushed grout. By contrast, failure at the bottom compression strut is caused by tensile cracking, cf. Aritenang et al. (1990). Similar assumptions were stated by Boswell & d'Mello (1986) for fatigue tests.

Beside the impact of the  $h/s$  ratio, Forsyth & Tebbett (1988) report that the load bearing behaviour for grouted connections depends additionally on the radial stiffness  $K$  and respective  $D/t$  ratios, cf. Eq. 2-3. The steel tubes induce a confining pressure to the connection. Resulting radial stiffness was already considered by Billington & Lewis (1978) in the bond strength equation Eq. 2-2. The general mechanism of radial stiffness results from the vertical relative displacements that appear due to loading. Caused by the grout steel interface, a radial displacement arises which activates radial stiffness leading to an increased frictional capacity. The impact of the radial stiffness becomes apparent by comparing test results for grouted connections with varying stiffnesses. Figure 2-9 presents the normalised bond strength results  $F_{bu}$  for test specimens with and without shear keys and resulting radial stiffness  $K$ .

The majority of results for test specimens with shear keys, cf. diamonds in Figure 2-9, exhibit a larger bond strength than the specimens with plain pipes, cf. squares in Figure 2-9. This larger bond strength at test specimens with shear keys is caused by the interlocking effect due

to the shear keys. Even though the overall impression of the presented test results reflects a rather large scatter, Billington & Lewis (1978), Lamport et al. (1980) and Aritenang et al. (1990) concluded that the relationship between radial stiffness  $K$  and bond strength is approximately linear. For test results with a rather large grout annulus, Smith & Tebbett (1989) obtained that an increased radial stiffness being combined with closely spaced shear keys leads to a reduced strength being accompanied by a shear failure. By contrast, Lamport et al. (1986) concluded from static tests that the bearing capacity was unaffected by grout thickness's having a  $D_g/t_g$  ratio of 20. Moreover, Ingebrigtsen et al. (1990) resumed from documented radial deformations appearing for very thin sleeves, that these impacts of radial deformations might also be valid for thicker sleeves and high grout strength. As a result of the experimental tests, the radial stiffness parameter  $K$ , which allows to use empirically developed design equations, is limited to a value of 0.02 according to DIN EN ISO 19902 (2014).



**Figure 2-9. Relationship of bond strength parameter and radial stiffness for experimental test results and resulting validity limit according to DIN EN ISO 19902 (2014).**

As the loads have to be transferred from pile to sleeve in the overlapping area, the length of the connection  $L_g$  presents an additional important geometrical parameter. Larger overlapping length obviously increases the capacity of the connection, which was confirmed by tests considering varying overlap lengths performed by Billington & Lewis (1978), Billington & Tebbett (1980), Yamasaki et al. (1980) and Lamport et al. (1986). The later results by Lamport et al. (1986) as well as by Schaumann et al. (2008a) present that the overlapping length has an impact on the bearing behaviour of grouted connections being exposed to bending moments. Nevertheless, according to current validity limits, the length to pile diameter ratio  $L_g/D_p$  shall be in the range of 1 and 10 for axially loaded grouted connections according to DIN EN ISO 19902 (2014).

With regard to laboratory testing, the effect of test specimen scale has to be considered. In order to evaluate the scale effect Billington & Lewis (1978) performed full scale and large scale testing and concluded that the correlation allows for scaled tests. Lochte-Holtgreven (2013) questioned whether this assumption can be transferred identically to grouted connections in OWTs as the grain size of the high strength grouts cannot be downscaled. Large-scale specimens being not smaller than a tenth of the real structures were assumed to represent sufficient results, cf. Schaumann et al. (2011b) and Lotsberg et al. (2013). Notwithstanding, the larger the specimens and the smaller the test scaling, the more reliable and transferable are the results.

## 2.2.4 Impact of material characteristics

Beside the geometrical constitution, the applied materials influence the load bearing behaviour. Especially the compressive strength of the grout represents a crucial parameter for the connection's capacity. With regard to the steel tubes and interface characteristics, the surface condition of the steel depicts a material related influencing variable. Both material related characteristics were analysed by different experimental tests in the past.

To start with the filling material, earlier testing for the O&G industry concentrated on cementitious grouts without aggregates and with relatively low compressive strengths compared to current high strength grouts used for wind turbines. Figure 2-10 presents an overview of achieved bond strengths for different test specimens with varied filling materials being compared by their 28-days 75 x 75 mm uniaxial cube compressive strength. Test results in the O&G industry had used the filling materials: HAC, OPC and Oilwell B cements.

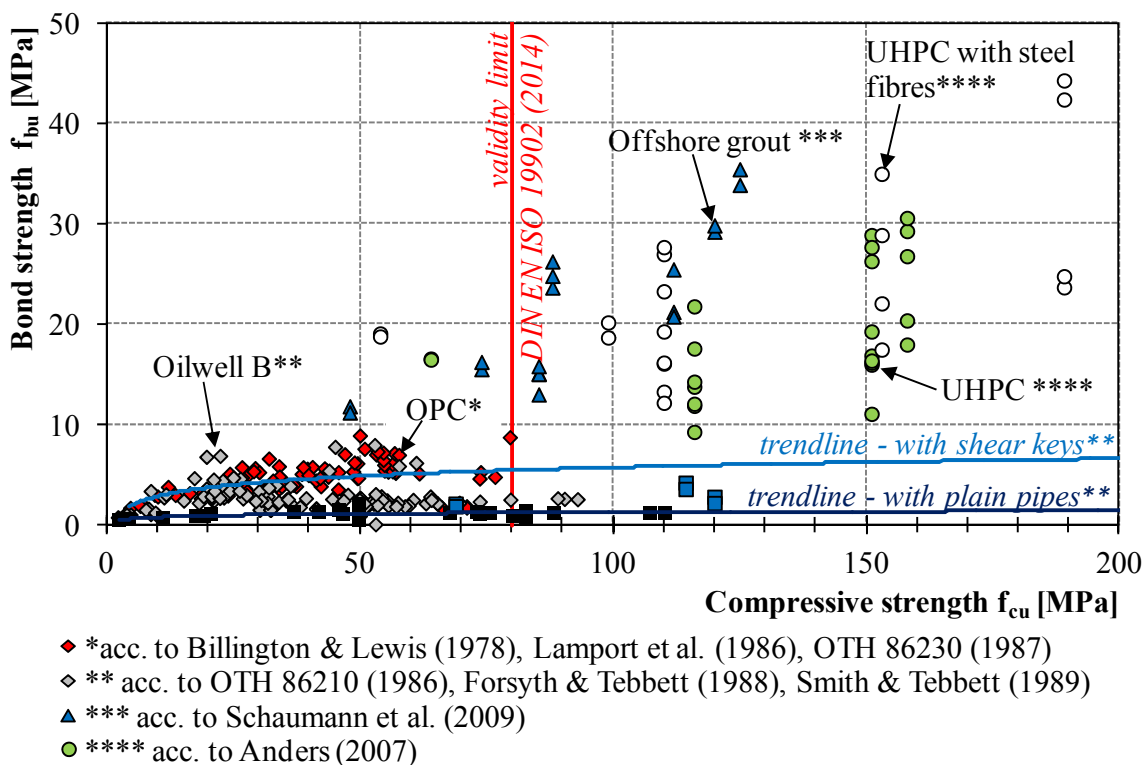


Figure 2-10. Relationship of bond strength and uniaxial compressive cube strength of cementitious materials for tests and resulting validity limit acc. to DIN EN ISO 19902 (2014).



Results achieved for the OPC and Oilwell B cements published by Billington & Lewis (1978), Lamport et al. (1986), OTH 86210 (1986), OTH 86230 (1987), Forsyth & Tebbett (1988) and Smith & Tebbett (1989) depict that the increased compressive strength leads to an enhanced bond strength  $f_{bu}$ . Billington & Lewis (1978) determined for test specimens with shear keys and with plain pipes an approximated parabolic curve based on their test results, cf. Figure 2-10. Beside the material strengths, Lamport et al. (1988) and Billington (1978) evaluated the materials with regard to their applicability, shrinkage and expansion behaviour. From these investigations it can be concluded that a mean shrinkage value of 0.2% for the tested cements leads to a reduced bond strength at grouted connections with plain pipes. Billington (1978) concluded that expansive as well as shrinkage is less significant for grouted connections with shear keys, as the resulting value of grout shrinkage will be smaller than the shear key height.

Scaled tests performed by Anders (2007) and Schaumann et al. (2009) focused on the impact of high and ultra high performance grouts (UHPC) used in grouted connections for offshore wind turbines. The test results visualised in Figure 2-10 show a significant increase in bond strength for increased grout compressive strengths. Nevertheless, Schaumann et al. (2009) observed a reduced bond strength for specimens without shear keys, which correlates to earlier plain pipe bond strength by Billington & Lewis (1978).

Anders (2007) performed experimental tests with ultra high performance grout being equipped with steel fibres. Anders (2007) concluded that increased compressive strength entails an increased bond strength, whereby the use of steel fibres enhances the capacity merely for a steel fibre volume larger than 2%. By contrast, Anders (2007) recommends to reduce the steel fibre content due to workability aspects. These conclusions correlate with recent material test results and evaluations by Lohaus et al. (2012). The bond strengths measured by Schaumann et al. (2009) for common offshore grouts are comparably larger than for cements used for O&G platforms. Achieved results correspond to bond strengths for UHPC filled grouted connections by Anders (2007). Consequently, the experimental results with varied material strength demonstrate a general increased grouted connection strength by increased strength characteristics of the cementitious filling material.

The interface strength between steel and grout is affected by the surface properties of the steel tubes, especially for plain pipe grouted connections. Billington (1978), Billington & Tebbett (1980) and Yamasaki et al. (1980) report about different surface preparations and its impact to resulting bond strength capacity. According to Billington (1978) the highest bond strength was achieved for shot blasted surfaces, whereas the bond strength was reduced by 50% for mill scale removed surfaces and by 80% for surfaces coated with epoxy resin. In consideration of these test results a surface condition parameter  $C_s$  was introduced to the bond strength equation for grouted connections with plain pipes. Investigations by Yamasaki et al. (1980) confirm the assumptions by Billington (1980). Later, Sele & Kjeoy (1989) developed design equations based on a physical model which encountered for surface conditions by a coefficient of friction  $\mu$  and a surface irregularity  $\delta$ , cf. Eq. 2-4. Based on their experimental test results, Sele & Kjeoy (1989) recommend a coefficient of friction for the grout steel interface of 0.7. Slightly smaller values for the

coefficient of friction were observed by tests according to Rabbatt & Russel (1985). However, the surface irregularity was defined as function of the pile radius  $0.00037 \cdot R_p$ . By expressing the shear strength of the grouted connections in terms of radial pressure in relation with surface irregularities, Sele & Kjeoy (1989) set the basis for the parametric formulae included in DNV-OS-J101 (2004). Observed slippage at offshore wind turbines in 2009 and consequent investigations, cf. Lotsberg et al. (2011), revealed that the surface irregularity correlates not with the pile radius. Moreover after observed slippage, the coefficient of friction was reduced for the design to 0.4. Wilke (2014) proposed from his experimental tests with plain pipes a coefficient of friction of 0.56. By comparison, the characteristic friction coefficient recommended for bridges with steel to grout bearings is 0.6 according to DIN EN 1993-2 (2010).

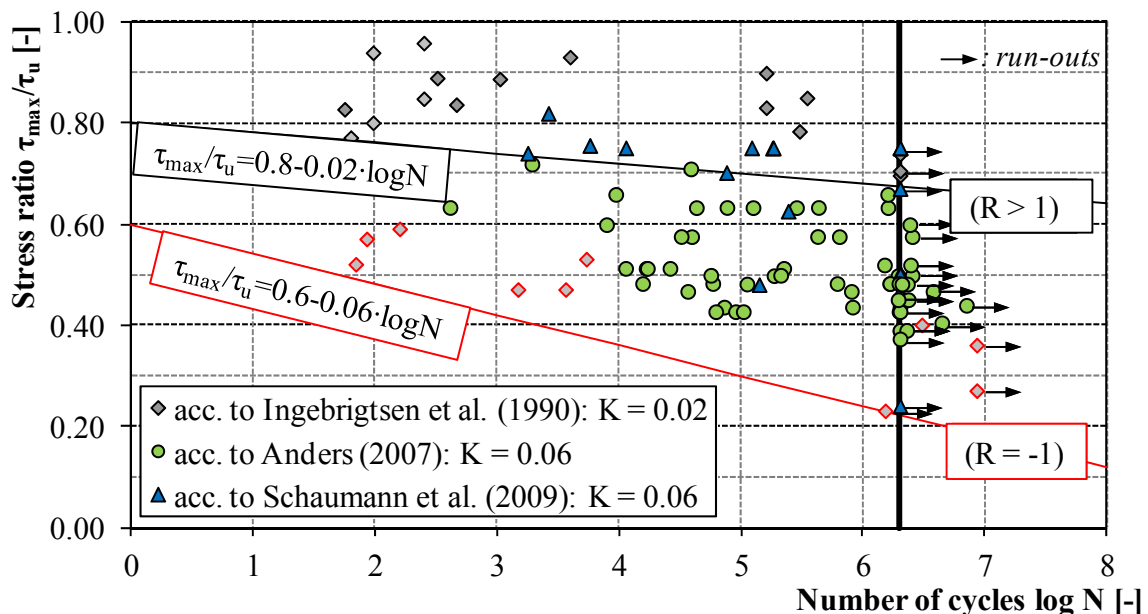
However, for grouted connections with shear keys, the h/s ratio, the radial stiffness K and the grout strength  $f_{ck}$  are more important for the bond strength capacity, than the friction coefficient  $\mu$  or the height of surface irregularities  $\delta$ .

### 2.2.5 Impact of load states

Apart from the geometrical and material related impacts to the load bearing behaviour, the strength of the connection is significantly influenced by the occurring load states. Previous considerations focused on the static axial load bearing behaviour of the connection. Cyclic loads have a more detrimental impact than static loads and thus are decisive for the design of grouted connections of offshore wind turbines. Even though O&G platforms and OWT support structures are exposed to cyclic wave loads, the impact of loads varies. O&G platforms are exposed predominantly to axial static loads caused by the heavy platforms. In contrast, OWT represent slender constructions which are very sensitive to structural dynamic loads caused inter alia by wave and wind actions. These loads cause changing stress distributions in the grouted connection and therefore influence the fatigue strength. Commonly, for the fatigue design characteristic S-N curves are used. For a specific construction detail or material, S-N curves provide for an applied stress amplitude or ratio the corresponding endurable number of load cycles. In the past, some few experimental tests were conducted to develop S-N curves for grouted connections, similar to the well-known curves for steel and concrete. But, due to the limited number of tests and the unclear impact of grout strength and interface conditions, until today no statistical reliable S-N curve could be developed. Notwithstanding, the outcome of the different investigations in the past considering axially loaded grouted connection shall be summarised to present an overview of impact factors regarding different load states.

First investigations on the dynamic behaviour of grouted connections were published by Lewis et al. (1980), Billington & Tebbett (1980) and Yamasaki et al. (1980). Other than the investigations by Lewis et al. (1980), who focused on the fatigue strength of a grouted connection for one specific O&G platform, Billington & Tebbett (1980) and Yamasaki et al. (1980) aimed develop S-N curves. Billington & Tebbett (1980) tested grouted connections with shear keys and proposed a tentative S-N curve for alternating load conditions. Yamasaki et al. (1980) performed grouted connection tests without shear keys and applied

alternating and pulsating compression loads. They observed a linear relationship between stress range and logarithmic endurable number of load cycles reflecting that fully reversal load cycles are more detrimental than pulsating compression loads. Apart from that, it was concluded by Yamasaki et al. (1980) that the resistance against cyclic deterioration reduces with increasing tensile loads. Subsequent to these initial investigations, further considerations to the fatigue strength of grouted connections with shear keys were reported by Billington & Tebbett (1982), OTH 86210 (1986) and Boswell & D'Mello (1986) in the 1980's. According to Billington & Tebbett (1982) and OTH 86210 (1986) grouted connections with shear keys appear to be more susceptible to fatigue failure than test specimens with plain pipes. This is a result of the much higher static strength capacity of grouted connections with shear keys compared to plain pipe connections and the corresponding applied fatigue stress. Previous suggestions by Yamasaki et al. (1980) were confirmed by the conclusion of OTH 86210 (1986), stating that reversal loading provoked earlier fatigue failure than unidirectional loading. Moreover, an endurance limit was observed for reversal loaded grouted connections with shear keys at stress ranges smaller than 0.4 times the static strength. Ingebrigtsen et al. (1990) summarised further experimental fatigue test results on grouted connections with shear keys and defined tentative S-N curves separately for pulsating compression loads and for alternating loads. Similar to earlier investigations, the stress range was characterised by the ratio of applied maximum load to ultimate bond strength. Figure 2-11 presents the proposed S-N curves by Ingebrigtsen et al. (1990) and related test results. It becomes obvious, that alternating loads ( $R = -1$ ) cause larger fatigue strength degradation than pulsating compression loads ( $R > 1$ ). It can be summarised that the fatigue strength for alternating loads is less the fatigue strength of connections at pulsating compression loads.



**Figure 2-11. S-N curves for unidirectional ( $R > 0$ ) and alternating loads ( $R = -1$ ) according to Ingebrigtsen et al. (1990) and tests results by Anders (2007) and by Schaumann et al. (2009).**

Supplementary to the former test results observed from tests in a scale of 1:3 and 1:5, Figure 2-11 includes data from small-scale test results in a scale of  $\sim 1:80$  with high and ultra high performance grout for OWT by Anders (2007) and Schaumann et al. (2009). Even

though these test specimens were exposed to unidirectional compressive loads, the results depict a reduced fatigue strength compared to Ingebrigtsen's test specimens for pulsating compression loads ( $R > 0$ ). Contrary to former test specimens having a radial stiffness  $K = 0.02$  and  $h/s$  ratio of  $h/s = 0.01$ , Anders (2007) and Schaumann et al. (2009) used very stiff connections with a radial stiffness value of  $K = 0.06$  as well as dense and large shear keys having a  $h/s$  ratio of  $h/s = 0.06$ . The small-scale tests by Anders (2007) and Schaumann et al. (2009) aimed to analyse the impact of different filling materials. Consequently, the steel tubes were chosen to be very stiff to force a grout strength failure.

With regard to code related recommendations, Harwood et al. (1996) summarised the test data of previous research investigations and presented design recommendations which were introduced by the DIN EN ISO 19902 (2008). As none of the grouted connections being exposed to cyclic loads failed at stress ratios smaller than the plain pipe capacity, a fatigue design check could be omitted for grouted connections fulfilling the static strength capacity limitations for plain pipe construction. For other cases, a logarithmic S-N curve was proposed by Harwood et al. (1996) reflecting the lower bound of all test results. Recently, new S-N curves were established and recommended by Billington & Chetwood (2012) and by DNV-OS-J101 (2014). As these curves reflect no individual impact factors, but are more design related recommendations, further explanations are presented in the chapter 2.3.3 addressing current design approaches.

It can be summarised that the load direction, being differentiated into unidirectional and fully reversal loads, the radial stiffness as well as the  $h/s$  ratio have a substantial impact to the fatigue strength of axially loaded grouted connections. Moreover, Ingebrigtsen et al. (1990) resumed, that the fatigue strength is strongly influenced by the stress ratio. Apart from that, it is not totally understood how variable load sequences may influence the fatigue performance. At present it is assumed that load sequences have no large impact, as the design is based on the linear damage accumulation according to the Palmgren-Miner rule. The disproportionate damage growth for reversal loadings in contrast to pulsating load conditions results from changing and crossing compression struts and stress states. Hence, the grout-specific application of uniaxial S-N curves is questionable, as multiaxial stress states appear in grouted connections.

In addition to cyclic loads arising over the operational lifetime of the construction, the loads appearing during the hardening process of the cementitious filling material reflect a significant impact factor. These early age cyclic loads that may affect the hardening process and the grout strength characteristics. Some considerations in the O&G industry focused already on the impact of early age cycling movements. According to OTH 86210 (1986) and Billington & Tebbett (1982) relative axial movements smaller than  $\pm 0.0035 \cdot D_p$  had no detrimental impact to the bond strength of the test specimen with cementitious filling material, but provoked a reduced stiffness. Sele et al. (1994) resumed from test specimens, which were exposed to fatigue load conditions after initial early age cyclic movements, that for closely spaced shear keys the early age cyclic movement has more detrimental impact than for widely spaced shear keys.

Nevertheless, as the analysed materials have significantly smaller grout compressive strengths than currently used high strength grouts at offshore wind turbines, the test results cannot be directly transferred. According to Lohaus et al. (2014) movements during the first 24 hours may cause sedimentation and segregation of the fresh high strength grout material. As a consequence, the increased autogenous shrinkage behaviour and related cracking may affect the load bearing behaviour. Initial testing by Lohaus et al. (2014) revealed varied compressive strengths for test specimens being exposed to early age cycling movements due to sedimentation of the aggregates. Recent investigations by Lohaus et al. (2015) concentrated on the impact of wave loads causing relative movements during the first 24 hours period after grouting. It was concluded that initial movements could have positive effects such as deaeration and negative impacts such as reduced strength and durability properties. Because these investigations focused on effects at large monopiles, results are not directly applicable to grouted connections in jackets, as these might be more affected by current than by large waves. As the impact of early age cycling is not quantified until today, further research is needed to focus on the effect of movements during grout hardening to the strength and fatigue capacity of grouted connections.

## **2.3 Current Design Approaches**

### **2.3.1 Standards and guidelines**

For the design of axially loaded grouted connections in latticed substructures different approaches were developed to consider the ultimate and the fatigue strength. Recently modified standards and guidelines cover relevant design situations and recommend appropriate approaches. The failure of grouted connections in monopiles provoked additional investigations by the certification bodies and industry leading to revised design standards. Even though current design guidance accounts for latest developments, in Germany for every offshore wind farm and offshore substation an approval in the individual case for the type of construction grouted connection and for the material grout has to be obtained. Reason for this is that neither the guidelines are listed in the "List of Technical Building Rules", DIBt Technische Baubestimmungen (2015), nor is the material listed in the "Construction Products Lists", DIBt Bauregellisten (2015), of the German Institute for Structural Engineering (DIBt). Procedural steps and recommendations with regard to the approval in the individual case are given by BSH Instruction Sheet (2011), Lohaus et al. (2013) and Schaumann et al. (2013b). Offshore structures in Germany can either be located in the 12 nautical mile zone or in the Exclusive Economic Zone (EEZ) in the North or Baltic Sea. The upper building authorities of the federal states take care of the inner 12 nautical mile zone, whereas the Federal Maritime and Hydrographic Agency (Bundesamt für Seeschifffahrt - BSH) is responsible for the EEZ. Even though different responsibilities are present, the general process does not differ significantly. The BSH released the standard BSH Standard - Design for Offshore Wind Turbines (2007) and recently the BSH Standard - Minimum Requirements for the Design of Offshore Structures in the EEZ (2015) including requirements for the approval process and

the time-steps for the implementation of offshore wind farms. Apart from these guidance, for the design of grouted connections the following design standards can be applied:

- DIN EN ISO 19902 (2014),
- DNV-OS-J101 (2014),
- GL Guideline (2012), and
- Norsok Standard N-004 (2013).

The Germanischer Lloyd additionally published the GL Technical Note (2013) for the design of grouted connections. Because DNV and GL merged in 2013 to the DNV GL Group it is expected that in the near future corresponding guidelines are consolidated to one set of guidance. Notwithstanding, the guidance of the individual guidelines by both certification authorities are considered for the present investigations. In addition to these recommendations different approaches and improvements have been developed by Anders (2007), Lochte-Holtgreven (2013), Lotsberg et al. (2013), Schaumann et al. (2014c), Schaumann et al. (2012a) and Wilke (2014) based on experimental tests for offshore wind turbines. Further design recommendations are reported by Fehling et al. (2013). In general the design approaches can be subdivided into considerations regarding the ultimate limit state, the fatigue limit state and developments for the numerical modelling. Following sections address the currently available design approaches by focusing on the design of axially loaded grouted connections in latticed structures.

### 2.3.2 Ultimate limit state

The ultimate limit state design requires a verification that applied maximum loads, usually represented by extreme load scenarios, can be safely transmitted by the grouted connection. Basic design equations recommended by DIN EN ISO 19902 (2014) and DNV-OS-J101 (2014) originate from earlier formulas developed for grouted connections in O&G platforms, cf. chapter 2.2. Prior to the application of the empirically developed equations, specific validity ranges have to be fulfilled, reflecting the geometrical limits of the originally tested specimens, cf. Table 2-2.

If the ranges of validity are fulfilled, the ultimate limit state design equations can be applied. With regard to the introduced failure modes in chapter 2.2.2, it is differentiated between the grout-steel interface strength and the grout matrix strength. The interface shear strength capacity can be determined according to DIN EN ISO 19902 (2014) by:

$$f_{g,sliding,ISO} = C_p \cdot \left[ 2 + 140 \cdot \left( \frac{h}{s} \right)^{0.8} \right] \cdot K^{0.6} \cdot f_{cu}^{0.3} \quad \text{Eq. 2-6}$$

Herein represents  $C_p$  a scale parameter accounting for the pile diameter,  $h/s$  the ratio of shear key height  $h$  to distance  $s$ ,  $K$  the radial stiffness factor and  $f_{cu}$  the compressive cube strength having an edge length of 75 mm. The radial stiffness  $K$  can be determined by Eq. 2-3. The scale parameter  $C_p$  is defined as

$$C_p = \left( D_p / 1000 \text{ mm} \right)^2 - \left( D_p / 500 \text{ mm} \right)^2 + 2 \quad \text{for } D_p \leq 1'000 \text{ mm} \quad \text{Eq. 2-7}$$

$$C_p = 1 \quad \text{for } D_p > 1'000 \text{ mm}$$

$C_p$  scales the strength capacity for pile diameters less than 1'000 mm, which was introduced to the design equation as a result of experimental tests, cf. Harwood et al. (1996).

**Table 2-2. Validity ranges for use of the empirical design equations according to DIN EN ISO 19902 (2014), DNV-OS-J101 (2014) and Norsok Standard N-004 (2013).**

Construction element	DIN EN ISO 19902 (2014)	DNV-OS-J101 (2014)	Norsok Standard N-004 (2013)
sleeve	$30 \leq D_s/t_s \leq 140$	$30 \leq D_s/t_s \leq 140$	$30 \leq D_s/t_s \leq 140$
pile	$20 \leq D_p/t_p \leq 40$	$20 \leq D_p/t_p \leq 60$	$20 \leq D_p/t_p \leq 40$
grout	$10 \leq D_g/t_g \leq 45$	$10 \leq D_g/t_g \leq 45$	$10 \leq D_g/t_g \leq 45$
	$20 \text{ MPa} \leq f_{cu} \leq 80 \text{ MPa}$	-	$20 \text{ MPa} \leq f_{ck} \leq 80 \text{ MPa}$
shear keys	$0.0 \leq h/s \leq 0.10$	$h/s \leq 0.10$	$0.0 \leq h/s \leq 0.10$
	$1.5 \leq w/h \leq 3.0$	$1.5 \leq w/h \leq 3.0$	-
	$h/D_p \leq 0.012$	$h/D_p \leq 0.012$	$h/D_p \leq 0.012$
	$(2.5)^* \leq D_p/s \leq 16$	$D_p/s \leq 16$	$(2.5)^* \leq D_p/s \leq 16$
	-	$h \geq 5 \text{ mm}$	-
	-	$s \geq \min \left\{ \begin{array}{l} (0.8 \cdot \sqrt{R_p t_p}) \\ (0.8 \cdot \sqrt{R_s t_s}) \end{array} \right\}$	-
radial stiffness	$K \leq 0.02$	$K \leq 0.02$	-
overlap length	$1 \leq L_e/D_p \leq 10$	$1 \leq L_g/D_p \leq 10$	$1 \leq L_e/D_p \leq 10$
* for helical shear keys			

Comparable to DIN EN ISO 19902 (2014), Norsok Standard N-004 (2013) and DNV-OS-J101 (2014) define the strength capacity for the interface strength as follows:

$$f_{g,sliding,DNV} = \left[ \frac{800}{D_p} + 140 \cdot \left( \frac{h}{s} \right)^{0.8} \right] \cdot K^{0.6} \cdot f_{ck}^{0.3} \quad \text{Eq. 2-8}$$

In addition, the grout matrix failure is described by DNV an ISO approach identically as follows:

$$f_{g, shear, ISO/DNV} = \left[ 0.75 - 1.4 \cdot \left( \frac{h}{s} \right) \right] \cdot f_{ck}^{0.5} \quad \text{Eq. 2-9}$$

The grout matrix failure depends on the characteristic compressive cube strength  $f_{ck}$  with an edge length of 75 mm and the shear key height to distance ratio  $h/s$ . By dividing the smaller value of  $f_{g, shear}$  and  $f_{g, sliding}$  by the partial safety factor of  $\gamma_m = 2.0$ , the design interface strength  $f_d$  is achieved. This value has to be larger than the applied design axial load  $P_d$  acting on the pile's surface in the overlapping region, represented by  $f_a$ . Moreover, a reduction factor  $k_{red}$  accounts for any effects arising from early-age-cyclic movements. Hence the design criterion has the following form:

$$\frac{P_d}{\pi \cdot D_p \cdot L_e} = f_{a, ISO} \leq \frac{f_{g, ISO} \cdot k_{red}}{\gamma_m} \quad \text{Eq. 2-10}$$

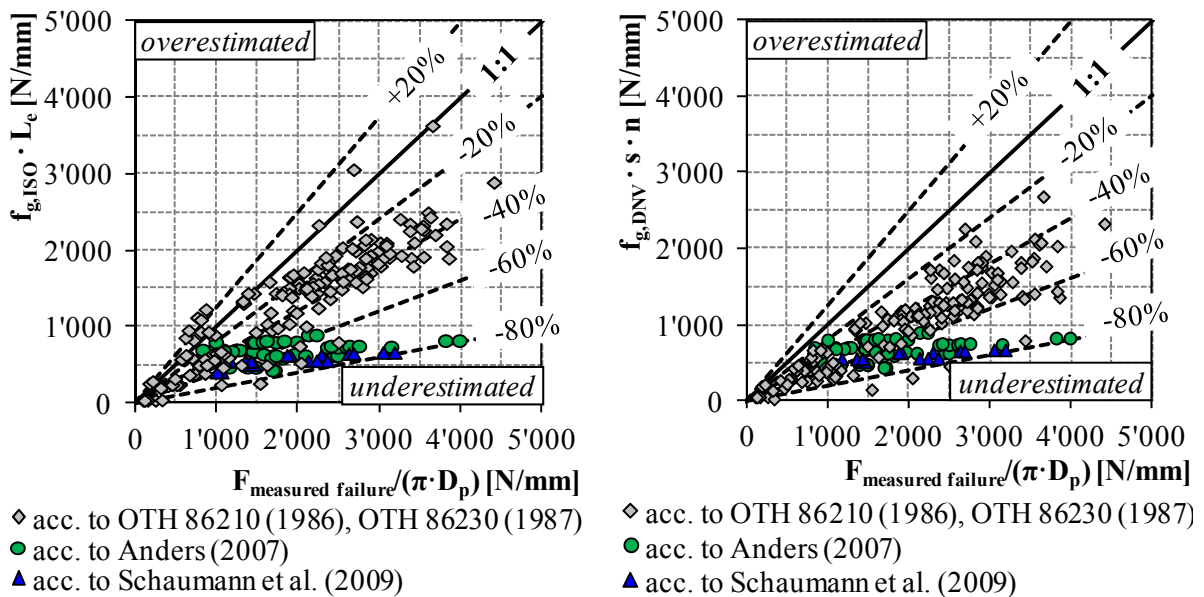
Contrary to the DIN EN ISO 19902 (2014), the design strength capacity is reduced according to DNV-OS-J101 (2014) to the unit length of one shear key by considering the shear key distance  $s$ . Hence, the design check concentrates on the number of shear keys  $n$  and the transferable loads by these while disregarding the connection's length:

$$\frac{P_d}{\pi \cdot D_p \cdot n} = f_{a,DNV} \leq \frac{f_{g,DNV} \cdot s}{\gamma_m} \quad \text{Eq. 2-11}$$

For further design recommendations regarding torsional or bending moments, reference is made to DIN EN ISO 19902 (2014) and DNV-OS-J101 (2014).

Even though these design equations represent the current design, their accuracy especially for high performance materials is in question.

Figure 2-12 represents a comparison of calculated bond strength according to DIN EN ISO 19902 (2014), and according to DNV-OS-J101 (2014), to the measured bond strength of tested specimens for O&G platforms and for OWTs. The test results performed by the O&G industry reflect an adequate fit to the calculated values, which is reasonable as these test results were used to develop the formula. However, the test results by Anders (2007) and Schaumann et al. (2009) were achieved by using high strength and ultra high strength grout, which in turn had much higher bond strength capacities, cf. Figure 2-12.



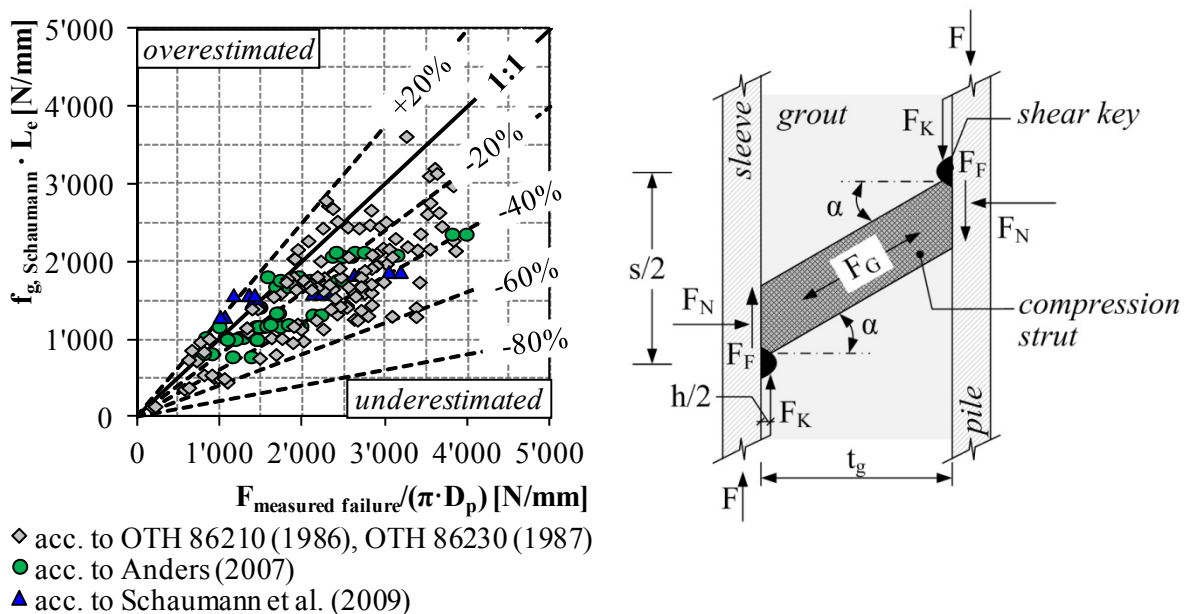
**Figure 2-12. Comparison of calculated and measured bond strength according to DIN EN ISO 19902 (2014) and DNV-OS-J101 (2014) based on Schaumann et al. (2012a) with test results.**

The current design equations lead to underestimation of the capacity of grouted connections with high strength materials. Hence, Anders (2007) and Schaumann et al. (2009) developed on the basis of the model by Lamport et al. (1986) an semi-empirical mechanical approach that accounts for the higher strength of the material. The approach is mainly based on the compression strut failure as the bond strength results from the individual horizontal and vertical force component, cf. Figure 2-13 right.

The approach by Anders (2007) and Schaumann et al. (2009) was improved further by Schaumann et al. (2012a) to account for the steel tube flexibility and the confinement pressure



induced by the steel tube surrounding the grout. This impact was considered by introducing a grout compressive strength depending on the lateral stress caused by the steel tubes and a triaxial factor. For detailed information, reference is made to Schaumann et al. (2012a). Comparison of the strength capacity due to this new approach to measured bond strengths are depicted in the left diagram of Figure 2-13. Contrary to the ISO and DNV equations, the approach according to Schaumann et al. (2012a) leads to an improved correlation between test results and calculated bond strength. Nevertheless, it has to be mentioned that the test specimens used by Anders (2007) and Schaumann et al. (2009) were only small-scale specimens with increased stiffness focusing on the grout material failure and not representing the true bearing capacity of scaled grouted connections for OWTs.



**Figure 2-13. Comparison of calculated and measured bond strength according to Schaumann et al. (2012a) (left) and compression strut model according to Lamport et al. (1986) (right).**

In addition to the ISO and DNV standard, the German certification authority published the GL Technical Note (2013) specifically for the design of grouted connections. This note represents a collection of latest developments, design considerations and research findings for grouted connections. It is recommended to use numerical simulations and an analytical plausibility check for verification. The verification has to be performed individually for grout layer, steel tubes, shear keys and welds. Beside the general strength analysis and verification, special requirements for the material, the structural design and the manufacturing, the quality control, the production, the installation and the monitoring processes are addressed. In addition to individual strength verifications for steel, grout and welds for the ultimate limit state, the GL Technical Note refers to latest developed approaches by DNV, ISO, Schaumann et al. (2012a) and Fehling et al. (2013). Contrary to usual design standards, this note includes latest research results reflecting a reduced capacity for submerged grouted connection specimens. For totally submerged grouted connections exposed to fatigue loading, GL recommends to reduce the endurable load cycles by a factor of 10.

Fehling et al. (2013) recommend to use as alternative to complex FE analysis, a so-called "strut-and-shell" model to idealise and simplify the complex multi-axial load transfer of axially

loaded grouted connections. The design check has to be performed for the middle part of the compression strut and the highly stressed area around the shear key. Moreover, the approach assumes a linear load transfer over the compression struts and does not consider any non-linearities of the grout at large load levels. Because this model represents a strong simplification of non-linear FE simulations, it is not further considered within this thesis.

Apart from the presented determination and verification of the bond strength capacity, the ultimate limit state design for the grout and the steel has to be performed individually. Since the bond strength is the design driver for the individual verifications, reference is made to the corresponding standards for the verification process. The steel tubes have to be designed in accordance with DIN EN 1993-1-1 (2010), DIN EN 1993-1-6 (2010), DIN EN 1993-1-9 (2010), GL Guideline (2012) and DNV-OS-J101 (2014), whereby for grout the DIN EN 1992-1-1 (2011) shall be applied.

### 2.3.3 Fatigue limit state

S-N curves are commonly used for the fatigue design of structural components like steel or concrete. These curves describe endurable number of load cycles  $N$  for a related mean stress level  $S$ . Different efforts have been taken in the past to develop empirical based S-N curves for grouted connections with shear keys. Based on dynamic loaded experimental tests for the O&G industry, Harwood et al. (1996) recommended with regard to the then new ISO standard the following S-N curve for axially loaded grouted connections:

$$S = 0.75 - 4 \cdot \frac{h}{s} - \frac{\log N}{14} \quad \text{Eq. 2-12}$$

The S-N curve is characterised by the stress ratio  $S$  being defined as the applied fatigue load to the estimated mean ultimate strength against the endurable number of load cycles, cf. Figure 2-14.

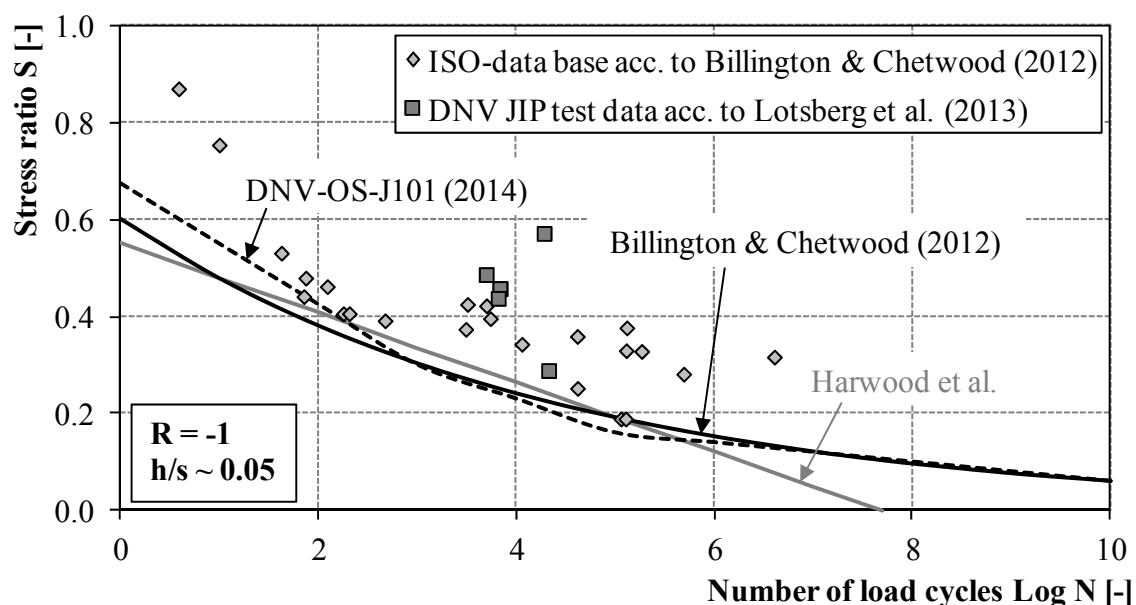


Figure 2-14. Proposed S-N curves for grouted connections with shear keys according to DNV-OS-J101 (2014), Billington & Chetwood (2012) and Harwood et al. (1996) and related fatigue test results, diagram based on Schaumann et al. (2012b).

The illustration reveals that the curve crosses the abscissa at  $N = 2 \cdot 10^7$  load cycles, which is not representative for occurring load cycles at offshore wind turbines being in the range of  $10^8$  to  $10^9$  load cycles.

Billington & Chetwood (2012) introduced a modified log S-log N curve having the following form:

$$\log S = -0.2214 - 0.0987 \cdot \log N \quad \text{Eq. 2-13}$$

Both equations are developed on a similar ISO data basis reflecting fatigue testing of reversely loaded grouted connections with shear keys. Test results are also included in Figure 2-14. As evident from Figure 2-14, the Billington & Chetwood curve intercepts at crucial points of the former linear S-N curve and represents a conservative approximation for a wider range of load cycles. Even though Harwood et al. (1996) represents design provisions for the ISO-Standard, the proposed S-N curve was never included in any officially published ISO 19902 version.

However, according to DIN EN ISO 19902 (2014), no detailed fatigue design assessment has to be performed if the structure is primarily exposed to cyclic wave loads and the ultimate strength capacity according to Eq. 2-10 is fulfilled. In other cases, the combined interface stress has to comply with the ULS design for the plain pipe connection. Billington & Chetwood (2012) suggest that this was resumed on the test data basis, as no fatigue test specimens with shear keys failed at an absolute value of reversal load lower than the plain pipe capacity. Lotsberg et al. (2013) proposed a quite similar S-N curve as a result of investigations performed during the JIP II on grouted connection with shear keys. The S-N curve and corresponding test results are added to the diagram in Figure 2-14. The derived S-N curve became a design relevant recommendation as it was included in the current design code DNV-OS-J101 (2014). Although the DNV S-N curve is similar to former proposal by Harwood et al. (1996) and by Billington & Chetwood (2012), cf. Eq. 2--2 and Eq. 2-13, the stress ratio results from the strength capacity per compression strut correlating with the ULS design approach according to DNV-OS-J101 (2014). The S-N curve is defined as follows:

$$S = 0.675 - 0.125 \log N \quad \text{for } N \leq 10^3 \text{ load cycles} \quad \text{Eq. 2-14}$$

$$S = 0.51 - 0.07 \log N \quad \text{for } 10^3 < N < 10^5 \text{ load cycles}$$

$$S = 0.26 - 0.02 \log N \quad \text{for } N \geq 10^5 \text{ load cycles}$$

$$\text{with } S = \frac{f_{\text{applied,DNV}} \cdot \gamma_m}{f_{g,\text{DNV}} \cdot S}; f_{\text{applied,DNV}} = \frac{f_{\text{mean}} + f_{\text{amplitude}}}{D_p \cdot \pi \cdot n}$$

Contrary to conventional S-N curves, which are established by a statistical evaluation considering failure probability and confidence interval, cf. E DIN 50100 (2015), these curves represent a lower bound solution. The real fatigue strength is assumed to be larger than the presented curves. Even though, the three S-N curves by Harwood et al. (1996), Billington & Chetwood (2012) and Lotsberg et al. (2013) seem to cover ISO-data basis quite well and the latter two were introduced for the design of offshore wind turbines, the underlying number of test results are rather limited. Commonly reliable S-N curves are established based cyclic tests

on varied levels with 3 to 6 cyclic tests performed per stress level, cf. E DIN 50100 (2015). Apart from the fact that the data basis is not statistically reliable, the majority of underlying test specimens represent geometric boundary conditions for grouted connections in O&G platforms and not for offshore wind turbines. Lotsberg & Solland (2013) recommend to perform further testing to consider numerous issues which are not in common with older tests. It is concluded by Lotsberg & Solland (2013) that cyclic large-scale fatigue testing is needed to investigate among others:

- the impact of shear key geometry,
- the impact of grout thickness,
- the impact of radial stiffness,
- the impact of different grout material,
- the impact of load ratio R,
- the impact of early age cycling,
- the impact of submerged conditions.

In compliance with Schaumann et al. (2013b), it seems recommendable to use the present S-N curves only for a pre-design. According to latest investigations, the detailed fatigue design shall be established by using finite element calculations taking appropriate material models and S-N curves for grout into account. The current status of detailed recommendations considering use and implementation of available numerical approaches is presented in chapter 2.3.4. The material specific fatigue behaviour for steel and grout are outlined in chapter 2.4.

For steel tubes the fatigue strength can be determined in accordance to DIN EN 1993-1-9 (2010). Commonly detail categories are defined for steel components. Nevertheless, shear keys are currently not covered by the detail categories (FAT) according to DIN EN 1993-1-9 (2010). Therefore Schaumann & Wilke (2006) investigated the impact of different shear key geometries to the fatigue behaviour by local concepts and fracture mechanics. As a result, a classification for the shear keys in FAT 71 and 80, depending on the weld bead type and cracking location, was recommended by Schaumann & Wilke (2006). DNV-OS-J101 (2014) recommends for the fatigue design of shear keys the S-N curve for non-load carrying attachments, for further input reference is made to DNV-OS-J101 (2014) curve E, Table 7-10, section 7.10.2.

### **2.3.4 Numerical approaches**

In order to determine the appearing stresses in the grouted connections more precisely than by analytical equations, finite element analyses (FEA), covering geometrical and material non-linearities are to be used. For grouted connections different advices are given by the standards and by different researchers.

DNV-OS-J101 (2014) presents in Annex K recommendations with regard to the general calculations using the finite element method. Apart from the introduction of different types of analysis and how to document the FEM analysis, recommendations for the modelling process itself are given. Nevertheless, the recommendations and advices are rather general and not

specific for grouted connections. GL Technical Note (2013) contains more grouted connection specific recommendations for the numerical verification. The interaction of the grout, the sleeve, the pile, the shear keys need to be considered while allowing the model for gapping and ovalisation.

Schaumann et al. (2014c) present an overview for the assessment of grouted connections in monopiles being exposed to predominantly bending moments. Beside the shell-based theory by Lotsberg et al. (2013) two numerical based procedures, by Lochte-Holtgreven (2013) and Wilke (2014) are described and compared. Both used solid elements to model the steel tubes and the grout layer. Wilke (2014) proposes to represent the shear keys by non-linear spring elements. Spring characteristics were defined by using load-displacement curves which were developed by the reverse engineering method. The shear key geometry was digitally measured and implemented to numerical models, in order to analyse the shear behaviour of realistic shear key geometries and define load-displacement curves. Contrary to Wilke (2014), Lochte-Holtgreven (2013) implemented the shear keys similar to the remaining structural components by solid elements. He used a mesh with a high-resolution at the shear key area. For the grout material a multiaxial failure surface was implemented, in order to account for multiaxial stress states and increased damage at the shear keys,. Lochte-Holtgreven (2013) combined the Ottosen (1977) failure surface with uniaxial S-N curves for high strength concrete according to Lohaus et al. (2011).

Both, Wilke (2014) and Lochte-Holtgreven (2013) conclude that for a global analysis of grouted connection with shear keys, the Drucker-Prager material model, which is available in public numerical software, is sufficiently accurate. Anyhow, for a more precise consideration of grout cracking and crushing, a multi parameter model like the Ottosen model shall be used. Both material models are discussed in chapter 2.4.2. The combination of the multiaxial failure surface with the uniaxial S-N curves according to Lochte-Holtgreven (2013), enables to determine stress increase and damage in the shear key vicinity. However, this model is validated by large-scale bending tests on grouted connections with shear keys. The application of the model and its reliability for axially loaded grouted connections with shear keys not been investigated. Even though according to Lochte-Holtgreven (2013) the underlying uniaxial S-N curves are applicable for the confined grout, it is not clear whether changing load ratios and load sequence effect may influence the damage process. The relevant material model parameters and equations for the multiaxial failure surface as well as the fatigue behaviour of high strength concrete are dealt with in chapter 2.4.2.

However, Schaumann & Wilke (2007) proposed a numerically based fatigue design procedure, which was modified by Schaumann & Lochte-Holtgreven (2011). The procedure is explained in detail by Schaumann & Wilke (2007) and Schaumann & Lochte-Holtgreven (2011) and summarised in Figure 2-15.

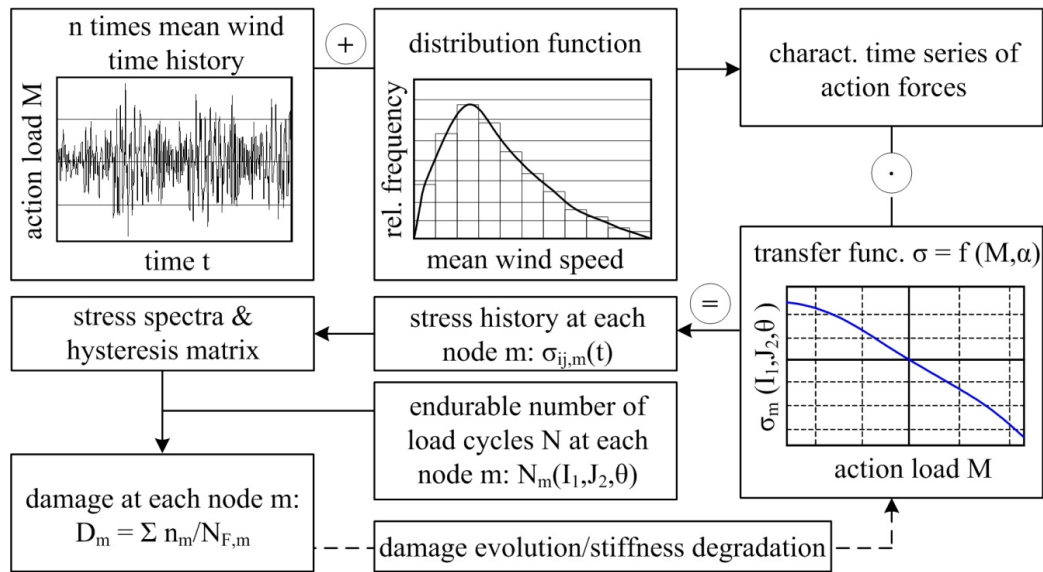


Figure 2-15. Flow chart for the fatigue design of grout layers in offshore wind turbines according to Schaumann & Wilke (2007) and Schaumann & Lochte-Holtgreven (2011).

## 2.4 Material Specific Fatigue Behaviour

### 2.4.1 Steel

In general, the steel material behaviour can be described by elasto-plastic material behaviour, cf. DIN EN 1993-1-1 (2010). The uniaxial material behaviour for static loads can be well described by tensile tests reflecting the most common material properties, the yield strength  $f_{yk}$ , the ultimate strength  $f_{uk}$ , the strains  $\epsilon$  and the relationship between these, characterised by the elasticity modulus as the slope of the curve. The uniaxial steel material behaviour is described by the Hooke's law.

The multiaxial material performance of steel is assumed to be isotropic, i.e. the material behaves in all directions similar. Hence, for all principal stresses the uniaxial material behaviour is proposed to be valid. For the transformation of the uniaxial material behaviour to the multiaxial material behaviour for steel, the failure criterion according to von-Mises is used. The yield surface according to the van-Mises yield criterion represents a cylinder, cf. Petersen (2013), and is described by the following equation:

$$F(\sigma) = \sigma - f_{yk} = \sqrt{3 \cdot J_2} - f_{yk} \quad \text{Eq. 2-15}$$

This equation accounts for the steel yield strength  $f_{yk}$  and the second invariant of the stress deviator  $J_2$ . A full description of the steel material behaviour and relevant material characteristics and testing can be found in Petersen (2013).

However, the cyclic stress strain behaviour is essential for the fatigue strength of grouted connections and the corresponding steel tubes. Repeated loading provokes a softening and hardening of the material, which can be depicted by stress-strain hysteresis loops, cf. Radaj & Vormwald (2007). A cyclic stress strain curve can be developed from the cyclic stress-strain hysteresis loop by connecting the maxima of each loop and by considering an elastic strain

part  $\varepsilon_{el}$  and a plastic strain part  $\varepsilon_{pl}$ . According to the three-parametric model by Ramberg & Osgood, the cyclic stress-strain curve is defined by Eq. 2-16:

$$\varepsilon_a = \varepsilon_{el} + \varepsilon_{pl} = \frac{\sigma_a}{E} + \left( \frac{\sigma_a}{K'} \right)^{1/n'} \quad \text{Eq. 2-16}$$

Herein  $\varepsilon_a$  represents the strain amplitude,  $\sigma_a$  the stress amplitude,  $E$  the elasticity modulus,  $K'$  the coefficient of hardening and  $n'$  the cyclic hardening exponent. The parameters can be determined according to Radaj & Vormwald (2007) by experimental testing of unnotched specimens. With regard to the fatigue strength formulation of steel materials being exposed to cyclic loads, Radaj & Vormwald (2007) recommend to use the maximum distortion energy hypothesis according to von-Mises due to the ductile material behaviour of steel.

The failure behaviour for cyclic loaded steel components is characterised by crack growth, which represents a more ductile failure than for concrete. The lifetime until failure is defined by the well-known S-N curves. These represent the endurable number of load cycles on the basis of the nominal stress approach. In order to account for any geometrical or material deviations, experimental tests were used to define specific detail categories for classification of notched specimens. The curves are in general defined by the following equation, cf. Radaj & Vormwald (2007):

$$\log N = \log a - m \cdot \log \Delta\sigma \quad \text{Eq. 2-17}$$

Herein represents  $N$  the number of load cycles,  $a$  the crossing of the abscissa,  $m$  the slope of the curve and  $\log \Delta\sigma$  the applied stress amplitude. For different classified notched steel components reference is made to DIN EN 1993-1-9 (2010), DNV-OS-J101 (2014) and GL Guideline (2012) numerous S-N curves and detail categories are summarised.

The fatigue failure for steel materials is typically defined by the Palmgren-Miner approach, where the total damage  $D$  results from summing up the applied load cycles  $n_i$  to the endurable load cycles  $N_i$  of each stress interval depending on the stress  $\Delta\sigma$ .

$$D = \sum_{i=1}^j D_i = \sum_{i=1}^j \frac{n_i}{N_i} \quad \text{Eq. 2-18}$$

Based on the linear damage accumulation and the isotropic material behaviour of steel, a damage equivalent single load spectrum can be determined for any load spectrum, cf. Radaj & Vormwald (2007). Different settings can be used to identify a damage equivalent load level. Either the equivalent number of load cycles resulting for the largest stress amplitude of the original stress spectra, the equivalent load amplitude for identical applied number of load cycles or the equivalent load amplitude for the fatigue limit can be calculated. For these different considerations, Eq. 2-19 represents the basic equation according to Radaj & Vormwald (2007).

$$N_{eq} \cdot \Delta\sigma_{eq}^m = \sum_i (\Delta\sigma_i^m \cdot N_i) \quad \text{Eq. 2-19}$$

Nevertheless, a prerequisite for the use of the damage equivalent load level is the validity of the linear damage accumulation according to Palmgren-Miner. Even though Radaj & Vormwald (2007) criticise that the Palmgren-Miner method does not account for load

sequence effects, crack opening or closing behaviour or the dependence on the mean stress level, it is a well-established method used in the offshore wind industry, cf. Schaumann et al. (2007). Hence, it was resumed that the linear damage accumulation is sufficient to evaluate the fatigue strength of offshore steel tubes.

#### 2.4.2 High performance grout

Several investigations focused on the fatigue behaviour of normal strength concrete (NSC), high performance or high strength concrete (HPC/HSC) and ultra high performance concrete (UHPC) in the past. Thus, the scientific knowledge about the fatigue behaviour of concrete is rather large and complex due to multiple influencing factors. The following section focuses on the relevant material characteristics for high strength grouts in grouted connections being exposed to multistage loading consisting of cyclic alternating and pulsating compression loads.

Normal concrete, high performance concrete and grout have in common their composition of cement, water, aggregates and additives. Although the basic components are in the essence similar, high strength grout is a specifically developed complex material addressing particularly offshore requirements which need to be considered with substantial care. According to Model Code 2010 (2012) NSC, HSC and UHPC are classified by their characteristic compressive strength, whereby NSC reveals to  $f_{ck} \leq 50$  MPa, HSC to 50 - 150 MPa and UHPC to 150 - 250 MPa. The uniaxial strength capacities influence the uniaxial compressive stress strain behaviour significantly. With increasing uniaxial strength, the brittleness of the material increases and the ductility decreases. For the description of the uniaxial material behaviour reference is made to DIN EN 1992-1-1 (2010) or Model Code 2010 (2012). In general the uniaxial stress-strain behaviour correlates with crack developments on the micro, meso and macro level, cf. Zilch & Zehetmeier (2010). Although the crack development of NSC and HSC is in many ways similar, cracks at HSC material appear through aggregates because the strength of aggregates and surrounding cement matrix converges. As the post-crack behaviour of HSC is characterised by an abrupt failure compared to NSC, appropriate hardening and softening descriptions were developed, as described for instance by Grassl et al. (2002) and König et al. (2001).

Due to the fact that the transverse strain in the grout layer is hindered by the inner and outer steel tube, the three-dimensional material behaviour has to be considered. For the description of the multiaxial concrete strength different parametric models can be used, e.g.:

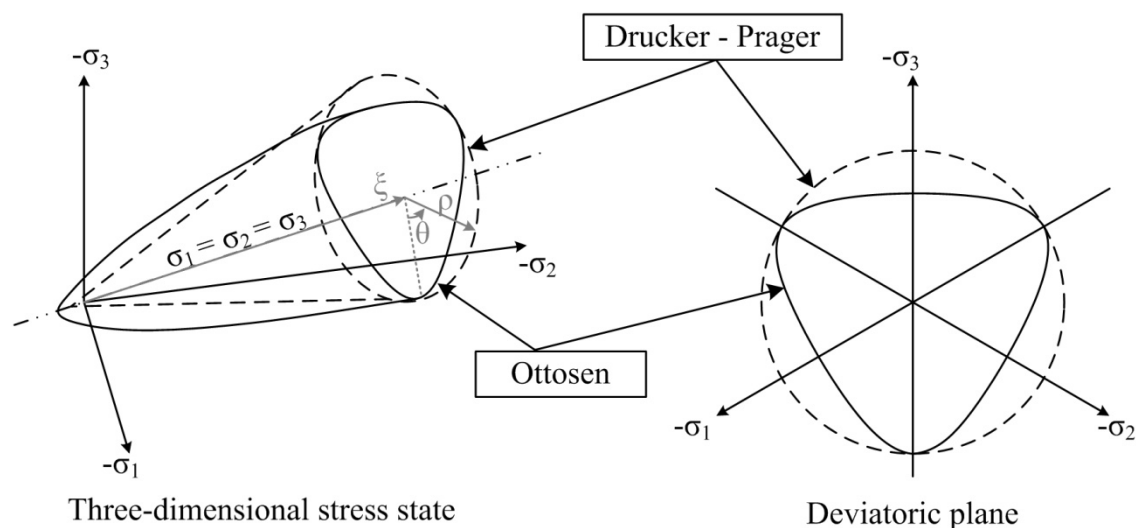
- the one- parameter model by Rankine, Van Mises, Tresca
- the two-parameter model by Mohr-Coulomb, Drucker-Prager
- the three-parameter model by Bresler-Pister, Willam-Warnke
- the four-parameter model by Ottosen, Hsieh, Teng, Chen
- the five-parameter model by Willam-Warnke, Kotsovos, Podgorski, Guo et al.

For a detailed description of these models reference is made to Speck (2008). Even though the Drucker-Prager model according to Drucker & Prager (1952) is a well-known model implemented in user-friendly finite element software, it does not account for the multiaxial



bearing behaviour of high strength concrete correctly. According to Speck (2008) it overestimates the tensile and the high compressive strength. Hence, this model is merely applicable to high strength grouts and concrete by useful modifications. Lochte-Holtgreven (2013) demonstrates that the Drucker-Prager criterion has a limited validity for compression or tension stress states, and does not account properly for mixed multiaxial stress states as present at axially loaded grouted connections. Nevertheless, Lochte-Holtgreven (2013) and Wilke (2014) both conclude, that the Drucker-Prager criterion is sufficient for the description of the global load bearing behaviour of grouted connections. For a detailed consideration multi parametric models like the Ottosen criterion are recommended by Lochte-Holtgreven (2013).

The Ottosen (1977) model represents a favourable model, because of its reasonable easy applicability and considerable compliance with test data. Its transferability and application for high strength concrete is proven and adapted by investigations of Chen (1982), Dahl (1992), Hampel (2006) and Speck (2008). Moreover, the Model Code 2010 (2012) recommends using this model for describing the strength at multiaxial stress states.



**Figure 2-16. Three-dimensional failure surface according to Ottosen (1977) and Drucker & Prager (1952) (left) and deviator plane (right).**

Comparison of the Drucker-Prager and Ottosen model in the three-dimensional stress state and the deviator plane depicts the differences of both yield criteria, cf. Figure 2-16. The Drucker-Prager describes a conical yield surface having a circular form in the deviator plane. Consequently, any three-dimensional principle stress combination  $\sigma_1$ ,  $\sigma_2$ ,  $\sigma_3$  provokes a failure on identical meridians. In other words, compressive and tensile induced failure are induced by identical stress combinations. By contrast, the Ottosen failure criterion accounts for a reduced tensile capacity by its yield surface description reflecting a fairly triangular shape in the deviator plane, cf. Figure 2-16. Convex curved meridians form the Ottosen failure surface in the three-dimensional stress space, cf. Figure 2-16 left, which can be described by the stress invariants  $I_1$ ,  $J_2$ , and  $J_3$ . The failure surface can be presented in the Haigh-Westergaard-coordinates  $\xi$ ,  $\rho$  and  $\theta$ . The hydrostatic axis  $\xi$  ( $\sigma_1 = \sigma_2 = \sigma_3$ ) depicts the stress state where all principle stresses have the same value. The deviator axis  $\rho$  being orthogonal to the hydrostatic

axis  $\xi$  defines the distance to the hydrostatic stress state. The parameter  $\theta$  represents the Lode angle in the deviator plane.

The Drucker-Prager failure criterion according to Drucker & Prager (1952) is described by the invariants  $J_2$  and  $I_1$  and the strength related parameters  $\alpha$  and  $K$  by the following equation:

$$F(I_1, J_2) = \alpha \cdot I_1 + \sqrt{J_2} - K = 0 \quad \text{Eq. 2-20}$$

The parameters  $\alpha$  and  $K$  are derived by considering strength characteristics of the concrete, cf. Annex C. The Ottosen (1977) failure model is based on the hydrostatic and deviator stress invariants and four additional parameters, which can be determined by material tests. The failure surface is described by the uniaxial compressive strength  $f_c$ , the invariants  $I_1$  and  $J_2$  and the material specific parameters  $A$ ,  $B$  and  $\lambda$ , whereby  $\lambda$  depends on the deviator angle  $\theta$  and is defined by material specific parameters  $K_1$  and  $K_2$ .

$$F(I_1, J_2, \theta) = A \cdot \frac{J_2}{|f_c|^2} + \lambda \cdot \frac{\sqrt{J_2}}{|f_c|} + B \cdot \frac{I_1}{|f_c|} - 1 = 0 \quad \text{Eq. 2-21}$$

with

$$\lambda = K_1 \cos \left[ \frac{1}{3} \arccos(K_2 \cos 3\theta) \right] \quad \text{for } \cos 3\theta \geq 0 \quad \text{Eq. 2-22}$$

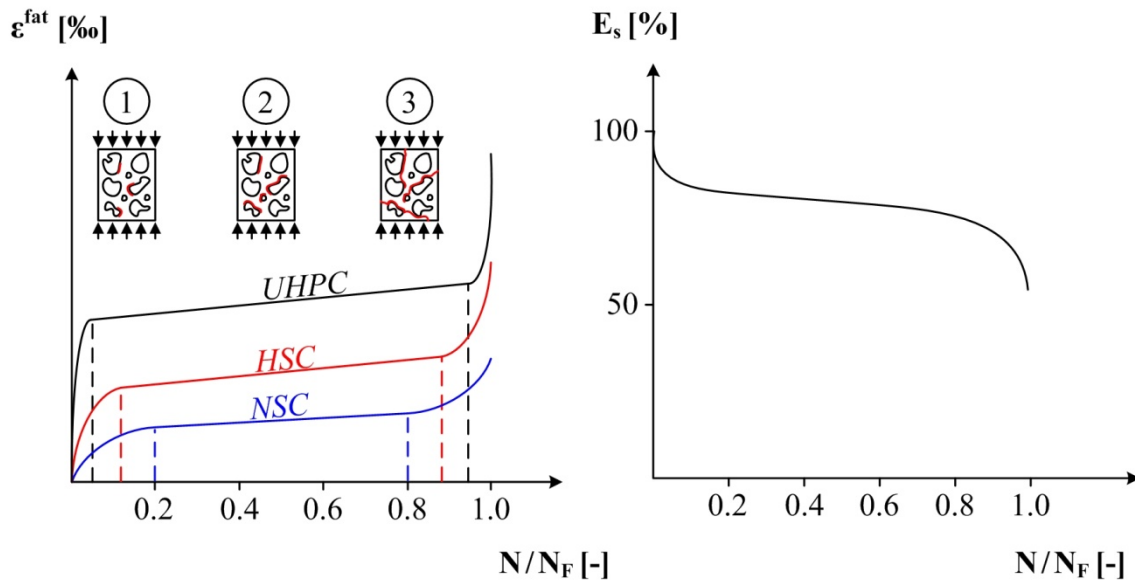
$$\lambda = K_1 \cos \left[ \frac{\pi}{3} - \frac{1}{3} \arccos(-K_2 \cos 3\theta) \right] \quad \text{for } \cos 3\theta < 0 \quad \text{Eq. 2-23}$$

The material specific parameters can be calibrated by material tests and available test data. Ottosen (1977) used four strength related parameters which are the uniaxial compression strength  $f_c$ , the uniaxial tension strength  $f_{ct}$ , the biaxial compression strength  $f_{cc}$  and a second value on the compressive meridian with possibly large hydrostatic stress. Reference equations in accordance to the current code regulations are presented in Annex C. Regarding crack formations related to the failure surface of three-dimensional stressed concrete cubes reference is made to Speck (2008).

Apart from the multiaxial behaviour, the fatigue behaviour of high strength concrete has to be considered as it substantially influences the fatigue performance of grouted connections. Generally, the fatigue performance is characterised by the progressive damage in a material being subject to repeated loading. The damage behaviour can either be described by analysing the stiffness reduction  $E_s$  or by considering the irreversible strain  $\varepsilon^{\text{fat}}$  development depending on the normalised number of load cycles  $N/N_F$ , cf. Figure 2-17.

With increasing load cycles, the stiffness reduces and the deformations increase. The deformation behaviour of concrete under repeated loading can be divided into three phases which are associated with the changes in the material structure, status 1, 2, and 3 cf. Figure 2-17. The initial phase is defined by non-linear strain increase and stiffness decrease, cf. Holmen (1979) and Grünberg et al. (2014b). Subsequent, the crack growth stabilises showing a nearly linear development. As micro cracks increase to macro and matrix cracking provoking in the end failure, the third phase is initiated by a considerable non-linear ascending strain and descending stiffness development. According to Wefer (2010) and

Grünberg et al. (2014b) the initial and last phase reduce for ultra-high strength concrete to 3% to 5 % of the related load cycles, cf. Figure 2-17 left.



**Figure 2-17. Schematic sketch of the cyclic strain development for normal strength concrete (NSC), high strength concrete (HSC) and ultra high strength concrete (UHPC) (left) and stiffness development (right) based on Holmen (1979) and Pfanner (2003).**

The stiffness development shows a similar progress as the strain development. The documentation of the continuously decreasing specimen stiffness due to fatigue loading and the determination of the secant modulus, it is possible to account for the material degradation and the damage development, cf. Grünberg et al. (2008).

In order to account for the non-linear strain development and damage progress induced by repeated loading, Pfanner (2003) developed the stress-strain relationship considering damage reduced stiffness based on the elastic-plastic damage model by Pölling (2000):

$$\sigma(\varepsilon) = (\varepsilon - \varepsilon_{pl}) \cdot (1 - D) \cdot E_c \quad \text{Eq. 2-24}$$

Herein  $\varepsilon$  represents the total and  $\varepsilon_{pl}$  the plastic strain,  $D$  the damage and  $E_c$  the tangent modulus at the initial loading. Pölling's (2000) model describes the stress-strain relationship by accounting for a reduced stiffness and plastic strains for monotonic initial loading followed by a reloading branch. Under consideration of the simplified assumption of an isotropic material damage, the equation describes the reduced stiffness  $E_D$  depending on the material damage  $D$ :

$$E_D = (1 - D) \cdot E_c \quad \text{Eq. 2-25}$$

The damage  $D$  according to the Palmgren-Miner rule reveals the damage on the basis of developed S-N curves. Relating the applied number of load cycles to the endurable number of load cycles identifies the damage  $D$ , cf. Eq. 2-18.

In other words, the fatigue behaviour of concrete materials is described by the developed S-N curves. Even though the fatigue behaviour of concrete has been studied extensively for many decades, current standards provide S-N curves developed on basis of uniaxial tests. The impact of triaxial fatigue loading is subject of recent research and until today not finally

identified. Therefore, applicable S-N curves are rare and limited. As the grout in grouted connections is exposed to both, fatigue loading and triaxial stress states, recent research findings considering triaxial fatigue tests are briefly summarised to support the evaluation of the investigated fatigue behaviour of the test specimens.

Takhar et al. (1974) focused on the triaxial fatigue behaviour by applying a cyclic axial load and a monotone active radial load to normal concrete specimen. By contrast, Hooi (2000) investigated the impact of a passive radial confining pressure to the triaxial fatigue behaviour by wrapping the cylindrical test specimens up with helical reinforcement. Both triaxial tests revealed, that a lateral pressure increases the endurable number of load cycles and therefore increases the fatigue strength. Nevertheless, it has to be differentiated between the beneficial effect of active and passive lateral pressure, cf. Hooi (2000). While the active lateral pressure remains constant, the passive confining pressure increases with increasing axial loading. Hence, the active confining pressure reduces micro crack formation and propagation, whereby the passive confining pressure has to be activated by initial cracking. With increasing cracking the passive radial pressure increases until the confinement yield strength is reached. Thus, the passive confinement prevents a sudden failure of the test specimen and leads to a more ductile behaviour. According to Hooi's (2000) proposed S-N curves the effect of lateral confinement declines with increasing load cycles compared to uniaxial loaded S-N curves. Based on the fact, that Takhar et al. (1974) investigated normal strength concrete, König & Danielewicz (1994) recommend to consider the positive effect of lateral compression by considering a higher compressive concrete strength and corresponding uniaxial S-N curves.

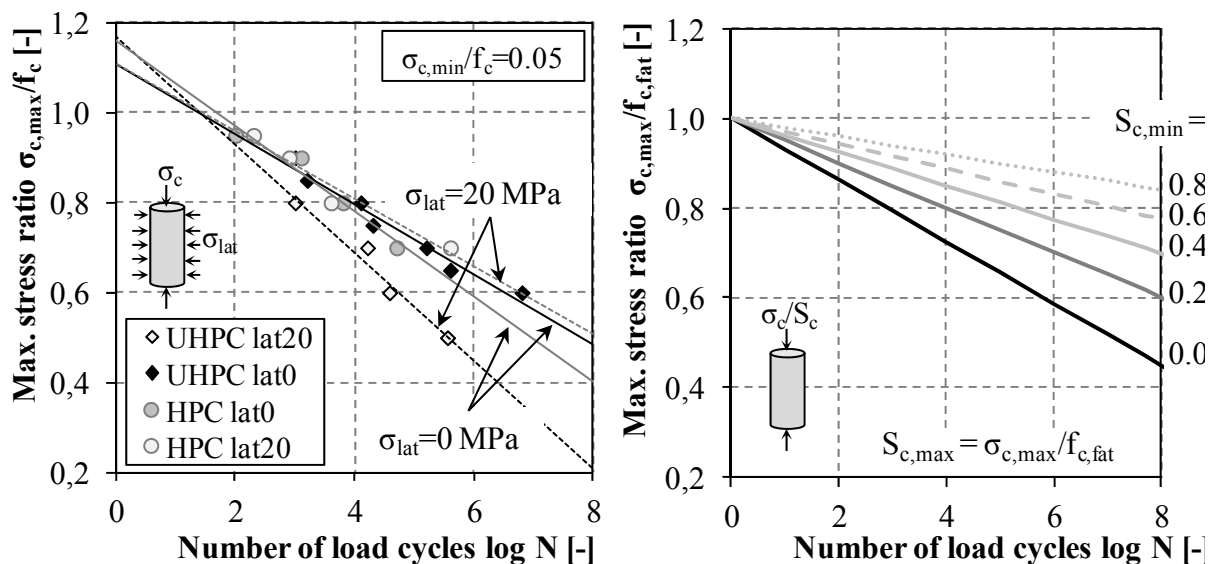


Figure 2-18. Fatigue test results for triaxial tested HPC and UHPC according to Grünberg & Oneschkow (2011) and Grünberg & Ertel (2012) (left) and S-N curves according to Model Code 2010 (2012) for uniaxial loaded HPC (right) based on Lochte-Holtgreven (2013).

Recent developments by Grünberg & Oneschkow (2011), Grünberg & Ertel (2012) and Grünberg et al. (2014a) deal with the fatigue behaviour of high strength and ultra high strength concrete at active triaxial loading conditions. Initial cyclic triaxial tests by Grünberg & Oneschkow (2011) indicated no clear trend for the triaxial fatigue tests compared to uni-

axial fatigue tests with HPC. Grünberg & Ertel (2012) observed from triaxial cyclic tests with UHPC that increased lateral compression provokes earlier fatigue failure, cf. Figure 2-18.

Hence, the S-N related regression curve for laterally loaded UHPC specimens ( $\sigma_{\text{lat}} = 20$  MPa) is steeper as for uniaxial loaded specimens ( $\sigma_{\text{lat}} = 0$  MPa). Even though this curve is steeper and corresponding number of cycles are smaller compared to the uniaxial loaded specimens, it has to be emphasised that triaxial loaded specimens have an increased uniaxial compression strength due to the lateral active confinement and an enormous increased fatigue stress level. Thus, for the comparison of the fatigue behaviour of confined and unconfined specimens, the substantial difference of the underlying uniaxial strength level has to be considered. It can be summarised that multiaxial loaded UHPC and HPC specimens are characterised by an increased uniaxial and fatigue strength. As UHPC is commonly equipped with fibres and has comparable large uniaxial compressive strength of  $f_c = 150 - 200$  MPa, the high performance concrete with uniaxial compressive strength of  $f_c = 50 - 150$  MPa depicts a more reliable reference for the herein analysed high performance grout. Based on the absence of triaxial fatigue tests with high strength grouts and the correlated material behaviour of high performance grout and concrete, it is assumed that the HSC fatigue behaviour covers the fatigue behaviour of grout sufficiently. As a result of previously presented triaxial fatigue test results, it is suggested that uniaxial S-N curves represent a good and conservative approximation to determine the fatigue behaviour of triaxially loaded grout. Similar assumptions for grouted connections have been successfully applied by Göhlmann (2008) and Lochte-Holtgreven (2013).

The uniaxial S-N curves were recently adapted for pulsating compressive loaded high strength concrete by Lohaus et al. (2011) and Wefer (2010) accounting for a modified reference fatigue compressive strength  $f_{\text{ck,fat}}$ , cf. Eq 2-26.

$$f_{\text{ck,fat}} = 0.85 \cdot \beta_{\text{cc}}(t) \cdot f_{\text{ck}} \cdot \left(1 - \frac{f_{\text{ck}}}{40 \cdot f_{\text{ck0}}}\right) \quad \text{Eq. 2-26}$$

The fatigue compressive strength accounts for the compressive strength  $f_{\text{ck}}$ , the coefficient  $\beta_{\text{cc}}(t)$  depending on the concrete age at the beginning of loading and  $f_{\text{ck0}} = 10$  MPa as reference strength. These S-N curves and the formula for the reference value represent latest developments which are included in current codes, cf. Model Code 2010 (2012). The S-N curve for a pulsating compression has the following form:

$$\text{for } \log N_1 \leq 8 \quad \log N_1 = \frac{8}{(Y-1)} \cdot (S_{\text{c,max}} - 1) \quad \text{Eq. 2-27}$$

$$\text{for } \log N_1 > 8 \quad \log N_2 = 8 + \frac{8 \cdot \ln(10)}{(Y-1)} \cdot (Y - S_{\text{c,min}}) \cdot \log \left( \frac{S_{\text{c,max}} - S_{\text{c,min}}}{Y - S_{\text{c,min}}} \right) \quad \text{Eq. 2-28}$$

$$\text{with } Y = \frac{0.45 + 1.8 \cdot S_{\text{c,min}}}{1 + 1.8 \cdot S_{\text{c,min}} - 0.3 \cdot S_{\text{c,min}}^2}; S_{\text{c,max}} = \frac{|\sigma_{\text{c,max}}|}{f_{\text{ck,fat}}}; S_{\text{c,min}} = \frac{|\sigma_{\text{c,min}}|}{f_{\text{ck,fat}}}$$

In addition to compression based S-N curves, Model Code 2010 (2012) recommends for compression-tension loading and tension-compression loading additional S-N equations depending on the provoked failure by either compression or tension forces:

$$\log N = 9 \cdot (1 - S_{c,\max}) \quad \text{for } \sigma_{ct,\max} \leq 0.026 \cdot |\sigma_{c,\max}| \quad \text{Eq. 2-29}$$

$$\log N = 12 \cdot (1 - S_{ct,\max}) \quad \text{for } \sigma_{ct,\max} > 0.026 \cdot |\sigma_{c,\max}| \quad \text{Eq. 2-30}$$

Herein  $\sigma_{ct,\max}$  represents the maximum applied tensile stress and  $\sigma_{c,\max}$  the maximum applied compression stress,  $f_{ckt,\min}$  the minimum characteristic tensile strength and  $f_{ck,fat}$  the fatigue reference compressive strength.

As aforementioned, current fatigue design for concrete structures is based on the Palmgren-Miner rule, which presumes a linear relation between load and damage accumulation. Thus, for multi-stage loading, individual damage values are added to an accumulated damage neglecting any load sequence impacts. In fact, numerous research investigations in the past intended to quantify the load sequence effect to the fatigue behaviour of concrete for compressive and tensile loading conditions. Hilsdorf & Kesler (1960) performed two-stage bending tests with an ascending load scenario, descending load scenario and an one-stage load scenario on the larger level. Comparison of the number of endurable load cycles revealed that the ascending load scenario provokes a reduced fatigue strength and the descending load scenario a larger fatigue strength compared to the one stage load scenario. Contrary to these findings, Holmen (1979) observed for a two-stage pulsating compressive loading condition that decreasing load stages provoked earlier failure than increasing load stages. As proposed by Göhlmann (2008), reason for the results by Holmen (1979) might be the rather large load level provoking early failure. The experimental investigations by Klausen (1978), Klausen & Weigler (1979) and Tepfers (1977) indicated no clear trend of load sequence effect to pulsating compression loaded test specimens. Moreover, tensile fatigue tests by Cornelissen (1984), Cornelissen & Reinhardt (1984) revealed a large scatter of test results with no exact conclusion.

According to Göhlmann (2008) an ascending load sequence provokes slightly smaller damage than a descending load sequence. With regard to the interrelation of load sequence and fatigue strength the Palmgren-Miner method was modified and adopted by some researchers, e.g. Holmen (1979), Oh (1991) and Cao et al. (2006). Nevertheless, the modifications are closely related to their test settings and experimental results. Until today no general applicable modification exists that accounts reliably for the effect of load sequences to the fatigue behaviour. Hence, current codes as the Model Code 2010 (2012) recommend to use the Palmgren-Miner hypothesis.

## 2.5 Conclusion

Previous chapter presents the current state of the art and state of the scientific knowledge for grouted connections by focusing connections at latticed support structures for offshore wind turbines having a considerable large grout annulus. This type of grouted connection was set in contrast to the connections in monopile substructures and O&G platforms, as the majority of

research findings and design approaches originate from investigations on these kind of constructions. Grouted connections at monopile substructures correlating to wind turbines, are exposed to predominant bending moments, which influences the load bearing behaviour substantially. Even though a large number of experimental tests have been performed for axially loaded grouted connections at O&G platforms, the size and load conditions differ significantly from grouted connections in jackets for offshore wind turbines. Present grouted connections with large grout annulus are exposed to a numerous load cycles. Moreover, the connection's dimensions were enlarged, compared to grouted connections at O&G platforms, to meet reliability and safety requirements for offshore wind turbines.

Nonetheless, previous developed approaches enable to describe the basic load transfer mechanism and relevant geometric and material related impact factors. The loads are predominantly transferred by contact forces in the grout-steel interface and compression struts arising between opposed shear keys. Thus, the bearing behaviour is mainly influenced by the geometric parameters in form of the radial stiffness  $K$ , related slenderness ratios  $D/t$ , the shear key height to distance ratio  $h/s$ , the length  $L_g$  and the number of shear keys. Secondly, the behaviour is pronounced by the grout material strength and stiffness. Despite the connection's configuration, evaluation of arising actions at offshore wind turbines have revealed that cyclic loads are the design driver. Thus, the fatigue behaviour displays a central role for the design. Grouted connections at jackets are exposed to axial cyclic tension and compression loads. According to experimental fatigue tests, these alternating loads noticeably reduce the fatigue strength of grouted connections. By contrast, at present no reliable design S-N curve for grouted connections exists. Merely tentative best-fit curves were developed on the basis of comparably small-scaled tests. In addition, current design approaches are based on uniaxial S-N curves for high strength concrete and steel. The required stress states are determined by complex numerical calculations, which should preferably account for multiaxial material behaviour.

The overview of current knowledge, design approaches and related previous research investigations has revealed that neither increased grout thicknesses have been addressed by conducted investigations nor have large-scaled cyclic axially loaded tests been performed. Although the general load transfer mechanism can be described by former tests, the impact of the up-scaled grout thicknesses to the fatigue behaviour especially with respect to varied load ratios and appearing failure states are currently unknown. As current grouted connections have immense grout thicknesses of up to 500 mm and  $D_g/t_g$  ratios are far outside previous design limitations, the need for experimental investigations becomes obvious. Due to a lack of knowledge for grouted connections with large grout thicknesses, the following issues need to be investigated experimentally:

- identification of the fatigue performance for increased grout thickness  $t_g$  adapted from connections at latticed substructures,
- determination of the impact caused by different high strength materials covering the available range of strength,
- consideration of cyclic axial loads covering different load levels and load ratios,

- examination of the fatigue failure mode for grouted connections with large grout annulus,
- validation of the applicability of present design approaches.

Current numerical approaches and design concepts are not validated by cyclic axially loaded grouted connections with large grout annulus. Thus, it is not clear whether available approaches consider appropriately the bearing behaviour and fatigue performance for this kind of grouted connections. As present design concepts rely on numerical calculations, the substantial need for numerical investigations addressing the following aspects becomes apparent:

- identification of applicable material models,
- adaptation of material models with respect to high strength grout characteristics,
- consideration of cyclic material degradation,
- validation of numerical high-resolution models by experimental results with increased grout thicknesses,
- determination of the fatigue performance of grouted connections with large grout annulus by varying different parameters,
- examination of possible load sequence effects,
- enhancement of current numerical design concepts if necessary.

To overcome the presented knowledge gap for cyclic axially loaded grouted connections with large grout thicknesses, experimental and numerical investigations covering the mentioned issues are performed and presented in the following chapters.



### 3 Experimental Investigations

#### 3.1 Test Concept

The overview and discussion about the state of the art and the state of the scientific knowledge for grouted connections from O&G platforms and from former tests for monopiles have revealed that current design approaches and concepts do not cover present dimensions and load situations of grouted connections used in latticed substructures of offshore wind turbines. As today's grouted connections for those substructures have extensive large grout thicknesses of up to 500 mm and  $D_g/t_g$  ratios being far beyond previous design limitations, the need for experimental investigations becomes obvious. Moreover, the impact of cyclic axial loads on the fatigue performance of grouted connections with large grout annuli are comparatively unknown at present. Hence, large-scale tests with up-scaled grout annuli become necessary and are performed by experimental investigations of this thesis. For economical and time-consuming reasons, a limited number of experiments is conducted focussing on the obvious uncertainties as follows:

- increased grout thickness  $t_g$  adopted from connections at latticed support structures of offshore wind turbines,
- different high strength grout materials representing the available strength range,
- cyclic axial loads covering different load levels and stress ratios,
- testing until failure to examine failure modes and related damage characteristics.

Consequently, the experimental test program is composed of four test specimens being exposed to cyclic axial loads. Two parameters, the grout layer thickness and the grout material strength, are varied. Effects of other geometrical parameters like the  $h/s$  ratio of the shear keys are considered by subsequent finite element analysis. By this, a detailed study of arising stresses, related fatigue behaviour and cyclic degradation was possible, cf. chapter 4.

The series of large scale fatigue test specimens (TS) in a scale of  $\sim 1:2$  and  $\sim 1:4$  being numbered from TS01 to TS04 are summarised in Figure 3-1.

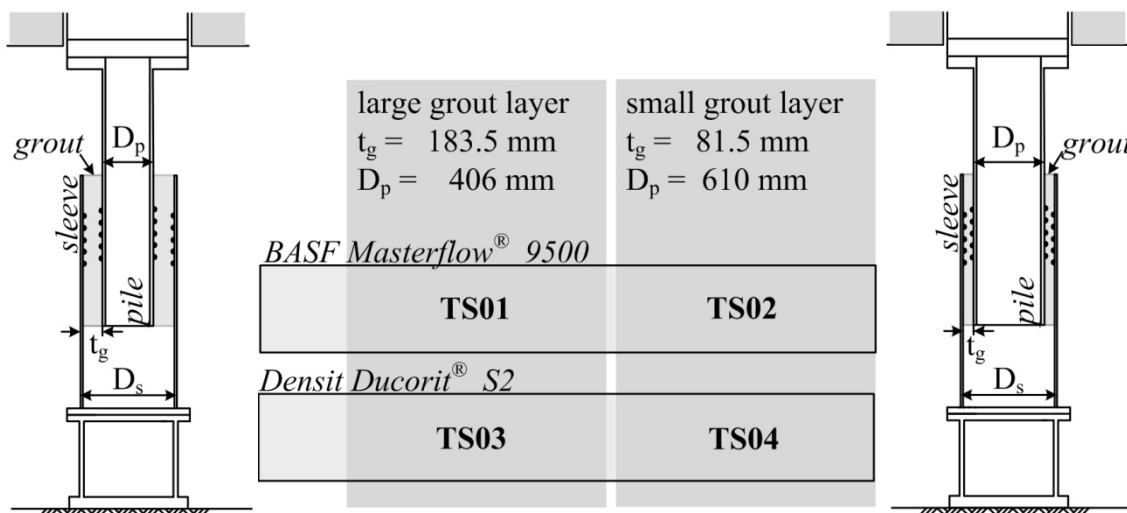


Figure 3-1. Overview of large-scale fatigue test specimens and their configuration.

Offshore reference structures from the test wind farm alpha ventus (2012), a pre-piled jacket and a post-piled tripod, are used to define the geometric dimensions and to choose adequate materials for the scaled specimens. The grout layer thickness is varied by using two different inner steel tubes with a diameter of  $D_p = 406$  mm and  $D_p = 610$  mm. In combination with a sleeve diameter of  $D_s = 813$  mm, the large grout layer results to  $t_g = 183.5$  mm, at the test specimens TS01 and TS03, and the small grout layer results to  $t_g = 81.5$  mm at the test specimens TS02 and TS04. All four test specimens are filled with high strength performance grouts, whereby BASF Masterflow<sup>®</sup> 9500 is used for TS01 and TS02 and Densit Ducorit<sup>®</sup> S2 is used for TS03 and TS04. These two grout materials are chosen in order to cover a wide range of compressive strengths. The Densit Ducorit<sup>®</sup> S2 mixture relates to the year of testing, 2014, thus, may not represent the current product behaviour as mixtures have been changed.

A specified loading program consisting of alternating and pulsating compression loads is applied. During testing, the occurring deformations and strains are measured by lasers, potentiometer and strain gauges. In order to determine installed material characteristics and surface condition, specific tests of the grout and steel are performed. The grout characteristics are defined by testing the fresh and hardened material. By tensile testing and surface roughness measurements of the steel tubes general steel properties can be derived. The surface roughness measurements are performed before and after conducting the fatigue test program to facilitate an evaluation of the surface roughness degradation during testing and to enable a comparison of the test results for the different test specimens. The following sections deal with the conducted experimental tests in detail. Finally, the fatigue performance is evaluated on the basis of measured deformations, relative displacements, strains and observed crack patterns. Achieved fatigue test results are compared to present design approaches, cf. chapter 5.2, in order to evaluate their applicability to grouted connections with increased grout thickness. Moreover, the tests provide the basis for the validation of subsequent finite element analysis.

## 3.2 Test Specimen

### 3.2.1 Geometry and reference structures

With the intention to assess the fatigue performance of present grouted connections in latticed substructures of offshore wind turbines, two appropriate offshore wind turbine substructure types are chosen as reference structures: a pre-piled jacket and a post-piled tripod, cf. Figure 2-3. Compared to grouted connections in monopiles, both reference structures have a relatively large grout annulus for compensating installation induced inclinations. Modified dimensions of two reference structures are adapted from originally designed and installed offshore wind turbines in the North Sea at the research offshore wind farm alpha ventus. This research wind farm is located 45 km to the north of the island Borkum in the German Exclusive Economic Zone (EEZ). At alpha ventus water depths of about 40 m are present. The wind farm consists of 12 offshore wind turbines each with 5 MW nominal power output, 6 with a tripod substructure and 6 with a jacket substructure. Further facts on the wind farm are reported by the alpha ventus (2012).

The dimensions of adapted reference structures and corresponding test specimens are summarised in Table 3-1.

**Table 3-1. Geometric dimensions of reference grouted connections and related test specimens.**

<i>section</i>	<b>dimension</b>	<b>unit</b>	<b>reference jacket</b>	<b>TS01/ TS03</b>	<b>reference tripod</b>	<b>TS02/ TS04</b>
<i>pile</i>	outer diameter $D_p$	[mm]	1'000	406	2'250	610
	thickness $t_p$	[mm]	50	25	70	25
	$D_p/t_p$	[-]	20	16	32	24
<i>sleeve</i>	outer diameter $D_s$	[mm]	2'000	813	3'000	813
	thickness $t_s$	[mm]	50	20	70	20
	$D_s/t_s$	[-]	40	41	43	41
<i>grout</i>	outer diameter $D_g$	[mm]	1'900	773	2'860	773
	thickness $t_g$	[mm]	450	183.5	305	81.5
	$D_g/t_g$	[-]	<b>4.2</b>	<b>4.2</b>	<b>9.4</b>	<b>9.5</b>
	$L_g$	[mm]	5'000	1'240	4'000	1'240
<i>shear key</i>	distance	[mm]	180	100	250	100
	height	[mm]	10	6	15	6
	width	[mm]	20	12	30	12
	number	[-]	20	5	12	5
<b>scale</b>		<b>[-]</b>	<b>-</b>	<b>~1:2</b>	<b>-</b>	<b>~1:4</b>

Test specimens named with odd numbers represent the jacket geometry and test specimens with even numbers represent the tripod geometry. The test specimen dimension is defined by focusing on the grout layer as most relevant test parameter. The grout thicknesses of the specimens are adjusted by the grout diameter to grout thickness ratio  $D_g/t_g$  of the reference structures, cf. Table 3-1. Resultant, the jacket structure and the corresponding test specimens have a grout slenderness ratio of  $D_g/t_g = 4.2$ , whereas the tripod structure and the assigned test specimens have a grout slenderness ratio of  $D_g/t_g = 9.5$ .

A second criterion for the test specimen configuration constitutes the test facility. The test specimen's geometry and expected failure load have to fit in the limitations of the available testing rig. Attempting to minimise any scale effects, it is aimed to realise test specimen as large as possible and in close relation to the dimensions of the offshore connections. In the end, the scale of the pre-piled jacket with a large annulus related test specimen results to approximately 1:2 and the post-piled tripod with a small annulus related test specimen to approximately 1:4. The grout thickness variation is achieved by different inner steel tube dimensions. By merely changing the inner steel tube dimension, cf. Table 3-1, further geometric parameters, e.g. of shear keys or sleeve, remained the same and additional adaptations for the test facility installation are dispensable.

The test specimens are attached to the test rig by a loading plate at the top and an adapter at the bottom. A load cylinder, which is connected by prestressed bolts to the loading plate at the

top, induced the compression and tension test loads. To allow the application of tensile loads, the adapter is attached similarly at the bottom by prestressed bolts to the machine floor. The connection of the plate and the adapter to the test specimens is realised likewise by prestressed bolted flange connections. Configuration and geometrical dimensions of the four test specimens and applied adaptations are illustrated and summarised in Figure 3-2.

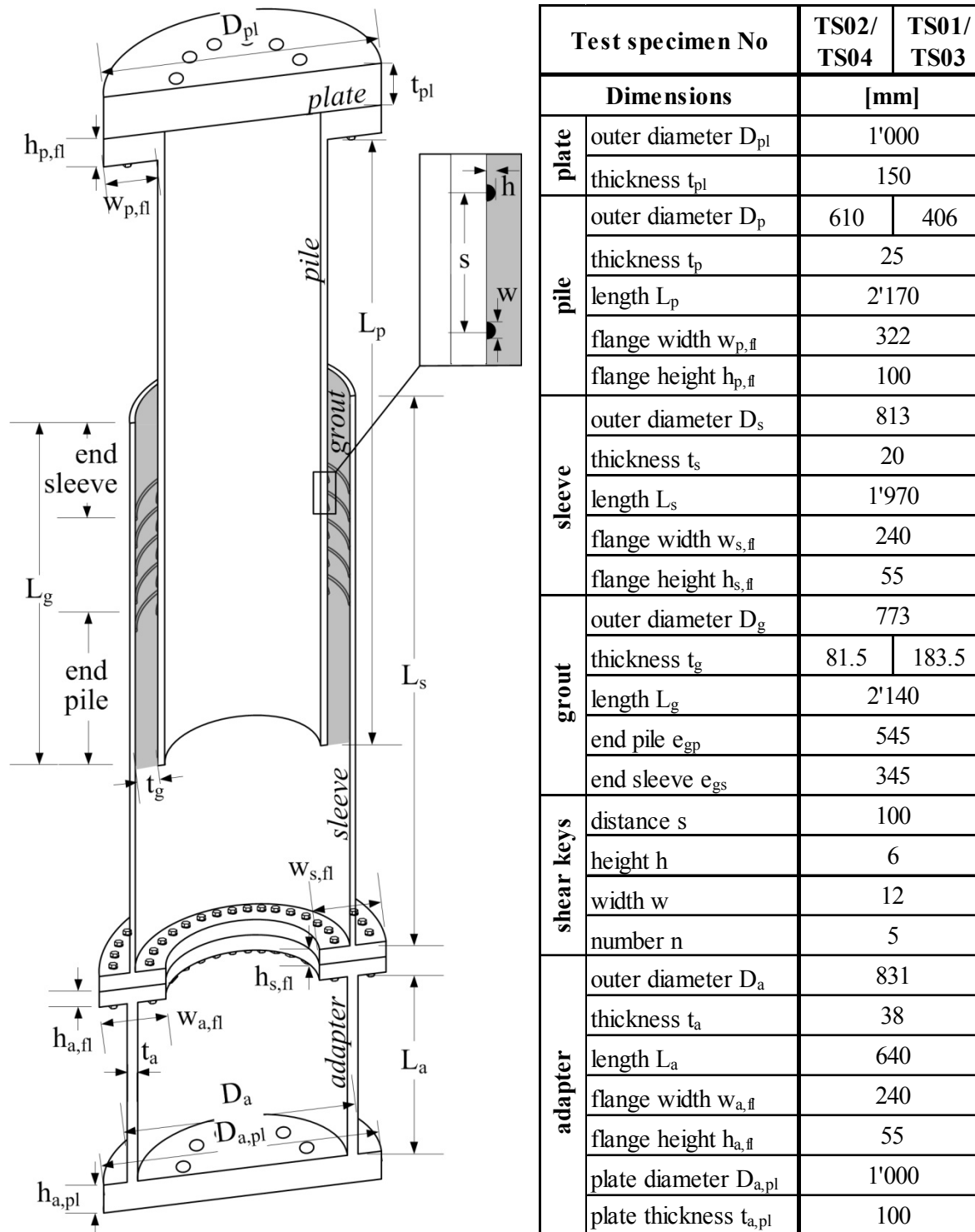


Figure 3-2. Sketch and table representing test specimen geometry and configuration.

In consideration of the current state of the art as well as latest designed and installed grouted connections, both test geometries are equipped with shear keys as circumferential weld beads. The weld beads are placed diagonally, offset vertically, on the opposing surfaces of the steel tubes inside the grout layer. As stated in chapter 2.2.2 and 2.2.3, shear keys increase substantially the interlocking effect of the tubular sections, as compression struts between opposing shear keys occur. The test specimens are designed with five shear keys on sleeve and pile. Due to the test load patterns consisting of alternating loads and pulsating compression loads, it is forced to have a higher transferability for compression loads than for tension loads. Thus, the shear keys are arranged in such a way that five shear key pairs can be activated for compression loads and only four shear key pairs could be activated for tension loads, cf. Figure 3-2. The shear keys are uniformly distributed over the effective connection length compliant with current design guidance. According to current standards, e.g. DNV-OS-J101 (2014) and DIN EN ISO 19902 (2014) the total grouted connection length should be reduced at the top end and bottom end by either the shear key spacing  $s$  or twice the grout thickness ( $2 \cdot t_g$ ) to encounter for potential weak interface zones. In fact, this reduction represents a safety measure to consider a reduced design capacity originating from grout mixture separation or sea water impact at the grouted connection edges. For the test specimens this influence can be excluded. To keep the comparability between both test geometries, the shear keys are positioned equally on all test specimens. The dimensions of the shear keys are selected to represent shear key height to shear key distance ratios  $h/s$  identical to reference structures, cf. Table 3-2. In this respect, Table 3-2 presents the complete overview of geometrical ratios for reference structures and test specimens and their compliance to code related validity ranges. Apart from the radial stiffness  $K$ , cf. Eq. 3-2, and the grout slenderness, remaining geometric parameters of the test specimens coincide with the validity ranges according to the standards.

**Table 3-2. Comparison of validity ranges with reference connections and test specimens.**

Geometrical validity range according to current standards*	reference jacket		TS01/ TS03		reference tripod		TS02/ TS04	
	value	ok	value	accord	value	accord	value	accord
$20 \leq D_p/t_p \leq 40(60)**$	20	✓	16	✗	32	✓	24	✓
$30 \leq D_s/t_s \leq 140$	40	✓	41	✓	43	✓	41	✓
<b><math>10 \leq D_g/t_g \leq 45</math></b>	<b>4.2</b>	<b>✗</b>	<b>4.2</b>	<b>✗</b>	<b>9.4</b>	<b>✗</b>	<b>9.5</b>	<b>✗</b>
$1 \leq L_e/D_p \leq 10$	4.1	✓	2.2	✓	1.5	✓	1.8	✓
<b><math>0.0 \leq h/s \leq 0.10</math></b>	<b>0.06</b>	✓	<b>0.06</b>	✓	<b>0.06</b>	✓	<b>0.06</b>	✓
$1.5 \leq w/h \leq 3.0$	2	✓	2	✓	2	✓	2	✓
$D_p/s \leq 16$	6	✓	4	✓	9	✓	6	✓
$h/D_p \leq 0.012$	0.010	✓	0.015	✗	0.007	✓	0.010	✓
<b><math>K \leq 0.02</math></b>	<b>0.07</b>	<b>✗</b>	<b>0.07</b>	<b>✗</b>	<b>0.04</b>	<b>✗</b>	<b>0.04</b>	<b>✗</b>

\* Norsok Standard N-004 (2013); DNV-OS-J101 (2014); DIN EN ISO 19902 (2014)  
 \*\* according to DNV-OS-J101 (2014)

### 3.2.2 Materials

The test specimens are composed by the two materials steel and grout. The manufacturing company Erndtebrücker Eisenwerke GmbH & CO KG, a steel tube supplier for offshore wind turbines, provides the steel tubes for the test specimens. The steel tubes are ordered as S355 representing a typical yield strength for primary steel components of offshore structures, cf. GL Guideline (2012). The steel properties of the received tubes are summarised according to the corresponding inspection certificates according to EEW (2011) in Annex A.1. However, subsequent to the connection's fatigue tests, steel tensile tests of sleeve tube segments are performed by the Institute for Materials (IW) of the Leibniz Universität Hannover in accordance to the DIN EN ISO 6892-1 (2009). The tensile test results, cf. Annex A.2, correlate well with the certificate values. Table 3-3 summarises the material properties of the individual test specimens, whereby for the sleeve the test results and for the pile the manufacturer's data are presented.

**Table 3-3. Steel material properties of the test specimens.**

Test specimen			TS01	TS02	TS03	TS04
Component			sleeve / pile			
Yield strength	$R_{eh} (f_y)$	[MPa]	447 / 360*	457 / 427*	471 / 360*	456 / 427*
Tensile strength	$R_{em} (f_u)$	[MPa]	549 / 450*	537 / 558*	575 / 495*	549 / 558*
Young's modulus	E	[MPa]	210'000**			
Poisson's ratio	$\nu$	[-]	0.3**			
*according to manufacturer's inspection certificates according to EEW (2011)						
**according to DIN EN 10225 (2009)						

The grout materials are selected on the basis of currently available offshore grout products. In an attempt to cover a wide range of material strength, available products and related strength characteristics are scanned to identify a material on the upper and lower strength range of 80 to 150 MPa. On the one hand, the grout material BASF Masterflow<sup>®</sup> 9500 with a mean uniaxial compressive cube strength of  $f_c = 140$  MPa and on the other hand the Densit Ducorit<sup>®</sup> S2, product from 2014, with a mean uniaxial compressive cube strength of  $f_c = 90$  MPa are chosen for the grout layers. In order to consider the as-built material properties inside the test specimens, material tests of fresh and hardened material are performed. Detailed test results are presented in Annex A.3. Table 3-3 summarises the strength parameters provided by the manufacturer and resulting material data from accompanied material tests performed by the Institute of Building Material Sciences of the Leibniz Universität Hannover. Obtained test data reflect the strength properties after testing at the grout age of 28 days according to DIN EN 196-1 (2005). Although different material strengths are initially selected, the comparison of the 28-day strength values reveals a much smaller compressive strength bandwidth than expected. Upon request, the material supplier Densit declared, that the material composition was changed lately, which caused altered

material characteristics. In addition to the 28-day strength, the grout properties at the start of cyclic fatigue tests are determined, cf. Annex A.3.

**Table 3-4 Grout material strength characteristics according to BASF Masterflow<sup>®</sup> (2011) and Densit Ducorit<sup>®</sup> (2013) and fatigue test accompanied material testing**

Test specimen	Material	Manufacturer's data			Material test results**		
		uniaxial compressive cube strength $f_{c,cube,75}$ [MPa]	bending tensile strength $f_{ct,fl}$ [MPa]	Young's Modulus $E_{cm}$ [MPa]	28-days uniaxial compressive cube strength $f_{c,cube,75}$ [MPa]	bending tensile strength $f_{ct,fl}$ [MPa]	Young's Modulus $E_{cm}$ [MPa]
TS01	BASF Masterflow <sup>®</sup> 9500	140	18	50'000	143.13	15.11	47'033
TS02					143.44	17.59	44'250
TS03	Densit Ducorit <sup>®</sup> S2	90	n.a.*	40'000	123.35	14.44	43'700
TS04					131.26	15.07	45'433

\*n.a. → not available; \*\*according to DIN EN 196-1 (2005)

### 3.2.3 Specimen preparation

The test specimens, the load inducing plate and the bottom adapter are prepared by the local steel welding company G + F Strate GmbH, Hannover. The steel tubes are equipped with shear keys and ring flanges.

Geometric dimensions are precisely documented to evaluate any geometrical inaccuracies and imperfections regarding tube thickness, shear key parameters and tubular out-of-roundness. Results of the measurements are presented in Annex A.4. The measured values demonstrate that the geometrical imperfections considering tubular out-of-roundness and steel thickness are within the range of normative allowed tolerances according to DIN EN 10210-2 (2006). Measurements of the shear key parameters have the largest discrepancy, which results from the manual welding process and the relatively small proposed dimensions of the weld beads. Nonetheless, the shear key dimensions comply with the normative allowed tolerances according to DIN EN ISO 5817 (2003). Consequently, the imperfections are not considered by further test documentations and finite element calculations.

To achieve comparable surface conditions for all test specimens, the steel surfaces in the overlapping area are mechanically cleaned. After removing loose corrosive particles, mill scale and impurities, the obtained surface condition has the steel surface preparation grade St2 according to DIN EN ISO 12944-4 (1998), cf. Annex A.5. Detailed information on the surface roughness according to DIN EN ISO 4287 (2010) and DIN EN ISO 4288 (1998) are obtained by tactile surface roughness measurements before and after cleaning of the surfaces. The comparison of the tactile measurements for the different test specimens reveals that similar surface conditions were reached by the mechanical cleaning process, cf. Annex. A.5.

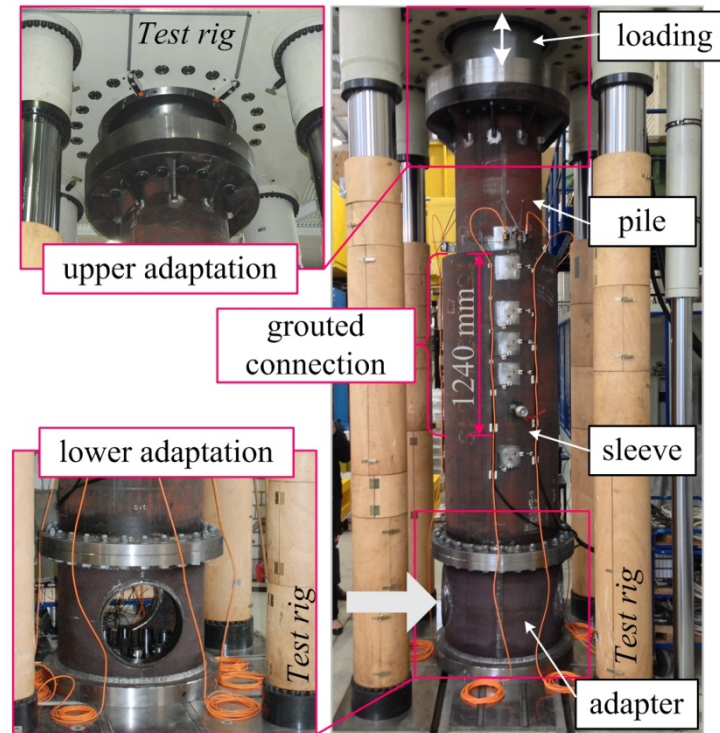
Prior to the final test specimen preparation by grouting, strain gauges are applied to later on inaccessible locations on the inner surface of the pile. For the final assembly of the test specimens, the pile is placed inside the sleeve, the steel tubes are located on top of the adapter and the construction is positioned in the servo-hydraulic testing machine. The adapter is fixed by bolts to the ground plate of the testing machine, while the pile is fixed by bolts to the load application plate being itself mounted to the load cylinder. The pile is positioned in the centre of the sleeve with an overlapping length of  $L_g = 1'240$  mm. Moreover, it is focused to acquire an uniform grout thickness over the length and circumference. The performance of the filling process inside the testing machine provides the opportunity to reduce any eccentricities, to ensure the accurate position of pile and sleeve and to reach a reproducible test specimen configuration. Inside the sleeve a formwork panel is installed at the bottom of the pile for the subsequent grouting procedure. The grouting of the specimens is supported by the respective material supplier with experienced experts and appropriate mixing and pumping equipment. For the filling procedure a two inch grout hose and a Putzmeister S5 pump is used. The hose is made useable by pumping a binder or cement slurry through it prior to the grout material. Despite the actual offshore procedures, the binder is pumped in an empty tray before the hose with the grout material on the tip is connected to the test specimen. A grout overflow as commonly performed at offshore grouted connections is not possible. Similar to offshore grouting procedures, the annulus is grouted bottom-up wise to avoid segregation, sedimentation and voids. A pictured documentation of the filling process is included in Annex A.6. The grouting procedure is accompanied by tests of the fresh grout mix and preparation of material test specimens, cf. chapter 3.2.2. Test results are summarised in Annex A.3. Within the first days of hardening, the accessible grout surface cures while keeping the surface moistened. Once sufficient initial strength of the material is achieved after 7 days, the test specimen is removed carefully from the testing machine and parked in a working area to remove the formwork and apply further strain gauges to the exterior surfaces of pile and sleeve.

### **3.3 Test Procedure**

#### **3.3.1 Test set-up**

The test specimens are connected to the testing machine by two adaptations: an adapter at the bottom and load application plate at the top, cf. Figure 3-3. The fixation is achieved on both sides by prestressed bolts giving the opportunity to realise tension and compression loads during testing. Two manholes at the adapter allow to prestress the bolts for joining the test specimen to the bottom plate of the testing facility. Moreover, the two holes function as cable feed-through for the measurement instrumentation applied inside the pile. During performance of the fatigue tests, the holes assist to control the measurement instrumentation and to observe any grout damage at the interior bottom of the grouted connection.





**Figure 3-3. Test set-up: Large-scale grouted connection adapted to the test rig.**

### 3.3.2 Test load scenario and reference loads

The following subsection introduces the selected test load scenario for the large-scale cyclic tests. Moreover, the ultimate capacity and predicted design related failure eventuation are determined for the test specimens. In order to assess the chosen load levels with regard to real design load cases at offshore substructures, a reference load scenario for a grouted connection at an offshore jacket substructure is presented and evaluated. In the end comparison of test loads and real loads and related capacities of test specimen and reference grouted connections enable to classify the applied test load scenario.

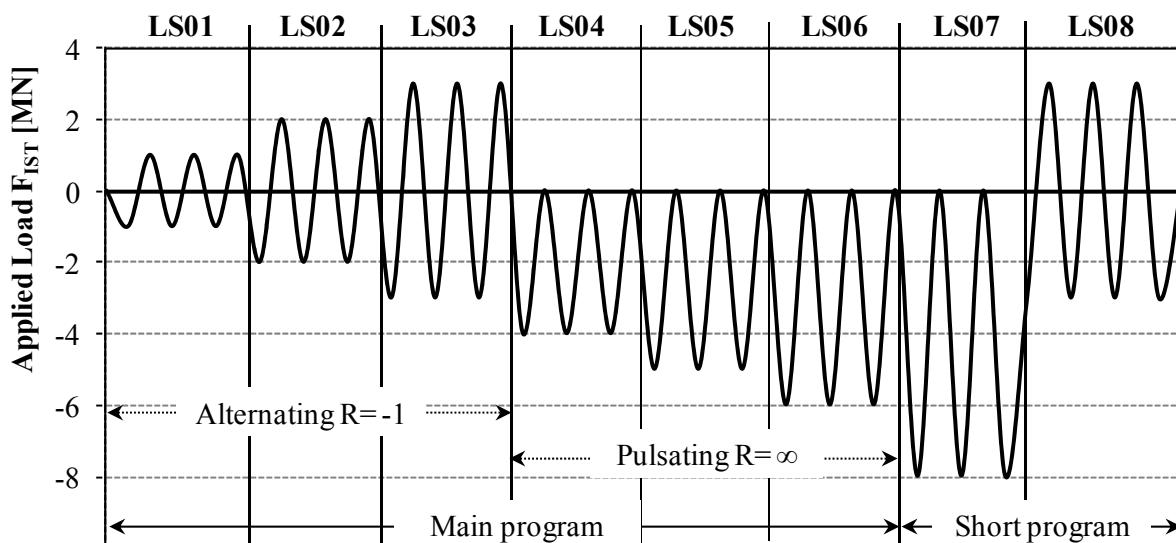
#### Test load scenario

The intension of present experimental tests is to evaluate the fatigue behaviour of grouted connections in latticed substructures by focusing on the load-deflection behaviour, the failure behaviour and the occurring damage patterns. According to Lotsberg et al. (2013), the largest contribution to damage at grouted connections appears for extreme loads between 10'000 and 100'000 load cycles, which is most likely caused by stress cycles arising during large storms or some emergency shut downs. As known from literature, cf. chapter 2.2.5, alternating loads consisting of reversal compression and tension forces cause a reduced fatigue strength. Moreover, extreme load scenarios at jackets comprise alternating loads. Pulsating compression loads have the highest probability to appear at real latticed offshore structures. Thus, it is chosen to expose the test specimens to a load scheme consisting of a stepwise increased amplitude and considerably large compression and tension forces aiming to provoke failure of the specimens. Limiting factor for the choice of the maximum tension and compression loads represent the capacity of the testing machine and the test set-up including

adapter, load application plate and prestressed bolted connections. The Instron (IST) testing rig enables cyclic testing with a maximum load amplitude of  $\pm 8$  MN, while a maximum load of 10 MN can be achieved during static tests.

The test program is divided into load stages (LS) considering alternating loads ( $R = -1$ ) and pulsating compression loads ( $R = \infty$ ), having the aim to cover reversal and pulsating loads. The first three test load stages, LS01 to LS03, represent the alternating load with a stepwise increased maximum tension and compression force from  $\pm 1$  MN in LS01 to  $\pm 3$  MN in LS03. Subsequently, three pulsating compression load stages, LS04 to LS06, with a stepwise increased maximum compression force by 1 MN and corresponding mean load level is applied. In order to provoke damage, each of these test load stages encompasses 100'000 load cycles constituting the main test program. For cases, where no failure is observed after this load program, an extension by a short program is proposed. This short program is started by applying the largest possible compression force of - 8 MN for 15'000 cycles. Afterwards, the alternating load level of LS03 is repeated for 15'000 load cycles to analyze the degradation behaviour and damage, which the test specimen have experienced during load stages LS04 to LS07.

Load stages and corresponding lower, upper and mean load level are summarised and illustrated in Figure 3-4 by sinusoidal curves. The loads are applied in the force-control mode with a test frequency of 1 to 2 Hz by the load cylinder of the servo-hydraulic testing machine.



Load stages (LS)	01	02	03	04	05	06	07	08
Number of load cycles N	Each 100'000						Each 15'000	
upper load $F_{max}$ [MN]	+1	+2	+3	0	0	0	0	+3
lower load $F_{min}$ [MN]	-1	-2	-3	-4	-5	-6	-8	-3
mean load $F_{mean}$ [MN]	0	0	0	-2	-2.5	-3	-4	0

Figure 3-4. Applied main and short test load program and related load levels.

### Test specimen capacity and design related failure eventuation

As the ultimate capacity of each test specimen is not defined by testing of the static load bearing capacity, the ultimate load bearing capacity is calculated based on characteristic values according to DIN EN ISO 19902 (2014) and DNV-OS-J101 (2014), cf. Eq. 3-1 and Eq. 3-2.

$$F_{ULS,ISO} = f_{bk} \cdot A_p = f_{g, shear} \cdot A_p = \left[ 0.75 - 1.4 \cdot \left( \frac{h}{s} \right) \right] \cdot f_{c, cube, 75}^{0.5} \cdot \pi \cdot D_p \cdot L_e \quad \text{Eq. 3-1}$$

$$F_{ULS, DNV} = f_{g, shear} \cdot s \cdot \pi \cdot D_p \cdot n = \left[ 0.75 - 1.4 \cdot \left( \frac{h}{s} \right) \right] \cdot f_{c, cube, 75}^{0.5} \cdot s \cdot \pi \cdot D_p \cdot n \quad \text{Eq. 3-2}$$

The interface shear strength  $f_{bk}$  is limited by the grout matrix shear failure  $f_{g, shear}$ , which is defined by the ratio  $h/s$  reflecting shear key height  $h$  to shear key spacing  $s$  and by the characteristic compressive grout cube strength  $f_{c, cube, 75}$ . For the calculation of test strength values, the mean and not the characteristic values are considered. To determine the ultimate capacity, the shear strength is related according to DIN EN ISO 19902 (2014) to the pile surface in the overlapping region or according to DNV-OS-J101 (2014) to the single shear key capacity. The effective overlapping length  $L_e = L_g - 2 \cdot t_g$  results from the overlapping length  $L_g$  being reduced by twice the grout thickness  $t_g$ . Although this reduction is recommended for offshore connections being affected by segregation or sea water in the grout edges, it is identically considered for the test specimen to achieve a reasonably comparable ultimate bearing capacity between ISO and DNV design recommendations. The number of shear keys  $n$  being arranged over the length  $L_e$  results to four effective shear keys for the test specimens.

The calculated ultimate strength value is set in relation to the applied maximum compression load of each load stage. Thus, the utilisation in terms of the static bearing capacity can be evaluated for each test specimen and each load stage according to DIN EN ISO 19902 (2014) and DNV-OS-J101 (2014), cf. Figure 3-5.

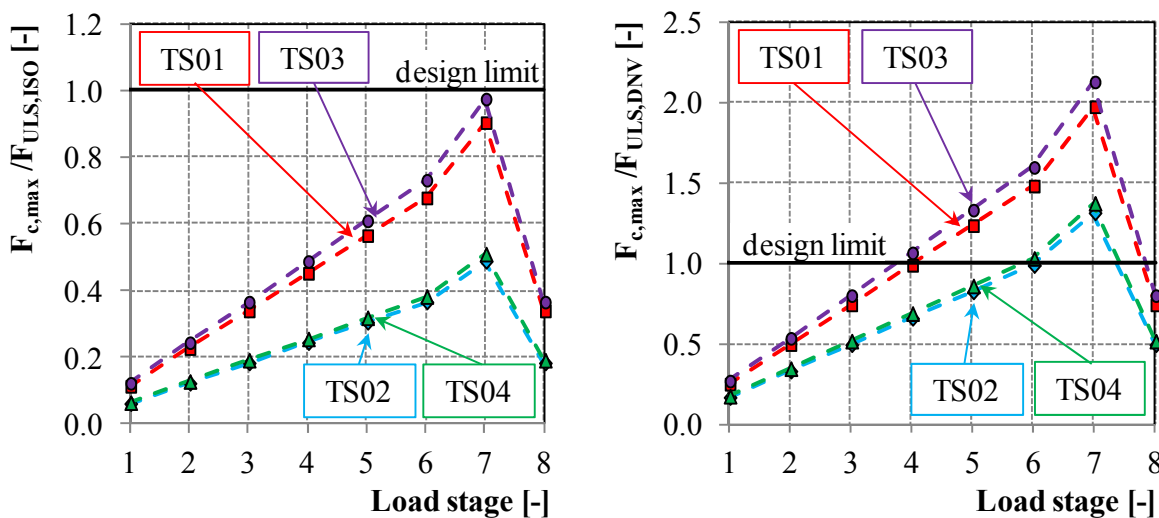


Figure 3-5. Comparison of characteristic bearing capacity according to DIN EN ISO 19902 (2014) (left) and DNV-OS-J101 (2014) (right) for LS01 to LS08.

The comparison of the individual results for the two standards shows that the capacity according to the DNV-OS-J101 (2014) equation results in a substantially lower ultimate resistance. An utilisation of 1.0 is already achieved at load stage LS04 for test specimens with a large grout annulus, TS01 and TS03, cf. Figure 3-5 right. Although both design equations are in the essence similar, the DNV lowers the force transmission to the shear key related compression struts. By contrast, the ISO related capacity suggests a uniform load transfer over the effective grouted connection length. However, irrespective of this difference, it can be concluded by the characteristic ULS utilisation ratios that the applied cyclic forces are compared to the ultimate capacity of the test specimens considerably large. This is particularly the case for consideration of partial safety factors.

In addition to the ULS utilisation, it is of importance to quantify the fatigue capacity of the test specimens according to current design recommendations as introduced in chapter 2.3.3. In DIN EN ISO 19902 (2014), a simplified approach is proposed, which implies that no fatigue failure will appear as long as the ultimate strength capacity for the connection without shear keys  $F_{ULS,ISO,plain}$  is higher than the maximum applied load, cf. chapter 2.3.3. The individual characteristic ultimate strength capacity for each test specimen is calculated by neglecting the shear keys ( $h/s = 0$ ). Resultant utilisation ratios of  $F_{c,max} / F_{ULS,ISO,plain}$  are tabulated for the initial three load stages, cf. Table 3-5. All four test specimens obviously exceed the fail-safe region at load level of LS03 according to the simplified approach of DIN EN ISO 19902 (2014).

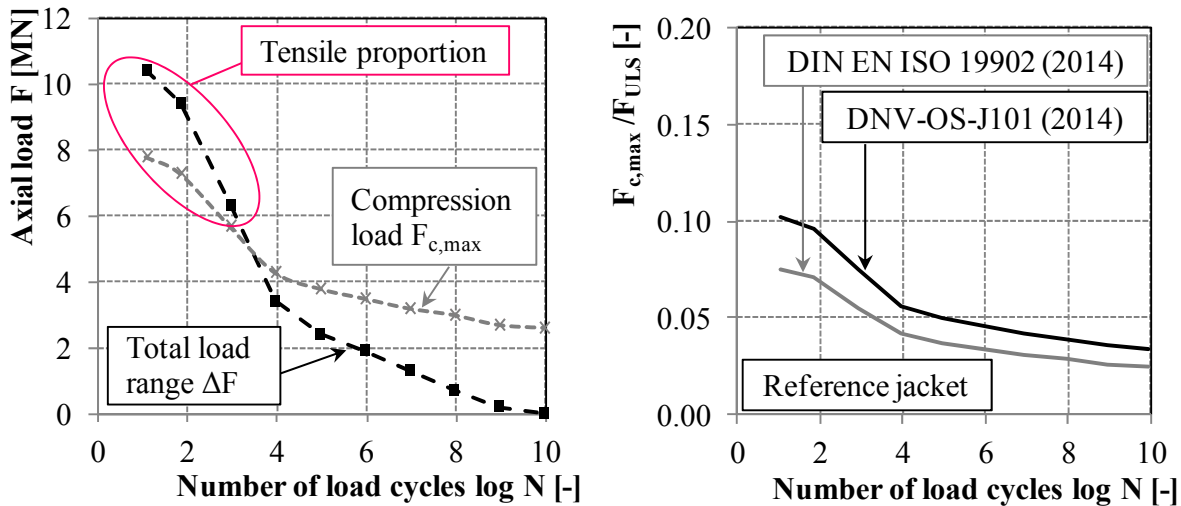
**Table 3-5. Fatigue design results for the test specimens TS01 to TS04 according to DIN EN ISO 19902 2014) and DNV-OS-J101 (2014).**

Test specimen	$F_{ULS,plain,ISO}$ [MN]	$F_{c,max}/F_{ULS,ISO,plain}$ acc. to DIN EN ISO 19902 (2014)			Damage and endurable load cycles acc. to DNV-OS-J101 (2014)	
		LS01	LS02	LS03	LS01; $S_{amplitude} = 1$ MN	
		$F_{c,max}$			damage D for $N=100'000$	number of load cycles N for $D = 1.0$
		-1 MN	-2 MN	-3 MN		
TS01	2.72	0.37	0.73	<b>1.10</b>	1.33	5'890
TS02	2.94	0.34	0.68	<b>1.02</b>	1.04	64'554
TS03	2.50	0.40	0.80	<b>1.20</b>	1.43	3'126
TS04	2.88	0.35	0.69	<b>1.04</b>	1.13	27'735

DNV-OS-J101 (2014) provides S-N curves for grouted connections, cf. chapter 2.3.3. By using this method and accounting for the applied loads and number of load cycles of each load stage, the total damage D according to the Palmgren-Miner summation can be obtained. The right part of Table 3-5 summarises resulting characteristic damage values for the individual test specimens with respect to the first load stage LS01. By the end of LS01, the damage D for each test specimen exceeds the fatigue limit. Consequently, it is expected that the aimed fatigue failure of the test specimens occurs at a quite early stage due to considerable large load levels. The number of endurable load cycles according to DNV-OS-J101 (2014) are additionally listed for all four test specimens in Table 3-5.

**Load scenarios at reference structures**

For a reference jacket substructure located in the North Sea, the loads arising from wind and wave action are calculated by industrial partners within the research project GROWup. This load range, cf. Figure 3-6, is based on defined load cases and their probability of occurrence for a design life time of 20 years.



**Figure 3-6. Load spectrum for a reference grouted connection provided by industrial partners of GROWup (left) and comparison with its ultimate characteristic capacity according to DIN EN ISO 19902 (2014) and DNV-OS-J101 (2014) (right).**

The load calculation is based on the design load case (DLC) 1.2 according to DIN EN 61400-3 (2010), representing normal operation in combination with start-stop operations and idle states. For the calculation of the loads, varied mean stress situations for a representative grouted connection of a jacket substructure at an approximated water depth of 30 m are used. The left diagram in Figure 3-6 illustrates the total load spectrum for the axial force. Complementary, the contribution by compression loads are included with a grey dashed line. Apparently the tension loads appear merely with a limited number of load cycles, cf. Figure 3-6 left.

In addition to the load spectrum, the maximum ULS load is provided by the industrial partners for the reference jacket. The maximum characteristic axial load is determined for DLC 6.1 with a compression force of -13 MN and a tension force of 9 MN, cf. Table 3-6.

**Table 3-6. Characteristic ULS load and utilisation U for the reference grouted connection according to DIN EN ISO 19902 (2014) and DNV-OS-J101(2014).**

Axial load $F_{max}$ for DLC 6.1 [MN]	$U = F_{max}/F_{ULS,ISO}$ [-]	$U = F_{max}/F_{ULS,DNV}$ [-]
-13	0.13	0.17
9	0.09	0.12

By using the ULS design equations proposed by DNV and ISO, the utilisation of the bearing capacity can be assessed for the reference grouted connection at the jacket, cf. Table 3-6. On

the basis of these utilisation ratios, the test specimens utilisation for varied load stages, cf. Figure 3-5, and the scale of the test specimens, the applied test load levels can be evaluated qualitatively to represent a large cyclic loading.

Taking the load bearing capacity of the grouted connections without shear keys into account, the utilisation of the reference jacket and the test specimen TS01 according to DIN EN ISO 19902 (2014) can be compared to each other. Table 3-7 includes the values for the load of the first three test load stages, the load bearing capacity of TS01 without shear keys as well as the load and load bearing capacity of the reference jacket without shear keys.

**Table 3-7. Comparison of utilisation ratios  $U$  according to DIN EN ISO 19902 (2014) for the test specimen TS01 and the reference grouted connection at a jacket.**

Load scenario	[-]	Test specimen TS01			Reference jacket
		LS01	LS02	LS03	DLC 6.1
Load $F_{\max}$	[MN]	1.0	2.0	3.0	13.0
Bearing capacity $F_{\text{ULS, plain}}$	[MN]	2.7	2.7	2.7	23.0
$U = F_{\max}/F_{\text{ULS, plain}} =$		0.37	0.74	1.10	0.57

The utilisation of the reference grouted connection at the jacket results to 0.57. The utilisation of the test specimen varies in dependence of the test load stages LS01 to LS03 between 0.37 and 1.10. Thus, a comparable utilisation to the reference grouted connection is reached for a test load level in between LS01 and LS02 for TS01. It can be concluded, that by passing load stage LS01, the test loads exceed the analytical extreme load scenario for real structures in DLC 6.1. The application of the test load stage LS02 is beyond the fatigue load scenario of real grouted connections.

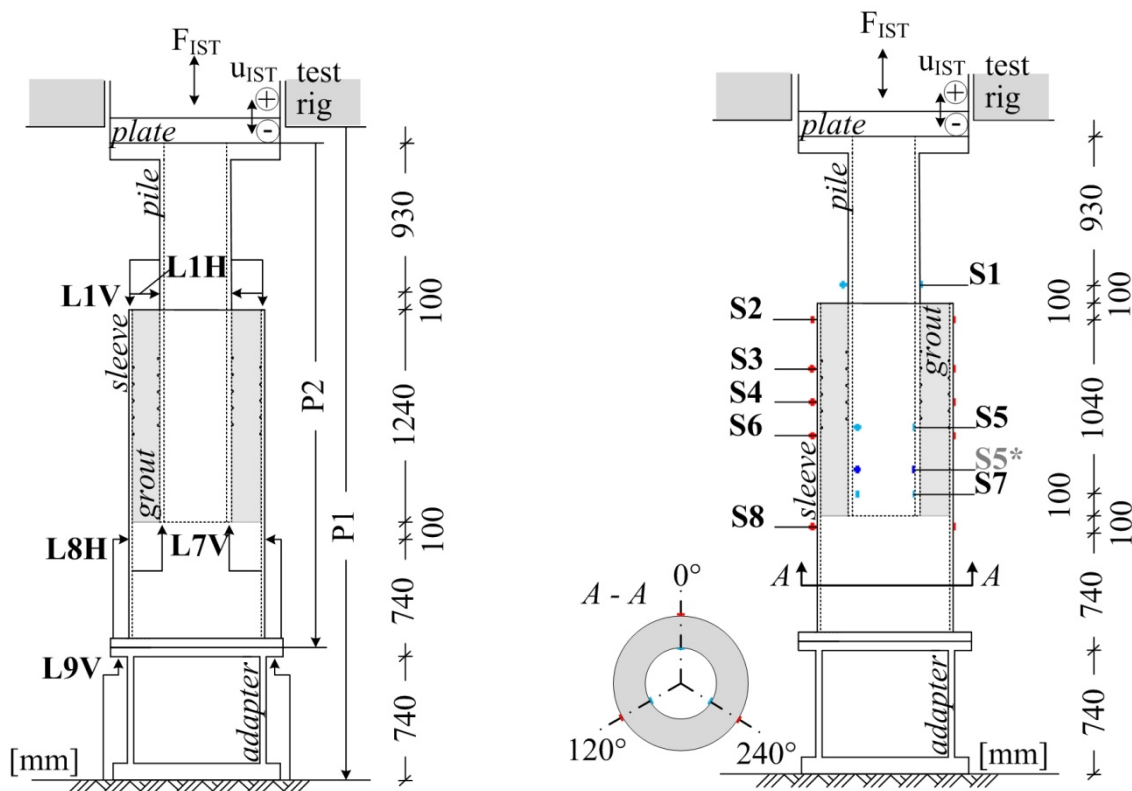
In conclusion, the previously outlined comparison of reference load scenario and applied test load stages allow to classify the applied test loads. Achieved experimental results are set in relation to the load bearing capacity of the reference structures with regard to occurring load scenarios. Even though exact values for the utilisation of reference structure and test specimens are compared, it has to be underpinned that these values result from the empirically developed design equations according to DIN EN ISO 19902 (2014) and DNV-OS-J101 (2014). Even though the analytical design equation originates from numerous tests, it is not necessarily appropriate for other geometrical configurations. Neither the test specimen nor the reference jacket structure coincides with the associated geometrical validity range. The classification of the applied test loads by the load scenarios has shown that the test loads are large. Thus, it can be assumed that the intended damage will occur during testing.

### 3.3.3 Measurements and test documentation

For the evaluation of the test specimen's bearing behaviour, the experimental tests are accompanied by measurements of the global and local deformations. Occurring displacements and strains are recorded by lasers, potentiometers and strain gauges in axial and

circumferential direction. Moreover, the applied force and displacements by the load cylinder of the testing rig are documented.

The location of the measurement devices are defined by preliminary numerical simulations of the load bearing behaviour. Figure 3-7 presents at the left cross-section the position of lasers (L), potentiometer (P) and at the right cross-section the position of the strain gauge (S). The measuring levels are named from top to bottom with ascending numbers. The vertically arranged lasers at the top edge of the sleeve (L1V) and at the bottom edge of the pile (L7V) are used to quantify the relative displacement occurring at the grouted connection. To achieve redundancy, the potentiometer P2, being installed between loading plate and adapter top, provides information about the test specimen's displacement. Potentiometer P1 is used to determine any displacements appearing by the test rig deformation. P1 is arranged between the pillared traverse and the laboratory floor. Vertical deformations of the cylindrical steel adapter are registered by L9V. Even though buckling is excluded by a previous design check, the lasers L1H and L8H are applied to document any radial deformations at pile and sleeve.



**Figure 3-7. Cross-section of the test specimen depicting the location of lasers L (left), potentiometers P (left) and strain gauges S (right).**

Circumferential and vertical strains appearing during testing are recorded by strain gauge measurements at the steel surfaces of pile and sleeve, cf. Figure 3-7 right. S1 and S8 allow strain measurement at pile and sleeve surfaces beyond the grouted connection. Strain developments at the edge of the grouted connection are obtained by S2 and S7. Substantial focus is set on the data generated by S3 to S6 reflecting the strain development and related load transfer in the shear key area of the grouted connection. It has to be mentioned that due to the restricted accessibility of the inner pile at TS01 and TS03, the S5\* is positioned only

100 mm above S7. At TS02 and TS04 it is possible to locate S5 inside the pile beneath the lowest shear key at the pile.

In order to observe a statistical representative mean value out of three measurements and to have a backup for any blackout of measuring devices, the lasers and strain gauges are applied at three vertical axis at  $0^\circ$ ,  $120^\circ$  and  $240^\circ$ . Exact positions of strain gauges and laser for all three longitudinal axis on all horizontal levels are illustrated in Annex A.7. Moreover, an illustration in Annex A.8 shows the individual measuring devices at test specimen TS01.

Two different laser types are chosen for the documentation of the varied displacements, having different measuring ranges. The laser type OWLG 4003 AA S2 Welotec has the smaller measuring distance of 16 to 26 mm and is used for L8H and L9V, due to the slight displacements that are expected to appear at these positions. The resolution of this laser kind is in the range of 0.002 to 0.005 mm with a linearization mistake of 0.006 to 0.015 mm. At the remaining laser positions the laser type OWLF 4007 FA S1 Welotec with the larger measuring distance of 30 to 70 mm is applied. This laser has a resolution of 0.04 to 0.02 mm and a linearization mistake of 0.012 to 0.06 mm. Linearization mistake and resolution are taken into consideration for the evaluation of the measured values. The strain gauges consist of two half bridges of the type K-XY31-3/350 being combined to one full bridge. This kind of strain gauge compensates any temperature effects.

The data is registered with a frequency of 40 Hz, which leads to a storage of 20 values per load cycle for a testing frequency of 2 Hz. In consideration of the feasible machine displacements and capacity the test frequency ranges in between 1 - 2 Hz. The cyclic loading is started and ended by slowly increasing the load level starting from the mean load level to the maximum and minimum test loads. Either 20 load cycles for a test frequency of 2 Hz or 10 load cycles for a test frequency of 1 Hz are considered for starting and ending. For the number of load cycles, merely full load cycles covering both intended peak loads are counted to obtain the aimed number of load cycles. The test load program is stopped after achieving the intended number of load cycles at each load stage automatically.

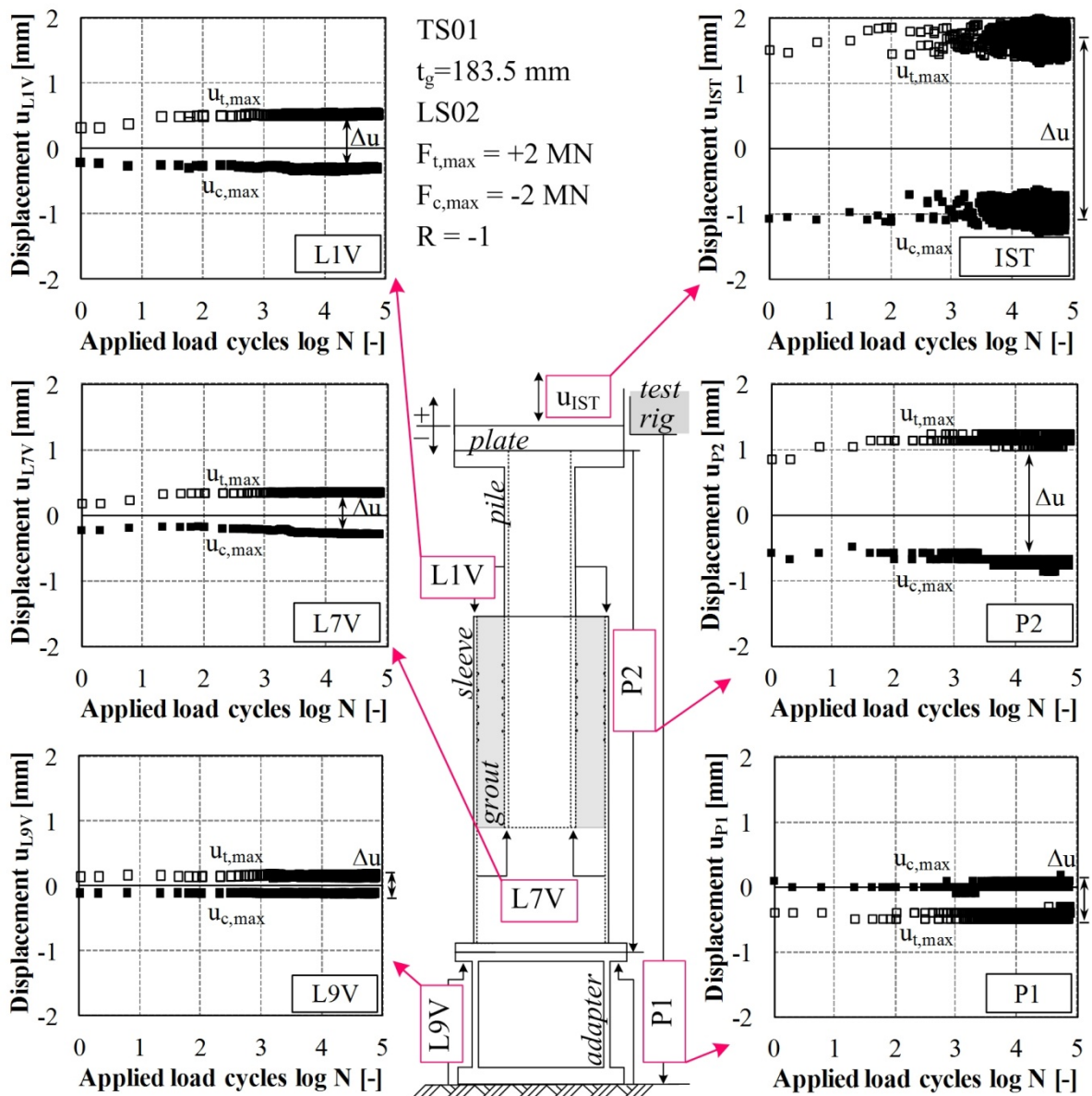
### 3.4 Fatigue Test Results

#### 3.4.1 Global deformation behaviour

A global overview of the axially measured displacements at the different measuring positions and levels is presented exemplarily for TS01 at LS02 in Figure 3-8. The individually measured displacements are linked to their origin at the drawing of the test specimen and applied measuring devices. For each measuring device the peak values of the deformations are depicted by Figure 3-8. Thereby, blank symbols represent tensile induced displacements ( $u_{t,max}$ ) with index t for tension and filled symbols reflect compressive induced displacements ( $u_{c,max}$ ) with index c for compression. Visualised laser values are obtained as mean value resulting from circumferentially arranged lasers at  $0^\circ$ ,  $120^\circ$  and  $240^\circ$ . Thus, a complete picture of the individually appearing displacements at the test set-up becomes visible.



The global displacements are recorded by the load cylinder displacement  $u_{IST}$  of the testing facility, cf. Figure 3-8 right top. Below that graph, displacements measured by P2 reflecting the total deformation of the test specimen are depicted, cf. Figure 3-8 right center. Complementary, deformations of testing rig are documented by P1, cf. Figure 3-8 right centre. Displacements at the cylindrical adapter are identified by L9V. The remaining two lasers L7V and L1V, cf. Figure 3-8 left center and top, display arising relative displacements at the grouted connection.



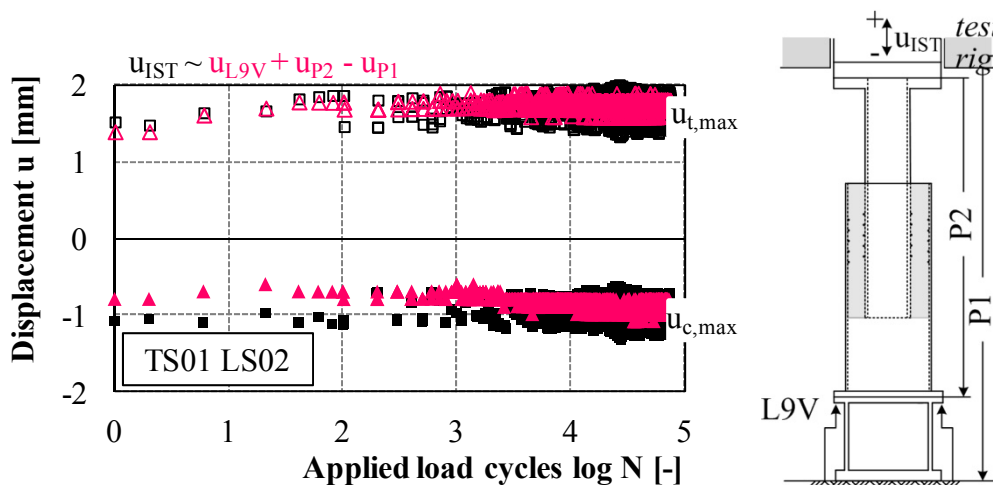
**Figure 3-8. Overview of vertical displacements exemplarily displayed for TS01 at LS02.**

As expected, the largest displacement range is registered by the global displacements  $u_{IST}$  occurring at the load cylinder, cf. Figure 3-8. In view of the individually load related measured displacements it results, that the tensile induced displacements  $u_{t,max} = 1.5 \text{ mm}$  are larger than the compressive induced displacements  $u_{c,max} = -1 \text{ mm}$ . This indicates that the tensile stiffness of the test specimen is smaller than the compressive stiffness. Similar, but slightly smaller results are achieved at P2 representing the total displacement of the test

specimens. In Figure 3-8 bottom right, considerable small deformations appearing at the testing rig are displayed by P1. Moreover, the compression induced displacements at P1 tend to be around zero, whereby tensile induced displacements represent a negative value. Tensile loading of the test specimens leads to compressive induced displacements at the pillared test rig. Compression induced displacements are due to the stiffness of the test rig comparable small. With respect to a comparable stiff cylindrical adapter, arising displacements at L9V are very small.

Displacements documented by L1V and L7V describe the relative displacement appearing between pile and sleeve. These are assumed to be representative for the load induced degradation effects to the grouted section of the test specimen. Thus, these measurements are used to evaluate the stiffness development and the damage process during testing. For the test load of  $\pm 2$  MN the relative displacements at TS01 result to  $u_{t,max} = 0.5$  mm and  $u_{c,max} = -0.36$  mm, cf. Figure 3-8. Similar to results by P2 and  $u_{IST}$ , L1V and L7V registers larger tensile induced relative displacements than compressive induced displacements. The following chapters deal with a further analysis of the relative displacements.

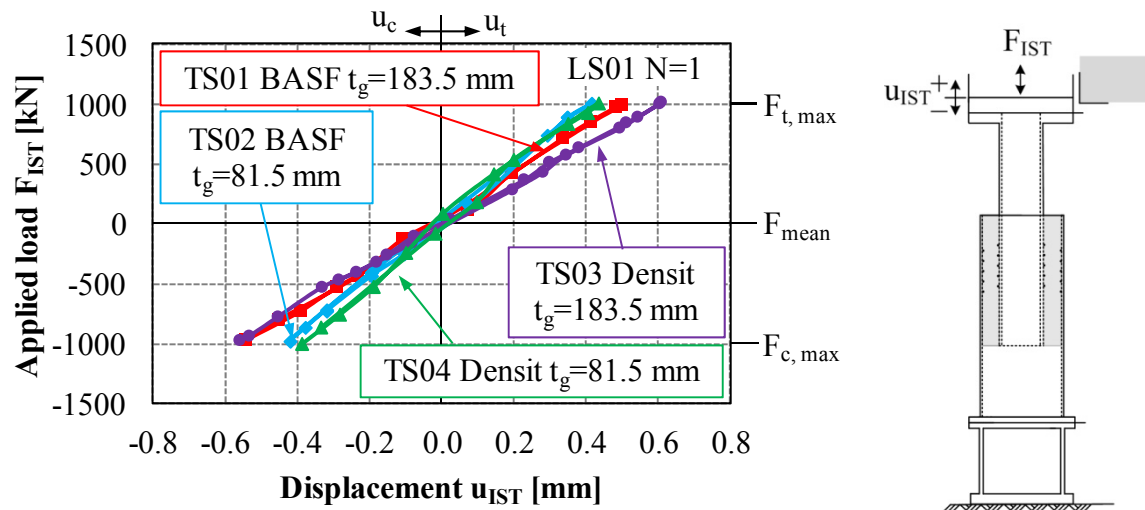
As mentioned, the global displacement of the test specimen results from measurements by the load cylinder  $u_{IST}$ . Apart from that, a combination of the displacements measured at P2, P1 and L9V reflect the global displacements, cf. Figure 3-9.



**Figure 3-9. Comparison of the measured global displacements by varied devices at TS01.**

Additionally, L9V and P2 represent the global displacement of the test set-up. By subtraction of the test rig deformations P1 resulting values are almost identical to the measured displacements by the load cylinder  $u_{IST}$ . Figure 3-9 displays this comparison exemplarily for TS01 at LS02, whereby magenta points represent a combination of L9V, P2 and P1 and black points display  $u_{IST}$  results. The tensile and compressive induced displacements comply very well.

To round of the picture of the global deformation behaviour, it is important to address the initial load displacement behaviour of each test specimen. For that purpose, the load-displacement hysteresis of each test specimens is illustrated for  $N = 1$  at LS01 in Figure 3-10.



**Figure 3-10. Global load-displacement behaviour at LS01 N = 1 at test specimens TS01 to TS04.**

The load displacement curves in the initial load state of loading reflect for all four test specimens an approximately linear elastic behaviour, cf. Figure 3-10. The opening of the hysteresis is barely visible. Apart from the linear-elastic behaviour, appearing displacements of the test specimens for the maximum loads differ. The test specimens with the smaller grout annulus  $t_g = 81.5$  mm, TS02 and TS04, react stiffer than the test specimens with the larger grout thickness  $t_g = 183.5$  mm, TS01 and TS03. The global displacement at TS02 and TS04 amounts to  $u_{i/c} \approx \pm 0.4$  mm for the maximum test load of  $F_{IST} = \pm 1$  MN, whilst a tensile induced displacement of  $u_t \approx 0.5$  mm at TS01 and of  $u_t \approx 0.6$  mm at TS03 arises. The compressive induced displacement results for both, TS01 and TS03, to  $u_c \approx -0.55$  mm. The difference of the displacements at TS01 and TS03 for the tensile force is associated to the varied tensile grout strength and stiffness of the different materials. As the difference for the tensile induced displacements at TS02 and TS04 differs minimal, it is suggested that the impact of the filling material increases with the grout layer thickness.

On the basis of the compared initial load hysteresis, it can be summarised that the tested specimens reveal a linear-elastic behaviour which is influenced predominantly by the grout thickness and slightly by the grout material characteristics. With increasing grout annulus and decreasing pile diameter the connection tends to be less stiff which is accompanied by larger displacements. Concurrently, the displacement behaviour of test specimens with larger grout annulus appears to be more sensitive to different filling material strengths.

### 3.4.2 Relative displacements

Complementary to the global deformation behaviour providing a first impression on the load bearing behaviour of the test specimens, in this section the focus is set on the recorded relative displacements. Occurring relative displacements reflect the local behaviour of the grouted connection being exposed to axial cyclic loads. Thus, the fatigue performance in consideration of the grout steel intersection can be evaluated.

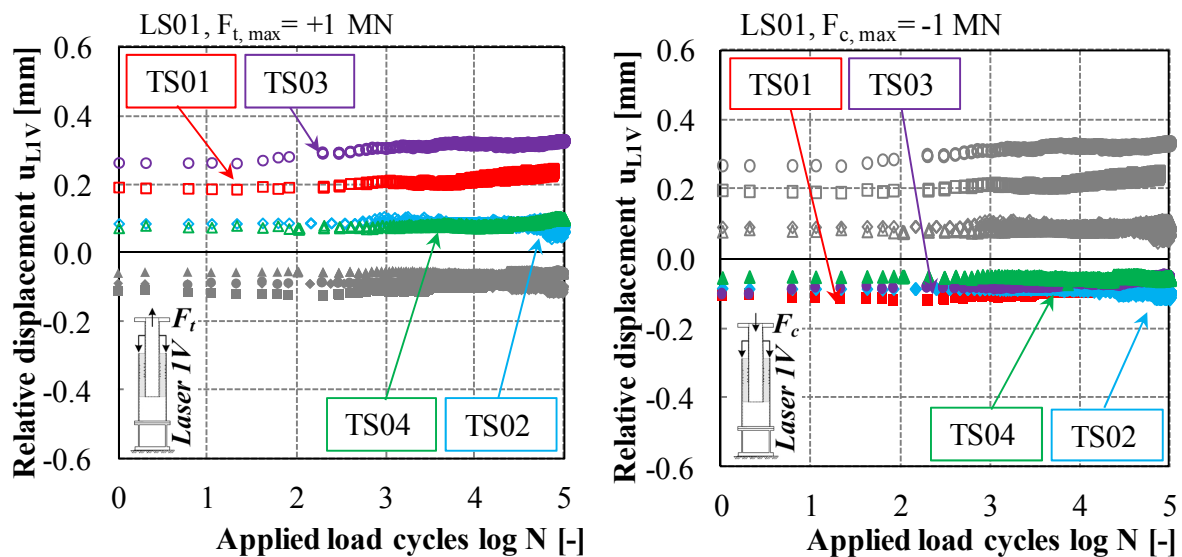
As introduced, the relative displacements are measured by L1V and L7V. By a first observation of obtained results it became obvious that the development at both laser positions

is rather similar. Notwithstanding results at L1V are slightly larger and, thus, effects might be better discernible. Therefore, the following results are limited to mean values of L1V originating from laser measurements at  $0^\circ$ ,  $120^\circ$  and  $240^\circ$ .

With regard to the load scenarios it can be differentiated between the initial three load stages considering a stepwise increased alternating load which is then followed by a stepwise increased pulsating compression load. In the first place results for the alternating load stages are presented. Secondly, relative displacements provoked by the pulsating compression load stages are evaluated. Each load stage is addressed individually to focus on the load level related behaviour of the test specimens and to avoid mixture of load size induced effects.

### Alternating load stage LS01

The relative displacements  $u_{L1V}$  arising in the first load stage LS01 at TS01 to TS04 are plotted in consideration of the applied number of load cycles by a logarithmic scale in Figure 3-11. At the left diagram, peak values induced by the maximum tension load and on the right diagram peak values induced by the maximum compression load are coloured with respect to the individual test specimens.



**Figure 3-11. Relative displacements at L1V for maximum tension (left) and compression (right) of the alternating load stage LS01 at test specimens TS01 to TS04.**

It becomes apparent at a first glance of tension and compression induced relative displacements, cf. Figure 3-11, that displacement variation between the individual test specimens is comparable small for the peak compression loading (right diagram), while the tension loading causes varied displacement values and development (left diagram). For all four test specimens the compression induced relative displacements remain almost constant for the applied number of load cycles, having a value of  $u_{L1V,c} \approx -0.1$  mm. Although the results for TS01 and TS03 are slightly larger than for TS02 and TS04, the varied annulus thicknesses have minor impact to the compression behaviour. Comparison of the compressive and tensile induced relative displacements indicates that the load bearing behaviour is substantially influenced by the load direction. One reason might be the reduced number of

shear key pairs for the tensile actions. A second reason displays the contraction of the pile by tension loading causing a debonding of the grout-steel interface between pile and grout.

In light of the tensile induced displacements, cf. Figure 3-11 left, it becomes obvious that the displacements at TS02 and TS04, having both a grout annulus of  $t_g = 81.5$  mm, develop equally constant during LS01, regardless of the varied materials. Neither a significant increase nor a decrease is observed. Unlike this, the test specimens with the larger grout annulus TS01 and TS03 ( $t_g = 183.5$  mm), reflect ascending relative displacements. The increase for TS01 amounts to 20% from 0.2 mm at the starting point to 0.24 mm at the end of LS01. For TS03 the displacements ascend by 30% from 0.26 mm at the beginning to 0.34 mm at the end of LS01. Hence, the first load stage causes a stiffness reduction at TS01 and TS03.

By comparing the test specimens with identical materials, TS01 and TS02, it becomes apparent that the tensile relative displacement for TS01 is approximately twice as large as for TS02, cf. Figure 3-11 left. The results for TS03 are even three times larger than results achieved for TS04. Consequently, increased relative displacements are observed with increasing grout thickness. It can be suggested that the larger grout thickness at TS01 and TS03 evokes a reduced tensile stiffness compared to TS02 and TS04.

In addition, the grout materials have varied influence to the displacement behaviour with respect to the grout thickness. The large difference between the test results for TS01 and TS03 and the merely existing difference of TS02 and TS04 in Figure 3-11 left, can be explained by the grout material tests, which are observed meanwhile the cyclic large-scale testing of the grouted connections started, cf. Annex A.6. The compressive strength differs by 24 MPa for TS01 and TS03, whereas the difference between TS02 and TS04 amounts only to 6 MPa. Secondly, the impact of a reduced grout material strength might have a larger influence to the displacement and load bearing behaviour of grouted connections with larger grout thickness. The grout strength variation is accompanied by similar stiffness differences, cf. elasticity modulus of the materials in Annex A.6.

### **Alternating load stage LS02**

After applying 100'000 load cycles in LS01, the load level is raised to  $\pm 2$  MN in LS02, which in consequence provokes increased relative displacements, cf. Figure 3-12. In contrast to LS01, the illustrated relative displacements of the test specimens vary for both peak loadings. But analogue to LS01, observed relative displacements of TS02 and TS04 differ only slightly, cf. Figure 3-12. Nevertheless, the repeated tensile loading leads to a modest increase of the relative displacements at TS02 and TS04.

A more distinct relative displacement increase is documented for the test specimens with a large grout annulus, TS01 and TS03. At TS03 the tensile induced relative displacements, cf. Figure 3-12 left, increase by  $\sim 45\%$  from  $u_{LIV,t} = 0.4$  mm to 0.75 mm, which indicates a strong stiffness reduction by material degradation. The displacements at TS01 increase likewise by 40%. Corresponding tensile related displacements at TS01 display an abrupt change at  $\log N = 1$ . As this sudden shift is accompanied by a concrete crack sound, it is assumed that a compression strut provoked by tension forces cracked.

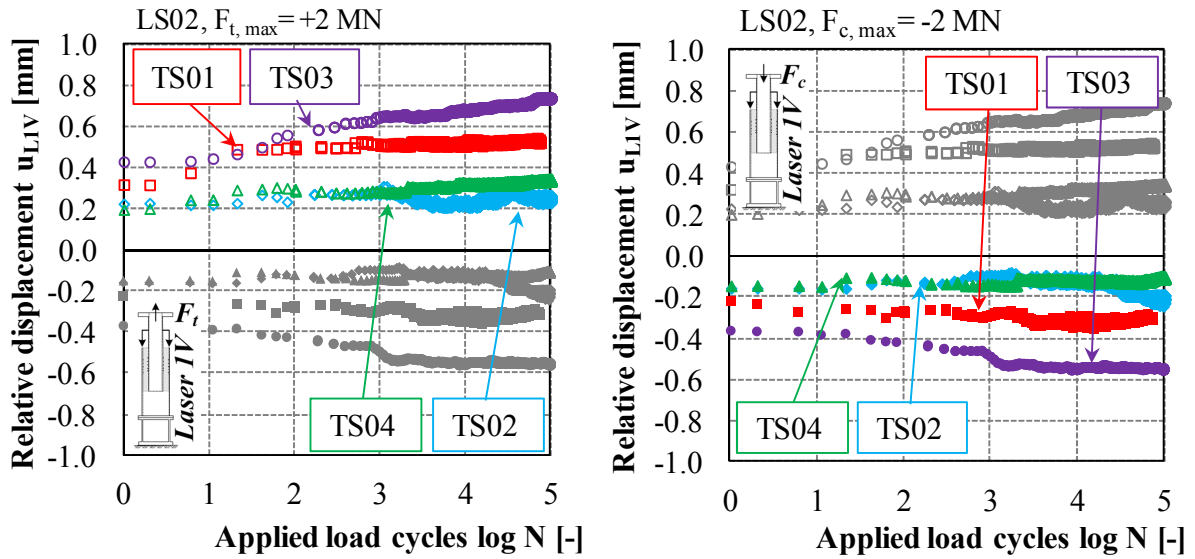


Figure 3-12. Relative displacements at LIV for maximum tension (left) and compression (right) of the alternating load stage LS02 at test specimens TS01 to TS04.

Compressive and tensile load induced relative displacements at TS01 and TS03 correlate in so far, as for both loadings a distinct increase is depicted in Figure 3-12. According to the illustrated results provoked by the maximum compression force, cf. Figure 3-12 right, at TS03 a noticeable increase of displacements between 100 and 1'000 load cycles appears. This stiffness reduction is likewise suspected to be caused by compression strut failure.

### Alternating load stage LS03

Results observed for TS01 to TS04 at the alternating LS03 are depicted in Figure 3-13. In principle, the relative displacements increase slightly at all test specimens due to the tensile and the compressive loads, cf. Figure 3-13.

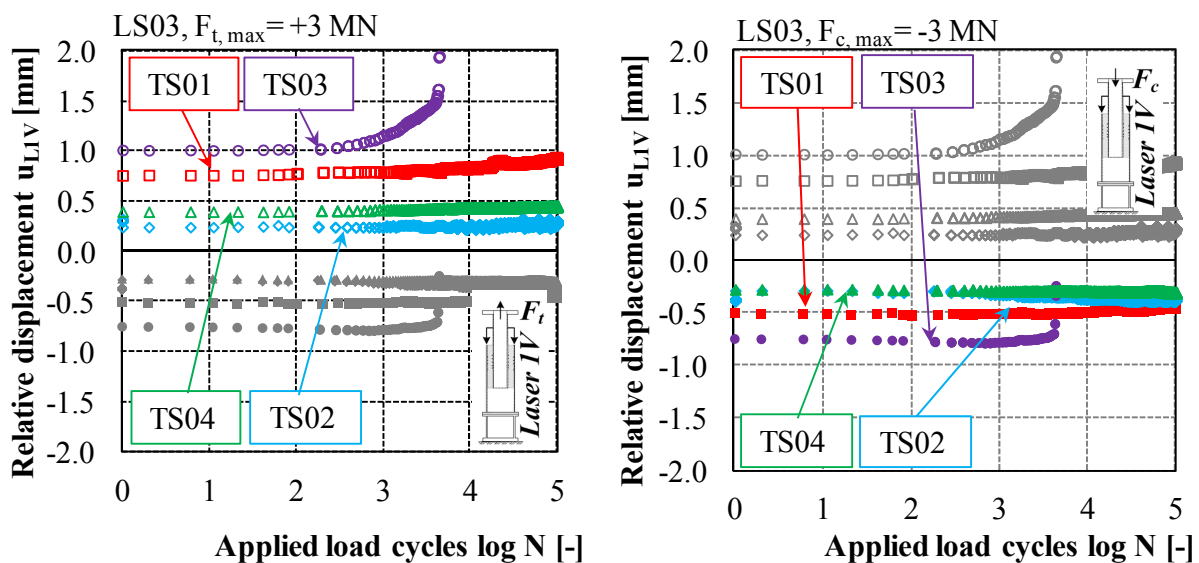


Figure 3-13. Relative displacements at LIV for maximum tension (left) and compression (right) of the alternating load stage LS03 at test specimens TS01 to TS04.

Except for TS03, the displacement growth in LS03 is smaller than observed for LS02, as for instance the tensile induced relative displacements at TS01 increase only by ~17% as against by ~40% in LS02.

By contrast, at TS03 a remarkable displacement increase after 1'000 load cycles induced by the tension loading appears. This tensile induced stiffness degradation leads to an extreme non-linear displacement rise after ~4'400 load cycles, which is declared as failure. A progressive non-linear displacement increase is defined as failure of the test specimens. The failure criterion is defined in conjunction with the applicable load-displacement ranges of the testing facility. In light of previous load stages and in comparison with the other test specimens, TS03 reflects the largest displacements and displacement increases for the applied load cycles. By comparison, the development of the relative displacements at TS01 depicts a less distinctive increase. The pronounced displacement increase, especially in LS02, might have caused pre-damage at TS03 that substantially reduced the stiffness and bearing resistance. As the tensile induced relative displacement increase is remarkably larger than the compression induced relative displacement increase at TS03, cf. Figure 3-12, it is suggested that the failure is evoked by tension loads. Moreover, TS03 confirms the presumption that failure might occur during LS03 according to the ISO approach, cf. Table 3-5 in chapter 3.3.2. Concluding, the alternating load stages have a substantial impact to the relative displacement behaviour of the different test specimens. It appears that especially for the test specimens with a larger grout annulus the repeated and increased tensile forces provoke a material degradation of the grout leading to larger relative displacements. In the end, the test specimen TS03 having the smallest characteristic ultimate load bearing capacity, cf. chapter 3.3.2 experiences a disproportionate displacement increase during load stage LS03 after 4'400 load cycles.

### **Pulsating compression load stages LS04 to LS06**

Even though it is not possible to continue the application of alternating loads at TS03 in LS03, the specimen is exposed to the pulsating compression load of +/- 4 MN in order to test the residual fatigue strength with respect to cyclic compression loads. Documented relative displacements, cf. Annex B.1, show an initial push back of the pile inside the sleeve. The testing is stopped after 12'800 load cycles by reaching a displacement of - 12 mm, being identical to one shear key width  $w$ .

The remaining three test specimens are exposed to all three pulsating load stages LS04 to LS06 consisting of 100'000 load cycles. The load stages LS04 and LS05 do not provoke any noticeable changes to the relative displacements over the applied load cycles. As the principle response of the test specimens to the applied pulsating compression loads can be sufficiently described by the data obtained for LS06, results for LS04 and LS05 are included in the Annex B.1.

During LS06 the relative displacements for zero loading, cf. Figure 3-14 left, and the maximum applied compression force, cf. Figure 3-14 right, develop without remarkable changes until an approximately applied number of load cycles of  $N = 20'000$ .

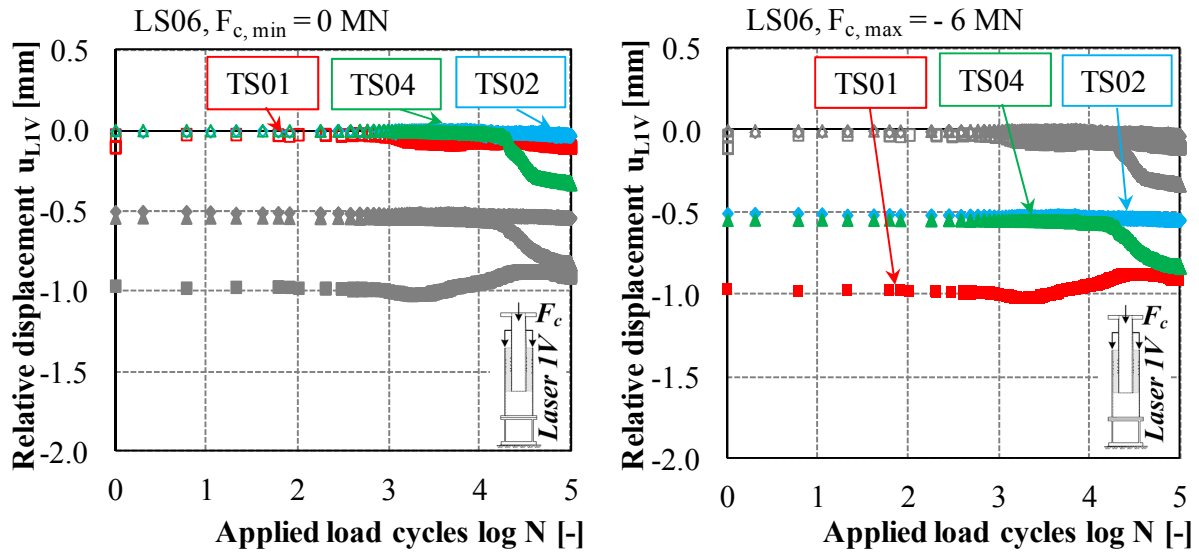


Figure 3-14. Relative displacements at LIV for unloading (left) and maximum compression load (right) of pulsating compression load stage LS06 at test specimens TS01, TS02 and TS04.

While the relative displacements at TS02 reflect no changes throughout LS06, at TS04 after  $\sim 20'000$  load cycles a progressive increase is documented for the relative displacements, cf. Figure 3-14. As the displacements develop parallel for unloading and peak loading, the pile is pushed into the sleeve by 0.4 mm during loading. The displacements at TS04 are only slightly larger than at TS02, up to the variation of displacements at TS04.

The results for TS01 are approximately twice as large as the compression induced relative displacements at TS02 and TS04, cf. Figure 3-14 right. At TS01, the test specimen with a large grout annulus, documented values in Figure 3-14 present a slightly decreasing relative displacement after applied load cycles of  $N = 10'000$ . This displacement reduction indicates a stiffness increase, although the test specimen is evidently damaged by alternating load stages. It is suggested that pre-damage caused by previous and present loading provokes a re-arrangement of loose grout particles inside the grout annulus. While large compression forces cause crack growth, during the stress-released unload situation crushed grout moves in the opened cracks. Thus, it appears as if pulsating compression loads cause a healing of the pre-damaged specimen. The re-arrangement and stiffness increase caused by crushed grout material is accompanied by the interlocking of the expanding pile evoked by the compression load. With respect to the fatigue performance, compression loads seem to have a beneficial impact as displacements at the pre-damaged test specimen TS01 are reduced.

### Pulsating compression load stage LS07

Measured relative displacements for LS07 displayed in Figure 3-15, reflect for all three test specimens a displacement increase caused by the applied maximum load of  $F_{\max} = -8$  MN. Observed results for TS01 depict a progressively increasing displacement, which is accompanied by a plastic deformation. After 402 load cycles the combination of disproportionate displacement increase reflecting resistance loss and the induced pre-damage lead to a failure of TS01. Neither further cyclic nor any static loading of the test specimen is



possible. Comparable to the failure at TS03, the failure appears after a significant progressive non-linear displacement increase.

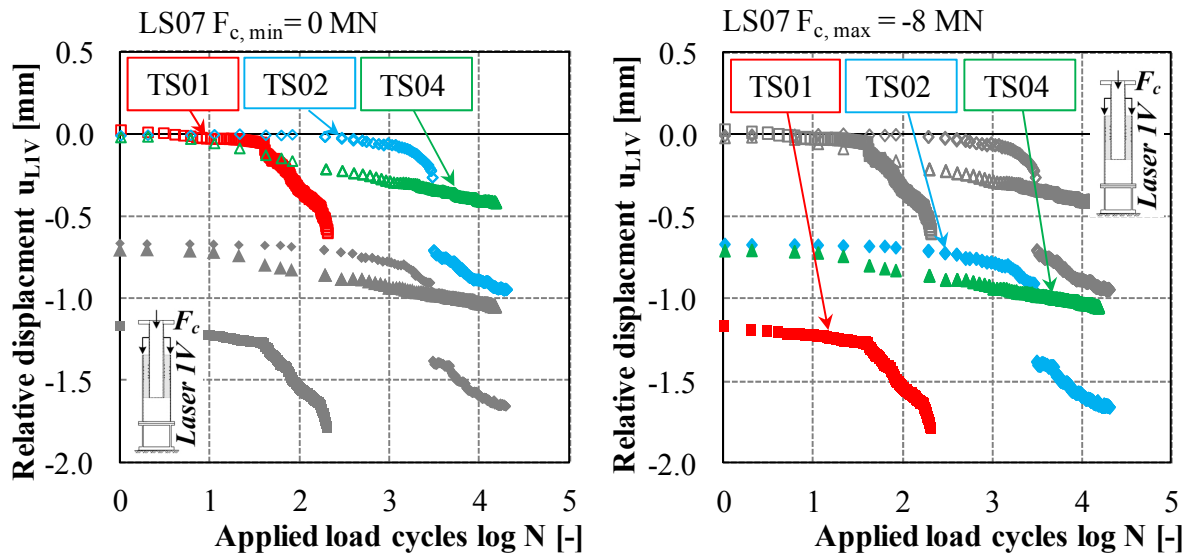
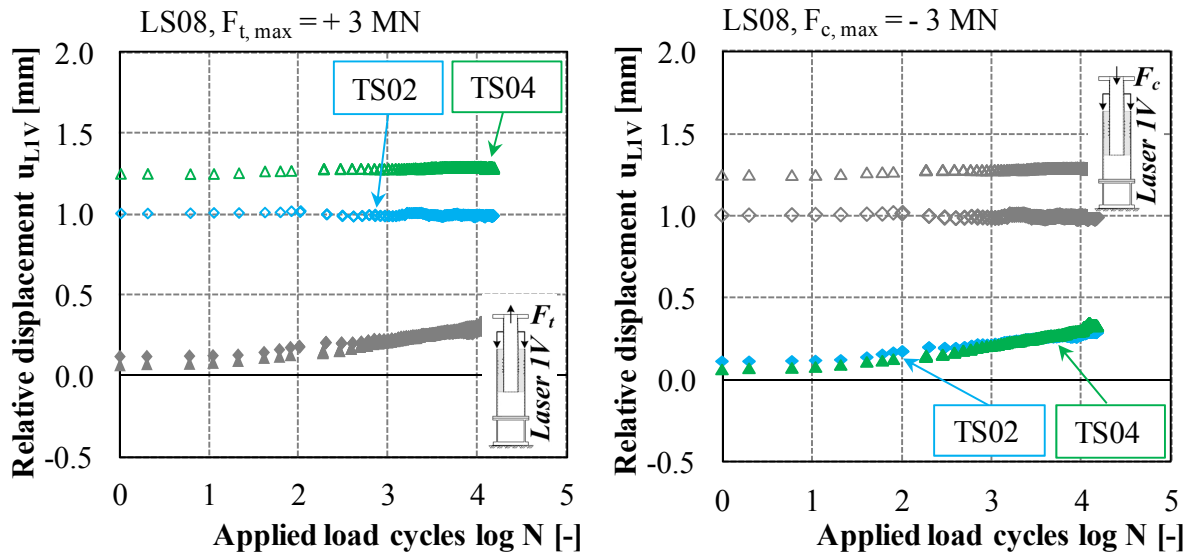


Figure 3-15. Relative displacements at LIV for unloading (left) and maximum compression load (right) of LS08 at test specimen TS01, TS02 and TS04.

The test specimen with a smaller grout annulus can be exposed to the intended 15'000 load cycles. Notwithstanding both test specimens, TS02 and TS04, show a displacement increase, cf. Figure 3-15. Displayed relative displacements for TS02, cf. Figure 3-15, increase progressively until an abrupt large sliding over  $\sim 1$  mm occurs. Although this abrupt movement deviates from previous observed displacement changes, it is suggested that crack growth results in a compression strut failure. After redistribution of the forces, further repeated loading causes a constant increase of the relative displacements until the testing is stopped after 15'000 load cycles. Unlike the distinctive development of displacement at TS01 and TS02, the test specimen TS04 represents a more or less continuous displacement increase. From the reported relative displacement behaviour so far, it can be concluded that both test specimens with a large grout annulus failed. The failure is introduced by a progressive displacement increase. Although both test specimens with a smaller grout thickness, TS02 and TS04, are affected by damage, a failure likewise to TS01 and TS03 is not observed.

### Alternating load stage LS08

Even though significant changes of the relative displacement are observed during LS07, the test specimens with a small grout annulus TS02 and TS04 have still sufficient resistance to transfer the loads of the last load stage LS08. Figure 3-16 presents the relative displacements for the maximum tension force of  $F_{t, \max} = +3$  MN (left) and for the maximum compression force of  $F_{c, \max} = -3$  MN (right). During the start up of LS08, the stepwise increased load cycles lead to a pull out of the pile. The previous induced downwards push during the pulsating load stages is counteracted by the first load cycle at LS08.

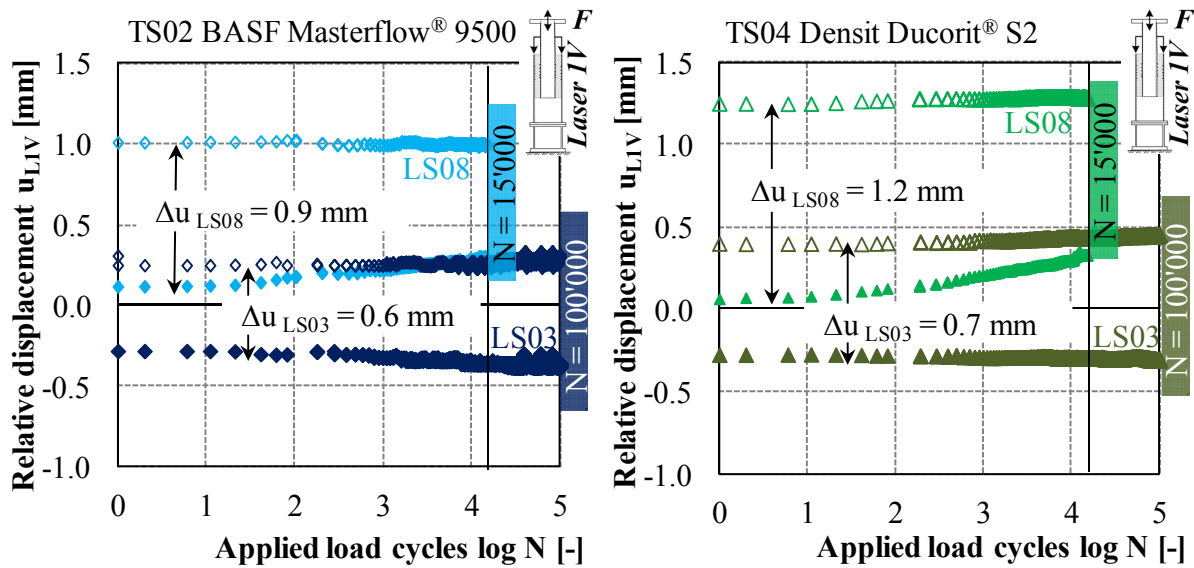


**Figure 3-16. Relative displacements at LIV for maximum tension (left) and compression (right) of the alternating load stage LS08 at test specimen TS02 and TS04.**

Thus, the documented relative displacements in Figure 3-16 starts with values larger than zero. The tensile induced relative displacements show an almost constant development over the applied load cycles, whereas the compression induced relative displacement decrease. Even though this displacement reduction is commonly associated to represent a stiffness increase, it is rather a result of the pre-damaged grout being rearranged. Compression struts being activated by tension loads transfer loads, while the compression struts evoked by compression loads appear to be characterised by cracks caused in LS04 to LS07. It is suspected that loose grout material particles are not interlocked during zero-loading and tensile loading, thus, moving in cracks and provoking that compressive induced relative displacements reduce. It can be concluded that even though a degradation process occurred during previous load stages, the test specimens are able to resist repeated alternating loads being accompanied by changes in the relative displacements.

Due to the fact that the load levels LS03 and LS08 correlate, it is possible to compare corresponding relative displacements for TS02 and TS04. Documented test data for TS02 are depicted in the left diagram of Figure 3-17 and for TS04 in the right diagram. The lighter colours in both diagrams show the relative displacement for the last load stage LS08, whereas the dark coloured points represent the results for LS03.

A first comparison of the relative displacement range shows, as could be expected by the observed damage during LS04 to LS07, that for both test specimens the relative displacement range is larger in the later load stage LS08, cf. Figure 3-17. This indicates that the test specimen's stiffness is reduced by the meanwhile applied pulsating compression load stages. For the test specimen TS02, the relative displacement range results to  $\sim 0.6 \text{ mm}$  in LS03 and to  $\sim 0.9 \text{ mm}$  in LS08. This reveals a vertical relative displacement increase by  $\sim 0.3 \text{ mm}$ . For the test specimen TS04 the range increased by  $\sim 0.5 \text{ mm}$  from  $\sim 0.7 \text{ mm}$  in LS03 to  $\sim 1.2 \text{ mm}$  in LS08.



**Figure 3-17. Comparison of the relative displacements for LS03 and LS08 at test specimen TS02 (left) and TS04 (right).**

As outlined previously, the fatigue induced damage process during LS03 results in a stiffness reduction. By contrast, during LS08 the induced damage provokes an interlocking which in the end reduces the appearing relative displacements. In LS03 the displacement ranges of TS02 and TS04 differ only by 0.1 mm, cf. Figure 3-17, while the difference is increased to 0.3 mm in LS08. As the geometric dimensions are equal for both test specimens, it is obvious that the different materials caused differing fatigue performance. The material with the lower compressive and tensile strength, TS04, depicts the larger displacement increase and, thus the lower fatigue resistance.

It can be concluded from the presentation and evaluation of the relative displacements that the relative displacements are associated with the fatigue behaviour and related damages. Whether displacements increase or decrease more continuously or disproportionate enables to evaluate the material degradation by the cyclic loading. In general, the test specimens with a larger grout annulus have revealed a lower fatigue resistance than the test specimens with a smaller grout thickness. The reduced fatigue resistance of the test specimens with large grout thickness seems to correlate to the qualitative lower characteristic ultimate bearing capacity, cf. Figure 3-5. Nevertheless, TS03 fails much earlier than TS01, which is a result of the varied grout materials.

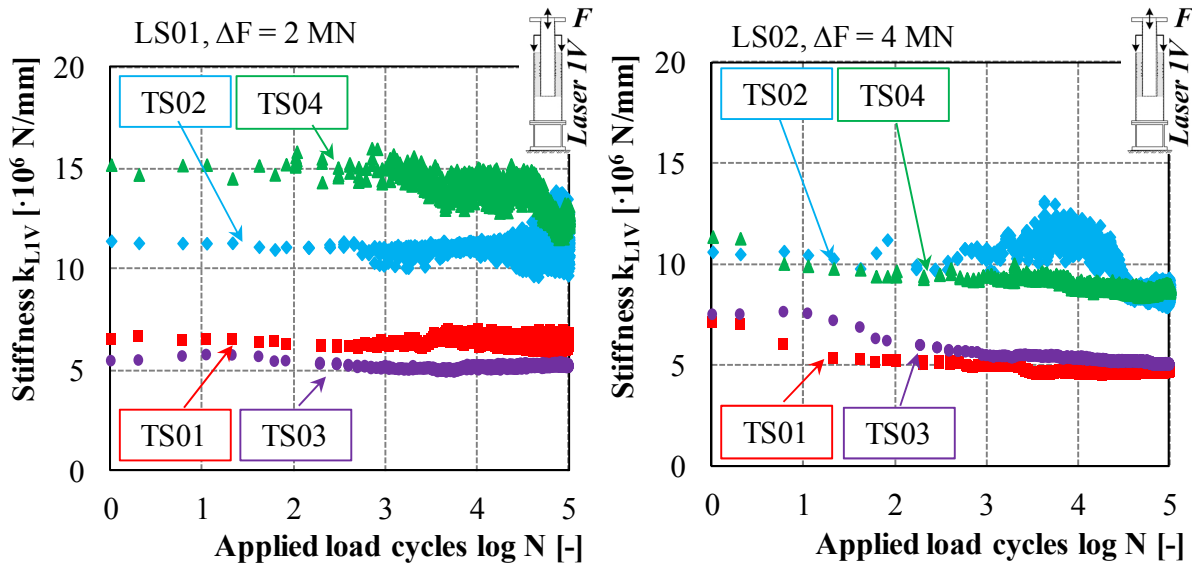
### 3.4.3 Stiffness development

A common parameter for evaluation of material degradation due to fatigue loading reflects the stiffness development. The stiffness  $k$  is defined by the quotient of applied load  $F$  and corresponding displacement  $u$ :

$$k = \frac{F}{u} \tag{Eq. 3-3}$$

Because previous evaluation of the relative displacements has shown reliable results, the focus is set on the applied loads and corresponding relative displacements at L1V. Thus,

obtained stiffness changes are limited to the fatigue induced variations at the grouted connection. Initially the stiffness resulting from the complete applied force range and resulting displacement is presented for each test specimen during the alternating load stages LS01 and LS02 in Figure 3-18. Supplementary, stiffness results for LS03 to LS08 are presented in Appendix B.2, Figure B-2.

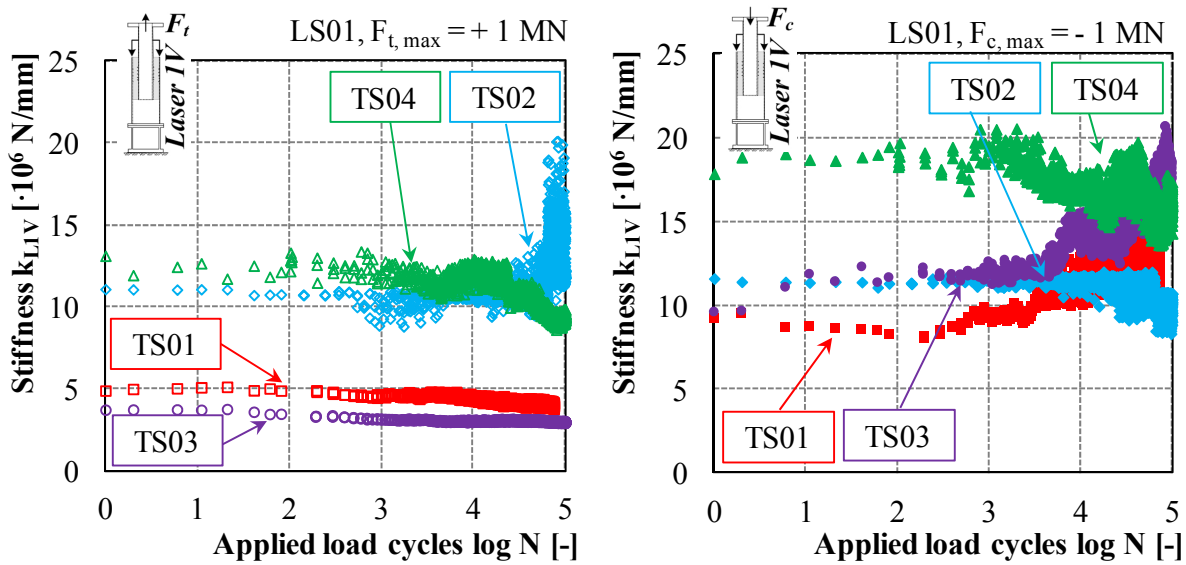


**Figure 3-18.** Development of the stiffness  $k_{LIV}$  at the test specimens TS01 to TS04 for the alternating load stages LS01 (left) and LS02 (right).

In general, the test specimens with a smaller grout thickness, TS02 and TS04, have larger stiffness values than the test specimens with a larger grout thickness, TS01 and TS03. According to the initial stiffness values in LS01, cf. Figure 3-18 left, the specimen's stiffness of TS02 is almost twice as large as for TS01 and TS03.

The course of the curves during the LS01, left diagram in Figure 3-18, displays an almost constant stiffness development for the test specimens TS01, TS02 and TS03. Merely the stiffness at TS04 degrades slightly with increasing number of load cycles. By contrast, the increased load level in LS02, right diagram in Figure 3-18, reveals for all four test specimens a decreasing stiffness development. Thus, the force range related stiffness declines with increasing load level and load cycles. Apparently, the test specimens with a larger grout annulus have a lower stiffness than test specimens with a small grout annulus and reveal a slightly larger stiffness decrease. In order to have a detailed view on the stiffness development, further evaluation focused on compression and tension related stiffness behaviour.

In Figure 3-19 the compressive and tensile induced stiffness development are exemplarily depicted for LS01. Comparison of the tensile and compression induced stiffness developments reveals, that except for TS02, the tension load cycles lead to a stiffness reduction, cf. Figure 3-19 left. Contrary, compression related stiffness increases at TS01 and TS03 and decreases at TS02 and TS04, cf. Figure 3-19 right.



**Figure 3-19. Development of the stiffness  $k_{LIV}$  at the test specimens TS01 - TS04 during LS01 for the compression load -1 MN (left) and the tension load +1-MN (right).**

This first impression of a compression induced stiffness increase seems to be contrary to the expected behaviour. But with respect to the presented relative displacements in Figure 3-11, it becomes obvious that the apparent stiffness increase is caused by a shift of the mean value. The displacement range illustrated in Figure 3-18 left supports this explanation, as the overall stiffness neither decreases nor increases significantly at TS01 and TS03.

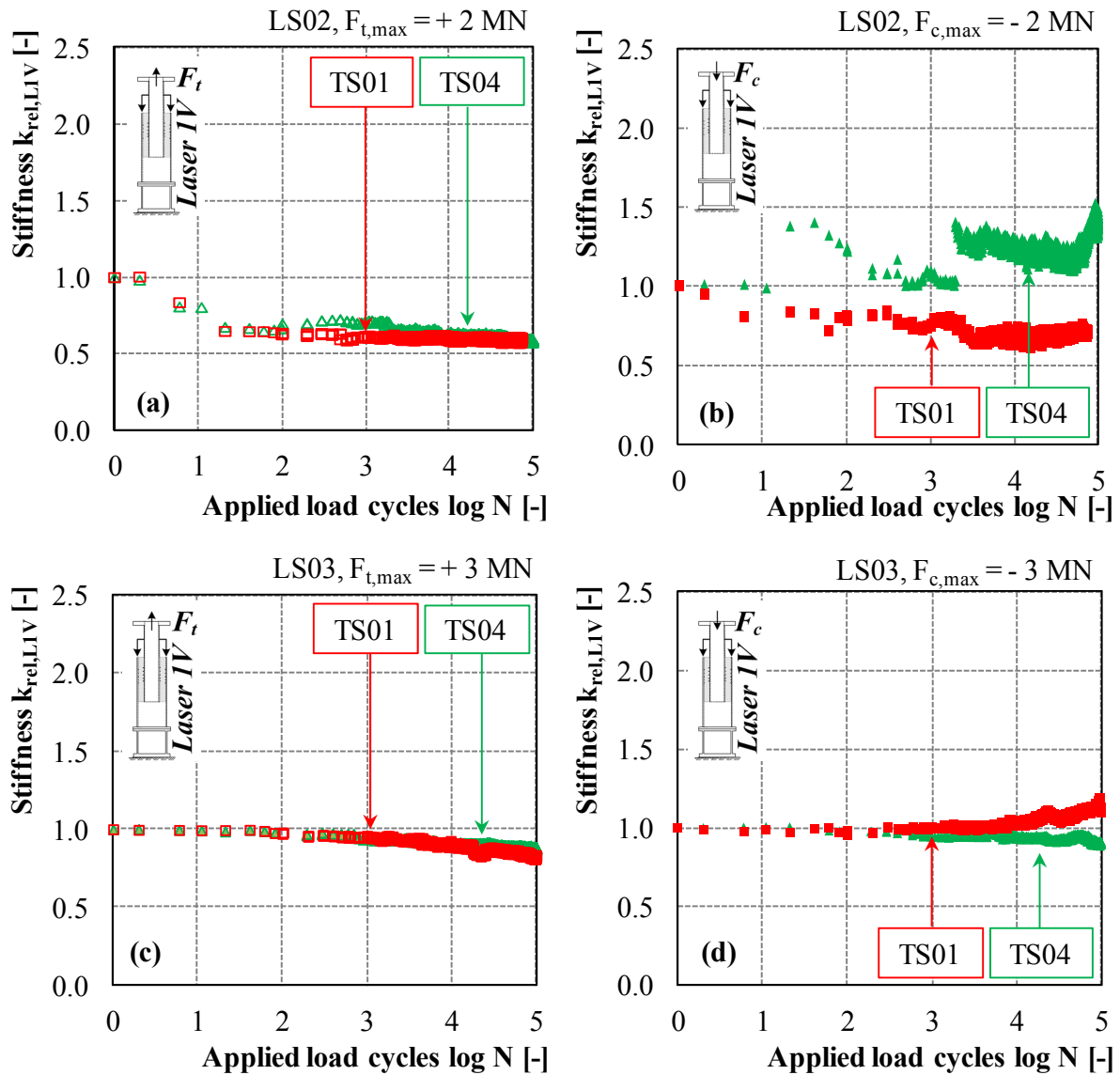
In principle, stiffness values of the test specimens with identical geometric configuration correlate. That does not apply to results for TS04, as this test specimen has a larger compression evoked stiffness than TS02 in LS01. This difference is only observed in LS01 and might be a result of the smaller relative displacements at TS04, cf. Figure 3-11. Therefore, this variation is assumed to be of subordinate significance.

Comparison of the tensile and compression induced stiffness values in Figure 3-19 reflects, that the stiffness due to tension loads is substantially smaller than the stiffness provoked by compression load cycles. At the test specimens with a larger grout annulus, the tensile related stiffness amounts approximately to half of the compression evoked stiffness. Thus, it is expected that the tensile fatigue resistance is lower than the compression resistance. One reason for the stiffness variations might be the varied deformation behaviour of the pile. Tension forces cause a contraction of the pile leading to debonding and reduced interlocking, while contrary the compression forces cause a circumferential expansion of the pile increasing the interlocking. This effect becomes more important for the test specimens with larger grout annulus. A second impact on the tensile bearing behaviour has the number of compression struts being activated.

In order to quantify the percentile stiffness decrease or increase a related stiffness is determined. The related stiffness can be evaluated by setting the stiffness value at each load cycle in relation to the initial stiffness value at the beginning of each load stage, cf. Eq. 3-4.

$$k_{rel,LIV} = \frac{k_N}{k_{N=1}} [-] \tag{Eq. 3-4}$$

Figure 3-20 contains the related stiffness exemplarily for TS01 and TS04 as observed in the load stages LS02 (top) and LS03 (bottom) for the individual load directions, tension and compression. By presenting TS01 and TS04, both the varied thickness and the different grout materials are covered. Complementary results for TS01 and TS03 as well as for remaining load stages are depicted in Annex B.2.



**Figure 3-20.** Related stiffness  $k_{rel,LIV}$  at TS01 and TS04 for LS02 (top) and LS03 (bottom) separated for tension induced (left) and compression induced (right) values.

It can be identified from the tension provoked results in Figure 3-20 (a) and (c), that the stiffness of both test specimens TS01 and TS04 is significantly reduced in both load stages. The compression related stiffness is somewhat different regarding the test specimens and the load level, cf. Figure 3-20 (b) and (d). While the stiffness of TS04 appears to increase, the stiffness of TS01 tends to reduce for the peak compression load in LS02. In combination with the tensile induced stiffness results it can be concluded, that the stiffness at TS01 is substantially minimised in LS02. The apparent compression induced stiffness increase at TS04 results from the shift of the mean relative displacement, as the tensile induced results clearly show a reduction in Figure 3-20 (a). The reverse behaviour applies to the reaction of

TS02 and TS04 in LS03, cf. Figure 3-20 (d). The compression evoked stiffness at TS01 tends to increase, which is caused by the shift of the mean relative displacement while tensile relative displacements increase and in consequence the related stiffness decreases. With respect to TS04, the LS03 causes for both load direction a related stiffness reduction indicating a material degradation. Consequently, it can be concluded, that LS02 causes a substantial material degradation and damage at the test specimen with a large grout thickness, whereas the test specimens with a smaller grout annulus show a clear material degradation in LS03.

The observed tensile induced stiffness reduction at TS01 and TS04 is mainly provoked by the initial 10 to 20 load cycles, cf. Figure 3-20 (a). The tensile induced stiffness reduction amounts for both test specimens to ~40% in LS02 and to ~20% in LS02. Notwithstanding in combination with the individual compression induced stiffness values, the mean stiffness and therefore the overall stiffness deviates for both test specimens. For each test specimen the percental stiffness increase or decrease based on the related stiffness value  $k_{rel,L1}$  is determined individually for tension and compression forces, cf. Annex B.2. Based on these values, the mean stiffness is calculated reflecting the overall stiffness development, cf. Table 3-8.

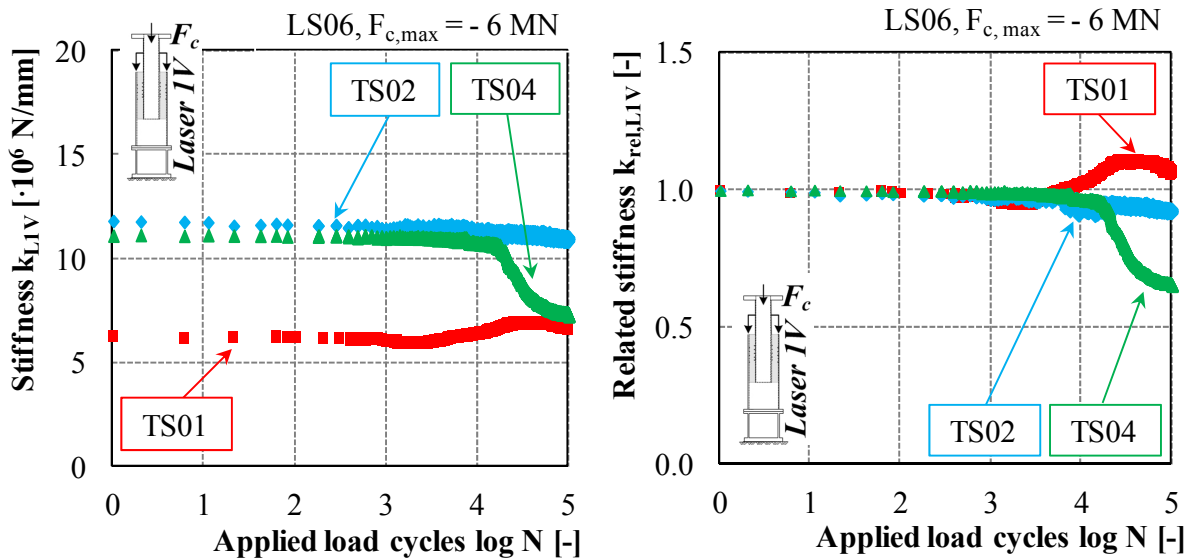
**Table 3-8. Percental stiffness variation at TS01 to TS04 for LS01 to LS03.**

Load stage	Load ratio	$F_{max}$ [MN]	Percental stiffness variation based on the related stiffness $k_{rel,L1V}$			
			TS01	TS02	TS03	TS04
01	R = - 1	+/- 1	14%	5%	29%	-20%
02		+/- 2	-38%	-24%	-39%	-5%
03		+/- 3	-4%	-21%	failure	-9%

According to the results in Table 3-8, the mean stiffness is reduced at all test specimens for LS02 and LS03. LS02 provokes at the test specimen with large grout thickness, TS01 and TS03, a substantial stiffness reduction of nearly 40%. However, TS01 to TS03 experience a stiffness increase at the first load stage LS01. This percental increase is caused by the compression peak load, which provokes radial expansion of the pile leading to increased interlocking. This impact results in increased stiffness values, which appear at TS01 to TS03. Regardless of these initial stiffness increase, the second and third alternating load stage entail significant stiffness degradation leading at TS03 to failure during LS03. Therefore, the beneficial impact of compression loads increasing the stiffness dominates only if no substantial material damage is caused by the applied loads. Compared to TS01 and TS03, the overall stiffness degradation at TS02 and TS04 caused by alternating load stages is smaller.

In a similar manner to the stiffness evaluation for the alternating load stages, subsequent stiffness behaviour induced by the pulsating compression load stages is determined. Because the upper load level during the pulsating compression load stage equals unloading, resulting stiffness shows a large scatter. Therefore, the determination of the stiffness is limited to the maximum compression load and corresponding relative displacements.

The stiffness development during the pulsating compression load stages is affected by the previous stiffness and material degradation caused by the alternating loads. Hence, different stiffness behaviour can be observed for test specimens with a small grout annulus and a large grout annulus. Figure 3-21 displays the stiffness and the related stiffness corresponding to load stage LS06 with a maximum compression force of  $F_{c,max} = -6$  MN for TS01, TS02 and TS04. Results for TS03 can not be observed as this test specimens failed in LS03.



**Figure 3-21. Stiffness development (left) and related stiffness development (right) for TS01, TS02 and TS04 in LS06.**

As analysis of the previous load stages LS04 and LS05 have indicated no significant stiffness increase or decrease, the detailed evaluation is limited to the LS06. A minimal stiffness reduction appears at all three depicted test specimen results until  $10^4$  load cycles, cf. Figure 3-21. While the stiffness progressively decreases by nearly 35% at TS04 and continuously decreases by nearly 10% at TS02, the observed stiffness at TS01 increases slightly by  $\sim 6\%$ . Thus, the test specimens with a smaller grout annulus indicate a material degradation caused by the compression load cycles. In contrast, the test specimen with the larger grout annulus apparently gets stiffer. Reason for this contradictory stiffness development results from consideration of the test specimen's behaviour during previous load stages. It can be assumed by the substantial stiffness reduction of TS01 in LS02 results from crack growth and grout material crushing. As TS02 and TS04 are presumably not as much affected by the alternating load stages, the increased compression load cycles in LS06 might cause material degradation. Repeated loading at TS01 may induce a different damage. As the grout layer might be characterised by cracks, further loading may provoke crushing of the grout into smaller particles. During the unloading, the compression induced interlocking disappears provoking a stress-relieve situation where loose particles may become rearranged. Thus, stiffness increase at TS01 can be assumed to be caused by the rearrangement of crushed grout particles causing a reduction of the relative displacements and thus an increased stiffness.

Table 3-9 summarises the percental stiffness increase or decrease for the pulsating compression load stages. It becomes apparent, that the test specimens with a small grout

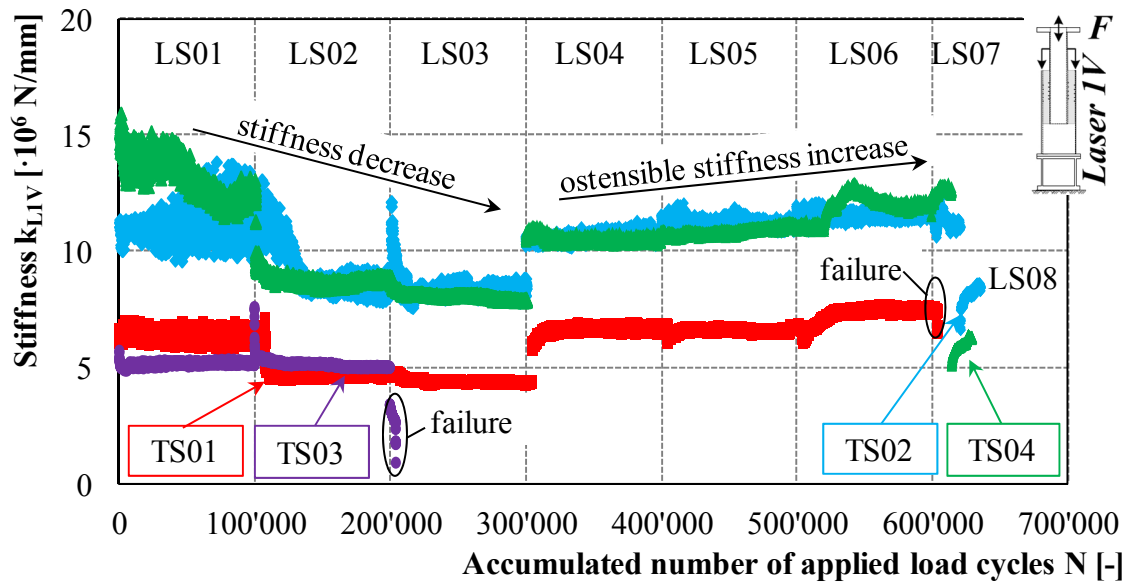


thickness, TS02 and TS04, observe a stiffness reduction. In contrast the test specimen TS01 reveals a stiffness increase at LS04 and LS06 which might be caused by rearrangement of crushed grout material. The significantly increased compression loading of  $F_{c,max} = -8$  MN in LS07 leads to a distinctive stiffness reduction at all three test specimens.

**Table 3-9. Percentual stiffness variation at TS01 to TS04 for LS04 to LS07.**

Load stage	Load ratio	$F_{max}$ [MN]	Percentual stiffness variation based on the related stiffness $k_{rel, LIV}$			
			TS01	TS02	TS03	TS04
04	R = ∞	- 4	9%	-2%	-	-7%
05		- 5	-2%	-5%	-	-9%
06		- 6	6%	-9%	-	-34%
07		- 8	-35%	-58%	-	-32%

In order to achieve an overview of the stiffness development for the complete fatigue test program, the achieved stiffness values are arranged in a row which is determined on basis of the applied load and displacement range for each test specimen. Figure 3-22 displays the stiffness values determined on basis of the applied load range and corresponding relative displacement ranges for TS01 to TS04 in LS01 to LS08. Even though the load range is set in relation to the occurring displacements, the stiffness values are influenced by the load level. Nevertheless, the general impact of alternating and pulsating compression loads becomes obvious by the overview.



**Figure 3-22. Comparison of the stiffness development for the test specimens TS01 to TS04 in consideration of the accumulated number of load cycles corresponding to LS01 to LS08.**

The curve progression depicts for all test specimens that stepwise increasing alternating load stages cause in the same manner a stepwise stiffness reduction, cf. Figure 3-22. In contrast increasing pulsating load stages reveal an ostensible stiffness increase. The stiffness increase observed at the pulsating compression load stages results from the increased interlocking caused by the pile extension. Although the load stages LS01 to LS03 are equally composed by

stepwise increasing compression forces, the ascending tensile forces characterise stiffness reduction.

Previous evaluation of the stiffness development reveals that increased grout thickness and reduced pile diameter entails a lower stiffness of the connection. The stiffness development for the applied load stages demonstrates that the dominant tensile forces provoke a stiffness reduction, especially at the test specimens with a larger grout annulus. Moreover, stiffness developments caused by compression loading was influenced by expansion of the pile and the damage status initiated by previous load stages. It can be concluded that the alternating load stages reduce the fatigue strength more than the compression load stages. Further evaluation of the appearing damage mechanism is provided in the following chapter by analysing the arising strain developments.

#### **3.4.4 Strain development**

The occurring strains at the steel tubes are documented by strain gauges applied in longitudinal and circumferential direction. Therefore, the introduced strain gauge names S1 to S8 are added by a "V" for vertical and by "H" for horizontal or rather circumferential measured strains. In general, S1V and S8V represent the strain development in the plain steel tubes without any effect of the grouted connection. These two strain gauges show a force-equivalent strain behaviour over all load stages for all test specimens. As applied loads are determined adequately, it is evaluated that the strain measurements are reliable for any further evaluation.

The longitudinal strain developments are illustrated by measured strains over the vertical axis of the grouted connection at the test specimens. Figure 3-23 presents the longitudinal strain development exemplarily for TS02 for the first load cycle  $N = 1$  at load stage LS01. Thus, an undisturbed force transmission can be assumed. The blue curves display the strain development at the pile, whereas the red curves demonstrate the strain development at the sleeve. Corresponding strain gauge positions are outlined by the drawing, cf. Figure 3-23.

For both peak loads, it becomes obvious that the longitudinal strains decrease nearly linear from top to bottom at the pile, cf. Figure 3-23. These results are obtained by three vertical measuring locations, due to the restricted accessibility of the pile interior. The strain developments at the sleeve show that the majority of loads are transferred within the shear key section. This becomes obvious, by the related strains increasing noticeable from top S3V to bottom S6V. The remaining strain increase between S6V and S8V is comparably smaller. As this strain development is qualitatively representative for all test specimens, it verifies the general load transfer mechanism being based on the shear key section.

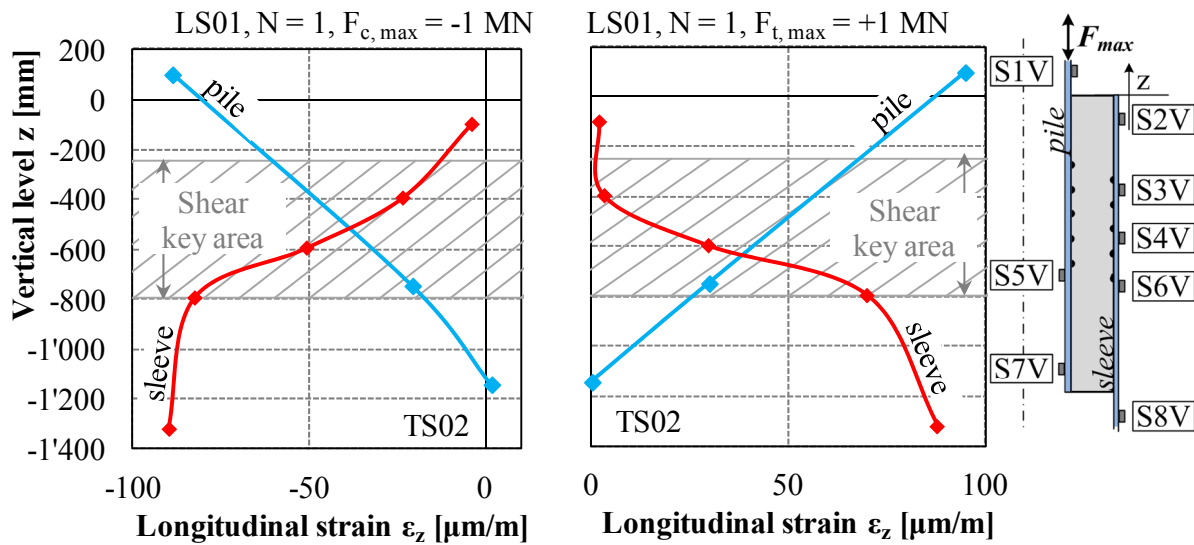


Figure 3-23. Longitudinal strains displayed by vertical level at TS02 for the maximum compression load (left) and tension load (right) at the beginning of LS01.

According to Figure 3-23, compression loads provoke a compression strain, also called contraction, while tension loads induce an elongation. Comparison of the tensile and compression induced strains at the sleeve S6V reflects that strains caused by compression are larger than caused by tension at this level. As the absolute strain values are nearly identical at S8V, it follows that a larger frictional force transfer between S6V and S8V appears by tensile loading. This effect might be caused by the applied number of shear keys enabling 5 compression struts for compression loads against 4 compression struts by tension loads. In addition, comparison of the strains at S3V reveals larger values for the compressive loading than for the tensile loading. This deviation might be a result of the expansion of the pile increasing the interlocking as opposed a radial contraction by tension evoking a reduced interlocking. Anyhow, the deviating strains at S3V and S6V outline that compression induced stresses and strains are transferred in the upper section while tension induced stresses and strains are transmitted in the lower section. Therefore, the observed strain development clearly confirms findings by Aritenang et al. (1990) that the force transmission concentrates on the external shear keys.

Previous analysis of the relative displacements reveal that the majority of cyclic induced material degradation appear during load stage LS02, cf. chapter 3.4.2. Figure 3-24 depicts the strain development during LS02 for selected load cycles (N = 1/ 100/ 100'000) exemplarily for TS01, in order to derive suggestions about the force transmission changes.

The strain developments at the remaining test specimens correlate with these displayed results in Figure 3-24. The strains at the pile decrease from top to bottom for both peak loads indicating a continuous load transfer, cf. Figure 3-24.

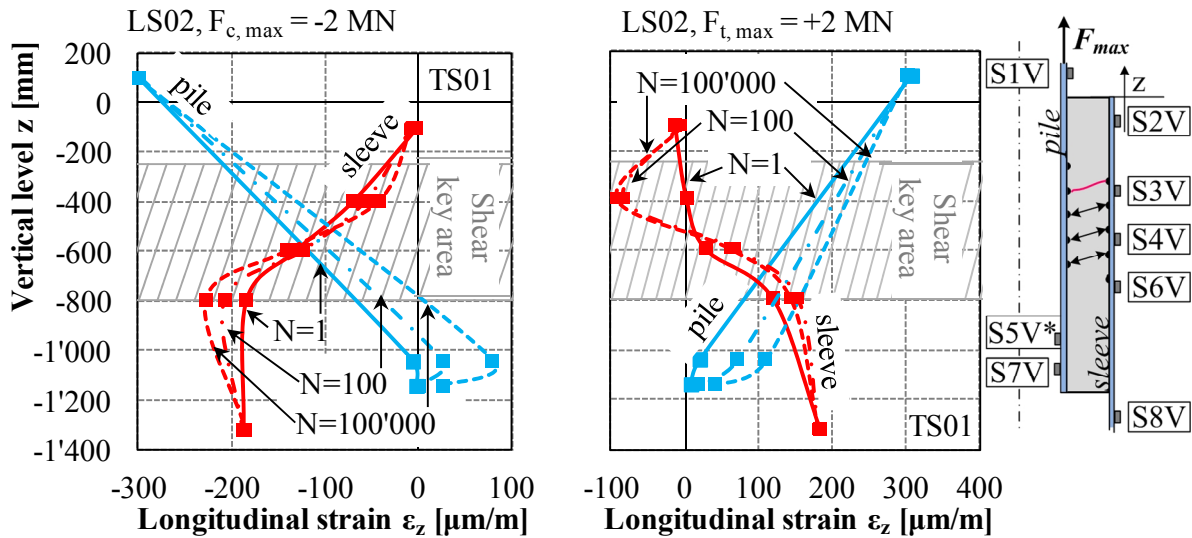
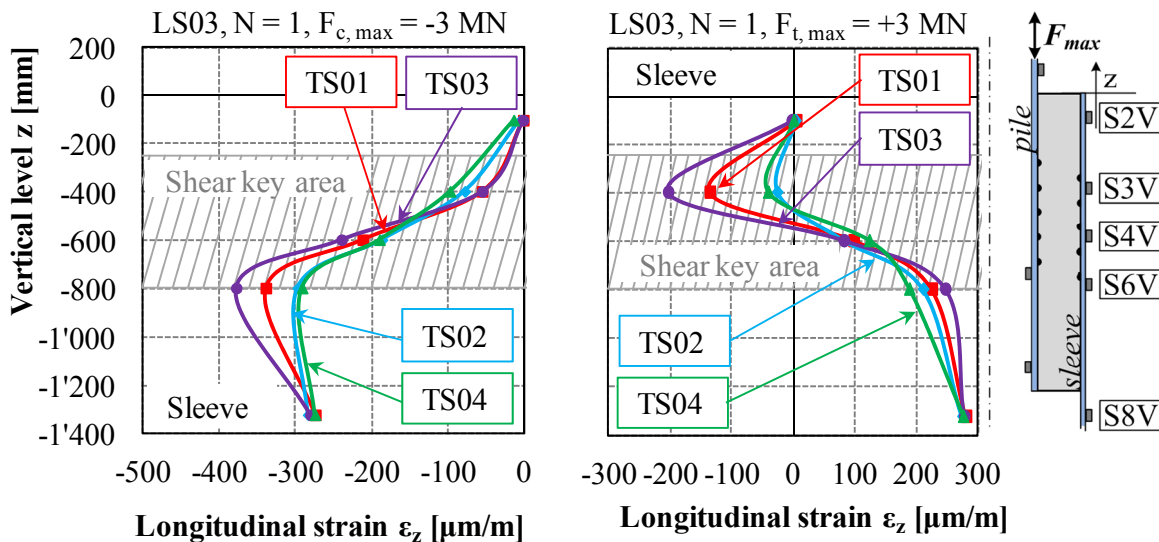


Figure 3-24. Longitudinal strains displayed by vertical level at TS01 for the maximum compression load (left) and tension load (right) in LS02.

Increasing number of load cycles causes increasing strains at S5V\*. Likewise, strains at S6V increase and at S3V decrease with increasing number of load cycles displaying a change of the load transfer mechanism. The strain measurements for tensile loading at the sleeve display a significant increase of vertical compression strains at S3V developing between load cycle 1 and 100. Due to the strain development at S3V, the observed increase of the relative displacements after load cycle 10, cf. Figure 3-12 left, and the crack like sound during load cycle 10 and 11, cf. chapter 3.4.2, it can be suggested that these mentioned issues result from a compression strut failure provoked by the tensile loading. While the tensile induced compression strut between the first active shear key pair fails, cf. Figure 3-24, the load transfer shifts to the remaining intact compression struts. As a result the strain gauge S3V is exposed to a compression strain introduced by the increased compression stresses at the adjacent shear key. The compression induced strains at S3V are less affected by the compression strut failure, as cracks are closed by the compression loading. It can be concluded by the increased vertical compression strain at S3V that an interlocking of the shear key above S3V still exists and, thus the shear key still takes part in the load transfer, even though tensile related compression strut failure exists.

The maximum compression load, cf. Figure 3-24 left, affects the strain development at the sleeve, especially in the upper and lower shear key area, by increasing load cycles. Compression induced strains reduce at S3V, while a strain growth is observed at S6V. Thus, the aforementioned dominating force transfer in the upper region tends to shift to the lower section of the shear key area. While measured strains at S3V and S6V change, the values at S4V are nearly unaffected. Thus, it is supposed that external shear keys are much more stressed by the cyclic loading.

In Figure 3-25, the different test specimens are compared by resulting strains arising at the sleeve for the initial load cycle in LS03. Supplementary strain data for the pile are depicted in the Annex B.3.



**Figure 3-25. Longitudinal strains at the sleeve displayed by vertical level at TS01 to TS04 for the maximum compression load (left) and tension load (right) at the beginning of LS03.**

In Figure 3-25, it can also be identified that occurring strains at S3V and S6V are smaller at the test specimens with the smaller grout thickness than at the test specimens with the larger grout thickness. The increased grout thickness and the pre-damage caused by LS02 leads to particular larger strains in the upper and lower shear key area. At TS01 and TS03, the tensile induced strains rise significantly in the upper part at S3V, while the corresponding compression load evokes substantially increased strains in the lower section at S6V. This can be explained by the slope of the compression strut.

As the strains originating at TS02 and TS04 show a flatter curve along the vertical axis, it is suggested that the load transfer is less influenced by cyclic damaged than at the specimens TS01 and TS03. This assumption is supported by comparing the vertical strain development in Figure 3-25 and Figure 3-23. It can be reasonably concluded, that the strain developments are affected by cyclic degradation processes in the grout layer. Repeated loading resulting in crack initiation and growth leads to a force transmission change which can be identified by achieved strain variations. In principle, the strain gauge measurements support the earlier assumption that grouted connection with large grout annulus are stronger influenced by cyclic degradation than connections with smaller annulus.

On the basis of previous obtained results, distinct changes caused by the alternating load stages were noted especially at TS01 and TS03. In order to identify strain variations caused by the pulsating load stages, a comparison of the last load cycle in LS03 and the initial load cycle in LS08, covering identical peak loads to LS03, are used. Because TS01 and TS03 failed before, the results of TS02 and TS04 are investigated. Figure 3-26 presents the strain development exemplarily at TS04 for both load stages LS03 and LS08 individually for the maximum tensile load of  $F_{t,max} = +3 \text{ MN}$ , right, and for the maximum compression load of  $F_{c,max} = -3 \text{ MN}$ , left. The solid line forms the strain development at LS03  $N = 100'000$  and the dashed line the strain development induced by LS08  $N = 1$ , whereby the red lines show sleeve strains and the blue lines pile strains.

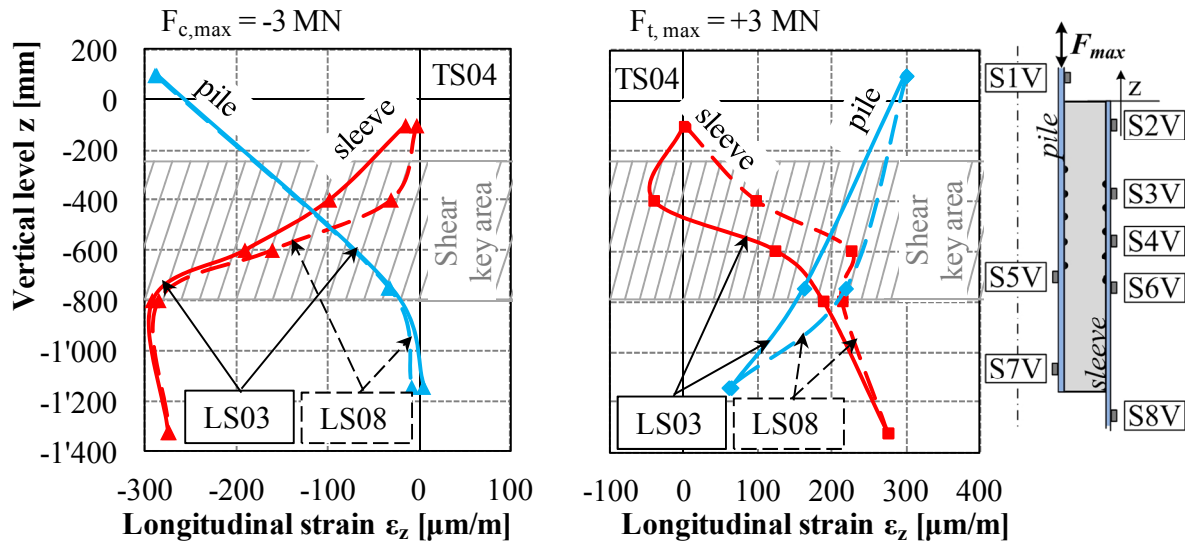


Figure 3-26. Longitudinal strains displayed by vertical level at TS04 for the maximum compression load (left) and tension load (right) at the end of LS03 and the beginning of LS08.

As evident from the left diagram in Figure 3-26, the strain developments at pile and sleeve are almost identical for both load stages, except for measurements at S3V. At this position, the strains decrease, which may be ascribed to a compression strut failure at the first shear key pair. As consequence of this crack, stresses at the strain gauge beneath this compression strut achieve lower compression strains. Remaining strains are slightly affected by the load transfer change.

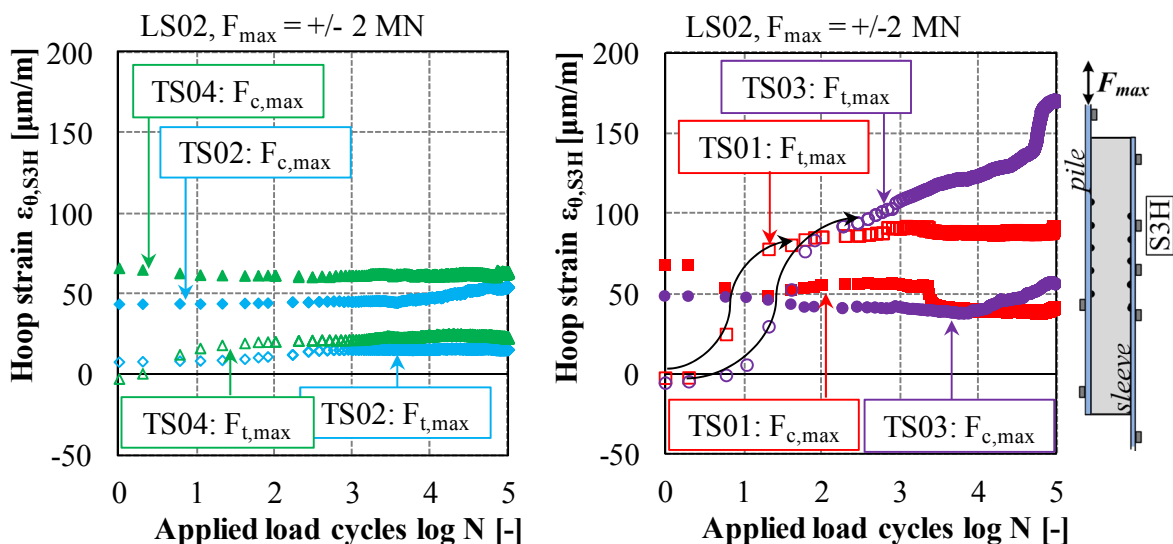
However, tensile provoked strains are much more affected by the pulsating compression induced damage, as detailed by the comparison of LS03 and LS08 in Figure 3-26 right. Pile related strains increase at S5V, which means that the load transfer by the shear key area is reduced. Thus, the force transmission by surface friction is intensified, as tensile stresses have to be transferred below the shear key area. This leads to the assumption that degradation effects, e.g. compression strut failure, cause a shift of the load transfer from the shear key area to the plain pile area where the loads are transferred by frictional and adhesive forces.

Focusing on the tensile strain development at the sleeve, Figure 3-26 underlines that a degradation process is caused by different load transfer mechanism. Tension loads arise compression strains in LS03 at S3V as opposed tensile strains engender in LS08 at S3V. This change of strains at the sleeve may arise from failure of the second compression strut. This correlates with significantly increasing strains at S4V, which may result from increased load transfer at the third compression strut. It is assumed, that in response of cyclic material degradation at the external shear keys, the shear keys in the center and the interface friction in the lower part dominantly contribute to the load transfer. By contradicting the two load stages, it is concluded that the pulsating load stages may have caused further cyclic degradation to the grout material affecting the force transmission in LS08.

In addition to the assessment of the longitudinal strain development at the vertical axis of pile and sleeve, the hoop strains are analysed by focusing on the development resulting from the applied load cycles. As longitudinal and circumferential strains correlate, the following considerations apply qualitatively also for longitudinal strains. According to the previous

discussion, the most interesting strain changes appear at S3V and S4V. Thus, it is chosen to describe the circumferential strain development at S3H and S4H in LS02, cf. Figure 3-27 and Figure 3-28.

The compression and tension induced hoop strains at S3H detailed in the left diagram of Figure 3-27, develop comparably constant at TS02 and TS04 in contrast to the conspicuous variation at TS01 and TS03, cf. Figure 3-27 right. At TS02 and TS04, the tensile induced strains increase slightly from 0 in the beginning to 15 to 20  $\mu\text{m}/\text{m}$ . The compression loads lead to tensile hoop strains in the range of 40 to 60  $\mu\text{m}/\text{m}$ , showing an ascending development at TS02. It is assumed that, in response of the load transfer by the upper compression strut, an expansion of the sleeve steel tube at S3H appears. The circumferential strains are larger for the compression loading than for the tensile loading since the compression load transfer dominantly appears in the upper region in contrast to tension load. This becomes evident by the vertical strain distribution explained previously by Figure 3-23. Moreover, it indicates clearly that the tension member of the trust model appears and, thus the compression strut model is valid.

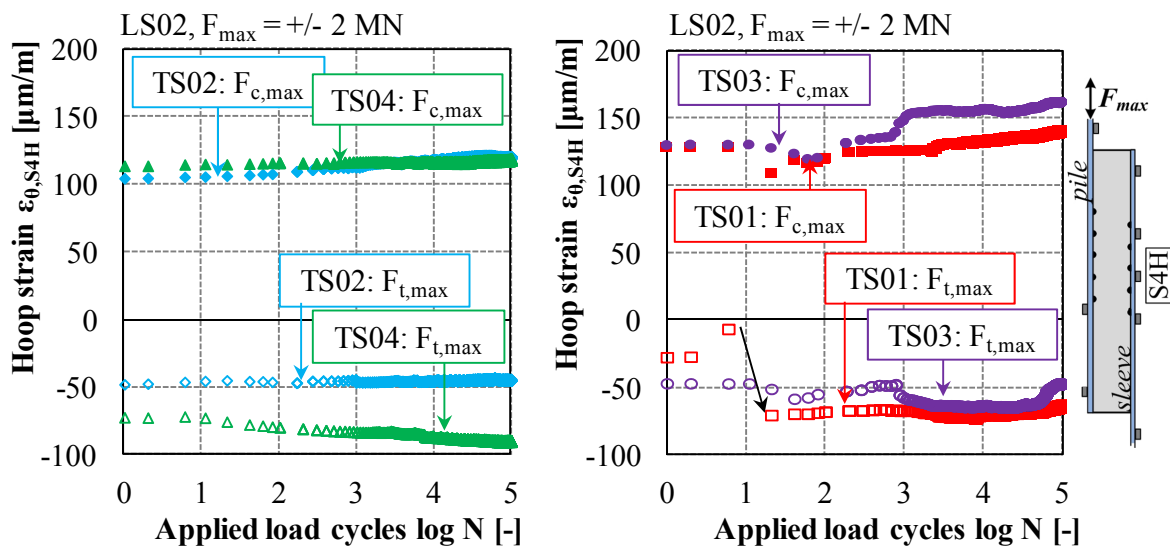


**Figure 3-27. Hoop strain development at S3H in LS02 at TS02 and TS04 (left) as well as TS01 and TS03 (right).**

The measured hoop strains at the test specimens with a larger grout thickness, TS01 and TS03, reflect a more pronounced variation after  $\sim 10$  load cycles, cf. Figure 3-27 right. Tensile related hoop strains increase substantially from 0 to 150  $\mu\text{m}/\text{m}$  at TS03 and from 0 to 90  $\mu\text{m}/\text{m}$  at TS01. By contrast, the compression loads lead to slight changes of the tensile hoop strains around values of 50  $\mu\text{m}/\text{m}$ . Thus, the tensile strain development seems to be influenced by changing load transmission, while the compression bearing behaviour is not affected. Intensified steel tube expansion at S3H might be a result of the previously mentioned compression strut failure at the first shear key pair, cf. Figure 3-24. The shift of the failure of the first compression strut leads to vertical compression strains and increased circumferential expansion of the steel tube at S3H. Thus, previous assumption that appearing fatigue damage influences the tensile bearing behaviour is confirmed by the hoop strain development. It is suggested that tensile related compression strut failure causes significant

local tensile hoop strains for test specimens with larger grout thickness. The compression induced strains are only slightly affected by the compression strut failure because compression forces provoke a crack closure and, thus change the bearing behaviour not remarkably. While the tensile evoked strains at TS01 stabilise after the initial force transmission change, the strains at the TS03 increase progressively with ascending load cycles. This strain increase can be interpreted as signifier of the failure, which occurred in the subsequent load stage.

In addition to the hoop strains at S3H, the documented strain values at S4H are depicted in Figure 3-28 displaying the hoop strain development in the center of the shear key area.



**Figure 3-28.** Hoop strain development at S4H in LS02 at TS02 and TS04 (left) as well as TS01 and TS03 (right).

The hoop strain development at TS02 and TS04 reflects an almost constant progress with slightly increasing tensile induced strains at TS04. The compression load provokes in both test specimens, TS02 and TS04, a circumferential tension strain of about 100 to 110  $\mu\text{m/m}$ . Apart from that, the tension related strains appearing at TS04 amount to -70 to -90  $\mu\text{m/m}$  and at TS02 to values of nearly -50  $\mu\text{m/m}$ . This difference might be a result of the different grout materials having varied tensile and compressive strengths affecting the bearing behaviour and cyclic material degradation. Contrary to S3H, at S4H the compression loads lead to tensile hoop strains while tension loads evoke compression hoop strains. Thus, the load transfer due to tension loading and compression loading resembles in the center of the shear key area. Comparison of the compression related strains in Figure 3-27 and Figure 3-28 confirms the continuously increasing load transfer from top to bottom, being mentioned previously in reference to Figure 3-23.

Opposed to the pronounced strain development at S3H of TS01 and TS03, the arising strains at S4H are less affected, cf. Figure 3-28. The compression induced strains rise at both test specimens slightly from 130 to 160  $\mu\text{m/m}$ . In correlation to the significant increase of S3H, the hoop strain at S4H increase abrupt to 70  $\mu\text{m/m}$ . The initial drop might result from the rearrangement of the loads due to a compression strut failure. Initial strain values for TS01 and TS03 lie in a range of -30 to -50  $\mu\text{m/m}$  increasing to values of approximately -70  $\mu\text{m/m}$ .



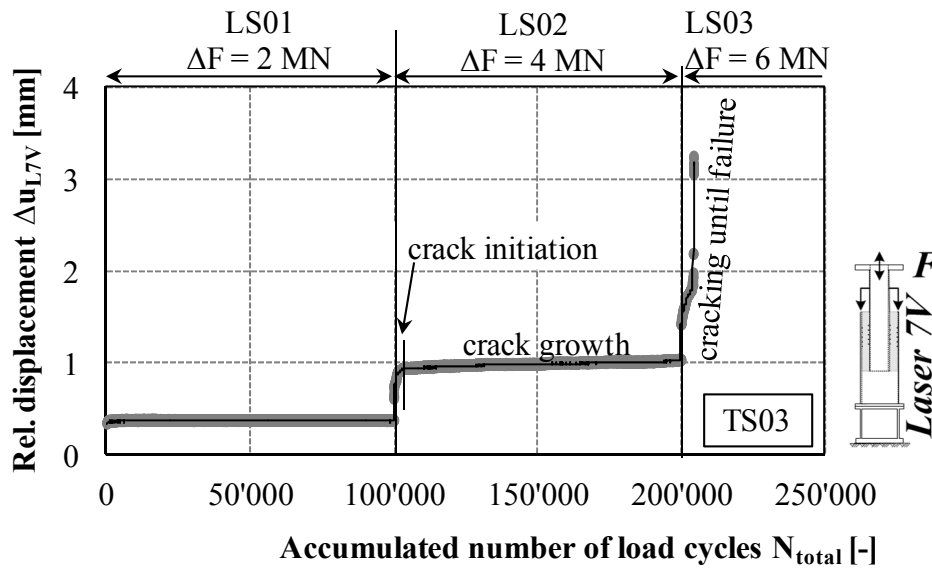
Comparing the results with respect to the varied test specimen geometries, the grout thickness has only a subordinate influence to the hoop strains at S4H. Notwithstanding, it has to be mentioned that the compression evoked values at TS01 and TS03 are slightly larger than at TS02 and TS04. Identical to TS02 and TS04, the tensile loads induce compressive strains and the compressive loads cause tensile hoop strains at the sleeve of TS01 and TS03.

By analysing the longitudinal and circumferential strain developments it becomes apparent, that fatigue induced damage provokes strain variations at the steel tubes. Comparison of the vertical strain distributions for different load directions outlines that it has to be differentiated between tensile and compression evoked strains and related force transfer. The compression loads are almost completely transferred within the shear key area, while large strains are generated in the upper part, cf. Figure 3-23. By contrast, the tension loads seem to be transferred by the shear keys and additional surface friction in the lower part. At all test specimens the obtained strains reflect that the external shear keys are predominantly influenced by cyclic loading and degradation as the stresses are larger than in the center of the shear key area. This phenomenon of predominantly loading of the external shear key pairs is confirmed by the less affected strains at S4. Moreover, the arising strains at the different test specimens have revealed, that particularly larger strains appear at the test specimens with an increased grout thickness. This might be caused by increased local stresses and large radial stresses provoking larger fatigue damage in the grout layer. The damage process is further analysed by considering the displacement behaviour with regard to the number of load cycles to failure.

### **3.4.5 Damage process**

The documented relative displacements at L7V are used for an additional evaluation of the damage process occurring in the grout layer. According to Pfanner (2003), the damage evolution of concrete can be described by three phases: the initial phase characterised by micro cracking, the second phase defined by crack growth and occurrence of meso crack and the third phase where matrix cracks will lead to a failure, cf. Figure 2-17. Pfanner (2003) based this description of the damage evolution phases on the distortion development for a calibrated number of load cycles. The progress of the relative displacement ranges at the test specimens enables to describe the damage evolution in a similar manner. In order to analyse all three phases of the fatigue damage process and to concentrate on the alternating load stages, it is chosen to focus at first on the phases observed at TS03, which fails in LS03.

Figure 3-29 illustrates the relative displacement range at L7V for TS03 in the alternating load stages LS01 to LS03 by the accumulated number of load cycles.



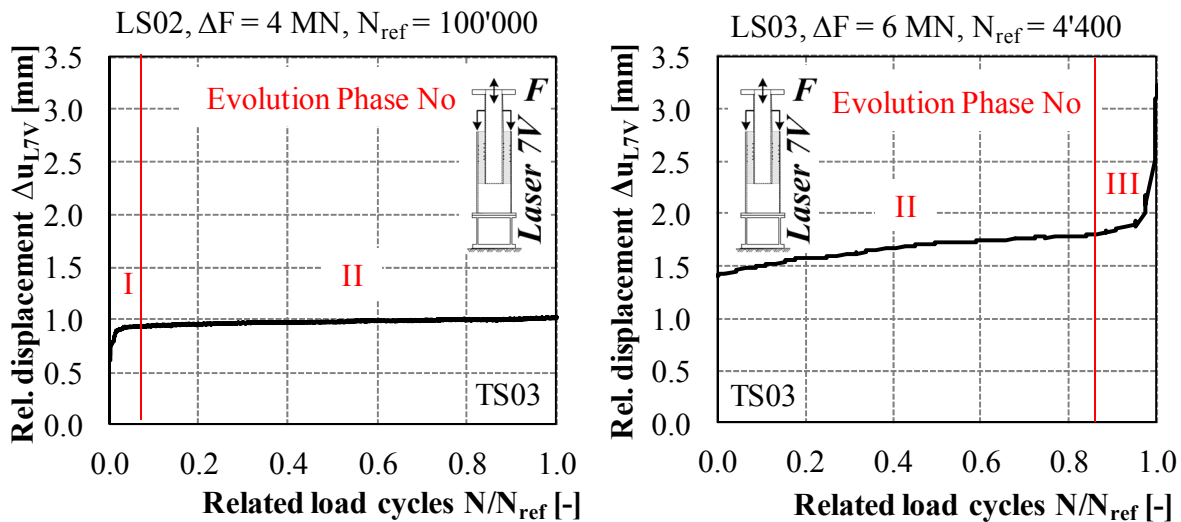
**Figure 3-29. Relative displacement range at TS03 for the alternating load stages LS01 to LS03.**

Due to the stepwise increased load ranges from LS01 to LS02 and from LS02 to LS03, the displacement levels are increased stepwise to some extent. This gradual increase is not caused by material degradation. The initial load stage is characterised by a comparable linear development of the relative displacement ranges, cf. Figure 3-29. Start and end phase of LS01 reflect no pronounced non-linear increase as it is known from pure high strength concrete material tests, e.g. by Wefer (2010) and Grünberg et al. (2014b). Nonetheless, it is expected that even micro cracks appeared in the grout section in this linear phase.

The relative displacement range induced by LS02 presents a much more distinctive progress in the initial load phase, cf. Figure 3-29. This disproportionate displacement growth at a low number of load cycles indicates that micro and meso cracks arise in the grout layer. The initial phase is followed by a linear increase of the displacement. During this load phase the micro cracks in the grout annulus grow and meso cracks are likely to appear. Over the test duration in LS02, no failure is caused, but significant damage occurs influencing the behaviour in the next load stage. Based on Pfanner (2003), it seems possible that further cyclic testing at LS02 might have lead to failure at load cycles  $N > 100'000$ . As depicted in Figure 3-29, the displacement behaviour at LS03 is characterised by a progressive non-linear increase leading to failure of the test specimen after 4'400 load cycles. Thus, LS03 represents the third and last phase of the damage evolution, where matrix cracks lead to fracture surfaces and finally to a failure.

Commonly, the evolution phases during fatigue loading are examined by relating the applied number of load cycles to the number of load cycles until failure, as reference number of load cycles  $N_{ref}$ . The normalisation over the total accumulated number of load cycles consisting of load stages LS01, LS02 and LS03 reveals a curve development similar to Figure 3-29. Even though this procedure is usually applied, it does not allow to identify the displacement increase and related stiffness degradation at the individual load stage. By focusing on the reference number of load cycles at each load stage, the individual curve progress is obtained. Therefore, the damage evolution phases are identified for the relative displacements appearing

at TS03 for the load stages LS02 and LS03. These are set in reference to the number of load cycles related to the respective load stage, cf. Figure 3-30.

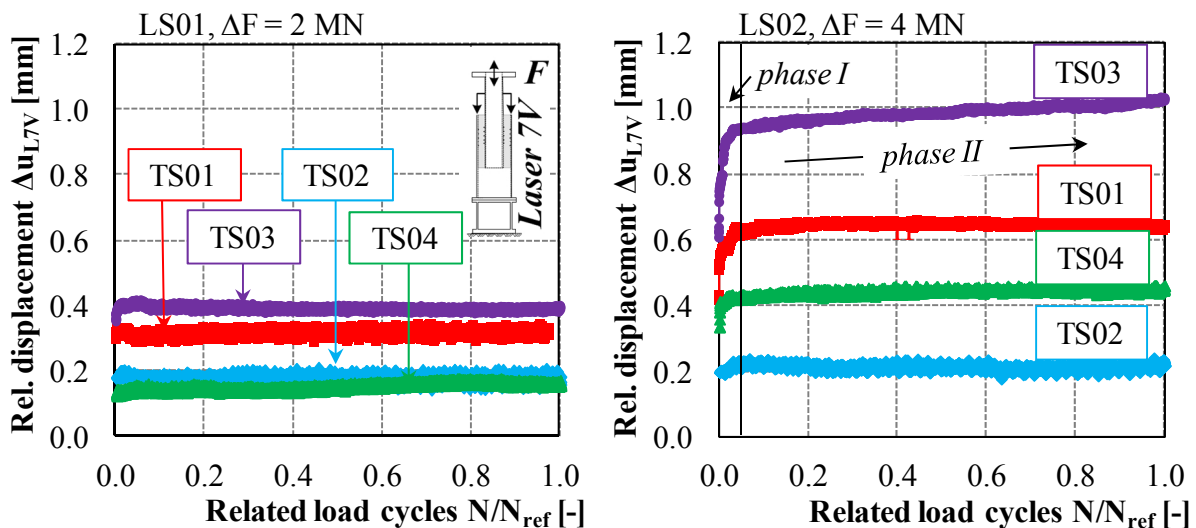


**Figure 3-30. Evolution phases with regard to the relative displacement ranges appearing at TS03 in LS02 and LS03.**

The left diagram in Figure 3-30 reflects the displacement related evolution phases for LS02 with the reference number of load cycles of 100'000. The initial phase of LS02 is characterised by a disproportionate non-linear increase of the displacements representing the damage evolution phase I. This phase is accompanied by micro crack growth of shrinkage and load induced cracks in the grout material. According to high strength grout material testing, cf. Grünberg et al. (2014b), this phase results to 3% to 5% of the total strain development. At the grouted connection test specimens the initial non-linear phase observed for LS02 amounts to 8% of the related load cycles, cf. Figure 3-30 left. It follows the second phase being influenced by micro crack growth and arising meso cracks. The LS02 ends with a displacement range of 1 mm showing no significant non-linear increase. Subsequent displacement ranges in LS03 begin at approximately 1.4 mm, cf. Figure 3-30 right. The uneven progressive displacement develops until the turning point of the curve introduces the disproportionate increase by nearly 85% of the related load cycles. This third phase of the damage evolution process is linked to matrix cracking. Due to failure of the test specimen TS03 during LS03, the right diagram presents the evolution phases on the basis of 4'400 load cycles. The progressive non-linear increase of the relative displacement range in the third phase of the damage evolution characterises the failure of the test specimen. By relating the number of load cycles to the number of cycles until failure, the curve development smoothens and turning points can be identified. But, this procedure disregards the comparable early failure in contrast to the intended number of load cycles of 100'000. Setting the obtained displacement range in relation to the intended number of load cycles illustrates that LS03 equals completely the evolution phase 3, cf. Figure 3-29. Anyhow, it is concluded that these two procedures describe two different approaches associating the known damage characteristics to the observed displacement phases. It is further concluded from the test results, that a progressive non-linear relative displacement range increase, cf. Figure 3-30

right, equals a failure of the connection. In order to compare results of varied test specimens, the underlying reference load cycles has to be considered carefully.

With respect to the cyclic tested grouted connections, a comparison for selected load stages is conducted. Figure 3-31 presents the relative displacement ranges measured at L7V of TS01 to TS04 for the load stages LS01 and LS02.



**Figure 3-31. Damage evolution phases based on the relative displacement range during LS01 (left) and LS02 (right) for the test specimens TS01 to TS04.**

Results displayed in Figure 3-31 are based on the maximum applied number of load cycles for each load stages, i.e.  $N = 100'000$ . Obviously, the curves of the relative displacement ranges resulting from LS01 show for all test specimens more or less identical linear developments. An initial non-linear increase is visible at TS03 solely. Nevertheless, comparison of the individual displacement values for the test specimens shows identical to previous analysed relative displacements larger values for the test specimens with the larger grout thickness. The range amounts to nearly 0.3 mm for TS01 and to 0.4 mm at TS03. The displacement range at TS02 and TS04 are more closely arranged at a magnitude of about 0.2 mm. However, the order of curves from top to bottom seems to correlate with the fatigue strength and apparently with the fatigue performance.

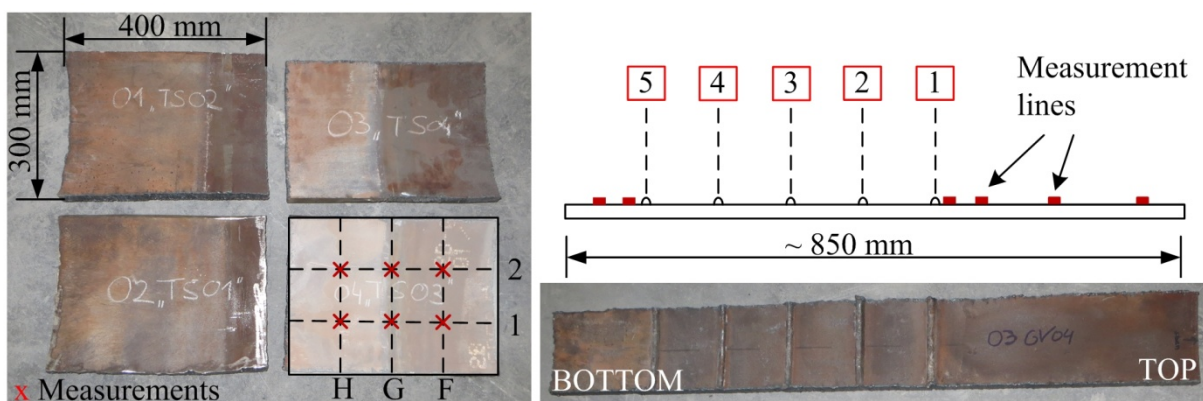
Opposed to the approximate linear development for LS01, the damage related displacement evolution during LS02 displays a much more pronounced development. The initial phase I, outlined in Figure 3-31, is clearly recognisable at all test specimens. The disproportionate curve development enlarges with ascending load displacement range. Moreover, the order of curves from bottom to top can be linked to the descending ultimate bearing capacity of the individual test specimen, cf. chapter 3.3.2. Thus, the damage evolution derived for TS03 reflects the largest disproportionate growth in the initial phase, which is followed by a strong linear increase in the second phase. Although TS01 is described by a disproportionate increase in phase I, the phase II is characterised by a nearly constant linear development. By contrast, TS02 and TS04 reveal a small displacement increase at phase I and a comparable constant progression during phase II. This disproportionate and linear displacement development is suggested to correlate with the stiffness degradation and related damage

process by crack growth. The displacement evolution during LS02 is especially at TS03 associated with an increased micro and meso crack growth in the grout layer. The crack growth caused by LS02 influences the failure in the next LS03 at TS03. Apart from that, the TS01 as well as TS02 and TS04 are characterised by a micro crack growth in the first phase, which stabilises in the second phase.

Consequently, the load stage related displacement evolutions are assumed to represent a stiffness and strength degradation of the grout material, which is similar to plain concrete fatigue testing as described by Pfanner (2003). Determined curves have revealed that all test specimens are influenced by disproportionate displacement increase during LS02. Moreover, the individual evolution phases can be identified with respect to the tested grouted connections. Nonetheless, consideration of the local arising strains and relative displacements enable a more detailed identification of appeared cracking than the comparison based on the displacement range and related number of load cycles, cf. chapter 3.4.2 to 3.4.4.

### 3.4.6 Steel surface changes

The surface roughnesses are measured after cyclic testing in order to evaluate the amount of abrasive wear between the different test specimens. These values are compared to measurements conducted prior to the grout filling process. Pre-testing is performed subsequent to the mechanical cleaning at the inner surface of the sleeve at the lower part of the grouted connection. While the sleeve is opened after testing for examination of the damaged grout, steel plate segments (length · width · thickness  $\sim 300 \cdot 400 \cdot 20$  mm) for tensile tests of the steel and a segment with the shear keys (length · width · thickness  $\sim 850 \cdot 150 \cdot 20$  mm) is separated from the tested specimens, cf. Figure 3-32. These segments are used for the surface measurements after cyclic testing.

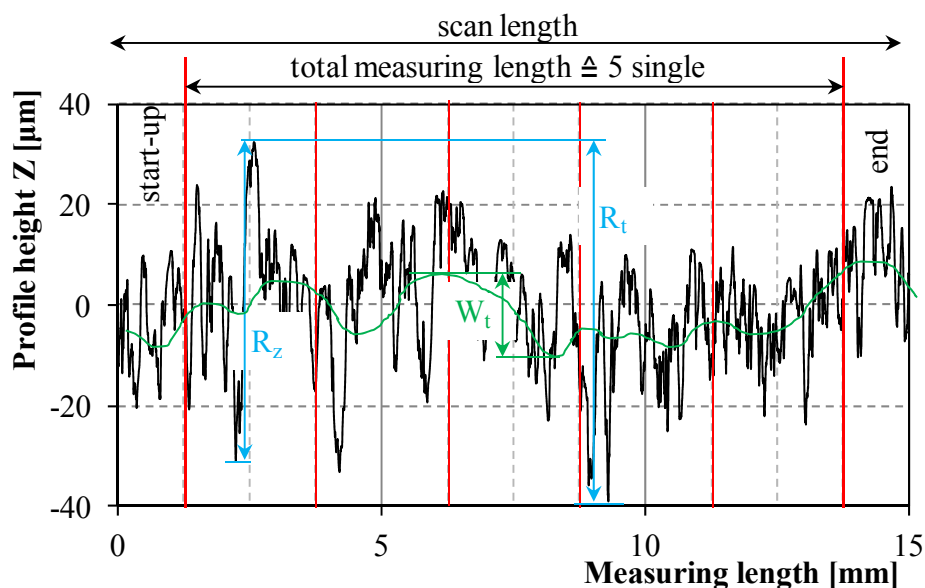


**Figure 3-32. Steel test plates from the sleeve (left) and shear key segment (right) for the surface roughness measurements after cyclic testing.**

The tactile measurements are performed at predefined positions of the steel plates and the shear key element. Before measuring the surface roughness, the steel surface is pruned of loose material and grout. As the steel surface is sensitive against corrosion and surface modifications, the surface properties are derived shortly after opening the sleeve, separating and cleaning the steel segments.

The surface texture of the test specimens is measured in accordance to DIN EN ISO 4287 (2010) and DIN EN ISO 4288 (1998) by the profile method using the tactile measurement device Hommel Etamic T1000 with the linear traverse unit waveline 20. By using this measuring device, it is possible to quantify both the surface roughness parameters and additionally the waviness of the surface. The surface condition is characterised commonly by the surface roughness  $R_z$ , the arithmetic surface  $R_a$ , the maximal roughness height  $R_t$  and the root mean square roughness  $R_q$ . The roughness parameters presented by the measuring tool are defined as a mean value out of five measurements taken in one predefined measuring section of 12.5 mm. The single measuring sections have a length of 2.5 mm with a cut-off length of 2.5 mm, cf. Figure 3-33. Illustrated surface roughness profile in Figure 3-33 originates from the surface measurement at position F2 of TS03 after cyclic testing, cf. Figure 3-32.

As reference values for a standardised surface preparation characteristic roughness values for a sand blasted steel segment with the grade Sa 2½ are used according to Lochte-Holtgreven (2013). A defined surface of Sa 2½ reflects the surface preparation quality prior to the application of corrosion coatings at offshore steel structures, cf. DIN EN ISO 12944 (2008).



**Figure 3-33. Surface roughness profile measured at TS03 before testing showing relevant surface roughness parameters and measuring lengths.**

Table 3-10 summarises the roughness values for the reference and tested surfaces at the test specimens TS03 and TS04 achieved prior and after testing. Comparison of reference and measured values prior to cyclic tests reflects that the roughness values at the test specimens are slightly smaller than at the reference steel segment having defined properties. Thus, by the surface preparation a slightly smoother surface is reached than for sand-blasted surfaces.

However, the impact of the cyclic loading to the surface roughness is determined on the basis of the pre- and post-testing roughness values, cf. Table 3-10. The comparison is limited to the results of TS03 and TS04 including a failed specimen and covering both grout thicknesses. Analogue results are obtained for TS01 and TS02. Comparison of the determined surface

degradation for TS03 and TS04 reveals that the reduction at TS03 is noticeable larger than at TS04. The surface roughness is reduced by 23%, whereby the reduction of the surface roughness at TS04 amounts to 14%. Although the degradation is larger for TS03 than for TS04, the absolute post-testing values in the essence similar.

**Table 3-10. Surface roughness at the sleeves of TS03 and TS03 before and after testing.**

Specimen		Surface roughness $R_z$ [ $\mu\text{m}$ ]	Arithmetic surface roughness $R_a$ [ $\mu\text{m}$ ]	Max. roughness height $R_t$ [ $\mu\text{m}$ ]	Root mean square roughness $R_q$ [ $\mu\text{m}$ ]	Total waviness $W_t$ [ $\mu\text{m}$ ]
Reference surface Sa 2 ½		59.50	13.20	82.01	16.54	-
TS03	pre - testing	54.77	9.70	70.33	12.20	26.14
	post - testing	42.03	7.20	58.73	9.21	25.61
<b>Degradation</b>		<b>23%</b>	<b>26%</b>	<b>16%</b>	<b>24%</b>	<b>2%</b>
TS04	pre - testing	49.96	8.36	66.65	10.55	20.67
	post - testing	42.91	7.47	59.08	9.49	20.41
<b>Degradation</b>		<b>14%</b>	<b>11%</b>	<b>11%</b>	<b>10%</b>	<b>1%</b>

On the basis of the listed absolute values and the percental degradation in Table 3-10, it can be summarised that the roughness parameters are minimised by about 16% to 26% at TS03. The surface parameters obtained for TS04 reduces in the range of 10% to 14%. The reduction of the roughness parameters is ascribed to the frictional force transmission and appearing relative displacements. A second reason for the smoother surface may result from the cement being pressed into the steel surface valley and pores. By previous evaluation of the vertical strain development in chapter 3.4.4, it is suggested that at the test specimens with a larger grout thickness, a larger amount of forces are transmitted by friction than at test specimens with a smaller grout thickness. This assumption can be confirmed by the provided comparison of surface degradation at TS03 and TS04. Nonetheless, compression strut failure and crushed grout material increase likewise the relative displacements, which in consequence influence the surface roughness conditions. Even though the roughness parameters are influenced significantly by the cyclic loading, the values for the total waviness deviate marginally by 1% at TS04 and 2% at TS03 from the original values. Notwithstanding, the surface waviness, representing a parameter reflecting the surface texture, is apparently not influenced by local small frictional effects.

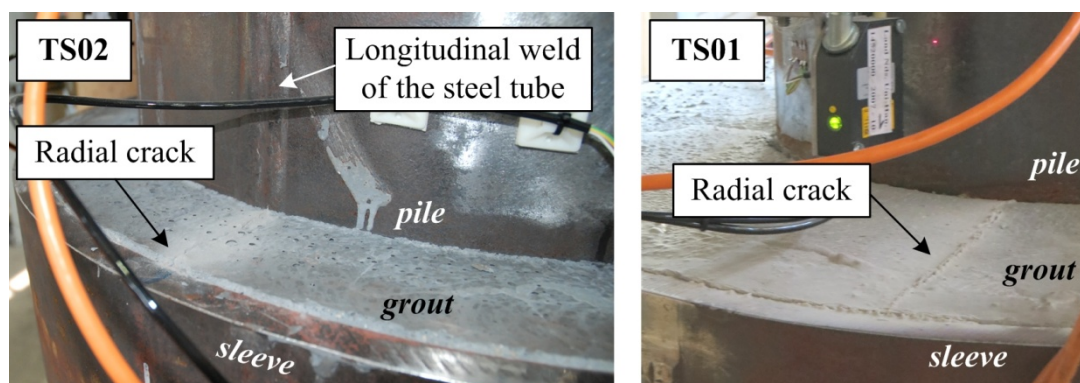
Thus, comparison of the surface degradation at TS03 and TS04 outlines, that the impact to the surface roughness are larger for TS03. Recalling that TS03 is exposed to less load cycles than TS04, exacerbates the measured degradation difference between these specimens.

### 3.4.7 Damage characteristics

In advance to the cyclic testing, the grout surfaces at the top and at the bottom of the grouted connection are visually inspected for any cracks. At the test specimens TS01 and TS02 filled with BASF Masterflow<sup>®</sup> 9500 no visible cracks appear. The top grout surfaces at TS03 and

TS04, filled with Densit Ducorit<sup>®</sup> S2, indicate marginal cracks all over the top grout surface, which appear during the hardening process. Later on, inspection exhibits that the top layer is porous and without any strength, so that the first 10 to 20 mm have to be removed. Thus, the grouted length is reduced by 10 to 20 mm, which can be assumed to be negligible with respect to the load transfer. It has to be mentioned that the used Densit Ducorit<sup>®</sup> S2 represents a composition from 2014, which has been changed meanwhile. The test specimens TS03 and TS04 are filled with grout at different days and with different charges of material. Due to the fact that both test specimens have porous material at the top layer and both grouting procedure are supervised by material experts delegated by the material supplier, the reason for the inhomogeneous material is expected to result from the material itself. It is expected that the porous surface layer results from a strong deaeration process in combination by a surface closure being influenced by the synthetic superplasticizer. Thus, beneath the closed surface air bubbles concentrate leading to a porous layer. Moreover, requests at the material supplier have revealed that the material composition was recently changed. Thus, an increased amount of synthetic superplasticizer might have hindered the deaeration process. The surface of the hardened grout underneath the porous material displays many small short surface cracks at both test specimens TS03 and TS04, which are limited to the surface and, thus have no impact to the bearing behaviour. In addition, TS03 has radial cracks having a width of 0.2 mm, cf. Annex B.4. These radial cracks are visually monitored, as it is expected that this shrinkage induced crack might grow during testing. In contrast to the top surface, the bottom grout surface does not show any cracks at all test specimens. Therefore, it is assumed that merely the top layer is influenced and the residual grout is well enough to perform the cyclic testing.

However, during the cyclic testing the grout surfaces are subjected to inspections. All four test specimens exhibit radial cracks at the top surface of the grout layer after the load stage LS02, cf. Figure 3-34. The cracks appear at the weld of the inner pile at the test specimens TS02 and TS04. Because the small piles of TS01 and TS03 are welded by High Frequency Induction (HFI) no notch effect caused by the weld exists and the radial crack appears at the potentially otherwise weakened locations around the circumference.



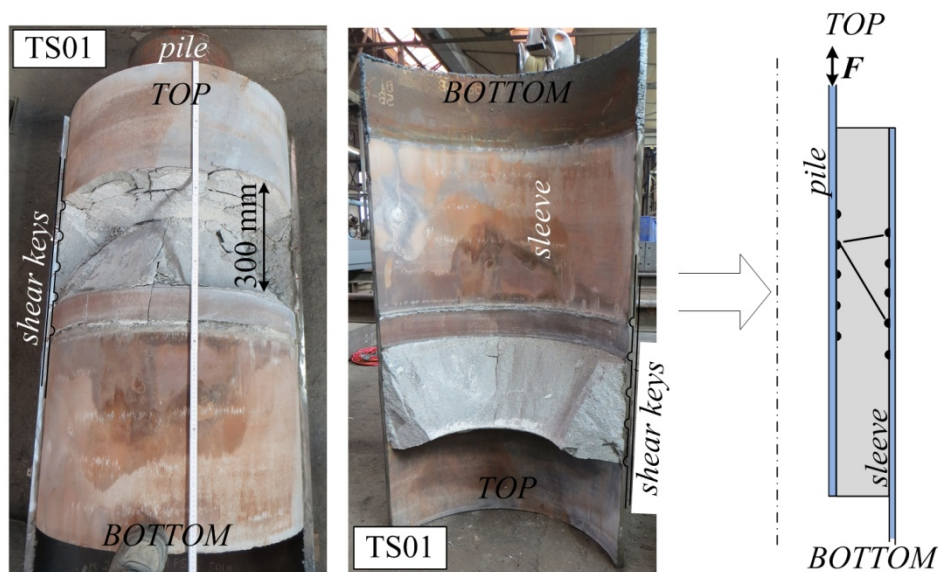
**Figure 3-34. Radial cracks and grout powder at the grout surface of TS02 (left) and TS01 (right) after the alternating load stage LS02.**

While testing continues, grout powder is blown out of the visible cracks at the top surface. After load stage LS08, large grout fragments fall down inside the adapter indicating that these have been broken off the grout section at TS02. Contrary to TS02, at all other test specimens



only small shell shaped spallings at the bottom grout surface are observed by the end of testing.

Finally, the test specimens are opened after testing to analyse the fracture patterns by focusing on the status of the grout. In order to examine crack patterns, the sleeve is separated carefully with a blowpipe. In view of the grout layer, cf. Annex B.4, it becomes apparent that the grout is substantially more damaged at the test specimens TS01 and TS03 than at the test specimens with a smaller annulus TS02 and TS04. Moreover, at both test specimen with a large grout thickness, an exceptional large grout wedge sticks to the separated sleeve segments. Figure 3-35 depicts exemplarily the view of the grout segment and the removed sleeve segment with the sticking grout wedge at TS01. Shown missing grout wedge has a length of 300 mm at the sleeve and forms a triangular shape. Thus, it becomes apparent that compression struts induced by tensile and compression forces have been broken, cf. Figure 3-35 right. It can be further concluded, that adhesive bonding still exists sequentially in the sleeve-grout intersection. Similar results are observed for TS03, cf. Figure B-6 in Annex B.4, whereby the grout wedge length results to 400 mm developing from the first sleeve shear key to the third pile shear key and back to the bottom sleeve shear key.



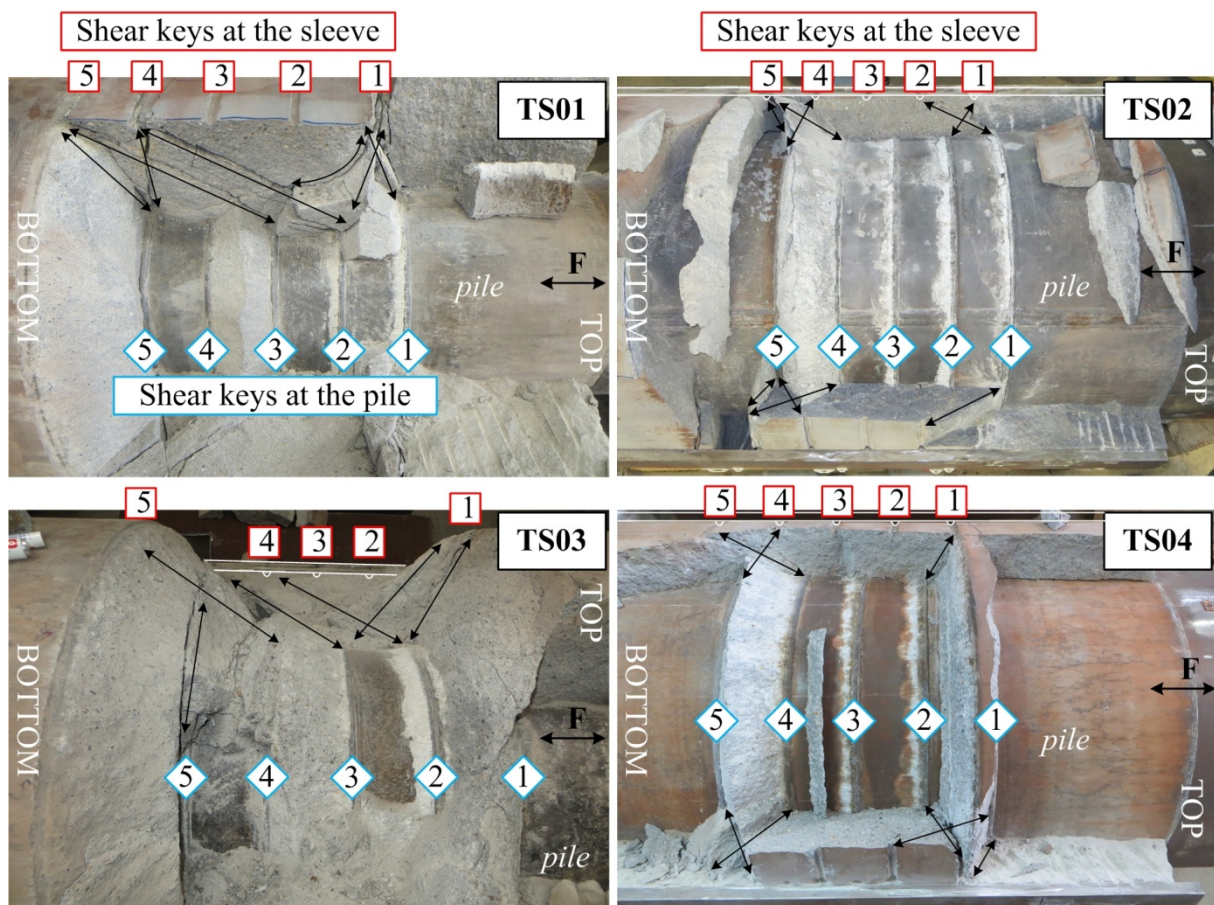
**Figure 3-35. Grout wedge sticking to the sleeve and resulting cracks at TS01.**

At TS04 slight cracks at the shear key tips are visible merely after removing the sleeve. In Annex B.4, Figure B-6 to Figure B-9 summarise damage characteristics for each test specimen, prior, during and after testing. Prior and during testing the grout surfaces are observed, while after testing the specimens are opened. Especially at the test specimens with a large grout annulus radial cracks appeared. Combination of radial and diagonal compression strut cracks lead to a considerable destroyed grout layer.

Subsequent to the sleeve, the grout layer is opened carefully by taking off loose grout segments. As it is possible to remove grout particles easily from the pile interface, it can be concluded that debonding occurred at the majority of the pile-grout intersection. Figure 3-36 provides an overview of the opened and exposed grout layer and pile surface with shear keys. The illustrations are turned by 90° so that the loading is at the right side of the pictures. On

the left side of the figure are the test specimens TS01 and TS03 with a large grout annulus, and on the right side are the test specimens with a small grout thickness. The shear keys are numbered in red at the sleeve and in blue at the pile. In order to reconsider the force transfer the obtained cracks in the grout layer are highlighted by black arrows.

Figure 3-36 indicates that the test specimens with similar grout annulus size show comparable cracks arising between opposite shear keys describing the course of the compression struts. From the crack patterns it becomes obvious that alternating loads lead to crossing compression struts. This fact is independent of the grout annulus size as both test geometries show crossing cracks. Contrary to TS01 and TS03 showing fracture in the middle section of the shear key area, the test specimens TS02 and TS04 with a small grout annulus show crack patterns at top and bottom section of the shear key area.



**Figure 3-36. Fracture pattern at the test specimens TS01 to TS04 after testing.**

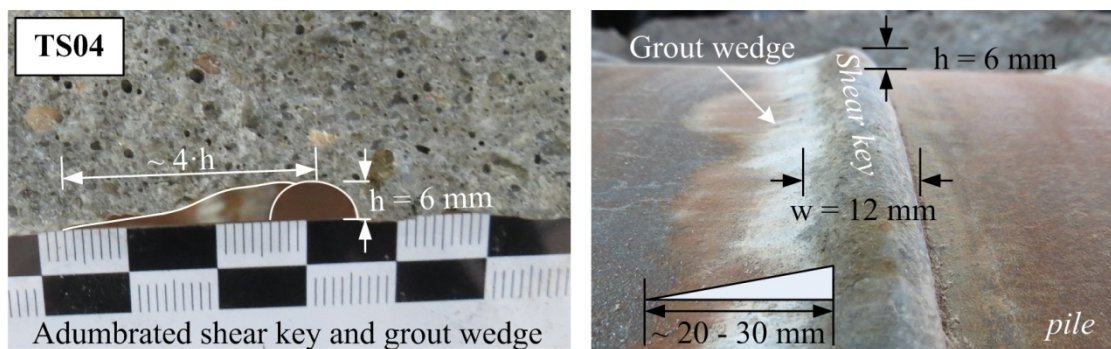
For test specimens TS02 and TS04, predominantly crossing compression strut between the upper and lower shear key pairs are visible. While the tensile induced cracks appear between opposed shear keys, the compression induced chinks skip in some cases one shear key at the sleeve. The compression struts develop from the first shear key on the pile to the second shear key on the sleeve. Apart from that, the tensile force provokes cracks arising from the second shear key at the pile to the first shear key on the sleeve.

By contrast, the test specimens with large grout annulus TS01 and TS03 depict compression struts that skipped two opposed shear keys and, thus developed between the second shear key at the pile and the fourth shear key at the sleeve as well as between the third at the pile and the

fifth at the sleeve. The direction of these cracks indicates that compression loads caused the failure. Opposed to these compression induced cracks, the tensile loads induce cracks mostly do not skip the next shear key. These cracks occur between pile shear key 2 and sleeve shear key 1 and at the bottom between pile shear key 5 and sleeve shear key 4 at TS01 and TS03.

It can be concluded that different compression strut inclinations develop depending on the force direction. Similar phenomenon is observed for TS01 and TS03. At the end of this section the crack patterns are summarised with reference to observed compression strut angles and resulting failure modes. The individual derived crack patterns are summarised in Annex B.4 for each test specimen.

In addition to the compression strut cracks, all four test specimens illustrate a grout segment which stuck underneath the pile shear keys in the form of a triangle, cf. Figure 3-37.

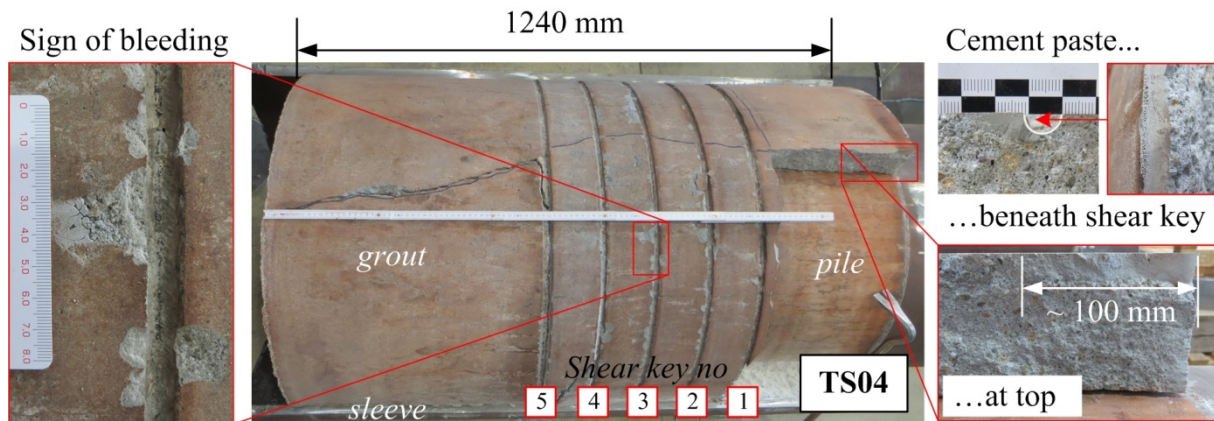


**Figure 3-37. Pile shear key and grout wedge exemplarily at test specimen TS04.**

At the sleeve only sequential grout wedges are registered at some shear keys. Thus, the grout wedge seems to be a pile related, or rather loaded steel tube phenomenon. The form of the grout wedge indicates that locally arising stress concentrations provoke shear failure forming a smooth sliding surface from the shear key tip to the steel tube. The grout wedge is already described by Krahl & Karsan (1985). The grout wedge dimensions are documented for all test specimens revealing not any grout thickness or material specific tendency. The height of the grout wedge depends solely on the shear key height which is equal to 6 mm for all test specimens. The length of the grout wedge is according to Krahl & Karsan (1985) equal to 4 times the shear key height. This value can be confirmed by the measured dimension at the tested specimens, as they are in the range of 20 to 30 mm.

It can be seen by the fracture surface in Figure 3-37 that the high strength grout material is cracked through cement and grains. Thus, cracks develop not along the circumference of particles, but develop through these as the strength of the surrounding cement has equal or even larger strength. This fracture behaviour of high strength materials is introduced in chapter 2.4.2 with reference to observations by numerous researchers.

With regard to the stated porous grout top surface layer at the test specimen TS03 and TS04, the opening of the grout section reveals areas of plane cement paste and dry, unfixed material, cf. Figure 3-38.

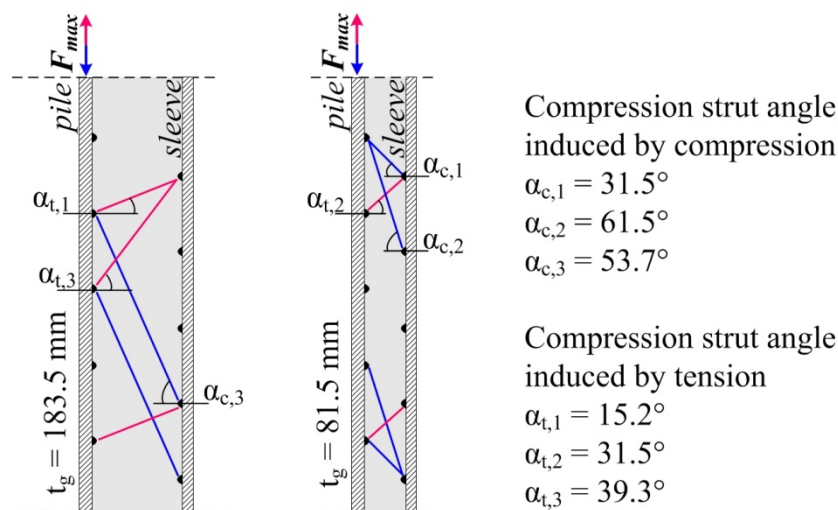


**Figure 3-38. Symptoms of inhomogeneous grout material behaviour at the test specimen TS04.**

These inhomogeneities appear at slight grout parts at the shear keys and in the grout segment below the shear key area. Plain cement paste is additionally located in the top area over 100 mm, cf. Figure 3-38, and beneath the shear keys by about 20 mm at the sleeve.

In addition, the surface of the grout underneath the sleeve shows parts where the grout has bled, cf. Figure 3-38 left. Even though these material inhomogeneities appear at TS03 and TS04, merely TS03 fails earlier than the other test specimens. The measured results reflect that TS03 fails in LS03 and TS04 shows a significant displacement increase in LS06, cf. chapter 3.4.2. Thus, it can be concluded that observed material inhomogeneities have an impact on the fatigue behaviour. Nevertheless, this assumption is only valid for the tested specimens, which are performed at ideal laboratory conditions.

For a better overview, the crack patterns are transferred in a sketch showing the predominant compression strut cracks initiated by tension and compression loads at the test specimens with a large and a small grout annulus, cf. Figure 3-39.



**Figure 3-39. Sketch of the derived compression strut cracks and angles for varied grout annulus.**

The crack pattern for the small grout annulus reflects that compression loads lead to cracks with an inclination of  $31.5^\circ$  and  $61.5^\circ$ , whereby the compression strut arising due to tension has an inclination of  $31.5^\circ$ . One explanation for the varied angles is that cracks appearing at an angle of  $31.5^\circ$  are caused by the initial alternating load stages, while the enlarged loads of

the pulsating compression load stages evoke the compression induced cracks with an angle of  $61.5^\circ$ .

The sketch of the large grout annulus presents for the tensile provoked cracks compression strut inclinations of  $15.2^\circ$  and  $39.3^\circ$ , cf. Figure 3-39. By contrast, the chinks induced by compression loads have an inclination of  $53.7^\circ$ . Apparently, tension evoked cracks appear during the alternating load stages. The appearance of the cracks provoked by compression loads presumably appears during the significantly larger compression loads in the pulsating load stages. But as it is not possible to monitor cracking inside the grout annulus while testing commences, this assumption is based on the hypothesis that larger loads result in fully formed cracks. Despite that, the tensile bearing capacity is lower than the compression bearing capacity. As a result tensile loading causes increased stresses at the shear keys leading to earlier cracking and crack growth than for compression forces. Moreover, it has to be emphasised that the observed crack patterns are a result of crack process, which constitutes of different phases of crack growth and a crack initiation accounting for varied crack sizes, cf. chapter 3.4.5. The previous considerations are based on the final damage patterns presenting predominantly meso cracks. Apart from the fully developed cracks used to determine compression strut angles, crack initiation starts close to the shear key tip, cf. documentation in the Annex B.4.

It can be concluded that the failure mode for both test specimens geometries complies with the common compression strut failure, as described by the failure mode b in Figure 2-7. Moreover, arising compression strut angles depend on the shear key spacing, the grout thickness, the shear key height and the load direction. It is shown that alternating loading may cause crossing compression struts. Although the grout layer suffers from substantial cracking, the test specimen can be exposed to numerous load cycles at considerable large load levels. Thus, the cyclic axially loaded grouted connections are characterised by a rather ductile behaviour, which is in contrast to the brittle behaviour of the high strength grout material.

### 3.5 Conclusion

In order to determine and evaluate the fatigue behaviour of grouted connections with large grout thickness, cyclic axially loaded experimental tests are performed at a large-scale for the first time. Four test specimens with two different grout thicknesses equivalent to a pre- and a post-piled reference grouted connection in latticed substructures being filled with two different high strength grout materials are exposed to a stepwise increased axial loading. As the worst fatigue load scenario represents a total reversal loading and predominant load situations at real offshore structures consist of compression loads, the applied cyclic load stages covered alternating and pulsating compression load scenarios. Due to the fact that the largest contribution to damage for extreme load scenarios apparently appears between 10'000 to 100'000 load cycles, the load level was increased after 15'000 or 100'000 load cycles. Extreme large cyclic test loads are used to achieve a fatigue failure, which allows to evaluate the damage characteristics and to determine relevant failure modes.

The initial global deformations represent for all four test specimens a linear-elastic behaviour. Nevertheless, the global load-displacement behaviour reflects that the reduced stiffness caused by a large grout thickness entails increased deformations. Local relative displacements and corresponding stiffness developments reveal, that with increasing load cycles and increasing load levels, a non-linear stiffness reduction occurs. Moreover, abrupt cracking which is assumed to origin from compression strut cracking, provokes abrupt changes of the relative displacement and corresponding stiffness. Even though, some sudden relative displacement changes indicate brittle grout behaviour, the holistic view on results considering the development of the relative displacements reflects a ductile fatigue behaviour of the large-scale test specimens.

The stiffness degradation is substantially caused by the initial three alternating load stages. Ascending load levels and load cycles provoke a stiffness reduction, mainly induced by tension loads, which indicates a reduced tensile bearing resistance of the test specimens. In contrast, pulsating compression loads lead to a progressive stiffness increase. This ostensible stiffness growth results from the increased confining pressure and interlocking of the steel-grout interface. In addition, it can be assumed that crushed grout material and crack surfaces cause enhanced interlocking. Notwithstanding, comparison of the status prior and after pulsating compression load cycles has outlined, that stiffness and fatigue degradation continue during pulsating compression load stages. Nonetheless, the alternating load stages have a higher detrimental impact on the fatigue resistance of the test specimens than pulsating load stages. Particularly tensile loads cause a fatigue strength reduction, because these loads are transmitted by a reduced number of active compression struts and are accompanied by pile contraction increasing the stress concentrations at the shear keys.

According to observed vertical and circumferential steel strain developments, cracking leads to a redistribution of the force transmission. The registered vertical steel strain development enables to correlate changing strains to failed compression struts. The analysis of horizontal and vertical steel strains in the shear key area confirms evidently, that the trust model can be used to explain the load transfer by arising compression struts. The majority of loads are transferred by external shear keys, while the center shear keys are less affected by arising stress and strain changes. Vertical steel strains reveal that compression induced stresses and strains are transmitted mainly in the upper section while tension induced stresses and strains are transmitted predominantly in the lower section of the shear key area.

The majority of grout crack initiation and growth appears non-linear with increasing load cycles. The known damage evolution phases usually based on the arising distortion developments for high strength concrete can be transferred to the development of occurring relative displacement ranges at the tested grouted connections. The three phases of crack growth can be identified for the test specimens who failed. Apart from that, the highly disproportionate displacement increase at the beginning of each load stage indicates the amount of damage and residual strength. After initial cracking and associated stress relaxation, the crack growth stabilised which confirms the proposed ductile behaviour. Notwithstanding progressive non-linear increase of the relative displacement ranges in the

third phase of damage evolution, the macro and matrix cracking, defines failure of the specimen.

On the basis of measured steel surface changes and strain developments at the sleeve, it can be concluded that the frictional resistance contributes to the load transmission. Notwithstanding, the frictional and adhesive bond plays a subordinate role to the fatigue performance. The observed crack patterns demonstrate that the general failure mode is linked to the compression strut failure. Despite grout cracking, the interlocking effect by shear keys is only slightly affected, representing that a post-cracking load transfer at the shear keys is still possible. As the fatigue loads are transferred mainly by shear keys, the interface capacity depends on the shear key dimension and position. Apart from that, the grout thickness and corresponding compression strut angles influence the fatigue and damage behaviour. Up-scaled grout thicknesses are accompanied by high transverse tensile stresses leading to radial cracking. The reversal loads consisting of tension and compression evoke crossing compression struts, irrespective of the investigated grout thickness. Especially at the grouted connection specimens with increased grout thickness the applied large load levels caused intensive grout splitting.

It can be concluded from the conducted experimental investigations, that increased grout thickness being accompanied by reduced stiffness leads to a reduced fatigue strength. Even though the material strength variation are small and have no significant impact to the fatigue performance, documented test results show that with increasing grout thickness, material inhomogeneities reduce the fatigue strength. Compared with calculated strength from offshore design codes, the observed fatigue performance and associated strength of the test specimens is higher than expected. While alternating loads cause significant cyclic degradation, the pulsating compression loads display an enhanced fatigue performance. In consideration of cyclic degradation, the fatigue behaviour need to be further investigated by numerical simulations, which enable to extend the parameter range and to intensify the knowledge gained so far with respect to arising stresses and stress concentrations during varied load stages.

## 4 Numerical Investigations

### 4.1 Purpose

As experimental investigations usually concentrate on a limited parameter set, one objective of numerical investigations is to extend the knowledge by varying parameters based on validated models. According to the results of the experimental investigations, the load bearing behaviour is significantly influenced by the interface characteristics as loads are transferred predominantly by the shear keys and secondly by interface strength. Thus, in addition to the material strengths and grout thickness, the numerical investigations shall be used to evaluate the influence of different surface conditions like the shear key height to distance ratio  $h/s$  and different friction coefficients. For this study, initially the numerical models have to be developed and validated on the basis of the experimental results.

Due to the significance of numerical simulations for the design of grouted connections, the use of appropriate material models for grout and steel as well as the selection of reliable model configurations and calculation procedures is of overriding importance. Several demands have to be met by the numerical model configuration and calculation procedure for the simulation of the non-linear fatigue behaviour of grouted connections. In consideration of the non-linear material behaviour of grout, a special focus has to be set on the multiaxial stresses arising in the confined grout layer. During the model configuration, the transfer of current numerical design approaches to cyclic axially loaded grouted connections with increased grout thicknesses has to be investigated. Moreover, varied load situations by tensile and compression loads provoke changing multiaxial stress states in the grout influencing the fatigue strength of the material significantly. Hence, degradation effects caused by the cyclic loads need to be accounted for by the numerical simulations. With regard to the experimental test program consisting of different load stages in the alternating and the pulsating range, it is focused on a method covering cumulative damage aspects. While the stress ratios and applied ascending load levels evoke varied impacts on the cyclic degradation and fatigue performance, the influence of the load sequence has to be addressed. It is chosen to use numerical simulations to cover the effect of ascending and descending loads. From the previous considerations the following tasks for the numerical investigations are summarised:

- Identification and calibration of appropriate material models for the numerical simulation by considering the multiaxial stress state in the grout layer and by use of appropriate experimental test results for the validation.
- Consideration of the cyclic degradation effects by implementation of appropriate approaches.
- Evaluation of the damage and degradation behaviour for alternating and pulsating compression loading.
- Determination of geometric and material strengths impact on the load bearing behaviour.
- Assessment of the load sequence effects to the fatigue behaviour.

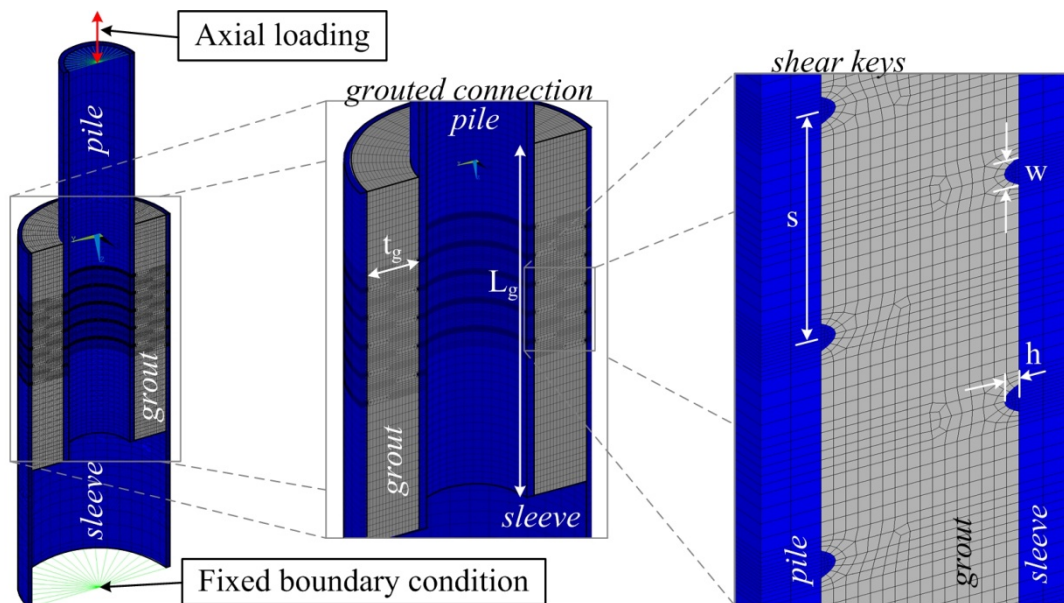


## 4.2 Model and Method Configuration

### 4.2.1 Finite element model

For the finite element analysis, different software programs are available, like Abaqus (2016), ANSYS (2014), Atena (2016) and Masa (2016). Based on the contact formulation, the variety of different available material models and the individual implementation of parametric based models, the finite element software ANSYS Academic Teaching Advanced version 14.5 is chosen for the numerical investigations. Besides, this software tool represents one of the most frequently used tools in the current design practice for grouted connections.

The numerical model is established by considering the geometric constitution of the test specimens TS01 to TS04, cf. chapter 3.2. Perfect geometric dimensions are considered by the finite element model, as the measured geometric imperfections of the test specimens are negligible small, cf. Appendix A. The load plate and adapter at the bottom are not modelled, as the increased calculation effort is not in a balanced benefit to the results. Hence, the model consists of the test specimen's steel tubes, pile and sleeve being equipped with discrete shear keys, and the grout layer between the steel tubes in the overlapping area, cf. Figure 4-1. Because of the axissymmetric construction, the grouted connection is modelled as half system in order to reduce the calculation effort.



**Figure 4-1. Three-dimensional numerical model of the grouted connection reflecting applied mesh and geometric parameters.**

For the steel tubes with shear keys and the grout layer, 3D solid elements, cf. Table 4-1, are selected to constitute the model. For the contact in the steel-grout interface the element types CONTA 173 and TARGE 170 are applied. This element pair enables a surface-to-surface contact formulation based on Coulomb's friction law. Consequently, a coefficient of friction has to be defined to consider an adequate frictional behaviour of the connection. Even though the majority of loads are transferred by the shear key interaction, the friction coefficient needs to be defined to guarantee the numerical stability and appropriately reproduce the bearing behaviour. With regard to latest investigations by Wilke (2014), Lochte-Holtgreven (2013)

and Lotsberg et al. (2013), a value of  $\mu = 0.4$  is assumed to represent an adequate static coefficient of friction. Adhesion is not considered by the model configuration. Moreover, the tangential and normal contact stiffness have a crucial impact on the axial global and local deformation behaviour of the connection. Following the experimentally measured relative displacements, the contact stiffness is calibrated. Table 4-1 represents the selected input parameters. Even though it is recommended to apply a relatively small contact tolerance factor, a too small value can cause penetration in the contact interface and a termination of the solver. Pre-investigations have revealed an optimal minimum value of 0.001 for the contact tolerance factor FTOLN.

**Table 4-1. Numerical model configuration in terms of element types and contact parameter.**

Element	Material model	Element type	Description/ values
Steel	Bilinear	SOLID 45	8-node 3-D solid element with 3 degrees of freedom at each node
Grout	Extended Drucker-Prager Cap Model	SOLID 185	8-node 3-D solid element with 3 degrees of freedom at each node; i.a. accounting for plasticity and stress stiffening
Contact	Coulomb friction	CONTA 173/ TARGE 170	surface-to-surface element accounting for contact or sliding interface action between 3-D solid elements; it allows for coulomb friction law, gapping is allowed.  Following settings have been used: tangential contact stiffness FKT = 1000 normal contact stiffness FKN = 0.01 contact tolerance factor FTOLN = 0.001

Preliminary convergence investigations are conducted to evaluate the ideal mesh size based on computational calculation time and accuracy of the results. A refined mesh is applied at the height of the shear keys, the overlapping area and at the top and bottom of the connection, cf. Figure 4-1. With regard to the test set-up, the bearing of the test specimen is realised by fixing the nodes at the bottom of the test specimen in all directions. The axial test load is applied at a central point connected by rigid beams to the pile flange to enable an uniform load transfer.

#### 4.2.2 Material models and characteristics

##### Steel

For the steel material a bilinear material model is used. Between measured material characteristics and the manufacturer data no large difference are observed. Having regard that the steel segments are separated and tested after the experimental large-scale tests are completed, it can be assumed that the steel material does not suffer from any plasticisation or damage during fatigue testing. The applied material parameters are presented in Table 4-2.

**Table 4-2. Material parameters for finite element calculation.**

Test specimen		TS01	TS02	TS03	TS04
Component		sleeve / pile			
Yield strength	$R_{eh} (f_y)$ [MPa]	447 / 360*	457 / 427*	471 / 360*	456 / 427*
Tensile strength	$R_{em} (f_u)$ [MPa]	549 / 450*	537 / 558*	575 / 495*	549 / 558*
Young's modulus	$E$ [MPa]	210'000**			
Poisson's ratio	$\nu$ [-]	0.3**			
*according to manufacturer's inspection certificates according to EEW (2011)					
**according to DIN EN 10225 (2009)					

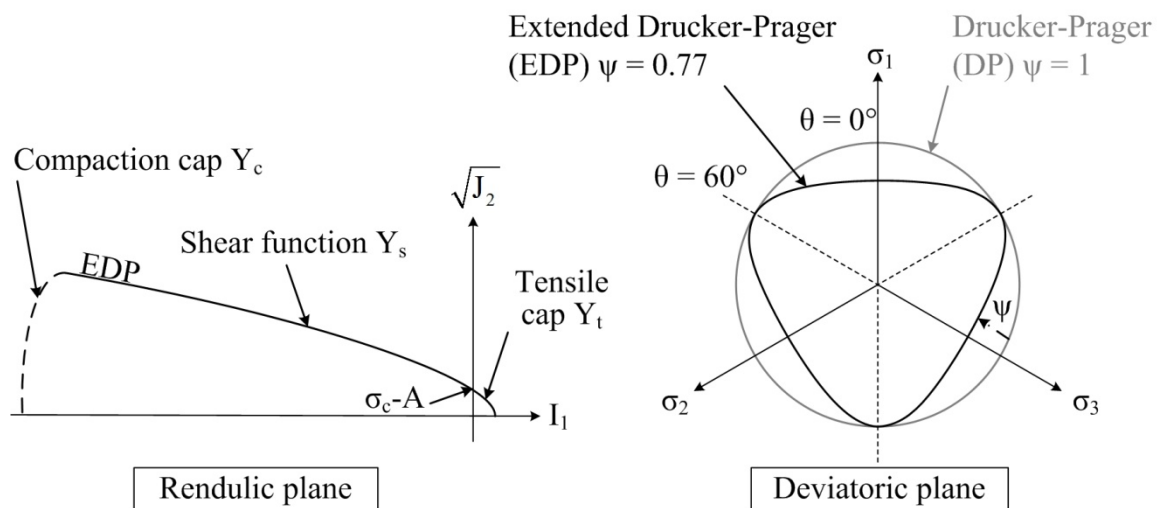
### Grout

For the input values describing the grout characteristics, material test results are used. Along with the start of the cyclic large-scale connection tests, grout strength parameters are determined frequently, cf. Table 4-3. Hence, the obtained uniaxial compressive cylinder  $f_{c,cyl}$  and cube  $f_{c,cube,75}$  strength as well as the tensile flexural  $f_{ct,fl}$  and uniaxial  $f_{ct}$  strength represent time-dependent material parameters. Nevertheless, for the Young's modulus  $E_{cm}$ , being tested only once after 28-days by three material test specimens, the time-dependent effects have to be considered for the individual grout-age ( $t$ ) by the function  $\beta_{cc}(t)$  according to Model Code 2010 (2012). In addition to the static Young's modulus  $E_{ci}(t)$ , the dynamic Young's modulus  $E_{dyn}$  is defined in accordance to the manufacturer's data information, BASF Masterflow<sup>®</sup> 9500 (2011) and Densit Ducorit<sup>®</sup> S2 (2010) to perform comparative calculations for the initial load stage.

**Table 4-3. Material parameters according to experimental testing.**

Test specimen		TS01	TS02	TS03	TS04
Material		BASF Masterflow <sup>®</sup> 9500		Densit Ducorit <sup>®</sup> S2	
Date		03.03.2014	11.06.2013	04.09.2014	02.06.2014
Grout-age	$t$ [dd]	98	117	63	76
Compressive strength	$f_{c,cube,75}$ [MPa]	152.75	144.66	128.35	138.52
	$f_{c,cyl}$ [MPa]	143.95	131.52	106.11	123.60
Tensile strength	$f_{ct,fl}$ [MPa]	18.29	19.12	14.97	14.71
	$f_{ct}$ [MPa]	8.0	8.4	6.6	6.5
Time effects	$\beta_{cc}(t)$ [-]	1.10	1.11	1.07	1.08
Young's modulus	$E_{cm}$ [MPa]	47'033	44'250	43'700	45'433
	$E_{ci}(t)$ [MPa]	49'274	46'569	45'181	47'255
	$E_{dyn}$ [MPa]	61'593	58'211	56'477	59'068

Even though the test specimens are exposed to an axial loading, the confining steel tubes provoke multiaxial stress states in the grout layer. Thus, the numerically applied material model should account for multiaxial stress states reflecting tensile and compressive behaviour properly. Different constitutive models exist, which have recently been adapted for high and ultra-high strength concrete, such as the Ottosen model by Speck (2008). Notwithstanding, these latest models are not implemented to commercial FE-software. The FE-software ANSYS contains a number of applicable material models for concrete, which are for instance the Drucker-Prager and the Willam-Warnke model. Even though the Willam-Warnke model is a five parametric material model describing a parabolic failure surface accounting for multiaxial stress states, the implemented version in ANSYS is highly unstable as own investigations have revealed. This can be explained by the negligence of any post-crack behaviour, which provokes an abrupt stiffness loss leading to convergence problems especially for models where many elements are exposed to high local stresses. Thus, the implemented version of the Willam-Warnke model is not applicable for the present investigation, as high stresses are inevitable for the intended application of cyclic loading. It is chosen to use the Drucker-Prager model, which was proven by Lochte-Holtgreven (2013) and Wilke (2014) to describe the global load bearing behaviour of grouted connections sufficiently. Nevertheless, the Drucker-Prager criterion overestimates the tensile and high compressive strengths. Thus, the yield surface represents merely an approximation of the real material behaviour by assuming a linear conical surface in the meridional plane and a circle in the deviatoric plane, cf. Figure 2-16 and Figure 4-2.



**Figure 4-2.** Yield surface of the Extended Drucker-Prager Cap plasticity model in the meridional plane (left) and deviatoric plane (right) compared to Drucker-Prager criterion based on ANSYS (2014).

However, the FE-software ANSYS offers a so-called Extended Drucker-Prager (EDP) material model with a tension and compaction cap. The Extended Drucker-Prager Cap plasticity model has a curved yield surface in the meridional plane and a triangle shape with smooth corners in the deviatoric plane, cf. Figure 4-2. Consequently, this material model represents an improved Drucker-Prager model, which is less sensitive to convergence problems than the Willam-Warnke material model and compensates inaccuracies of the

original Drucker-Prager model. The post-cracking behaviour is addressed by a defined plasticisation potential. The EDP failure surface is characterised by different functions, which are the tension cap  $Y_t$ , the compaction cap  $Y_c$ , the shear function  $Y_s$  and the Lode angle function  $\Gamma$ . The compaction cap function is equalised, because it lies outside the relevant stress states. Resulting yield function depends on the stress invariants  $I_1, J_2, J_3$  and the user defined cohesion yield parameter  $\sigma_c$ :

$$f(I_1, J_2, J_3, \sigma_c) = \Gamma^2 J_2 - Y_t(I_1, \sigma_c) \cdot Y_s^2(I_1, \sigma_c) = 0 \quad \text{Eq. 4-1}$$

The individual functions of the yield surface are described by:

$$\text{Lode angle function} \quad \Gamma(\theta) = 0.5 \cdot \left[ (1 + \sin(3\theta)) + \frac{1}{\psi} (1 - \sin(3\theta)) \right] \quad \text{Eq. 4-2}$$

$$\text{Tension cap} \quad Y_t(I_1, \sigma_c) = 1 - H(I_1) \cdot \left( \frac{I_1}{R_t \cdot Y_s(I_1, \sigma_c)} \right)^2 \quad \text{Eq. 4-3}$$

$$\text{Shear function} \quad Y_s(I_1, \sigma_c) = \sigma_c - A \cdot e^{B \cdot I_1} - \alpha \cdot I_1 \quad \text{Eq. 4-4}$$

At this  $\theta$  presents the Lode angle and  $H(I_1)$  the Heaviside step function. Remaining constants  $\psi, \sigma_c, A, B, \alpha, R_t$  depict user defined values, which have to be adjusted to the material strengths and the triaxial material behaviour. The value for  $\psi$  characterises the form of the yield surface in the deviator plane accounting for a reduced tensile capacity, cf. Figure 4-2. For detailed description, reference is made to the ANSYS (2013).

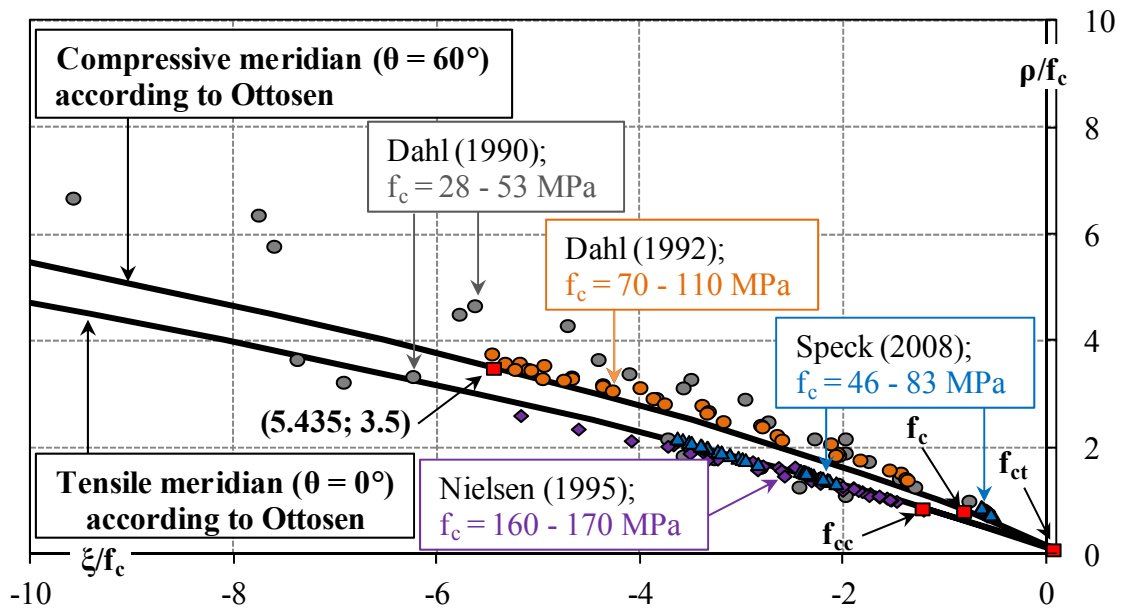
Similar to the Drucker-Prager material model, the EDP was originally developed for geomaterials, cf. Fossum & Fredrich (2000) and Foster et al. (2005). Consequently, the material model has to be calibrated for high strength grouts. Recent investigations by Lochte-Holtgreven (2013) have revealed that the Ottosen failure criterion describes the different failure states of grout in grouted connections adequately. In addition, it was proven by Chen (1982), Dahl (1992) and Speck (2008) by triaxial tests of high strength and ultra-high strength concrete that the Ottosen model describes the yield surface by a mathematical solution very well. Therefore, it is decided to use the Ottosen failure criterion according to Model Code 2010 (2012) and well-documented static strength test results on high strength concrete by Speck (2008) for the calibration of the EDP to the applied high strength grouts.

Initially the compressive and tensile meridian of the Ottosen failure criterion according to Model Code 2010 (2012) is determined for high strength grout materials with an uniaxial compressive strength of  $f_c = 141$  MPa and corresponding four representative calibration points:

1. uniaxial compressive strength  $f_c$ ,
2. uniaxial tensile strength  $f_{ct}$ ,
3. biaxial compressive strength  $f_{cc}$ , and
4. an additional point on the compressive meridian.

In addition to the calibration points 1 to 3, which depend on strength characteristics, the fourth parameter is chosen by Ottosen to  $(\xi, \rho) = (-5, 4)$  for normal concrete. Based on

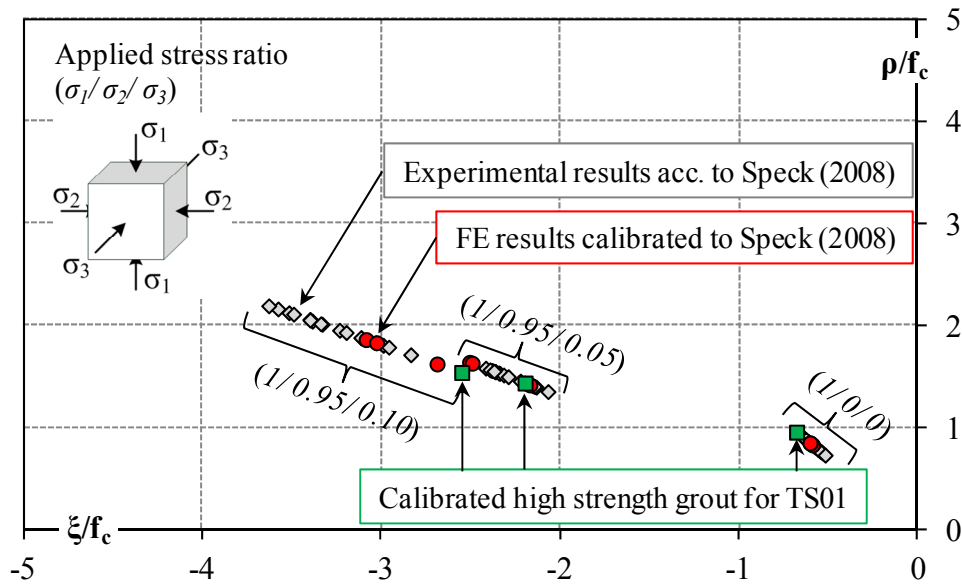
recommendations by Dahl (1992) for high strength concrete, the fourth value is defined as  $(\xi, \rho) = (-5.435, 3.5)$ , cf. Figure 4-3.



**Figure 4-3. Comparison of triaxial test results by Dahl (1990), Dahl (1992), Nielsen (1995) and Speck (2008) with the Ottosen failure criterion according to Model Code 2010 (2012).**

Figure 4-3 summarises experimental triaxial test results according to Dahl (1990), Dahl (1992), Nielsen (1995) and Speck (2008) for different concrete compressive strengths. The compressive and tensile meridian are derived for a high strength concrete with the uniaxial compressive strength of  $f_c = 141$  MPa by application of the Ottosen model according to Model Code 2010 (2012) and previous outlined calibration points 1 to 4. The illustrated Ottosen failure criterion complies very well with the provided test results, especially for the results by Dahl (1992) and Speck (2008) both representing high strength concretes. Although the test data by Nielsen (1995) seem to correlate with the tensile meridian, the results were derived for the compressive meridian. Depicted test data by Speck (2008) are selected for the calibration of the numerical material model, as this data set was attained by modern test equipment. Moreover, well-documented results for high strength concretes without fibres were achieved on the tensile and compressive meridian, cf. Figure 4-3.

Therefore, material input parameters for the EDP are calibrated by the triaxial cube tests conducted by Speck (2008). A cube with an edge length of 100 mm is modelled for recalculating three concrete strengths, which were tested by Speck (2008) at different stress ratios. The chosen stress ratios correspond to the compressive and tensile meridian of the Ottosen failure criterion, cf. Figure 4-3. In Figure 4-4 experimental and numerical results are plotted showing a good correlation. On the basis of these results, the relevant input parameters for the applied high strength grout of the test specimens are derived. Mean compressive strengths of the used materials constitute the basis for the calibration of the material model for the grout. The results for the grout cubes with the material of TS01 at different stress ratios are additionally presented by Figure 4-4 reflecting sufficient agreement with the scatter band of experimental results and thus with the failure criterion by Ottosen.



**Figure 4-4. Comparison of experimental triaxial test results according to Speck (2008) and calibrated numerical results for triaxial cube tests.**

For each grout material a calibration of the input parameters for the EDP material model is performed by comparing the element test results to the test results by Speck and the Ottosen failure criterion. Calibrated values are gathered by Table 4-4. Primarily the cohesion yield parameter  $\sigma_c$  and the shear envelope exponential coefficient  $A$  are of particular relevance as both reflect strength characteristics and influence the intersection of yield surface and abscissa, cf. Figure 4-2. Moreover, the shape parameter  $\psi$ , representing the ratio of tension to compression strength, forms the circular/triangle shape in the deviator plane. The yield surface equals a circle for  $\psi = 1$ , being representative for the original Drucker-Prager model, cf. Figure 4-2. Even though a compaction cap is not intended to apply, the corresponding material parameters  $X_i$  and  $R_c$  have to be defined. Thus, the intersection of the failure surface is defined by  $X_i$ , with the compaction cap being adjusted to a very large value, so that the cap becomes irrelevant for the calculations.

**Table 4-4. Calibrated input parameters for the EDP material model.**

Test specimen		TS01	TS02	TS03	TS04
Cohesion yield parameter	$\sigma_c$ [MPa]	150	140	125	135
Shear envelope exponent	$B$ [1/MPa]	0.004	0.004	0.004	0.004
Shear envelope exponential coefficient	$A$ [MPa]	141	132	118	131
Shear envelope linear coefficient	$\alpha$ [-]	0.1	0.1	0.1	0.1
Ratio of extension to compression strength	$\psi$ [-]	0.77	0.77	0.77	0.77
Compaction cap	$R_c$ [-]	1.0	1.0	1.0	1.0
Expansion cap	$R_t$ [-]	1.5	1.5	1.5	1.5
Compaction cap yield pressure	$X_i$ [MPa]	-1000	-1000	-1000	-1000

### 4.2.3 Calculation procedure

For the recalculation of the experimental tests and the subsequent parametric studies, a calculation procedure is used consisting of multiple steps. The numerical model and calculation procedure is developed to account for multiaxial stress states, triaxial strength of the high strength grout, cyclic degradation and stress dependent damage of the grout.

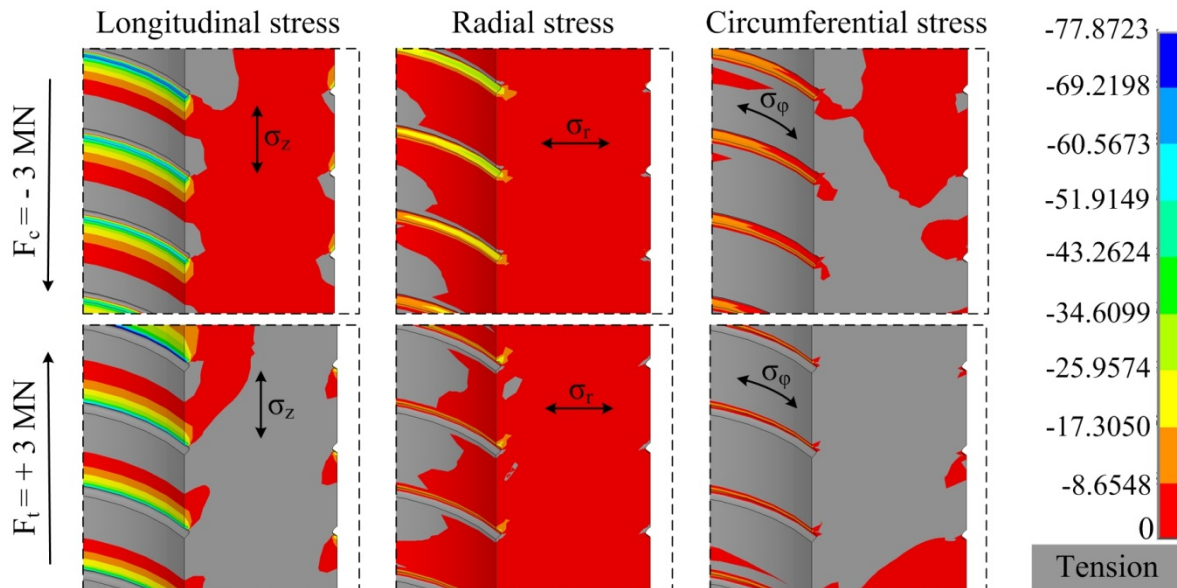
At first, it is focused on the validation of the numerical model configured as described in chapter 4.2.1 and 4.2.2 by determining the undamaged load displacement behaviour in the first load cycle of LS01 for each test specimen, cf. chapter 4.3.1. Numerical achieved global deformations, relative displacements and vertical strains are compared to the corresponding experimental results.

In a second step, the numerical calculation procedure is extended to consider the effect of repeated loading. As a result of the cyclic loading, a degradation of the grout material characteristics appears reflecting a reduced fatigue strength of the connection. Experimentally measured relative displacements reveal a stiffness reduction being accompanied by a strength decrease. Thus, for the numerical consideration of the fatigue behaviour being accompanied by cyclic degradation, the procedure has to account for reduced material parameters based on the cyclic loading. Lochte-Holtgreven (2013) developed an approach that enables to calculate the stress dependent damage for each grout element. On the basis of peak loads and corresponding numerical results, the maximum stresses for each element are determined and used to define the damage per grout element based on the applied number of load cycles and the uniaxial S-N curves for grout. In principle, this calculation procedure according to Lochte-Holtgreven (2013) is adapted, but substantial modifications and adjustments have to be performed, because Lochte-Holtgreven (2013) used different model configurations and established the implemented code for grouted connection being exposed to bending loads, thus reflecting a significantly different stress state in the grout layer.

To begin with, appropriate S-N curves have to be chosen and implemented for the damage calculation. For the selection of the S-N curve, the stress states have to be considered. These are significantly affected by the loading and the confinement effect of the steel tubes. In order to evaluate the appearing stress states without influences by any material plasticisation, a linear-elastic FE-calculation is performed and arising stress states for an applied tension and compression force are analysed, cf. Figure 4-5.

Figure 4-5 presents occurring longitudinal, radial and circumferential stresses for a compression load of  $F_c = -3$  MN and a tension load of  $F_t = +3$  MN. By colouring only the compression stresses and assigning the tension stresses the colour grey, the areas of tensile stresses are outlined. It becomes obvious, that the longitudinal stresses are exposed to a changing stress distribution strongly depending on the applied load direction, cf. Figure 4-5. In contrast, the radial stress plots depict compression stresses for both load situations. Moreover, it can be seen that, regardless of the load direction, large areas of tensile stresses arise in the circumferential direction. Even though in the longitudinal and radial direction compression stresses may be present, a tensile stresses in the circumferential direction occur, which may provoke radial cracks in the grout layer, cf. Figure 4-5 center.





**Figure 4-5. Comparison of different stress states for the grout layer being exposed to tension and compression force of 3 MN, coloured compression stresses and grey tension stresses.**

However, from the comparison it becomes clear that the triaxial stress state is highly influenced by changing values in the different directions depending on the applied load. Especially the presence of tensile splitting stresses in circumferential direction may influence the stress conditions due to local cracking. It results that the alternating load stages cause large stress reversals being composed of tension-compression or tension-tension stress states at the majority of elements. Merely adjacent to the shear keys pulsating compression stress states become relevant for the fatigue design.

From the evaluation of available cyclic triaxial tests of high strength concrete, cf. chapter 2.4.2, it can be concluded that a limited amount of tests address cyclic triaxial testing of high strength concrete. Especially for cyclic axial compression combined with transverse tension, a rare number of test results are currently available. Further research investigations are required for evaluating the cyclic triaxial behaviour of high strength concrete and grout. Nonetheless, investigations by Kupfer (1973) and Nelissen (1972) have proven that tensile induced failure for biaxial stress states is comparable to an uniaxial failure. Consequently, it is decided to apply available uniaxial S-N curves which were recently adapted for high strength concretes. Mathematical formulations of the uniaxial S-N curves according to Model Code 2010 (2012) are implemented, cf. Eq. 2-26 to 2-30. Alternative S-N curves are provided by DNV-OS-C502 (2012) for concrete at pulsating compression, alternating and pulsating tension stress states. The Model Code 2010 (2012) curves are preferred, because these have been recently modified for high strength concretes and are verified for load cycles up to  $10^7$ . Nonetheless, Lochte-Holtgreven (2013) has shown that both approaches might be applicable for high strength grouts.

By application of the uniaxial S-N curves, the impact of a triaxial increased compressive strength is omitted. In contrast, the EDP material model accounts for multiaxial stress states. Thus, combination of the uniaxial S-N curves with three-dimensional stress states determined on the basis of multiparametric yield conditions might cause inaccuracies. By referencing a

large triaxial maximum stress  $\sigma_{c,max}$ , obtained at grout elements by use of the EDP material model to the uniaxial fatigue strength  $f_{ck,fat}$ , a reduced applicable number of load cycles might be determined. One way to avoid this disagreement would be to account for triaxial S-N curves. But as long as no triaxial S-N curves for high strength concretes or grouts are available, cf. chapter 2.4.2, the application of uniaxial S-N curves represents a reasonable approach. Anyhow, a comparison with the experimental results is performed to evaluate the applicability of the uniaxial S-N curves.

In general the fatigue behaviour for concrete can be determined by S-N curves which reflect the endurable number of load cycles for a given stress state. On the basis of the applied number of load cycles and the stress related endurable number of load cycles, the damage value  $D$  can be evaluated by the Palmgren-Miner rule. For the aimed comparison of the numerical and experimental results, the Palmgren-Miner rule is applied after each load stage for determination of the damage  $D$ , so that any load sequence effects become irrelevant.

On the basis of the chosen S-N curves the element-based numerical implemented calculation procedure is modified in such that cyclic material strength and stiffness reduction is considered based on the determined damage  $D$ . The material strength reduction is based on the fatigue strength  $f_{ck,fat}$  formulation and related S-N relationship, while the stiffness degradation is performed on the basis of the damage  $D$ . According to Pölling (2000), cf. chapter 2.4.2, for an assumed isotropic material behaviour the stiffness reduction correlates with the damage  $D$ , cf. Eq. 2-25. As Göhlmann (2008) and Lochte-Holtgreven (2013) proved the applicability of this method for high strength concretes and grouts, the approach by Pölling (2000) is incorporated to the element based cyclic degradation of the material stiffness. Thus, the EDP material model and related material characteristics are amended by the modification of the grout stiffness and strength.

The developed calculation procedure, cf. Figure 4-6, accounts for EDP material model settings, adapts uniaxial S-N curves for concrete and considers a cyclic material degradation. Single load scenarios described by Markov matrices are used to define the input loads. The upper  $F_{u,i}$  and lower  $F_{l,i}$  load are established on the basis of mean load  $F_{m,i}$  and load range  $F_{r,i}$  for each load stage "i". In the basic step, non-linear finite element calculations are conducted with the basic numerical model of the grouted connection for the defined loads  $F_{u,i}$  and  $F_{l,i}$ . These basic numerical models allow to determine multiaxial stress states in the grout layer based on the adapted multiparametric material model. Initially resulting relative displacements  $u_{L7}$ , cf. Figure 3-7, are used for the validation of this basic model by the experimental results.

In the next step, for the post-processing a calculation procedure by Lochte-Holtgreven (2013) is adjusted for the present numerical model configuration. The post-processing code enables to identify the prevailing stress condition at each element, either tension or compression, based on the principle stresses. On the basis of the stress state and the leading principle stress, the S-N curve is selected and corresponding endurable number of load cycles  $N_{i,j}$  are specified, cf. Figure 4-6. By taking into account the applied number of load cycles  $n_i$ , introduced by the Markov matrix, and the determined endurable number of load cycles  $N_{i,j}$ , for each element the resulting damage  $D_{i,j}$  can be obtained.

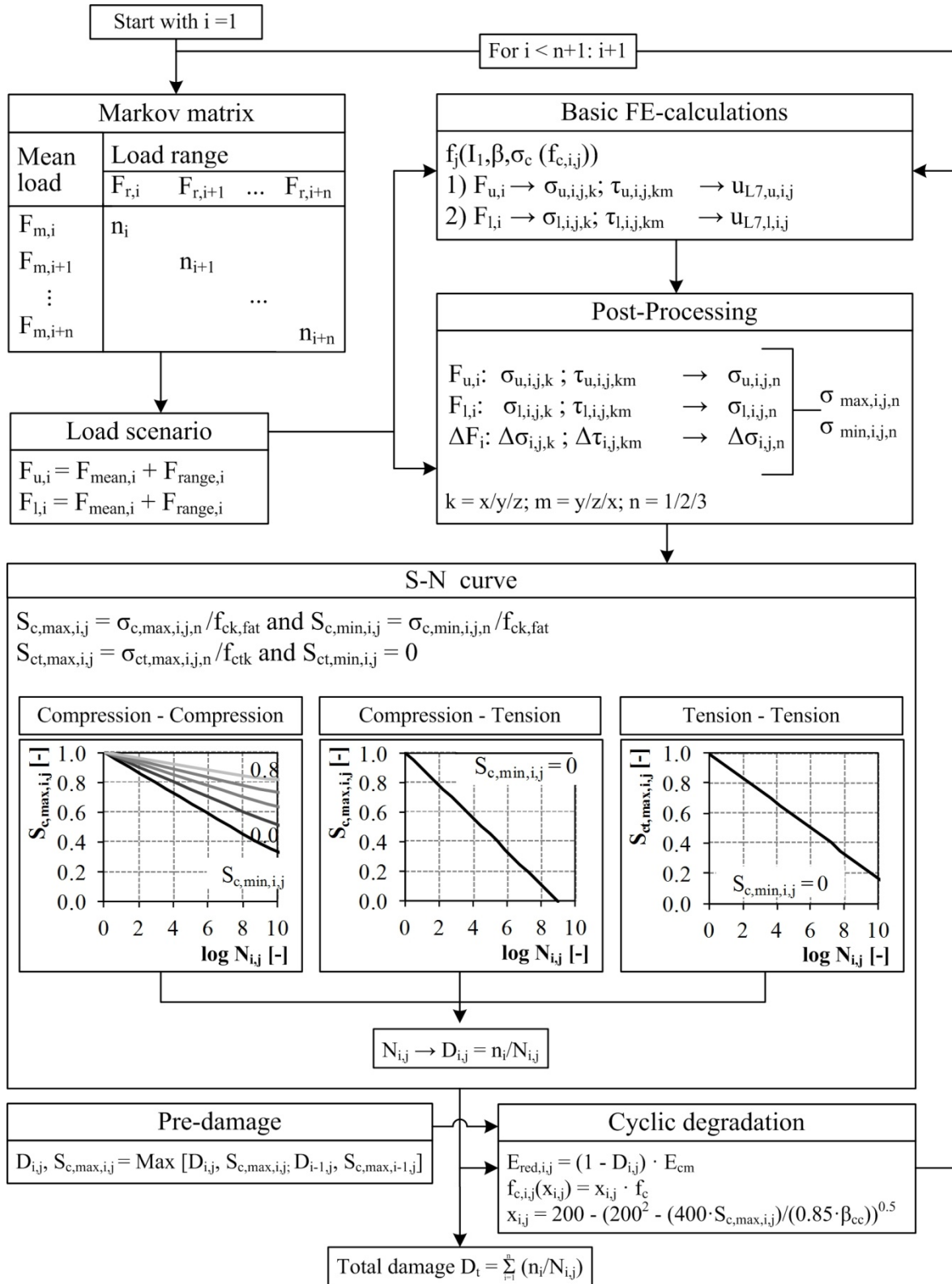


Figure 4-6. Calculation procedure to cover the fatigue behaviour by the numerical model.

As the cyclic induced damage is associated by a material degradation, a modification of the material strength and material stiffness is implemented within the subsequent calculation step. The material strength reduction is covered by the cyclic strength degradation parameter  $x_{i,j}$ , which is defined by the S-N curve related compressive fatigue strength, cf. Figure 4-6.

The reduced grout stiffness is determined on the basis of the element based damage  $D_{i,j}$  and the mean elasticity modulus. By taking the cyclic degradation of the material properties per element into account, the basic numerical model is recalculated. In order to allow for a procedure covering different load levels in variable sequence, the method is refined by introducing a restrictive condition for pre-damage consideration, cf. Figure 4-6. In the end the overall damage for each element becomes assessable. Thus, a calculation procedure is developed and implemented, which enables to determine the fatigue performance of grouted connections with numerical simulations by accounting for cyclic degradation and multiaxial stress states in the grout annulus. The applicability and its shortcomings are addressed in the following by comparing numerical and experimental results.

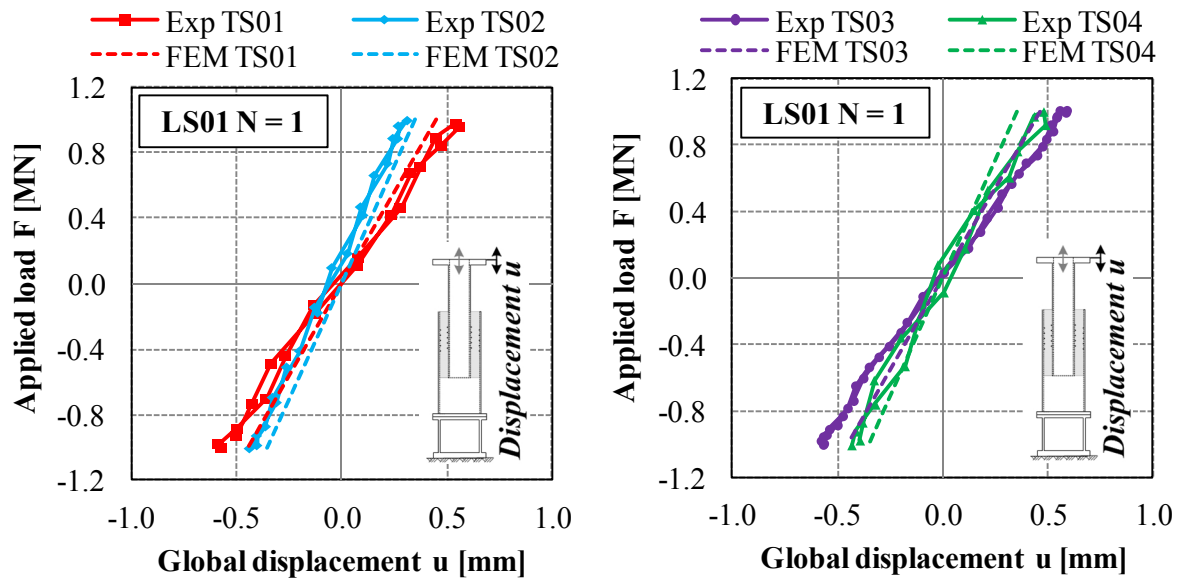
The numerical calculation procedure does not allow to consider vertical moved pile positions being induced by accumulated load cycles, as the static numerical simulation starts from the origin for every calculation. Nevertheless, by the calculation procedure it is possible to account for cyclic movements by a cyclic reduced material stiffness and strength used as input values for the repeated static numerical calculations. A comparable procedure is introduced by Achmus et al. (2009) for the degradation of the soil stiffness for monopile foundations due to cyclic loading. Referring to Achmus et al. (2009), the previous calculation procedure is not changed. Hence with increasing load cycles, a stiffness and strength reduction corresponding to the damage  $D$  is considered by the numerical simulation.

### **4.3 Validation of the Numerical Model**

#### **4.3.1 Global deformation behaviour**

Comparison of the measured and numerically derived global displacements for the initial load cycle of the performed test specimens facilitates to validate the static numerical model. Figure 4-7 depicts the comparison of experiment (Exp) and finite element model (FEM) results for the test specimens TS01 to TS02, left, and for the test specimens TS03 and TS04, right.

For all four test specimens, a good correlation between numerical and experimental achieved results is presented by the illustrated global deformation behaviour. Observed deviations between numerical and experimental achieved displacements are mostly less than 10% and can thus be assigned to be insignificant. The numerically derived load-displacement curves reveal for all four test specimens a nearly linear-elastic behaviour for the starting point of testing, which coincides with the experimental test results. The test specimens with a larger grout annulus, TS01 and TS03, are characterised by a smaller stiffness resulting in larger global displacements than the test specimens TS02 and TS04.



**Figure 4-7. Comparison of experimental and numerical global load-displacement behaviour for the initial load cycle  $N = 1$  of the first load stage LS01.**

Furthermore, the material strength variation between TS01, being filled with BASF Masterflow<sup>®</sup> 9500, and TS03, being filled with Densit Ducorit<sup>®</sup> S2, have a slight influence to the appearing initial load-displacement. Similar conclusion follows from a comparison of the results for TS02, BASF Masterflow<sup>®</sup> 9500, and TS04, Densit Ducorit<sup>®</sup> S2. Thus, the numerical models cover the individual behaviour of the test specimens satisfyingly. It can be concluded, that the chosen numerical model configuration enables to determine the load-displacement behaviour of the test specimens appropriately.

#### 4.3.2 Relative displacements

Complementary to the global deformation behaviour, the measured local relative displacements are compared to the numerical results at corresponding locations. The experimental relative displacements are measured at three locations in circumferential direction of the test specimens at two different vertical levels, L1V at the top, and L7V at the bottom inside the test specimen, cf. Figure 3-7. A mean value of the experimental achieved displacements is used for the comparison between numerical and experimental results. In consequence of the laser adaptation to the steel tubes being arranged in a distance of 100 mm to the measuring level, a local difference appears between the point of laser adaptation and the measuring level. For the comparison of experimental results to numerical displacements, values originating from identical locations are considered. Strain gauge measurements at the outside of the pile and the sleeve enable to ensure that the results are not affected by the difference between adaptation point and measuring level.

Figure 4-8 presents the relative displacements registered for all four test specimens at L7V for the initial load cycle in LS01. Complementary to these results, numerical and experimental achieved relative displacements at L1V are enclosed in Appendix D.1.

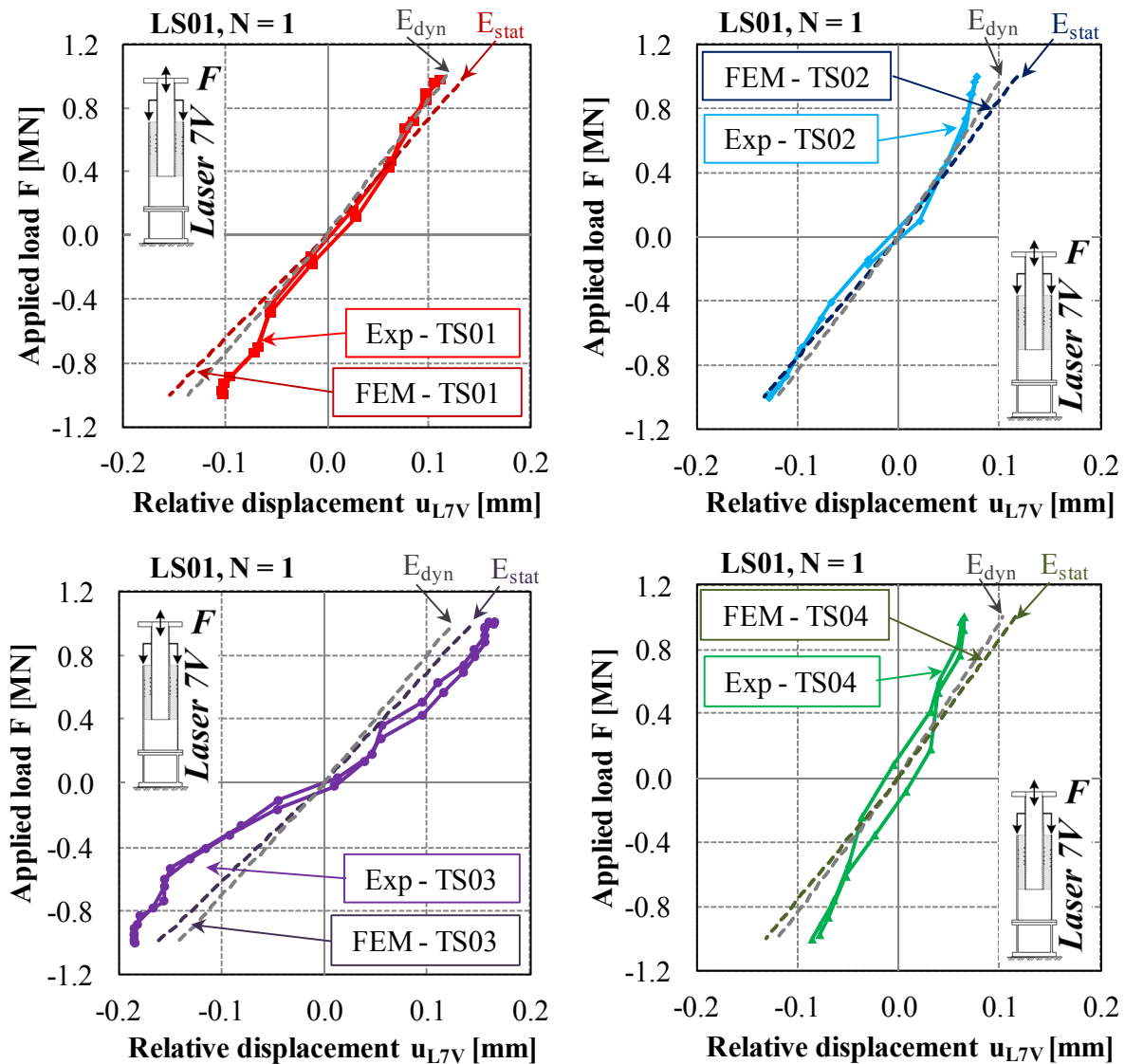


Figure 4-8. Comparison of numerical and experimental derived relative displacements at L7V for LS01, N = 1.

The depicted numerical results are achieved based on two different elasticity modulus for the grout material. On the one hand, calculations are performed accounting for the static modulus of elasticity  $E_{stat}$  being identical to  $E_{ci}(t)$  in Table 4-3, of the grout material and on the other hand for a dynamic Young's modulus  $E_{dyn}$ , cf. Table 4-3. Consideration of the dynamic stiffness value is conducted for comparative purposes. Due to the viscoelastic deformation behaviour of grout and concrete, a larger stiffness might be present in the large grout layer at the initial state of loading due to the very small strains. Even though the stiffness reduces generally with decreasing load frequency, according to Winkler (2010) and Meyer (2007) this effect diminish substantially for high strength concrete. In principle,  $E_{dyn}$  presents an upper bound value for the elasticity modulus, while  $E_{stat}$  represents the lower bound value, cf. Winkler (2010). Comparison of the relative displacements reveals that the application of the dynamic elasticity modulus leads to a stiffer load-displacement behaviour, which reflects at some test specimens a slight improvement of the correlation, whereas other show the opposite trend. The dynamic modulus is by about 20% to 25% larger than the static value. In contrast

to this difference, the resulting stiffness variation of the test specimens is less than 10%, cf. Figure 4-8. Thus, the impact of the dynamic elasticity modulus is rather small. As it is expected that the stiffness reduces with increasing load level and accumulated number of load cycles, the lower bound value  $E_{\text{stat}}$  is used for further numerical calculations.

By comparing the experimental to the numerical achieved relative displacements, cf. Figure 4-8, it can be concluded, that the numerical model accounting for  $E_{\text{stat}}$  behaves less stiff than three of the test specimens. The softer behaviour of the test specimen TS03 is assumed to be caused by material inhomogeneities of the grout. As the deviations between numerical and experimental achieved relative displacements are below 20% for the majority of results, the numerical model appropriately resembles the load displacement behaviour with respect to the local arising displacements at the grouted connection.

### 4.3.3 Strain development

Beside the global deformation behaviour and the relative displacements, local strains are used to validate the numerical model. Figure 4-9 presents the comparison of numerical and experimental results for each test specimen for  $N = 1$  load cycle at the maximum compression force in LS01. Correlating results for the maximum tension loading are included in Annex D.2.

The experimental results origin from measured longitudinal strains at different vertical positions at pile and sleeve, cf. chapter 3.3.3 and 3.4.4. Depicted experimental values in Figure 4-9 reflect mean values resulting from strain gauge measurements at the circumferentially arranged three vertical measuring lines at  $0^\circ$ ,  $120^\circ$  and  $240^\circ$ . In order to outline the strain development along the load transfer, strains are plotted corresponding to their vertical position at sleeve or pile from top to bottom at the grouted connection. It is differentiated between the strain development at the pile, marked by darker coloured lines, and at the sleeve, marked by lighter coloured lines. In addition to the strain gauge position at sleeve and pile, the area of the shear keys is outlined. To allow for a comparison, numerical results are presented Figure 4-9 by a dashed line and experimental results by a solid line.

The numerical derived strains in Figure 4-9 follow similar patterns to those recorded from the tests, displaying a longitudinal strain decrease from top to bottom at the pile and in turn a increase at the sleeve. It results a load transfer from the pile to the sleeve by the grouted connection, whereby the majority of loads are transferred in the area of shear keys. Apart from the coincident load transfer, the numerical results are nearly identical to the experimental results. Deviations appear barely at a few strain gauge positions. The fairly well correlation of calculated and measured strains induced by the peak compression load at the first load cycles in LS01 evidently shows that the numerical model configuration describes the load bearing behaviour of the grouted connection very well. Similar accordance is derived for the tensile induced strains, cf. Annex D.2.

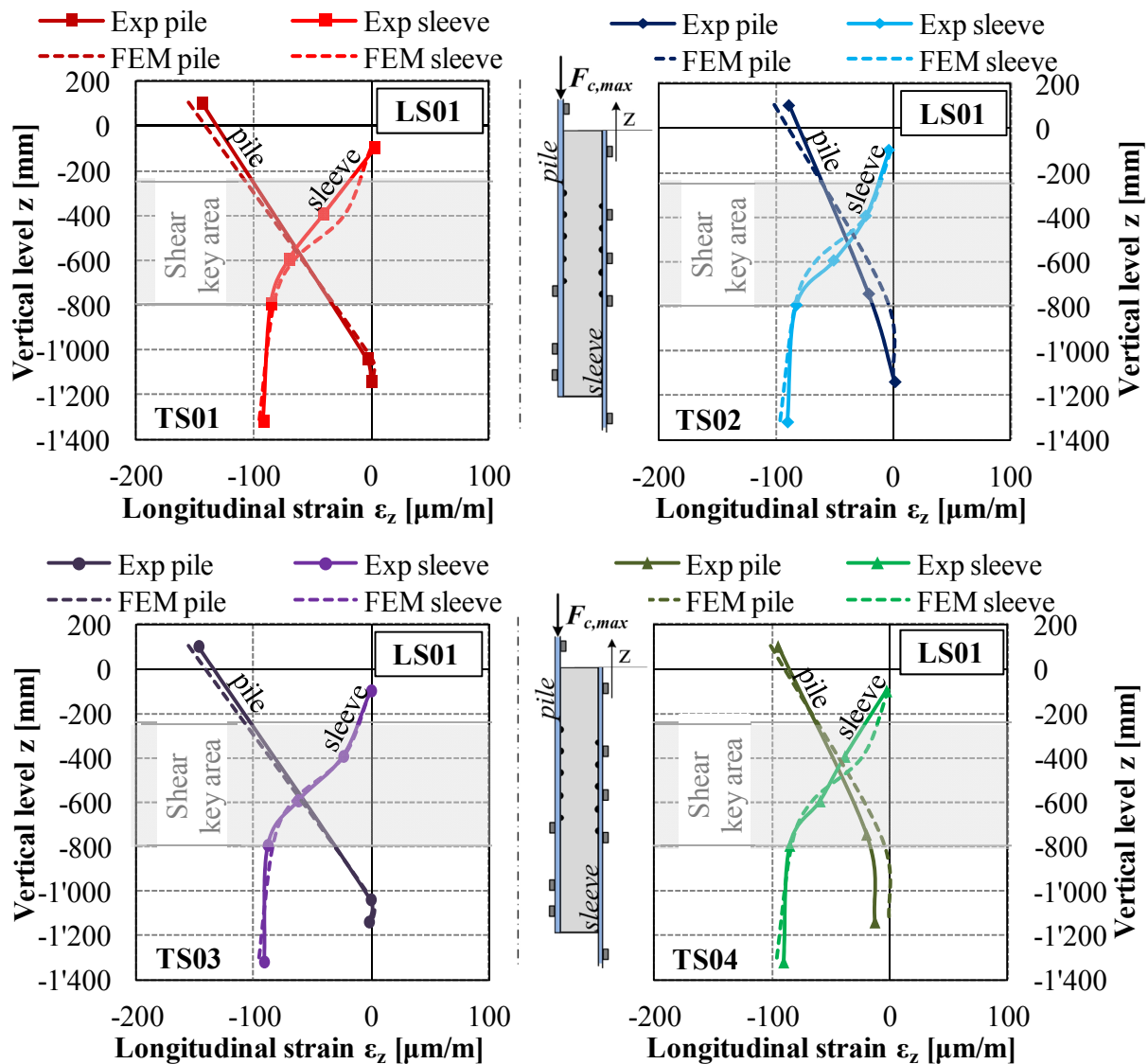


Figure 4-9. Comparison of numerical and experimental derived longitudinal strains for the peak compression load of  $F_{c,max} = -1$  MN in LS01,  $N = 1$ .

The comparison of the global load-displacement behaviour, the relative displacements and vertical strain development evoked by the first load cycle in the first load stage, evidently depicts a good correlation of numerical and experimental results. Thus, it can be concluded, that the individual finite element models are validated for the static initial load situation. The numerical model with the present configuration can be used for parametric studies, evaluating significant impact factors resulting from the grout material and geometry, cf. chapter 4.4. Nonetheless, the validation is limited to the static initial load scenario so far. The validation is extended in the subsequent chapter to cyclic impacts introduced by the implemented approach outlined in chapter 4.2.3.

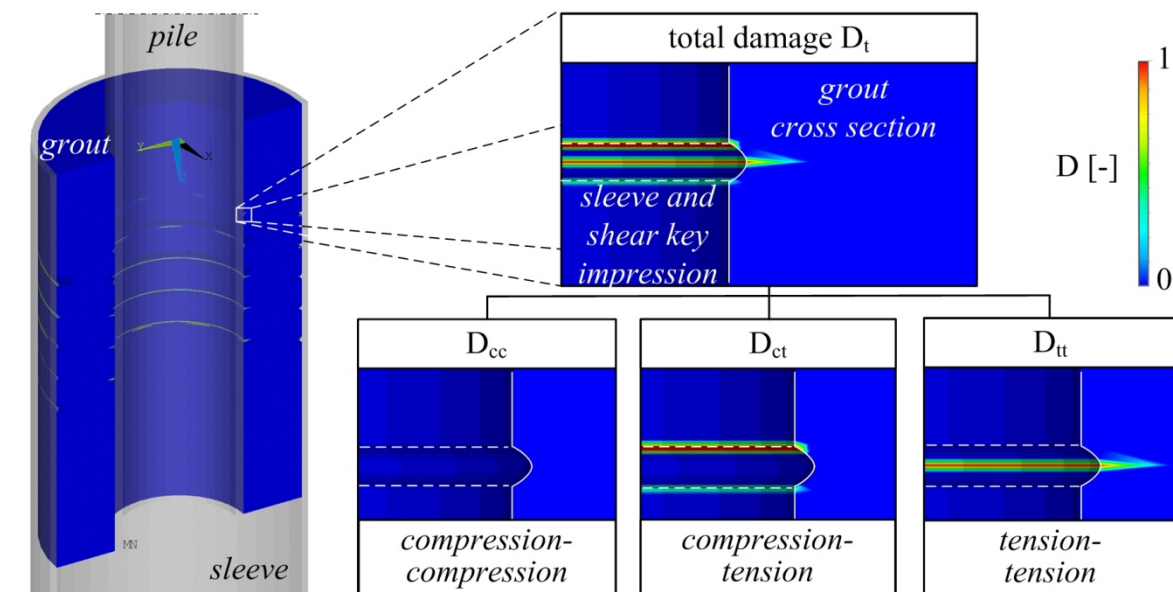
#### 4.3.4 Damage and cyclic degradation

The experimental tests prove that repeated forces and the stepwise increased test loads provoke cracking and crushing in the grout layer of the connections. The damage process is documented by changing load-displacement curves indicating a stiffness degradation for



repeated loading. These effects are considered numerically by implementation of the cyclic degradation factors and calculation procedure introduced in chapter 4.2.3.

By using the above described method, cf. chapter 4.2.3, which accounts for the varied stress states caused by the maximum compression and tension loads, it is possible to assess the damage  $D$  induced by the individual stress states. Thus, the damage caused by compression-compression  $D_{cc}$ , by compression-tension  $D_{ct}$  or tension-tension  $D_{tt}$  stress states can be located and evaluated. Figure 4-10 depicts the damage caused by the three stress states exemplarily for a shear key at the grouted connection with large grout thickness. The coloured damage  $D$  is associated to a value from 0 to 1.0, whereby 1.0 is identical to a damage of the element. That means local arising stresses in combination with the applied number of load cycles provoke local damage of the grout elements on the basis of the uniaxial S-N curves. Displayed results in Figure 4-10 correspond to the alternating load stage LS01. Arising stress related plots reflect that, pulsating compression stress states cause no significant damage for this load stage. As it can be seen, the damage appears at the shear key tip by predominant tensile stresses and at the weld transition of the shear key by a reversal stress state. These findings correlate with the observed crack initiation at the shear key tip and the crushed grout at the weld transitions at the opened test specimens, cf. Annex B.4.



**Figure 4-10. Achieved damage  $D$  components depending on the stress state at TS01 for LS01,  $N = 100'000$ .**

In order to evaluate the developed and implemented damage calculation procedure by the experimental test results, the focus is set on the load-displacement behaviour. The cyclic induced modification of the load-displacement behaviour is presented in the following by depicting the relative displacements for the initial and last load cycle of each applied load stage. The numerical achieved results are compared to the experimental measured values. For the purpose of covering a wide range of systems, representing the different applied grout materials and the varied grout thickness, achieved results for the test specimens TS01 and TS04 are used, cf. Figure 4-11.

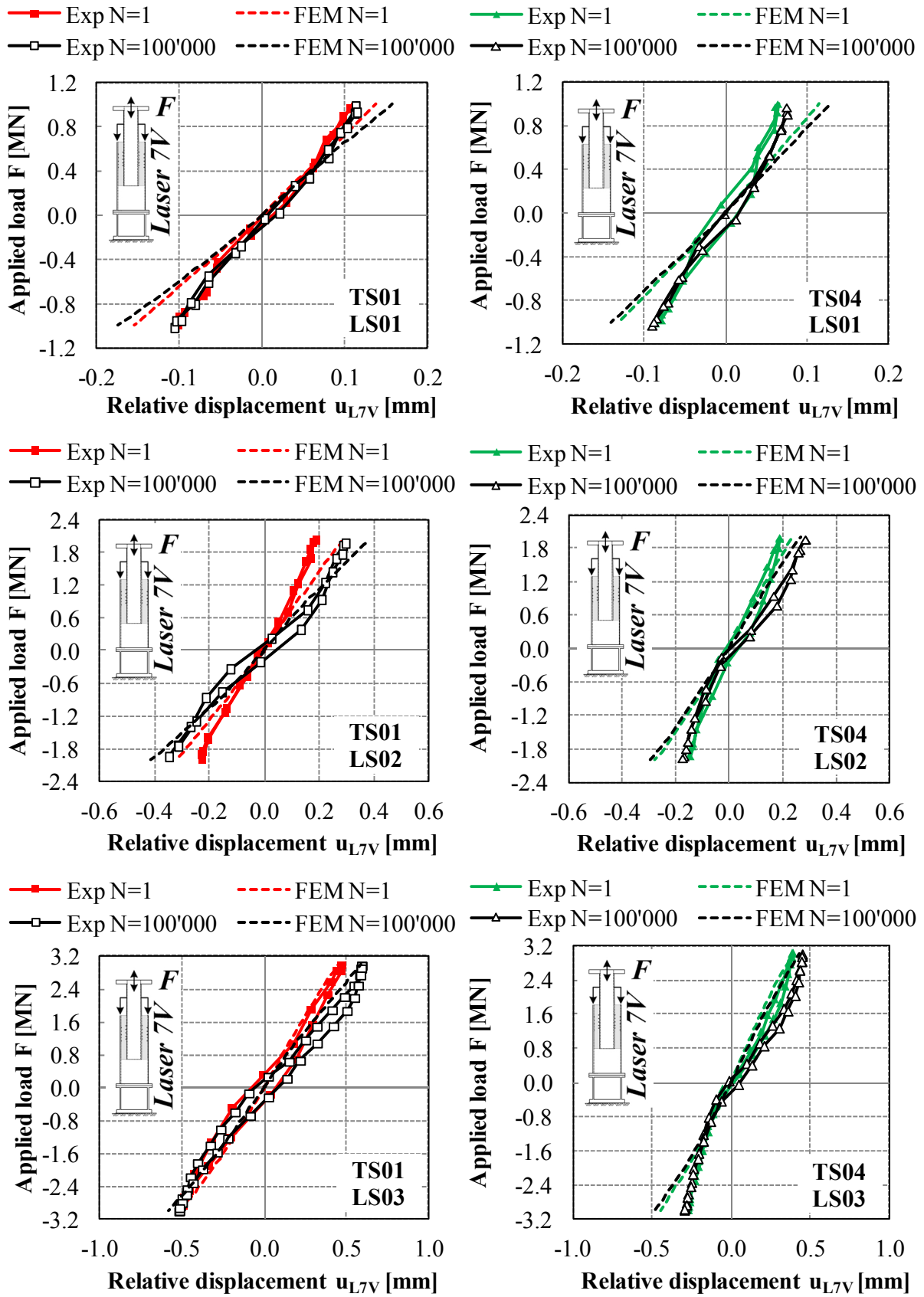


Figure 4-11. Comparison of numerical (FEM) and experimental (Exp) derived relative displacements at L7V for TS01 (left) and TS04 (right) for N = 1 and N = 100'000 in the load stages LS01 to LS03 including cyclic degradation effects.

Figure 4-11 reflects the relative displacement recorded for the alternating load stage LS01 to LS03. On the left hand, the data derived from the test specimen TS01 with a larger grout annulus filled with the BASF Masterflow<sup>®</sup> 9500 are depicted. Contrary, on the right graphs the values for the test specimen TS04 with a smaller grout annulus filled with Densit Ducorit<sup>®</sup> S2 are illustrated. The coloured lines are identical to the first load cycle  $N = 1$  while the black lines correspond to  $N = 100'000$  load cycles.

The numerical achieved relative displacements, cf. Figure 4-11, reflect especially for the test specimen with the larger grout annulus TS01 progressively increasing relative displacements. The stepwise increased loads and the number of load cycles provoke enlarged relative displacements for LS01 to LS03 at the FE model and at the test specimen TS01. It becomes obvious by Figure 4-11, that the growth of the relative displacements during each load stage agrees very well for all three alternating load stages. Moreover, for the stepwise increased load, an improved consistency can be observed for the maximum relative displacements.

Even though the experimental test specimen reflects a stiffer load-displacement behaviour than the numerical model during the first load stage LS01, it can be concluded that the numerical consideration of the cyclic degradation leads to coincident results with the experimental tests. Illustrated load-displacement hysteresis of the test specimen TS01, cf. Figure 4-11, reflect a non-linear behaviour with increasing cyclic loading, which is indicated by the widening of the hysteresis loop representing substantial damage and plasticisation of the grout.

For the test specimen with the smaller grout annulus TS04, the numerical as well as the experimental obtained relative displacements in Figure 4-11 increase only slightly with the accumulated number of load cycles and ascending loading. Similar to TS01, the numerical model overestimates the relative displacements in the first load stage compared to the experimental measured values. The difference between numerical and experimental results remains throughout the alternating load stages LS01 to LS03. However, the growth of the relative displacements within each load stage is about the same size for the numerical model and experimental tests. Moreover, for the tensile induced relative displacements, the experimental results indicate a stiffness reduction, which corresponds to the numerical results. Hence, the numerical considered stiffness degradation and strength reduction reproduces the cyclic degradation of the test specimen adequately. In view of the compression induced relative displacements a less pronounced degradation can be observed at TS04. As a result of pile expansion induced by compression loads and the additional activated shear key pair, the corresponding relative displacement values are less than the tensile related displacements.

Comparison of the numerical results for TS01 and TS04 reveals that the load-displacement behaviour differs individually for the varied connections. Thus, the consideration of cyclic reduced stiffness and strength characteristics by the FE-model calculations lead to progressively increasing relative displacements, which coincide considerable well to the displacement increase documented from the experimental investigations. It is concluded from the analysis of the alternating load stages that pre-damage from previous load stages and accumulated damage during one load stage are predicted reasonable by the developed

numerical calculation procedure. The fact that the FE-model reacts less stiff to the applied loads than the test specimen depicts the conservative character of the analysis.

Equally to relative displacements appearing in the alternating load stages, Figure 4-12 presents the relative displacements observed for the numerical and experimental connection for the pulsating compression load stages LS04 to LS06. The stepwise increase of the applied load is depicted from top to bottom in Figure 4-12. Likewise to the previous comparison, results for larger grout annulus at TS01 are depicted by the left graphs and results for TS04 are illustrated by the right graphs.

For both test specimens, the development of the relative displacements demonstrates a gradual movement of the pile into the sleeve, cf. Figure 4-12. From the experimental results it can be concluded that the damage process is contrary to the alternating load stages, presented by a progressive displacement growth instead of a stiffness degradation.

Comparison of the FE-results with the experimentally documented relative displacements shows that the numerical consideration leads to significantly larger relative displacements, cf. Figure 4-12. The numerically achieved displacements are up to 100% larger than the measured relative displacements at the test specimens. This difference is caused by the material specific behaviour, especially by the behaviour of the damaged grout material in the tests. Even though the grout material is crushed and damaged by previous load stages, the material remains inside the connection. Large compression stresses provoke an expansion of the inner pile against the grout layer. Consequently, the crushed grout is exposed to compression stresses transferring the loads. Moreover, cracks are closed and the crack surfaces are able to transfer loads by their interface shear capacity. Further crushed grout particles may change their position evoking new interlocking. In order to account for the impact of particle interlocking discrete crack growth would be required to be implemented. The current material model does not account for any additional load transfer by shear capacity of crack surfaces nor does the damage calculation distinguish between an opening or closing effect. Moreover, the Extended Drucker-Prager material model estimates a post-crack behaviour by ideal plasticity. In order to account for an increased load bearing capacity by crack interlocking, future material models may account for particle movement and shear transfer by crack surfaces. In addition, consideration of triaxial S-N curves, which need to be developed for high strength concretes, might improve the damage calculation further. Present uniaxial S-N curves underestimate the fatigue behaviour of the confined high strength grout. By referring arising stresses to the uniaxial strength and applying the uniaxial S-N curves to determine the endurable number of load cycles, the actual fatigue strength of the confined high strength grout might be substantially underestimated.

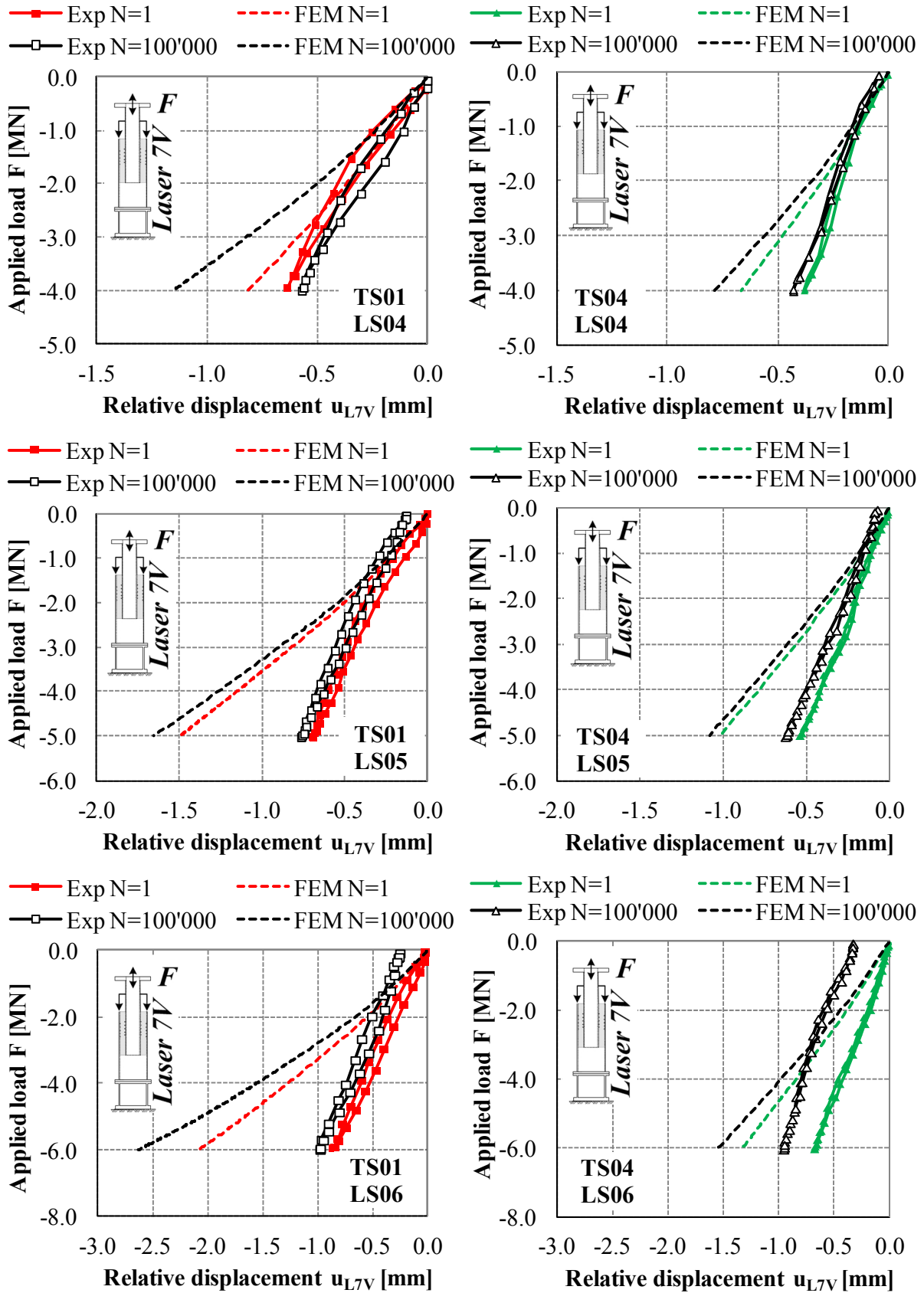
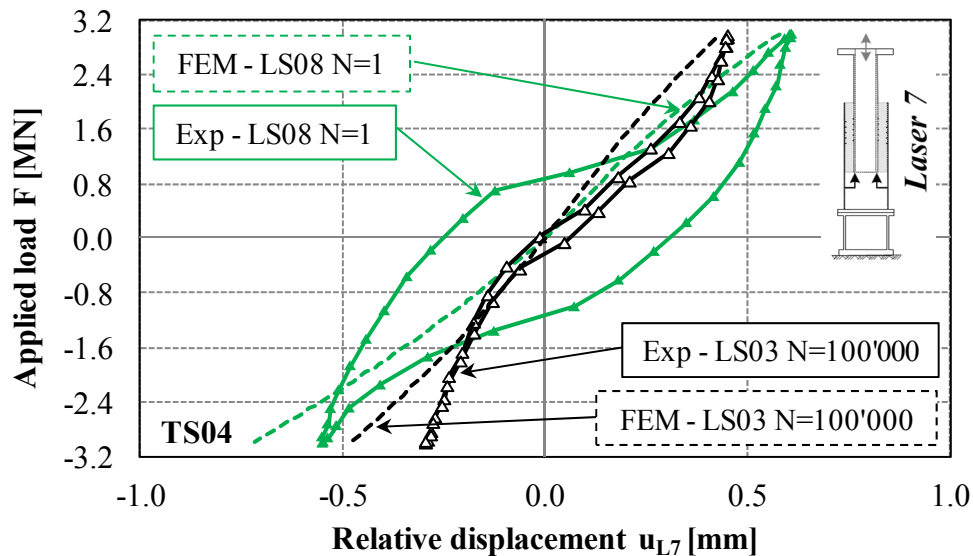


Figure 4-12. Comparison of numerical (FEM) and experimental (Exp) derived relative displacements at L7V for TS01 (left) and TS04 (right) for  $N = 1$  and  $N = 100'000$  in the load stages LS04 to LS06 including cyclic degradation effects.

As the interlocking of the crushed and cracked grout material is not taken into account, the ascending loads and load cycles provoke an increasing relative displacement caused by damage growth. Although the individual values of the numerical and experimental results do not correspond for the pulsating compression load stages, a comparison of the last alternating load stage LS08 with the alternating load stage LS03 reflects whether the cyclic degradation procedure is, notwithstanding, taken into account accurately. In Figure 4-13, appearing relative displacements for the last load cycle  $N = 100'000$  of LS03 and the initial load cycle  $N = 1$  of LS08 are summarised.

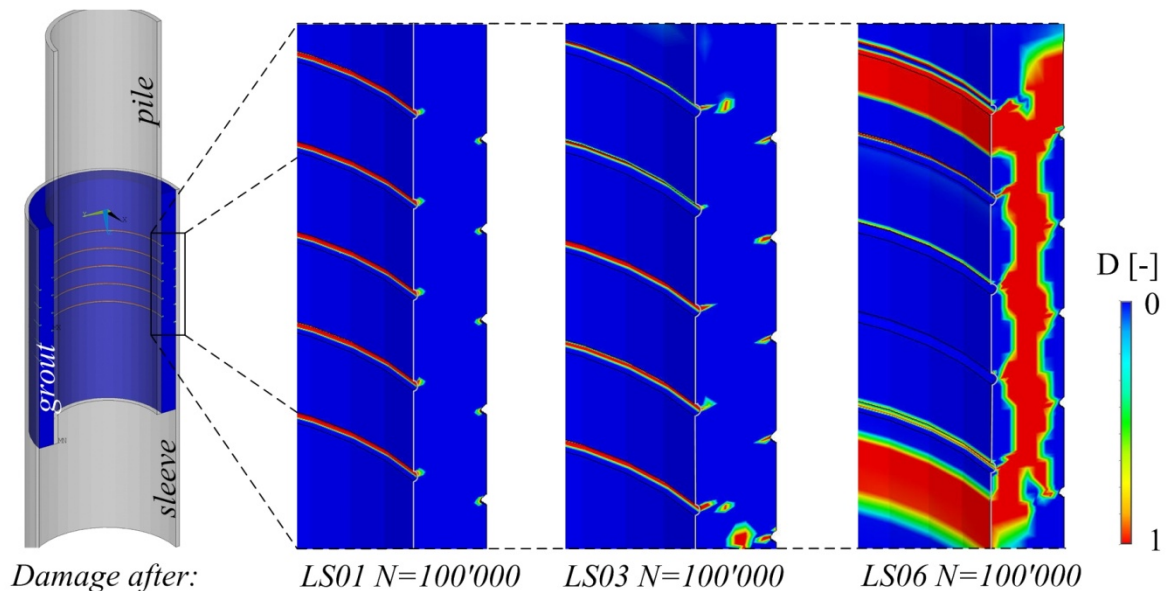


**Figure 4-13. Comparison of numerical and experimental derived relative displacements at the end of LS03 and at the beginning of LS08 for TS04.**

By contradicting the load hysteresis of the initial load cycle in LS08 to the last load cycle of LS03, the load-displacement behaviour can be analysed by identical load levels. Consequently, any pre-damage effects induced by the pulsating compression load stages LS04 to LS07 become visible. As evident by Figure 4-13, the load-displacement curve for the test specimen clearly indicates an increased relative displacement for the maximum compression and tension force of 3 MN. Furthermore, the hysteresis shows a considerably wider loop at LS08 than at the end of LS03. From the comparison of the experimental results, it becomes evident that the pulsating compression load stages increase the damage, even though the stiffness during these stages reflects an ostensible increase, cf. chapter 3.4.3. Although the numerical procedure shows a strong stiffness reduction during LS04 to LS07, the FE-results for the alternating LS08, cf. Figure 4-13, comply fairly well with the experimental results. Especially for the tensile induced relative displacements, a particular good correlation can be observed for numerical and experimental results. The compressive induced relative displacements for the numerical model are overestimated by 20% at LS08 and likewise at LS03. Thus, the displacement growth induced by compression corresponds well. Obviously, the numerical calculation procedure accounts adequately for cyclic degradation effects during the pulsating load stages, even though the relative displacements within the pulsating compression load stages are substantially overestimated. Increasing load cycles and stress states cause a damage of the grout material which results in a stiffness and strength

degradation. Therefore, the relative displacements for LS08 are larger than occurring at LS03. It can be concluded that the implemented cyclic degradation procedure accounts reasonably for the appearing damage.

Figure 4-14 displays selected numerical plots reflecting the total damage derived for the test specimen TS04.



**Figure 4-14. Damage growth for the test specimen TS04 with small grout annulus at selected load stages LS01, LS03 and LS06.**

From Figure 4-14 it can be seen that the stepwise increased loads and load cycles evoke a growing damage in the grout layer. Substantially high stress concentrations at the weld transition provoke damage. These stresses can be linked to the grout wedge cracking, which is observed at opened test specimens, cf. chapter 3.4.7. The damage at the shear key tip correlates well with the crack initiation of compression struts at the opened test specimens. Anyhow, incrementing the load level induces enlargement of the damage at the numerical model. The centrally displayed damage plot in Figure 4-14 outlines crack growth at the top shear key and even more pronounced at the lower shear key. Application of the ascending pulsating compression load causes further damage, which reveals a significant grout degradation by the end of load stage LS06. Arising damage pattern develops in between the shear keys. Although the observed cracking at the test specimens clearly show defined compression strut cracking, the smeared crack approach displays the failure behaviour initiated by compression strut failure. Therefore, it can be concluded from the comparison of numerically derived results and the damage at the test specimens that the implemented calculation approach accounts for the appearing damage in the grout layer in an appropriate manner.

## 4.4 Parametric Studies

### 4.4.1 Model configuration

In order to identify the impact of the grout thickness, the grout material strength, the interface conditions and the load sequences, previous validated numerical models are harmonised with respect to the applied materials. For the validation of the numerical model by the experimental test results, it is indispensable to adopt strength and stiffness values identical to the test specimen. For the sake of a parametric study, these values are adjusted to two materials: material A being representative for the tested materials and material B covering a material with a lower strength and stiffness. Both materials are characterised by their compression strength  $f_{ck,cube}$ , tensile strength  $f_{ct}$  and mean Young's modulus  $E_{cm}$ . Since the main objective of the investigation deals with the effect of different grout thicknesses, this geometrical factor is considered by model 01 and model 02. Reference for both geometrical configurations represents the two different tested specimen geometries, cf. chapter 3.2.1. Consequently four models can be differentiated, M01-A, M02-A, M01-B, M02-B, cf. Figure 4-15.

	<b>Material A</b> $f_{ck,cube} = 140 \text{ MPa}$ $f_{ct} = 8 \text{ MPa}$ $E_{cm} = 50'000 \text{ MPa}$	<b>Material B</b> $f_{ck,cube} = 90 \text{ MPa}$ $f_{ct} = 6 \text{ MPa}$ $E_{cm} = 40'000 \text{ MPa}$
<b>Model 01</b> $t_g = 81.5 \text{ mm}$	<b>M01-A</b>	<b>M01-B</b>
<b>Model 02</b> $t_g = 183.5 \text{ mm}$	<b>M02-A</b>	<b>M02-B</b>

**Figure 4-15. Adapted FE-model configurations based on validated models for the parametric studies**

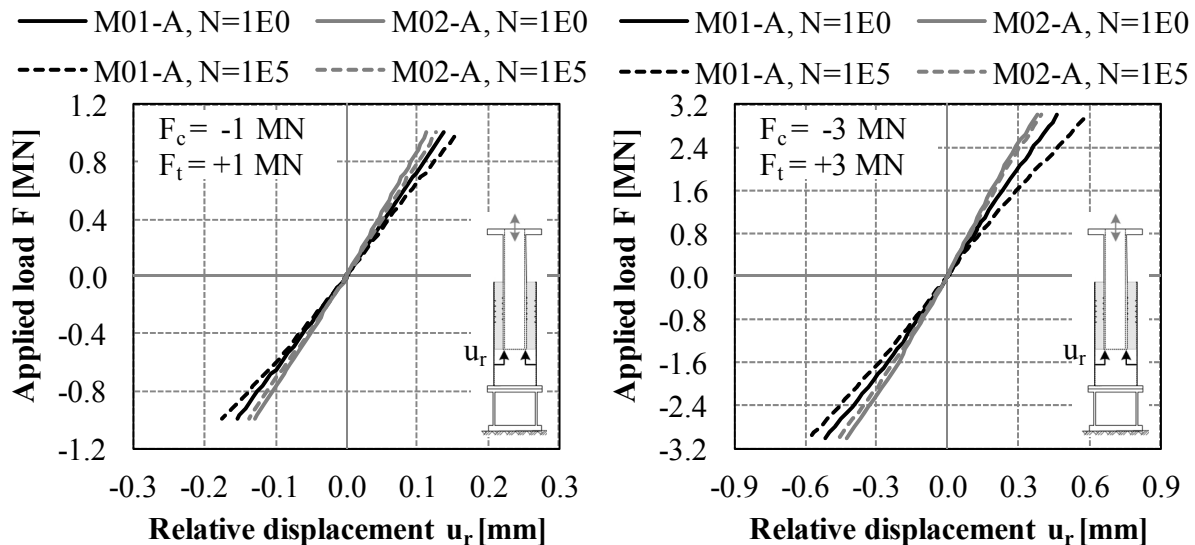
Thus, the following parametric study is based on these four different FE-models, which encounter for two different materials and two different geometries. Apart from the grout thickness and the material, the surface condition of the steel tubes, the load dimension, the repeated loading and load sequence effects are addressed.

### 4.4.2 Grout thickness

With the intention to quantify the impact of different grout thicknesses, the numerical models cover the grout annulus size of scaled reference jacket and tripod substructures. The grout layer size of  $t_g = 81.5 \text{ mm}$ , used for M02-A/B, is consistent to the scaled post-piled tripod structure, whereas the thickness of  $t_g = 183.5 \text{ mm}$ , applied to M01-A/B, correlates to scaled pre-piled jacket substructures. Figure 4-16 contains the numerically achieved relative displacements for the FE-models M01-A and M02-A corresponding to an alternating load range of  $\pm 1 \text{ MN}$ . Complementary, at the right graph results for M01-A and M02-A for the



peak loads of  $\pm 3$  MN are depicted. Both graphical illustrations display a larger relative displacement for the model with the larger grout annulus M01-A. Hence, the numerical results confirm the experimental results, cf. chapter 3.4.2, which indicate likewise increased displacements for the specimens with larger grout annulus. While remaining geometric parameters are not changed, the compression strut angle reduces with increasing grout thickness. As consequence, a reduced number of compression struts might be activated as one of the opposed shear key partners is skipped. Thus, the effect of increased grout thickness is substantial to the fatigue behaviour.



**Figure 4-16.** Impact of different grout thicknesses,  $t_g = 183.5$  mm at M01-A and  $t_g = 81.5$  mm at M02-A, to the cyclic relative displacements for two alternating load scenarios with  $F_{max} = \pm 1$  MN (left) and  $F_{max} = \pm 3$  MN (right) for  $N = 1$  and  $N = 100'000$  load cycles.

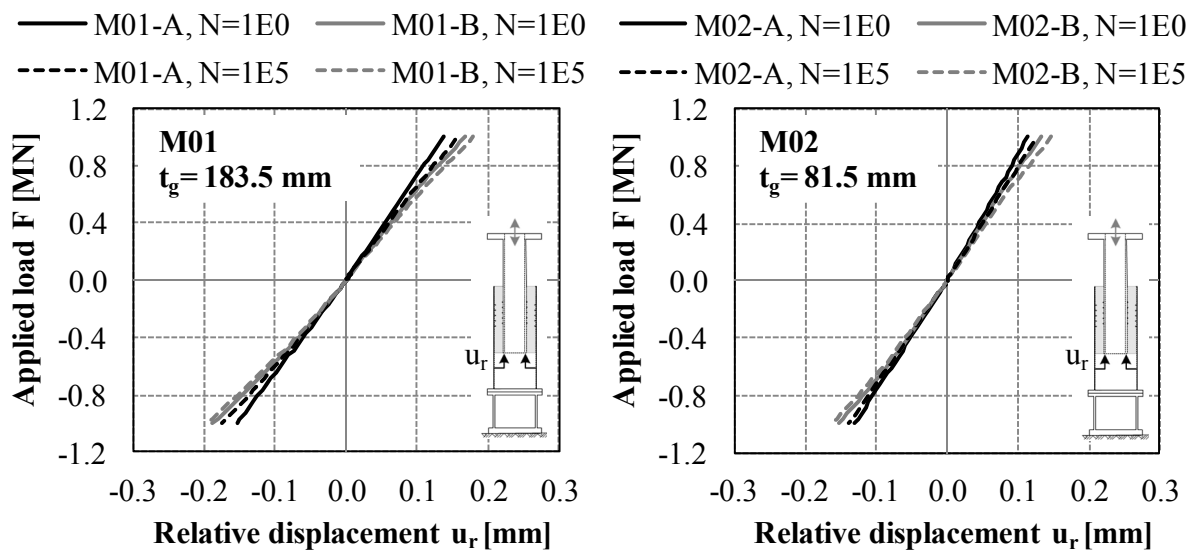
Dashed lines in Figure 4-16 represent the load-displacement behaviour after 100'000 load cycles. By analysing and comparing the cyclic increased displacements to their original values for  $N = 1$ , it becomes obvious that with increasing grout thickness the relative displacement growth rises. The tensile induced relative displacements for M01-A are increased by 15%, whereas the result of M02-A depicts an increase of 5% for  $N = 100'000$  at the load range  $\pm 1$  MN. In view of the larger load application of  $\pm 3$  MN, cf. Figure 4-16 right, it becomes obvious that the repeated loading ( $N = 100'000$ ) causes especially at the model with an increased grout thickness M01-A substantial displacement enlargement induced by the tensile load. The displacement increase results to 35% being accompanied by a strong stiffness reduction. By contrast, M02-A reveals a considerable smaller cyclic induced stiffness degradation for the applied loading of  $\pm 3$  MN. It results, that the increased grout thickness is more effected by large cyclic loads than grouted connections with a small annulus. Based on the investigated parameter range, it is suggested, that an increasing grout thickness provokes a reduced fatigue strength.

#### 4.4.3 Material strength

Two different materials are applied covering a compressive strength range of 90 MPa (Material B) to 140 MPa (Material A), cf. chapter 4.4.1. This range is representative for

commonly used high strength grouts at offshore structures. In this respect it is noted that smaller strengths are possible, e.g. by cement slurries. But as their usage is accompanied by additional issues, the impact of cement slurries is subject of current research work and thus not part of the numerical study.

In order to evaluate the impact of the cyclic degradation behaviour on grouted connections, numerical simulations for  $N = 1$  and  $N = 100'000$  load cycles are conducted. Results are displayed in Figure 4-17, whereby the results are separated with respect to the identical geometry. The left graph illustrates relative displacements for the model with a large grout annulus M01, whereas the right graph reflects results for the test specimens with a smaller grout annulus M02.



**Figure 4-17. Impact of two different materials A and B to the cyclic relative displacements for M01 (left) and M02 (right) depicted for  $N = 1$  and  $N = 100'000$  load cycles.**

As a result of varied material characteristics, namely the Young's modulus, the compressive and the tensile strength, the displayed load-displacement curves for the materials differ, cf. Figure 4-17. At both geometrical grouted connection models, larger relative displacements are observed for the material B. Although the material A leads to smaller relative displacements than material B, the cyclic accumulation of deformations seems to correlate between both materials A and B. The experimental tests indicate a slight impact of the different grout materials, whereby the impact of the material inhomogeneities seems to influence the fatigue behaviour of TS03 and TS04. The numerical results depicted in Figure 4-17 reflect that a material strength reduction from material A to material B by around 40% provokes a displacement increase of about 20%. Therefore, the increase caused by cyclic degradation amounts to 5 to 10%, whereby the increased grout annulus tends to induce larger ascending displacements. Nevertheless, it can be assumed that with respect to the grout annulus the impact of different high strength grout materials to the cyclic degradation is of less significance compared to the influence of the grout thickness.

#### 4.4.4 Surface conditions

On account of the load transfer mechanism of grouted connections, the condition of the steel surfaces has a considerable impact to the load bearing behaviour. Vice versa, the fatigue loading conditions influence the surface conditions, as repeated loading cause a degradation of the interface condition. Therefore, different surface parameters are investigated by considering different values for the numerical simulation. In principle, two parameters describe the surface condition of cylindrical grouted connections and its interlocking. These are the coefficient of friction  $\mu$  and the shear key height to distance ratio  $h/s$ .

According to the recommendations according to DNV-OS-J101 (2014), the design value of the coefficient of friction lies in the range of 0.2 to 0.5 in dependence of the surface treatment. Moreover, analytical and numerical design investigations are proposed to be based on the characteristic coefficient of friction  $\mu = 0.7$  at the edge of the grouted connection according to DNV-OS-J101 (2014). Previous numerical validations are based on the preparation status of the test specimen's steel tubes, which are mechanically cleaned to prune of loose corrosive particles, loose mill scale and loose impurities. As a result of the cleaning process and the reached surface condition, a coefficient of friction of  $\mu = 0.4$  is used for the numerical simulation. As mentioned, repeated loading and corresponding relative displacements can cause a reduction of the coefficient of friction. In view of the fatigue impact and the range recommended by DNV-OS-J101 (2014), the friction coefficient is varied in the range of 0.0 to 0.7. The variation is applied to both model geometries M01-A and M02-A for a compression  $F_c$  and a tension  $F_t$  load of 1 MN. Numerically observed relative displacements are illustrated in Figure 4-18, left.

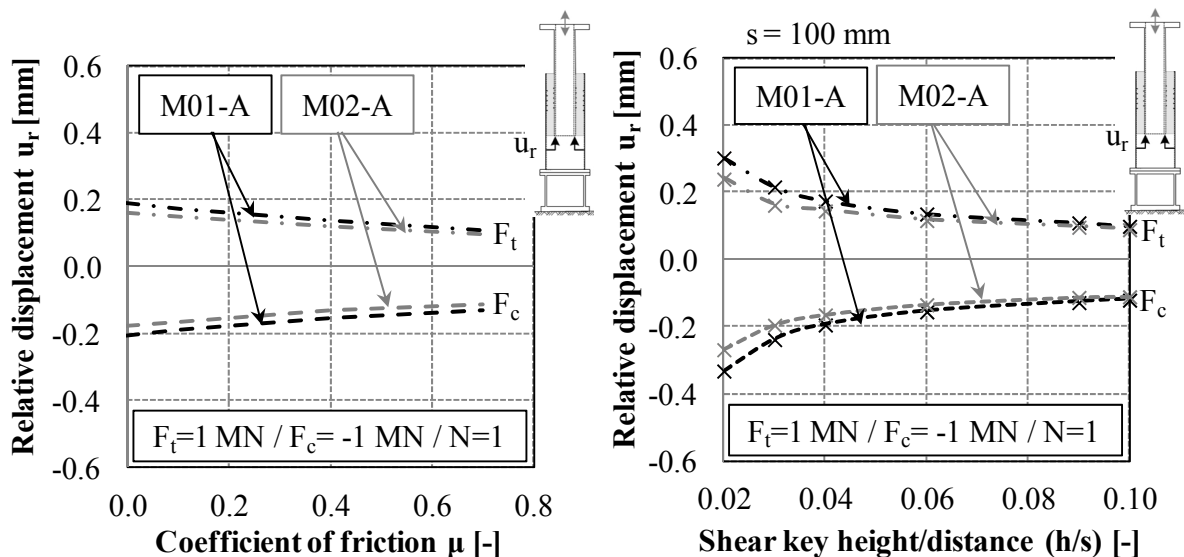


Figure 4-18. Impact of varied friction coefficients (left) and varied shear key height to distance ratios  $h/s$  (right) to the relative displacements at M01-A and M02-A for  $F_t = 1$  MN and  $F_c = -1$  MN.

As expected, the data presents a reduction of relative displacements with increasing friction coefficient. The compressive induced relative displacements decrease at M02-A from -0.176 mm for  $\mu = 0.0$  to -0.112 for  $\mu = 0.7$  representing a reduction of  $\sim 36\%$ . Furthermore, the tensile induced relative displacements decrease by  $\sim 45\%$ . Based on this, the friction

coefficient has a larger impact on the tensile load bearing behaviour than on the compression load bearing behaviour. It is suggested that the load transmission by friction is larger for tension loads than for compression loads. It may result from the 4 compression struts being activated for tension loading compared to the 5 compression struts being activated for compression loading. Therefore, the tension load transmission by friction is more pronounced and variations of the friction coefficient have a larger impact.

The development of the relative displacements for both models correlate, as the curves evolve nearly parallel, cf. Figure 4-18 left. However, as evident by the experimental results and previous numerical investigations, the grouted connection with the larger grout annulus, M01-A, reveals a larger relative displacement than the grouted connection with a smaller grout annulus. Due to the use of a linear friction law, relative displacements increase constantly with decreasing friction coefficient, cf. Figure 4-18 left.

The roughness reduction documented at the test specimen is determined to be  $\sim 33\%$ , cf. chapter 3.4.6. Assuming that the surface roughness correlates with the friction coefficient, a reduction of the friction coefficient being  $\mu = 0.4$  by 33% would result in a reduced value of  $\mu = 0.3$ . According to Figure 4-18, this reduction would entail an increase of relative displacements by  $\sim 2.5\%$  for a tensile load of 1 MN at the numerical model M01. In view of this small reduction for the comparable large loading, the cyclic reduced friction coefficient seems to be less remarkable for the considered model results. The test results correlate with this assumption, as measured strains indicated a small force transmission by friction compared to the force transmission by shear keys. Thus, the interlocking impact of shear keys is substantially larger than the frictional interface resistance.

As the loads are substantially transferred by the shear keys, their geometric constitution is varied to evaluate their impact. Similar to earlier studies, cf. chapter 2.2.2, the ratio of shear key height to distance is chosen to analyse the interlocking effect for varied dimensions. It is suggested that a reduced  $h/s$  ratio induces larger displacements as the height reduction is accompanied by a reduction of the interface strength. In order to concentrate on the interlocking effect, the shear key height and the width is modified correspondingly. It follows that the shear key distance  $s$  and the shear key width to height ratio  $w/h$  remain constant to  $s = 100$  mm and  $w/h = 2$ . A  $h/s$  ratio between 0.02 to 0.1 is covered by the parametric study. The right graph in Figure 4-18 presents the numerical results for the varied  $h/s$  bandwidth for the models M01-A and M02-A. As expected, a reduction of the shear key height provokes increasing relative displacements for both models. The curves reflect an exponential growth of the relative displacements for values lower than  $h/s = 0.04$ . This non-linear development is caused by flattening the shear keys resembling in the extreme state of  $h/s = 0$  to a plane surface. On basis of the depicted relationship between the relative displacements and the shear key height, a lower limit for the  $h/s$  ratio seems recommendable in order to avoid significantly increased relative displacements for considerable small shear keys.

Comparing the results for M01-A and M02-A indicates that the influence of different grout thicknesses becomes apparent with descending  $h/s$  ratios. For larger grout annuli, the impact of reduced shear key heights has a stronger effect on arising relative displacements. Due to the smaller pile surface, larger relative displacements are introduced by the load transmission.

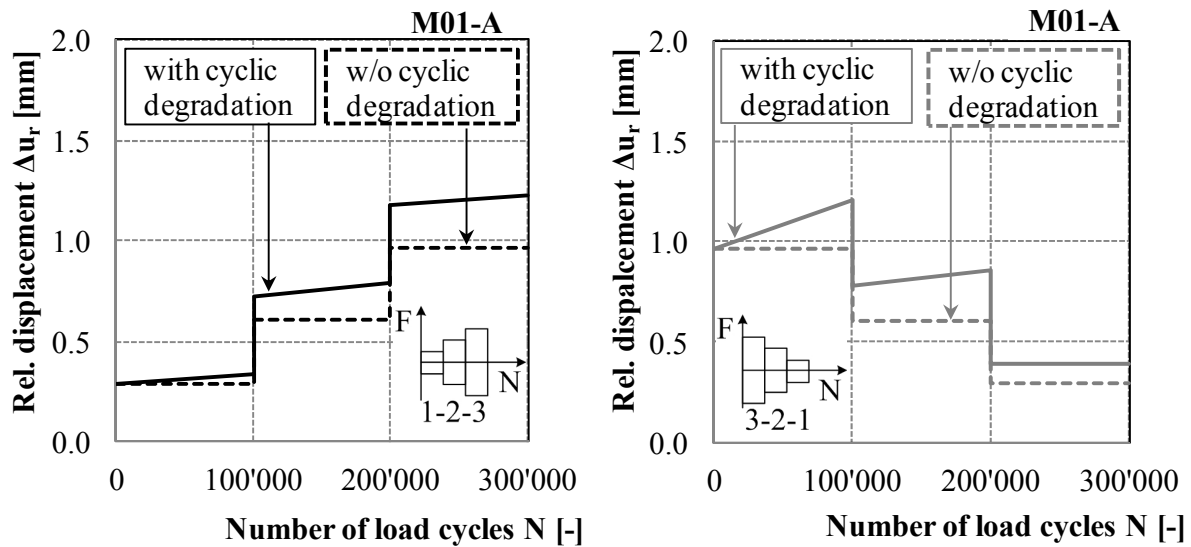
The frictional load transmission depends on the relative displacements and appearing perpendicular forces. The presented correlations and findings of the h/s impact to arising relative displacements depend significantly on the geometrical dimensions of the entire grouted connection. Therefore, additional geometric ratios have to be investigated in future, by transferring the achieved findings to real dimensions of grouted connections.

#### 4.4.5 Load sequence

The developed numerical calculation procedure for the determination of the stress-dependent fatigue damage, cf. chapter 4.2.3, provides the advantage to account for the pre-damage due to previous load scenarios. Thus, the implemented method is used for a first approximation of the load sequence impact on the stress dependent fatigue damage and corresponding load-displacement behaviour of grouted connections.

The following investigation is based on the validated numerical model M01-A. The numerical results for the alternating load sequence of LS01 to LS03 are used as reliable reference for the analysis. The reference load sequence consists of the alternating load ranges  $\pm 1$  MN,  $\pm 2$  MN and  $\pm 3$  MN being stepwise increased after application of 100'000 load cycles. With the intention to identify load sequence effects, it is chosen to apply these load ranges in reverse order. Thus, the numerical model M01-A is exposed initially to 100'000 load cycles on the alternating load level of  $\pm 3$  MN, followed by 100'000 load cycles each on the load level of  $\pm 2$  MN and  $\pm 1$  MN. This procedure allows to compare the obtained numerical results for the two load sequences 3-2-1 and 1-2-3 representing a descending and an ascending load scenario.

As the damage  $D$  according to the Palmgren-Miner summation is calculated numerically per element and per load stage, cf. chapter 4.2.3, it is chosen to conduct the comparison between both applied load scenarios on the basis of the connection's load-displacement behaviour, i.e. the stiffness and displacement development over the applied number of load cycles. A direct comparison of derived relative displacements is significantly affected by the applied load and corresponding cyclic degradation influencing the subsequent displacement ranges of the next load range. Consequently, a large initial load introduces damage to the model which reduces the bearing resistance in the following stages. As a result, relative displacement ranges of subsequent load stages are larger than they would appear if a small load would be predecessor. Comparison of the damage induced relative displacements to relative displacements neglecting pre-damage, enabling to expose the impact of the cyclic degradation of each load range and its consequences for subsequent displacement ranges. In Figure 4-19 observed displacement ranges for the model including and excluding the cyclic degradation approach are depicted for the model M01-A being exposed to an ascending (left) and descending (right) load sequence.

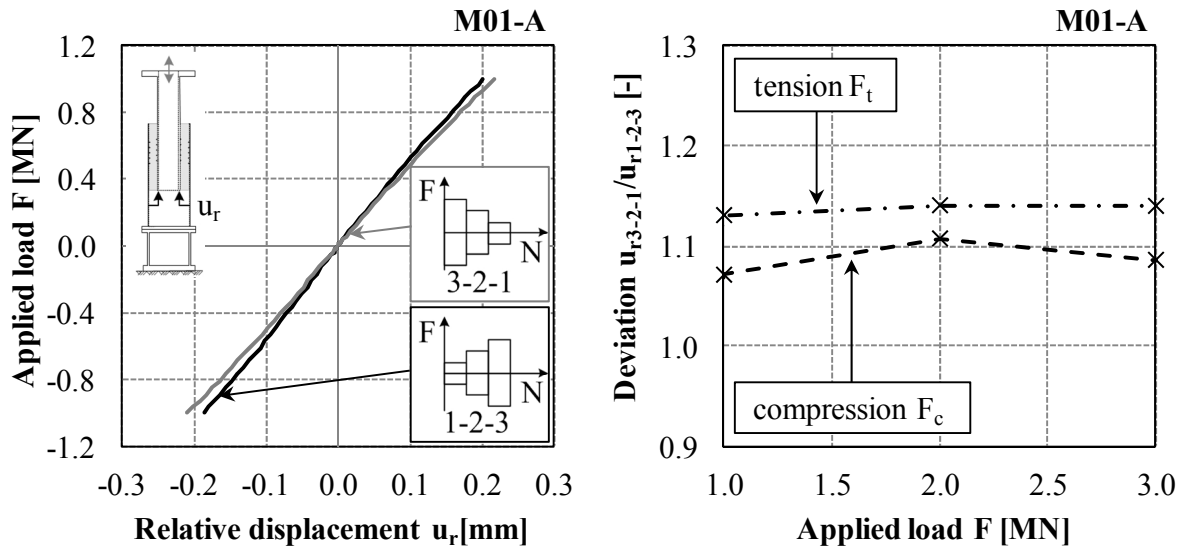


**Figure 4-19.** Comparison of the relative displacement range at M01-A with and without cyclic degradation for the alternating load scenarios 1-2-3 (left) and 3-2-1 (right).

For the ascending load sequence 1-2-3 it can be inferred, cf. Figure 4-19 left, that each load stage causes a small increase of the relative displacement range. Comparison of the results for the model with and without cyclic degradation indicates that pre-damage by previous load stages causes a larger starting value for the subsequent load stages. Similar effects can be observed for the descending load sequences 3-2-1, cf. Figure 4-19 right. The displacement increase within one load level seems to be comparable similar distributed over the applied ascending load scenario 1-2-3. In contrast, the load sequence 3-2-1 induces a strong displacement range increase in the first load stage, which is then followed by a lower increase in the second and an unnoticeable increase at the last load stage. The considerable large cyclic induced displacement increase in the first load stage of the scenario 3-2-1 can be attributed to the applied large load range. Subsequent load ranges evoke a less pronounced damage and displacement growth. Even though Figure 4-19 displays the load level related displacement growth, a second comparison is needed for the assessment of the load sequence induced damage.

In order to visualise the amount of damage indicated by the different load scenarios, the load-displacement behaviour is established on basis of a identical unit load. By exposing the damaged models to an unit load action subsequent to the applied load scenarios, it is able to evaluate the damage impact to the load-displacement behaviour. The unit action consists of one single load of 1 MN in compressive and tensile direction. Consequently, the load-displacement behaviour resulting for the unit load action can be contradicted for both damaged models, cf. Figure 4-20 left.

The curves reveal that for the descending loaded numerical model appearing displacements are larger than for the ascending loaded numerical model. Thus, the load scenario 3-2-1 has induced a larger damage and cyclic degradation than the sequence of 1-2-3. This causes a reduced stiffness of the connection, cf. Figure 4-20 left.



**Figure 4-20.** Comparison of the accumulated displacement ranges (left) and the residual load-displacement behaviour (right) for the alternating load scenarios 1-2-3 and 3-2-1 at M01-A.

The displacements for the model being previously exposed to the ascending load scenario, are about 10% smaller than for the descending loaded model. This becomes obvious by referring the relative displacement  $u_r$  induced by the load sequence 3-2-1 to the results obtained for the load sequence 1-2-3. Figure 4-20 right represents the resulting deviation for different applied loads. The tension load related deviations are slightly larger than the deviation provoked by compression loads. In principle, the deviations amount to approximately 10%. Thus, achieved results demonstrate that the descending load scenarios induce a larger damage to axially loaded grouted connections than an ascending load scenario. These trends are in line with findings by Göhlmann (2008), who analysed the fatigue damage for triaxial loaded concrete specimens exposed to three-stage ascending and descending load sequences.

Despite the obvious impact of the load scenarios, it has to be noticed that the drawn conclusion is limited to the applied load scenarios and the numerical model configuration. However, the implemented method enables a first approximation and assessment of the load sequence effect to the fatigue behaviour of grouted connections being exposed to alternating loads. In future, the method needs to be validated by experimental tests covering different load sequences. Furthermore, it is recommended to examine different loadings by alternating, pulsating tension and pulsating compression load scenarios. Beside the load sequence itself, the number of load cycles applied during each load stages should be varied. Moreover, variations of the load level especially focusing on one-time load actions appearing at offshore structures, such as the 100-year wave, need to be accounted for. An early appearance of a predominant large load action may provoke such a damage to the grout, that subsequent load actions lead to an earlier failure than predicted by using the Palmgren-Miner sum. This type of investigations is recommended to assess appropriate limits for the load sequence effects.

## 4.5 Conclusion

On the basis of performed experimental tests, three-dimensional numerical models are established in order to extend the analysed parameter range with respect to varied material strengths, geometric dimensions and load situations. The results enable to evaluate the fatigue behaviour of axially loaded grouted connections with large grout thicknesses.

Initially, it is focused on the finite element model configuration accounting for appropriate material models especially for the confined grout layer being exposed to multiaxial stress states. The Extended Drucker-Prager cap plasticity model, representing an improved version of the original Drucker-Prager material model, is used for the grout. The material model is calibrated on the basis of triaxial high strength concrete material tests and the Ottosen failure criterion depicting a convenient multiparametric mathematical description of the three-dimensional yield surface of grouts and concrete. By application and validation of the Extended Drucker-Prager model, it is possible to use a convenient and robust material model accounting for the increased triaxial compression strength and reduced tensile strength of high strength grouts.

For the validation of the model configuration accounting for shear keys and a multiaxial grout material model, static numerical calculations are performed and compared to the experimental results for the initial load cycle. The global load-displacements, the local relative displacements and the appearing strains at the pile and the sleeve are compared. As achieved deviations between numerical and experimental results are less than 20%, the applicability of the calibrated Extended Drucker-Prager model and selected high-resolution model configurations is appropriately validated. The initial static numerical results displayed a linear-elastic load-displacement behaviour, whereby the majority of loads are transferred by the shear keys.

Prior to further numerical calculation modifications, a linear-elastic calculation is performed, to assess the stresses in the grout layer for varied load directions. The results reveal, that axial tensile and compression loads provoke circumferential tensile stresses that correlate to the observed radial cracks at the test specimens.

In order to account for the experimentally observed cyclic degradation of the grouted connection being exposed to axial alternating and pulsating compression loads, a calculation procedure is developed and implemented. That procedure enables a stress-dependent damage calculation on the basis of uniaxial S-N curves for high strength grout. On the basis of the grout fatigue strength and occurred damage, a cyclic degradation of the strength and stiffness values is considered. Thus, repeated loading leads depending on the existing stress state at the elements in the grout layer to a fatigue strength reduction of the connection. Calculated damage values confirm that for axially grouted connections, predominantly tension-tension and tension-compression stress states cause damage in the grout. Particularly, at the weld transition and shear key tip increased stresses and damage are observed correlating with obtained cracks at the test specimens.

Comparison of derived numerical load-displacement behaviour with the experimental results reveals that the numerical approach enables to adequately account for cyclic reduced fatigue



strength. Deviations smaller than 15% verify that the experimental documented relative displacement growth during the alternating load stages is sufficiently covered by the numerical recalculation. Numerical results of the pulsating compression load stages show substantially larger relative displacements than observed during testing. It is assumed that this overestimation results from the implemented uniaxial S-N curves and the numerical negligence of shear force transmission by crack surfaces. Notwithstanding, subsequent recalculations of the last alternating load scenario including pre-damage from pulsating load stages reasonably comply with the experimental results. Thus, at present the applied calculation procedure sufficiently accounts for appearing damage and degradation effects.

On the basis of the validated numerical models, parametric studies are performed investigating the impact of varied grout thickness, material strength, interface conditions and load sequences. Corresponding to the experimental results, the FE-simulation shows a grout thickness dependent fatigue strength reduction. The cyclic degradation of the grouted connection is increased with increasing grout annulus and loads. Variation of the grout material strength confirms the previous test related conclusions that the material strength of the grout is of minor importance within the considered bandwidth.

In addition to the grout thickness, the impact of the bearing behaviour is influenced by the shear key configuration. Significantly reduced shear key height to distance ratios  $h/s$  causes a non-linear increase of the relative displacements. Secondly, the results for varied friction coefficients demonstrate that their influence is compared to the  $h/s$  ratio less important. Apparently, the interlocking is strongly related to the  $h/s$  ratio and the grout thickness, because the majority of loads are transferred by the arising compression struts.

Finally, the effect of an ascending and a descending alternating load sequences on the cyclic induced damage is investigated. The numerical results reveal that the descending load scenario evokes about 10% larger relative displacements than the ascending load scenario. Thus, it can be concluded on basis of the numerical investigations that an impact of varied load sequence might be present but appears to be of minor relevance.

With respect to grouted connections at offshore structures, the achieved results need to be classified to the current design approaches and used test conditions. On the basis of achieved numerical and experimental results, the subsequent chapter deals with the derivation of corresponding design recommendations.

## 5 Design Considerations

### 5.1 Intention

Achieved experimental and numerical results have evidently revealed the influence of large grout thicknesses, varied grout materials and interface conditions like the shear key geometry on the fatigue performance of cyclic axially loaded grouted connections. Provided data exhibit the load transfer and material degradation caused by alternating and pulsating compression load stages. In order to transfer obtained results for grouted connection tests with large grout annulus to real offshore constructions in a general manner, numerous aspects have to be considered carefully. For instance, the applied test loads represent an idealised load situation, which does not comply with stochastic loads caused by environmental and operational loads. Besides the covered axial loading, these actions induce simultaneously cyclic bending moments and torsion. Additionally, scale effects of the test specimens as well as the ideal laboratory conditions differ to some extent to real offshore conditions. By setting the test conditions in contrast to offshore conditions influencing parameters supporting the transferability of the derived results can be identified.

While present design approaches were developed on the basis of earlier experimental tests that do not cover the geometrical dimensions of grouted connections in latticed structures, it is essential to set achieved test results in contrast to current design approaches. This allows to evaluate the applicability and appropriateness of present design recommendations for grouted connections with large grout thicknesses. Moreover, it enables to derive general design recommendations for axially loaded grouted connections with large grout annulus.

With the intention to generalise the achieved findings of numerical and experimental investigations, the following issues are subsequently addressed:

- Transferability of test conditions to offshore structures
- Comparison and classification with existing design S-N curves
- Derivation of design recommendations based on experimental and validated numerical results under consideration of design relevant impact factors

### 5.2 Transferability of Test Conditions

Current design recommendations and approaches introduced in chapter 2.3 were derived on the basis of experimental tests for grouted connections at O&G platforms and offshore wind turbines. All experimental tests have been performed under ideal laboratory conditions comprising dry conditions, idealised load scenarios and scaled dimensions of the connection. Herein presented experimental and numerical investigations widen current knowledge. For the first time, large-scale tests on cyclic axially loaded grouted connections with very large grout thicknesses have been conducted. Analogous to earlier tests, deviations appear in contrast to offshore grouted connections at jackets being located totally submerged and loaded stochastically. In order to generalise achieved results, the transferability of applied test

conditions in terms of the load scenarios, early age cycling effects, geometric dimensions, imperfections and ambient conditions are outlined in the following.

### **Loads**

By applying the test load scenarios, it was aimed to evaluate the fatigue behaviour and failure mechanism of cyclic axially loaded grouted connections with increased grout annulus. In consequence, large load levels on a limited number of load cycles significantly contributing to damage were selected for the experimental testing. The loads were stepwise increased after a predefined number of load cycles, cf. chapter 3.3.2. Individual test load stages covered alternating and pulsating compression loading, because of their different contribution to the fatigue damage, cf. chapter 3.3.2. In contrast, real offshore load scenarios at grouted connections are predominantly subjected to compression-compression loads and only a limited number of reversal loads appearing in a stochastic manner. Comparison of test and real load scenarios in chapter 3.3.2 has additionally demonstrated that chosen load levels are comparable high with respect to real loads. This influence has to be taken into account for the evaluation of the observed fatigue strength of the test specimens, especially because the strength was significantly higher than predicted by the design approaches, cf. chapter 3.3.2.

While real load situations are characterised by a stochastic load distribution, test loads consisted of uniform load cycles in order to obtain comparable test conditions and fatigue strength based on a known stress- and load scenario. A first numerical study dealt with the impact of varied load sequence, cf. chapter 4.4.5. The difference of analysed ascending and descending load scenarios led to a damage variation of about 10%. Even though this variation might depend on the load level, the impact of load sequences is assumed to be of minor importance.

The focus of the investigations addressed the predominant axial loading at latticed substructures. Nonetheless, axial loads at offshore grouted connections are accompanied by bending and torsion. While torsional moments cause a rotation which needs to be transferred by the interface strength of the steel-grout intersection, bending moments lead to deformations and ovalisation of the steel tubes affecting the arising stress states. As torsional moments are transferred by the interface shear strength, these may reduce the frictional and interlocking resistance. According to GL Technical Note (2013) vertical shear keys similar to horizontal shear keys shall be applied. The impact of torsional moments and the need for additional interlocking mechanism has not been investigated so far. Latest developments and investigations in consideration of grouted connection being exposed to prevalingly bending moments in monopiles are summarised by Lochte-Holtgreven & Bechtel (2014). From this composition it follows that shear keys increase the load bearing behaviour significantly and that cyclic bending moments affect the axial load bearing capacity- The latter has been evidently shown by experimental investigations according to Schaumann et al. (2008b). The combination of cyclic bending moments and cyclic axial loads will additional increase the damage, as bending induced deformations are accompanied by gapping, debonding, increased relative displacements and local stress concentrations. Based on investigations by Lotsberg et al. (2013) and Schaumann et al. (2014b) it is known that in consequence of vertical relative

movements of the grout-steel interface by bending moments, abrasive wear and, thus, a reduced surface roughness may arise. This results in a reduced friction coefficient with increased number of load cycles. Even though bending moments at jackets are smaller than at monopile structures, the combination of cyclic bending and axial loads will cause an increased damage at the interface. Although local contact pressure due to bending may have a positive effect to the static bearing capacity, cyclic bending is assumed to have a rather negative impact on the fatigue behaviour. It is expected that in consideration of additional cyclic bending moments and torsion, the observed fatigue strength and resistance of grouted connections will be less than observed by the conducted experimental tests.

### **Early age cycling**

The piles and the substructure are permanently subjected to small wave and current loads during installation, which may affect the grout hardening process by corresponding movements. This so-called early age cycling influences the grout material strength properties and consequently the bearing capacity.

Beside slight positive effects like deaeration increasing the material strength, sedimentation and segregation evoke an unequal distribution of material components, cf. Lohaus et al. (2015). Aggregates sedimentate to the bottom of the annulus while lighter components such as cement paste and water are positioned at the top layer. Thus, irregular grout strengths can affect the bearing resistance of the connection. Moreover, early age cyclic movements might impair the contact between grout and steel. As a result of affected contact between steel and grout, the load transfer by compression struts is intensified to compensate the loss of friction resistance. Although the effect is not scientifically quantified for grouted connections at jackets, according to DNV-OS-J101 (2014) the relative movements during the initial 24 hours have to be minimised in general to a limit value of 1 mm by appropriate measures.

In contrast, the grouting and hardening at the test specimens was performed under ideal conditions without movement at an early stage. In view of the possible negative impacts of early age cyclic movements at offshore grouted connections, the fatigue strength of initially cyclic loaded grout test specimen is expected to be lower.

### **Geometric dimensions and scale effects**

Although the performed tests represent the largest cyclic axially loaded grouted connections with increased grout thickness at present, actual grout annulus sizes are approximately twice as big. This scaling may provoke variations and impacts to the highly non-linear bearing behaviour of the connection. In general, it can be differentiated between geometric and material related size and scale effects.

With respect to the geometric effect, it is expected that increased dimensions and loads entail increased relative displacements. In consequence, comparable smaller capacities are expected for larger dimensions. Focusing on the frictional portion of the capacity, Wilke (2014) discusses the varied influences to the three components: global imperfections like buckles, local roughness, and adhesion. All three are assumed to be modestly influenced by the scale.

According to the theoretical considerations by Wilke (2014), the bond strength decreases with increasing diameter. In order to compare small and large scale grouted connection capacities, DIN EN ISO 19902 (2014) recommends a scale factor for pile diameters smaller than  $D_p = 1'000$  mm leading to a reduced interface shear strength, cf. chapter 2.3.2. In relation to the tested specimens having diameters smaller than  $D_p = 1'000$  mm a scale effect might exist. However, this is only an approximation based on a best-fit regression of tests with significant smaller scale.

Beside the geometry, the material related scale effects influence the bearing behaviour of grouted connections. The test results have indicated that, radial cracks appear more frequently with increasing grout annulus. It was identified by performed finite element analysis that independent of the geometry circumferential tensile stresses appear, leading presumably to tensile splitting cracks in radial direction at real connections, cf. chapter 4.2.3. Moreover, radial cracking might be a result of shrinkage, which additionally is affected by the dimension of the grout annulus. Due to the composition of high strength grouts, their hardening process is accompanied among others by drying shrinkage and autogenous shrinkage. As grouted connections at jackets are submerged, the effect of drying shrinkage is of minor importance due to the influence by the ambient humidity. In contrast, the autogenous shrinkage is rather independent of the surrounding moisture and depends on the amount of cement and binder, cf. Zilch & Zehetmaier (2010). The process is characterised by a volume reduction in radial and axial direction. While the grout shrinks on the inner pile, radial shrinkage provokes volume reduction leading to debonding at the grout-sleeve interface. This shrinkage process is assumed to be accompanied by radial cracking. Thus, increasing the size of the grout annulus from test specimen to offshore connections may increase the impact of autogenous shrinkage. In order to minimise negative impacts to the bearing behaviour, Lohaus et al. (2012) recommends to limit the shrinkage value to 1‰ by appropriate grout composition. Even though radial cracking does not directly initiate failure of the connection, the cracks increase the effect of the ambient conditions. In order to determine the scaling effect with respect to radial cracking, monitoring of selected offshore grouted connections appears recommendable.

### **Geometric imperfections**

With the intention of avoiding any eccentricities, as these could have possibly weakened the testing facility, the grouting was performed in the test rig with a uniform grout thickness and grouted length. In contrast, imperfections are not unavoidable at offshore locations, because one function of the grouted connection is to compensate pile driving induced inclinations. Thus, a tilted or eccentric position of the pile may appear.

An eccentricity of the pile evokes irregular grout thicknesses. As a result arising compression strut angles vary between small and large grout thickness provoking an unequal load and stress distribution. First and simplified finite element investigations using linear-elastic grout material by Schaumann et al. (2010b) have revealed that arising stresses at the grout layer are modestly influenced by the investigated eccentricities. By these finite element analysis it was not determined to what extent multiaxial stress states are affected by geometric imperfections. In addition to these simplified investigations, preliminary numerical simulations by the author

and Wedel (2013) focused solely on the impact of tilted and eccentric positioning of the pile to arising tresca stresses in the grout layer neglecting shear keys. Geometrical dimensions of the large-scale test specimens TS01 to TS04 were used and the Drucker-Prager model was applied. The results in consideration of eccentricities correlate with the trends shown by Schaumann et al. (2010b). Similar to horizontal eccentricities, a tilting of the inner pile provokes unequal grout thickness leading to a stress redistribution and stress increase at narrower parts of the grout layer, which are associated with a larger fatigue loading.

A final quantitative assessment of the geometrical imperfection effect to the load bearing behaviour and the fatigue strength is not possible yet.

### **Ambient conditions**

The cyclic axially loaded tests were performed under laboratory conditions, which are characterised by ideal circumstances at room temperature. Moreover, the large-scale test were, similar to all previous experimental tests on grouted connections, cf. chapter 2.2, performed under dry circumstances. Submerged testing at large-scale was planned for the second step of the research project GROWup. The results of this thesis can be used as reference enabling to separate the impact of submerged cyclic tests on the fatigue performance.

The submerged condition evokes a water saturated grout layer leading to hydrostatic pressure inside the grout layer when being subjected to cyclic loading as described by Lotsberg et al. (2013). Moreover, grout shrinkage induced gaps in the grout-sleeve interface and cracks are filled with water. As soon as cyclic bending and axial loading induced deformations occur, the water pressure may strongly increase the damage of the grout especially at the shear keys which are exposed to high stresses. This effect is comparable to excess pore water pressure occurring in soil, cf. Achmus (2011). A second effect results from the water flow, which transports the crushed grout particles resulting in clearance of cracks and gaps. Thus, the obtained interlocking effect of the crushed material is presumably prevented at submerged connections.

Initial large-scale results presented by Schaumann et al. (2016) confirm proposed assumptions and reflect a significantly reduced fatigue strength of submerged large-scale test specimens. According to the GL Technical Note (2013), it is recommended to reduce the endurable number of load cycles by a factor of 10 with respect to the water impact. Due to the proposed water effect, the S-N curves recommended in DNV-OS-J101 (2014) were achieved by accounting for a reduction factor of 0.8, cf. Lotsberg et al. (2013). However, it can be concluded that the ambient conditions may have a dominating impact to the fatigue strength and, thus, presented fatigue strength values of the test specimens have to be reduced while transferring it to real structures.

In addition, the surrounding temperatures may affect the installation procedure and the connection's capacity because the grout material flowability and also resulting strength properties are influenced by the temperatures. According to Lohaus & Griese (2014), the air temperature at North Sea locations varies in between  $-5^{\circ}\text{C}$  to  $30^{\circ}\text{C}$  and the water temperature

being affected by tidal flows results to 3°C to 18°C. The superplasticizer are sensitive against temperatures leading to changing flowability of the grout material affecting the segregation and composition stability. Resulting inhomogeneities may reduce the fatigue strength of the connection. Moreover, reduced temperatures reduce the grout strength capacities of the material as tests for instance by Sørensen (2009) reflect. Sørensen (2009) states that the uniaxial compressive cube strength of high performance grout BASF Masterflow<sup>®</sup> 9500 at 7 days and 5°C is reduced by ~20% compared to the strength at 20°C. A reduced grout compressive strength might lead to an increased degradation of the grout.

Concluding, the considerations to the transferability of the test conditions have revealed that varied conditions at test and offshore location might affect the fatigue strength. In particular, impacts caused by cyclic bending moments and submerged condition require a reduction of the achieved test fatigue strength in order to transfer test results to real scale grouted connections. Notwithstanding, the achieved test results are compared to current design S-N curves and design recommendations in the following, because S-N curves and design recommendations originate likewise from tests under laboratory conditions.

### 5.3 Comparison with Existing Design S-N curves

A comparison with existing design approaches is performed on the basis of current design recommendations for evaluating the cyclic experimental test results.

As introduced in chapter 2.3.3, design recommendations for the fatigue limit state of grouted connections in offshore support structures were introduced by Harwood et al. (1996), Billington & Chetwood (2012) and recently by DNV-OS-J101 (2014). As the data basis for the S-N curves according to Harwood et al. (1996) and Billington & Chetwood (2012) are identical and the earlier approach by Harwood et al. (1996) constituted the basis for the Billington & Chetwood (2012) equation, the latter approach was preferred for the comparison. In addition, the recent code related S-N curve for grouted connections in jacket substructures according to DNV-OS-J101 (2014) was used for the evaluation of the test results.

It is necessary to reiterate, that the S-N curve according to Billington & Chetwood (2012), cf. Eq. 2-13, was developed by a best-fit analysis on basis of the Harwood approach and experimental test results achieved in the 1970's and 1980's for the O&G grouted connections. Contrary, the DNV derived the current S-N curve, cf. Eq. 2-14, on the basis of the S-N curves for concrete materials in air and water, cf. DNV-OS-C502 (2012) and in consideration of the lower bound capacity for grouted connections with small radial stiffness during the JIP II related investigations, cf. Lotsberg et al. (2013). However, for the application of both S-N curves, the stress ratio of the applied maximum stress to the ultimate stress capacity of the grouted connection has to be determined. For the proposal according to Billington & Chetwood (2012), it was considered to apply the corresponding ultimate bearing capacity according to the DIN EN ISO 19902 (2014), cf. Eq. 3-1. In contrast, the associated ultimate bearing capacity was used for the DNV formulation, cf. Eq. 3-2. These ultimate bearing capacities for the individual test specimens are determined in chapter 3.3.2. Comparison of the capacities  $F_{ULS}$  has revealed that the ULS capacities significantly differ for both

approaches and test specimens. Whilst the DNV method considers the capacity per shear key, the ISO method takes into account the effective length of the connection. As the shear keys at the test specimens are arranged not equidistant over the complete length, for the obtained  $F_{ULS}$  disparity appears. Thus, it can be expected, that the endurable number of load cycles related to these two approaches differ.

As the test specimens were exposed to varied load stages with a number of different load cycles, an equivalent number of fatigue cycles  $N_{eq}$  corresponding to the largest alternating load level LS03 was determined on the basis of the S-N curves. The results are listed exemplarily for the test specimen TS01 according to the ULS and FLS design procedure by DNV-OS-J101 (2014) in Table 5-1. Similar tables reflecting the results for TS02, TS03 and TS04 according to DNV-OS-J101 (2014) and the Billington & Chetwood (2012) proposal in combination with the ULS design according to DIN EN ISO 19902 (2014) are supplemented in Annex E.1.

**Table 5-1. Equivalent number of load cycles for TS01 according to DNV-OS-J101 (2014).**

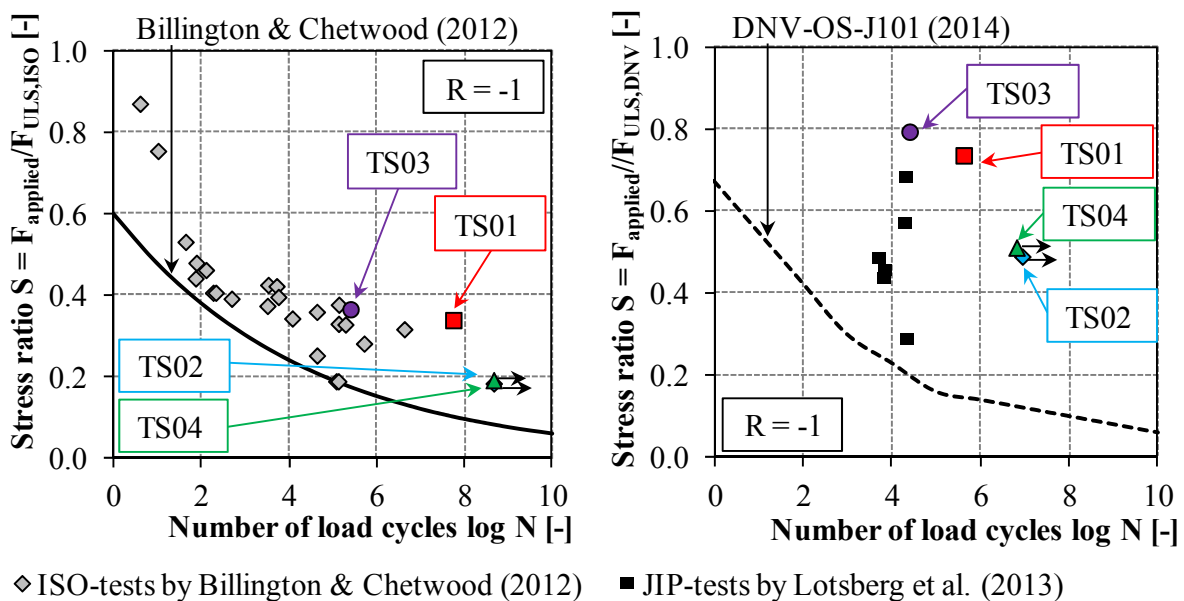
<b>TS01</b>							
$F_{ULS,DNV}$	4'063	kN					
Load stage [-]	$F_{max}$ [kN]	$F_{max}/F_{ULS}$ [-]	$\log n_i$ [-]	$\log N_{failure}$ [-]	D [-]	$D_{eq}$ [-]	$\log N_{eq}$ [-]
LS01	1'000	0.25	5.00	3.77	17	0.000	9.38
LS02	2'000	0.49	5.00	1.46	3'451	0.009	7.07
<b>LS03</b>	<b>3'000</b>	<b>0.74</b>	<b>5.00</b>	<b>0.00</b>	<b>100'000</b>	<b>0.248</b>	<b>5.61</b>
LS04	4'000	0.98	5.00	0.00	100'000	0.248	5.61
LS05	5'000	1.23	5.00	0.00	100'000	0.248	5.61
LS06	6'000	1.48	5.00	0.00	100'000	0.248	5.61
LS07	8'000	1.97	2.38	0.00	240	0.001	5.61
LS08	3'000	0.74	-	0.00	-	-	-
$\Sigma$					403'708	1.000	

The initial two columns of Table 5-1 present the applied load stages and the maximum load. The stress ratio depicted in column 3 results from load stage related maximum compression force and the ultimate bearing capacity  $F_{ULS}$ . The endurable number of load cycles for each stress ratio is derived by application of the S-N curve, here according to DNV-OS-J101 (2014). According to the Palmgren-Miner summation, the damage D can be determined based on the applied logarithmic number of load cycles  $n_i$  and the derived logarithmic number of load cycles until failure  $N_{failure}$ . Due to the fact that the test specimens resisted a larger number of load cycles than calculated, the total damage value was used to determine an equivalent damage value for each load stage. In consideration of the load stage related stress ratio, an equivalent number of load cycles can be provided for each load stage. For the comparison of the different test specimen results, it was chosen to apply the equivalent number of load cycles for the largest alternating load level LS03, cf. coloured numbers. Even though design related equations and curves constitute the basis, achieved results consider



characteristic values. Moreover, a failure of the test specimen was defined on the basis of progressive non-linear relative displacement range increase and substantial macro and matrix cracking appearing in the grout layer, cf. chapter 3.4.5. As the grouted connection is characterised by a ductile behaviour previous to the failure, damage in terms of grout cracking leads to a non-linear displacement increase. A failure is present when the non-linear relative displacements increase progressively with each number of load cycle.

The results for the cyclic test are depicted for the two different approaches by Figure 5-1. The left diagram represents the S-N curve according to Billington & Chetwood (2012) along with the corresponding test data. Even though for the determination of the test results, the design recommendations according to DIN EN ISO 19902 (2014) were applied, it is not known whether the presented ISO-data base had been determined on the similar design equation. Notwithstanding, the own and the ISO-data reflect characteristic values, i.e. the partial safety factor is not taken into account.



**Figure 5-1. Comparison of test results for TS01 to TS04 based on the ULS capacity according to DIN EN ISO 19902 (2014) with the Billington & Chetwood (2012) approach (left) and based on the ULS capacity according to DNV-OS-J101 (2014) with the S-N approach according to DNV-OS-J101 (2014) and corresponding test data according to Lotsberg et al. (2013).**

However, considering the ISO approach, cf. Figure 5-1 left, the derived results for the TSs all reflect a larger fatigue strength than expected by the design equation. For the individual grouted connection specimens, the fatigue results presented in Figure 5-1 left indicate that a reduced capacity  $F_{\text{ULS,ISO}}$  evokes a higher stress ratio  $F_{\text{applied}}/F_{\text{ULS,ISO}}$ , which in follow provokes a reduced equivalent number of load cycles  $N$ . By comparing the TS02 and TS04 results with the ISO-data base, it becomes obvious that the fatigue strength of TS02 and TS04 is noticeable larger than the ISO related experimental results. TS03 correlates well with the ISO-data base and TS01 has a slightly increased fatigue strength compared to the ISO-data base. It can be concluded from the comparison of achieved fatigue test results and the ISO related proposal, that the design S-N curve by Billington & Chetwood (2012) is applicable for

the design. Nonetheless, the impact of offshore conditions discussed in chapter 5.2 needs to be considered for the design for offshore grouted connections.

The right graph in Figure 5-1 shows the results for the test specimens according to DNV-OS-J101 (2014) with corresponding design S-N curve and test results reported by Lotsberg et al. (2013). The presented results outline that the fatigue strength of the test specimens is significantly larger than expected by the design S-N curve, which is influenced by the defined failure criterion and the ideal laboratory conditions. However, it depicts similar that the fatigue strength for TS01 and TS03 is lower than for TS02 and TS04. The impact of the grout thickness and related ultimate bearing capacity is emphasised by the approach according to DNV-OS-J101 (2014). From the comparison of test results with the DNV approach, it can be concluded that the S-N curves can be applied for the design of grouted connections with increased grout annulus. Due to the calculated considerable higher fatigue strength, it is assumed that the implied safety margin might account sufficiently for the actual existing offshore conditions.

Finally, the comparison of depicted results for the ISO-related proposal and the DNV-OS-J101 (2014) clearly indicate that the design according to DNV-OS-J101 (2014) predicts lower fatigue strength. In consideration of the tested connections, this lower fatigue strength is caused by the number of shear keys being arranged not equidistantly over the length of the connections. The design results for both methods would have correlated by application of an equidistant shear key configuration. Nevertheless, the comparison outlines the relevance of the stresses resulting from the tested grouted connections. For the evaluation of the connection's capacity, it seems more appropriate to refer to the number of effective shear keys than to the connection length, as the fatigue test results showed a compression strut failure. Even though the current design method leads to comparable conservative results for the test specimens, further optimisation of the method is due to recent submerged test results reported by Schaumann et al. (2016) not recommendable. Moreover, additional aspects discussed in chapter 5.2, would reduce the test results compared to offshore connections further.

## 5.4 Derivation of Design Recommendations

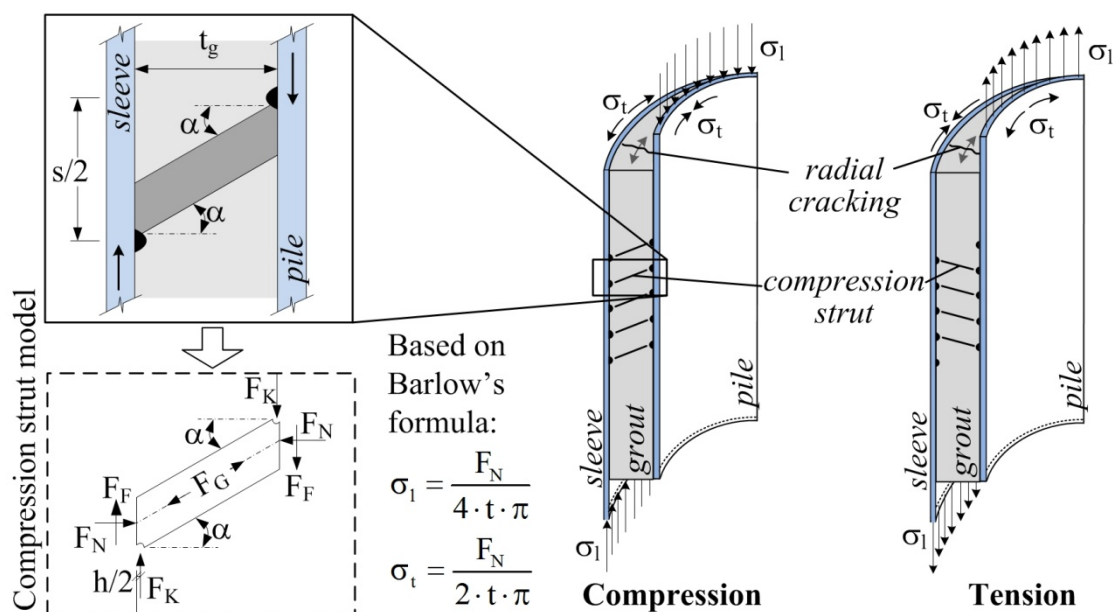
In addition to previous considerations regarding the transferability of test results and the comparison of test results with current design approaches, design recommendations can be derived on the basis of the performed experimental and numerical investigations. Initially, the observed load transfer mechanism is outlined, being followed by remarks to the individual influencing parameters on the load bearing and the fatigue performance of axially loaded grouted connections with large grout thicknesses.

### Load transfer mechanism

Evaluated data of the large-scale cyclic axially loaded test specimens showed a dominant load transfer by the shear keys and arising compression struts. Based on the documented longitudinal steel strain gauge measurements, it was concluded that compression loads are

transmitted at first by the upper part, while tensile load transmission initially concentrates on the lower part of the shear key area and adjacent grout-sleeve interface, cf. chapter 3.4.4. Nonetheless, repeated loading and increased loads provoked a compression strut failure by both load directions leading to a redistribution of the load transfer. Even though compression struts evidently failed, affected shear keys significantly contribute to the load bearing resistance.

In consequence, the test results confirm the applicability of the compression strut model by Lamport et al. (1986), which was improved by Anders (2007) and recently by Schaumann et al. (2012a). Figure 5-2 depicts the varied load transfer mechanism for tensile and compression loading and the compression strut model being based on the force equilibrium at the compression strut as described by Schaumann et al. (2012a).



**Figure 5-2. Tensile and compression loaded grouted connection (right) and compression strut model (left) based on Schaumann et al. (2012a).**

Tensile loading evokes a vertical elongation and circumferential contraction of the pile, cf. Figure 5-2 right. These stresses are transferred by compression struts to the sleeve causing longitudinal tensile stresses  $\sigma_1$  and circumferential compressive stresses  $\sigma_t$ . Arising steel stresses can be calculated by Barlow's formula taking into account the normal force part  $F_N$  of the compression strut, cf. Schaumann et al. (2012a). For the derivation and detailed description of the approach reference is made to Schaumann et al. (2012a). In contrast to tensile induced compression struts developing bottom-up, compression induced struts develop from top-down, cf. Figure 5-2, for a pre-pile grouted connections. At post-piled grouted connections, the compression struts induced by tensile and compressive loads arise vice versa. Irrespective of the load direction, the upper and lower shear keys are subject to increased stress concentrations, which is associated with an early failure of these compression struts. Crack patterns at the test specimens demonstrated impressively the grout crushing at the shear keys and diagonal cracks in the external parts of the shear key area. Finite element calculations confirmed these courses of compression struts by stress trajectories.

Moreover, it was observed by the performed investigations that the compression load strength of grouted connections is larger than the tensile strength. This can be traced back to the larger tensile induced relative displacements. Even though one reason might be the reduced number of shear keys being activated by the tensile loading, the differences in the global bearing mechanism are of larger importance. This can be also explained by Barlow's formula and the confinement effect entailed by the steel tubes, cf. Figure 5-2. As a result of compression loads and radial expansion of the inner steel tube, the grout strength is increased due to the confining pressure. Contrary, tensile loading leads to a circumferential contraction of the pile causing debonding and increased stress concentrations at the shear keys.

Presented load transfer and the associated bearing resistance are predominantly influenced by the grout thickness  $t_g$ , the shear key height to distance ratio  $h/s$ , the arising compression strut angle  $\alpha$  and the radial stiffness of the connection  $K$ . Thus, concluding remarks are given separately for each of these parameters on the basis of the observed results.

### **Grout thickness influence**

Own tests revealed that an increased grout thickness evokes increased cracking and relative displacements being accompanied by a reduced fatigue strength. The geometrical increase of the grout layer thickness  $t_g$  from 81.5 mm at TS02 and TS04 to 183.5 mm at TS01 and TS03 represents a factor of 2.25. This factor is not equivalent to the damage due to the observed non-linearities at the relative displacements and stiffness development, cf. chapter 3.4.2 and 3.4.3. Thus, it is not possible to specify a simplified percental factor for the displacement increase or fatigue strength reduction. Based on this, it is recommended to perform individual finite element analysis in order to evaluate arising stresses, especially circumferential tensile stresses and stresses at the external shear keys.

Nonetheless, it can be assumed that the ULS design equations according to DIN EN ISO 19902 (2014) and DNV-OS-J101 (2014) are also applicable for grouted connections with increased grout thicknesses under dry conditions, because all four test specimens resisted considerable large cyclic loads. It results, that the corresponding validity range for the  $D_g/t_g$  ratio being currently limited to 10, cf. chapter 2.3.2, might be adapted.

Furthermore, it can be concluded that compression load states cause less fatigue strength degradation than tensile load states. In addition, it has to be emphasised that an increased grout annulus results in a stronger radial cracking due to circumferential tensile stresses. It is expected that radial cracking and impacts caused by the material exceed a reasonable limit at some point of grout thickness. On the basis of the performed tests, the grout diameter to thickness ratio should be limited to a value of 4.2. Commonly, concrete structures are equipped with reinforcement bars for providing sufficient tensile bearing resistance. The application of reinforcement for the limitation of radial cracks in grouted connections might be a theoretical option, but induces a considerable effort for the installation and grouting.

### **Shear key influence**

As the majority of loads are transferred by shear keys, their size and location are to be selected with care. Thereby, especially the shear key height to distance ratio  $h/s$  and the compression strut angle  $\alpha$  are of major importance as these parameters predominantly influence the global failure behaviour.

With regard to the test specimens and arising compression struts, cf. chapter 3.4.7, it is recommended to arrange shear keys as such, that the optimal compression strut angle  $\alpha$ , which develops between opposed horizontal shear keys, results to an angle in the magnitude of  $30^\circ$  to  $50^\circ$ . Flatter angles may lead to skipping of the next diagonally opposed shear key. Thus, the effective number of shear keys might be reduced and thus compression struts stresses increase. In this regard, Zilch & Zehetmaier (2010) report that for common concrete structures the compression strut angle results in the range  $30^\circ$  to  $60^\circ$  on the basis of the framework model. This effect is to be set in correlation with the splitting grout strength.

According to GL Technical Note (2013), crossing compression struts have to be considered for angles lower than  $30^\circ$ . This recommendation is not comprehensible, as the appearance of crossing compression struts depends on the load direction. Crossing cracks appeared also under larger angles at the test specimens, cf. chapter 3.4.7, indicating that crossing compression struts develop irrespective of the angle. Although it can be expected that crossing cracks influence the fatigue strength, their appearance does not implicate directly a critical fatigue strength degradation of the grouted connection.

Based on the corresponding numerical investigations, an  $h/s$  ratio in the range of 0.04 to 0.06 seems to be recommendable for an optimised load transfer, cf. chapter 4.4.4. Larger values might have a beneficial impact, but cannot be assessed as these were not tested. A lower  $h/s$  value might decrease the interlocking effect provoking increased relative displacements as obtained by the numerical investigations, cf. chapter 4.4.4.

Beside the compression strut failure, shear failure at the shear key tips or in between the shear keys can arise, cf. chapter 2.2.2. In order to avoid these failure modes, it has to be omitted to arrange considerable dense or wide apart shear keys.

### **Radial stiffness K**

The radial stiffness factors  $K$  of the own tests, cf. Eq. 2-3, result to 0.04 and to 0.07 for the two different test geometries. Although these values exceed the recommended limit of 0.02 according to current design codes, cf. chapter 3.2.1, the resulting ultimate capacity was determined with these values. Comparison of test loads with these ultimate loads revealed, that considerable large cyclic loads could be transferred. Therefore, present limitation might be extended.

### **Grout material**

The tested specimens were filled with two different high strength grout materials with uniaxial compressive cube strengths, edge length 75 mm, in the range of 120 to 145 MPa. Although the fatigue strengths at the test specimens were in the essence similar, material

inhomogeneities in combination with the large grout thickness at TS03 lead to a reduced fatigue strength. The finite element analysis accounting for an extended compressive strength range of 90 to 141 MPa, reflects that the impact of the material strength has, as in steel constructions, a minor influence on the fatigue strength of the connection, cf. chapter 4.4.3. Thus, it can be concluded that less the material strength but rather the material composition influences the fatigue strength of grouted connections. Lochte-Holtgreven (2013) and Wilke (2014) concluded that increasing grout material strength in general leads to a slightly increased capacity of the connection. Even though observed results differed modestly, this assumption can be confirmed in the essence by documented test results, cf. chapter 3.4.2.

Moreover, the impact of radial autogenous shrinkage becomes more relevant with increasing grout thickness. This is due to a debonding of sleeve and grout reducing the interface transfer strength. Based on the test results, it is recommended to use high strength grout materials with considerable low shrinkage values. Special focus has to be set on the material composition and the grouting procedure leading to a homogenous material throughout the grouted connection.

### **Design procedure**

Previous considerations have identified, that current analytical design approaches are applicable for a pre-design of cyclic axially loaded grouted connections with large grout thicknesses.

In order to perform a detailed design assessment of the complex and non-linear bearing behaviour, it is proposed to use the finite element method with benchmarked models. For a proper finite element analysis care has to be taken while choosing appropriate element type and size, material models and properties, mesh size and calculation procedure. For grouted connections it is recommended to use solid elements for steel, grout and shear keys. The element size and mesh size depends on the geometry of the construction. It is advised to perform a mesh sensitivity study to evaluate the refinement of the mesh. Detailed recommendations in conjunction with element size, element types, load application and boundary conditions for finite element modelling are given e.g. by DNV-OS-J101 (2014). Due to the load transfer by shear keys and interface conditions between steel and grout, non-linear contact behaviour has to be taken into consideration. This approach provides a reliable tool to perform detailed investigations on the basis of three-dimensional numerical models. Due to arising local stress concentrations and grout crushing, it is suggested to model the shear keys by solid elements. While the bilinear material model for steel sufficiently represents the material behaviour, a multi-parametric material model accounting for multiaxial stress states and triaxial strength properties are preferably to be applied for the grout layer. Documented, validated and evaluated numerical results in chapter 4 have reflected that the Extended Drucker-Prager cap plasticity model represents a reliable model to account for the required grout material behaviour. The model parameters are to be calibrated to the grout characteristics, whereby presented values and relations, cf. chapter 4.2.2, can be used as reference for high strength grouts.

On the basis of three-dimensional high resolution models, stress concentrations at the shear keys can be investigated. For the design, an average stress value arising at one half of the shear keys is assumed to represent a reliable value. Experimental tests have proven that even though compression struts fail, affected shear keys still contribute to the global load transfer mechanism. It results, that although compression struts fail, load redistributions might enable an adequate bearing resistance. Therefore, it is recommended to focus not only on the shear keys, but also consider stress redistributions and related loading of remaining shear keys. Finally, the ultimate bearing capacity might be determined on the basis of the compression strut capacity for a sufficient amount of properly arranged shear keys. Applicable compression strut models are available, as for instance Schaumann et al. (2012a).

## 5.5 Conclusion

In order to derive design recommendations based on the achieved experimental and numerical investigations, the transferability of test conditions and a comparison with current design approaches was discussed.

For the first time large-scale tests of grouted connections with large grout annulus being subjected to cyclic axial loads were performed. Although, the ideal laboratory conditions are in line with former experimental tests, different conditions are present at offshore locations which might influence the load bearing behaviour. Variable stochastic cyclic loads, additional cyclic bending and torsional loads, geometrical scale effects, geometrical imperfections and ambient conditions have an impact on the transferability of the achieved test results. While scale effects can be identified by appropriate finite element analysis, the effect of geometrical imperfections and early age cyclic movements can be minimised substantially by the offshore installation procedure. The impact of simultaneously acting cyclic bending loads and torsion as well as the submerged position have to be considered by the design.

Because present S-N curves and design recommendations are all based on similar dry laboratory conditions, a comparison and classification of own tests with design approaches is performed. The comparison of the test results to the S-N curves reflects that for both geometrical test specimen configurations a considerable large fatigue strength was achieved. Based on the fact, that the test results were substantially larger than calculated by the design approaches, it is suggested that a sufficient safety margin for negative impacts caused by offshore conditions might be included in the design approaches. Thus, it is assumed that the design approaches according to DIN EN ISO 19902 (2014), the related S-N approach by Billington & Chetwood (2012) and DNV-OS-J101 (2014) can be applied for grouted connections with increased grout annulus.

The observed global load transfer mechanism is characterised by a compression strut failure. Provided data of the own large-scale cyclic axially loaded test specimens revealed that the loads are predominantly transmitted by the shear keys and arising compression struts. Thus, it is recommended to focus on the compression strut capacity for the design. For the pre-design current analytical design equations according to DIN EN ISO 19902 (2014), DNV-OS-J101 (2014) or Schaumann et al. (2012a) can be used to calculate the ultimate bearing

capacity of grouted connections with increased grout annulus. It is recommended to apply horizontal shear keys equidistantly over the length of the connection with an appropriate compression strut angle and shear key height to distance ratio  $h/s$ . The compression strut angle should be ideally realised by  $30^\circ$  to  $50^\circ$ , while for the  $h/s$  ratio values in the range of 0.04 to 0.06 seem appropriate. With respect to the grout thickness, current design limitations can be adapted considering used grout thickness dimensions and slenderness ratios. Notwithstanding, it has to be mentioned, that increasing grout thickness is accompanied by increased radial cracking due to circumferential tensile stresses influencing the fatigue behaviour. For the grout material, it is recommended to use high strength grouts with low shrinkage values being specifically developed for offshore conditions. Special focus has to be set on the material composition and the grout execution to ensure a homogenous material with uniform strength characteristics.

As the bearing behaviour of grouted connections is rather complex and non-linear, finite element analysis are indispensable. It is recommended to perform finite element calculations accounting for the multiaxial stress states in the grout by appropriate material models like the herein applied and validated Extended Drucker-Prager model. The model parameters are to be calibrated to grout characteristics, whereby provided values and relations can be used as reference for high strength grouts. For the steel a bilinear material model represents the material behaviour sufficiently. By three-dimensional high resolution models, stress concentrations at the shear keys and design relevant compression struts can be analysed. Moreover, the impact of grout thickness to arising tensile stresses becomes visible and can be evaluated with respect to the tensile splitting strength of grout. A numerical related fatigue strength evaluation of the connection can be performed on the basis of the introduced numerical calculation procedure accounting for grout damage on the basis of uniaxial concrete S-N curves. This procedure enables to account for reduced grout strength and stiffness characteristics influencing the global load bearing behaviour of grouted connections.



## 6 Summary and Outlook

### 6.1 Summary

This thesis deals with the fatigue behaviour of axially loaded grouted connections at latticed substructures for offshore wind turbines. Conducted investigations were motivated by the present lack of knowledge for this kind of connection at jackets or tripods entailing large grout thicknesses and being predominantly loaded by cyclic axial alternating and pulsating compression loads.

The presented state of the art and state of the scientific knowledge outline that geometrical dimensions and load situations at grouted connections in latticed substructures are not covered by earlier investigations and deduced design limitations. Notwithstanding, basic load transfer mechanisms and design recommendations are extensively described on basis of former tests. These tests demonstrated that loads are predominantly transferred by contact forces in the grout-steel interface and compression struts arising between opposed shear keys. Indeed, design driving cyclic reversal load situations at latticed offshore wind turbines and their negative impact on the fatigue behaviour of grouted connections were not investigated. However, the state of research emphasised that these issues need to be considered by more reasonable experimental and numerical investigations. In particular, the impact of up-scaled grout thicknesses to the fatigue behaviour especially with respect to varied stress ratios and appearing load bearing behaviour is unknown until now. In consequence, the applicability of current design approaches is not clarified and thus, demands for new experimental and numerical investigations.

In consequence, experimental large-scale tests were performed in order to identify and evaluate the fatigue behaviour of axially loaded grouted connections with large grout thicknesses. Four test specimens with dimensions adapted from grouted connections at jackets and tripods were filled with two different high strength grouts and subjected to a stepwise increased loading composed of cyclic alternating and pulsating compression load stages. The main findings of the performed tests can be summarised as follows:

- The **global load-displacement behaviour** of the tested specimens reveals an initial linear-elastic behaviour reflecting smaller stiffnesses for larger grout thicknesses. The number of load cycles and ascending load levels provoke a non-linear stiffness reduction especially for those specimens with a larger grout thickness. Nevertheless, the overall grouted connection represent a ductile fatigue behaviour, although brittle grout material behaviour was observed. In principle, grouted connections with larger **grout thicknesses** have a lower fatigue strength compared to connections with small grout thicknesses.
- The **material strength** has a minor influence on the fatigue behaviour. Notwithstanding, the material inhomogeneities had a negative impact on the fatigue resistance, particularly at the specimen with a larger grout thickness.

- The **load transfer** concentrates on the external shear keys, while intermediate shear keys contribute less to the load transmission as strain measurements revealed. Moreover, ascending relative displacements and presumed cracking in the grout induce a load redistribution being recognised by achieved steel strain measurements. Despite grout cracking, the interlocking effect by shear keys is only slightly affected. Thus, a post-cracking load transfer at the shear keys is still possible. Besides, a contact contribution consisting of adhesive and frictional forces to the load bearing behaviour was recognised, but assessed to play a subordinate role to the fatigue performance.
- The **failure mechanism** is evidently characterised by a compression strut failure at all four tested specimens, which is reflected by exposed crack patterns. Although arising compression strut angles were significantly affected by the grout thickness, crossing compression struts induced by varied load directions appeared at all test specimens. Apart from that, up-scaled grout thicknesses are characterised by high transverse tensile stresses leading to an increased radial cracking. Thus, large load levels caused intensive grout cracking and crushing at the test specimens with large grout thickness.
- **Alternating loads** cause a significant cyclic degradation, while **pulsating compression loads** lead to an enhanced fatigue performance due to interlocking at the crack surfaces. Particularly tensile loads cause a fatigue strength reduction, because these loads are transmitted by a reduced number of active compression struts and are accompanied by pile contraction increasing the stress concentrations at the shear keys. In contrast, compression loads evoke a pile expansion increasing the interlocking of grout and steel. Thus, alternating load stages have a substantially larger detrimental impact on the fatigue behaviour than pulsating compression loads.
- The **load bearing and fatigue behaviour** is dominantly influenced by the grout thickness and shear key configuration. With regard to applied large test loads and to the predicted fatigue resistance based on the analytical ultimate strength capacities, the test specimens reveal a larger fatigue strength than initially expected.

On the basis of experimental test results, three-dimensional numerical models were established accounting for multiaxial grout material behaviour and cyclic strength and stiffness degradation. These models were used for an extended parametric study to evaluate relevant impact factors influencing the load bearing and fatigue behaviour of axially loaded grouted connections. The results of the finite element analysis can be summarised as follows:

- The **Extended Drucker-Prager cap plasticity model** depicts an robust and convenient version of the original Drucker-Prager material model. By calibrating the material model to the used high strength grout materials, it allows to appropriately account for the multiaxial stress states in the confined grout layer. The finite element model was validated by measured global initial load-displacements and local steel strains at the experimental test specimens revealing the applicability of the model.
- A **stress-dependent cyclic damage calculation** based on uniaxial S-N curves for concrete was implemented considering cyclic grout strength and stiffness degradation. By considering the number of load cycles and the dominating stress state, the degradation of each individual grout element can be determined. The cyclic

calculation procedure was validated based on the load-displacement behaviour of the test specimens. While the numerical displacement growth for the alternating load stages agrees very well with the experimental results, the numerical results of the pulsating compression load stages showed an overestimation of the accumulated relative displacements. This overestimation results from the implemented uniaxial S-N curves and the numerical negligence of shear force transmission at crack surfaces. Notwithstanding, subsequent recalculations of the last alternating load scenario including pre-damage from pulsating load stages reasonably complied with the experimental results. Thus, the applied calculation procedure sufficiently accounts for appearing damage and degradation effects leading to conservative design results.

- The tension-tension and tension-compression **stress states** predominantly cause damage in the grout layer due to high local stresses arising at the shear key tip and the shear key weld transition. This effect was confirmed by calculated damage values for axially loaded grouted connections. These locally increased stresses correlate with observed cracks at the test specimens. Moreover, stress states in the grout layer additionally represent increased radial tensile stresses correlating with observed radial cracks at the test specimens.
- Performed **parametric studies** identified that the load bearing and fatigue behaviour is dominantly influenced by the shear key configuration reflected by the shear key height to distance ratio  $h/s$  and the compression strut angle associated with grout thickness. To be more exact, increased grout thicknesses as well as decreased  $h/s$  ratios provoke increased relative displacements and reduced connection stiffness. The material strength of the grout and the friction coefficient were assessed to be of minor importance within the considered bandwidths. Moreover, an descending load scenario evokes a modestly reduced fatigue strength compared to an ascending load scenario.

With the intention to generalise achieved findings and derive appropriate design recommendations, the transferability of the test conditions and a comparison with existing design approaches was performed. According to these considerations, the following conclusions were achieved:

- Analogue to former tests, experimental tests were performed under **ideal laboratory conditions**, which deviate to actual offshore conditions to some extent. It is inferred that variable stochastic loads, additional cyclic bending and torsional loads, geometrical scale effects, geometrical imperfections and ambient conditions have an impact on the fatigue behaviour. To this, the most influence is assumed to be caused by simultaneously acting cyclic bending loads and by the submerged condition. While scale effects can be considered by appropriate finite element analysis, the effect of geometrical imperfections and early age cycling are to be minimised substantially by the offshore installation procedure.
- For a **pre-design**, current simplified **ULS design approaches** accounting for the interface capacity based on shear keys can be used to determine the ultimate bearing capacity of grouted connections with increased grout thicknesses. Comparison of test results with current **fatigue design approaches** reflect that the achieved fatigue

strength for all geometrical test specimens were significantly larger than predicted by the analytical design approach. It is suggested that sufficient safety margins for negative impacts caused by offshore conditions are included in the present design approaches.

- It is recommended that for axially loaded grouted connections circumferential **shear keys** are applied equidistantly over the entire grouted length, excluding small edge regions, enabling for an idealised compression strut angle in the range of  $30^\circ$  to  $50^\circ$ . For the  $h/s$  ratio, a value in the range of 0.04 to 0.06 seems to be appropriate. Even though current design recommendations are applicable, large **grout thickness** are accompanied by intensive circumferential tensile stresses influencing the fatigue behaviour.
- For **detailed design**, finite element analysis are recommended, as the bearing behaviour of grouted connections is rather complex and highly non-linear. Thus, it is recommended to perform simulations accounting for the multiaxial grout stress states for instance by the validated Extended Drucker-Prager material model. Numerical fatigue strength and stiffness degradation calculations can be conducted by considering the proposed and validated numerical procedure accounting for grout damage by uniaxial S-N curves.

Numerical and experimental investigations and corresponding findings enabled to identify and evaluate the impact of increased grout thickness to the fatigue behaviour, to derive relevant influencing parameters and design recommendations for cyclic axially loaded grouted connections at latticed substructures in offshore wind turbines.

## 6.2 Outlook

The conducted investigations lead to a significant enhancement of the state of scientific knowledge and of the general understanding of axially loaded grouted connections in latticed substructures. Nevertheless, the investigations revealed that additional research is required to improve the current knowledge, design tools and approaches.

Particularly, the considerations on the transferability of applied test conditions has outlined that further aspects at offshore sites influence the fatigue behaviour of grouted connections with increased grout annulus. Thus, further experimental investigations addressing relevant influencing parameters are recommended as follows:

- In order to determine a **grout thickness limit** further experimental tests are needed extending the model family. It is proposed to test at least one more grout thickness larger than the tested dimensions. It might be worth to develop a grout thickness dependent design limit on the basis of intensified studies.
- As the load transfer depends mainly on the **shear keys**, further experimental tests are required to consider varied shear key height to distance ratios  $h/s$  and an equidistant shear key application over the entire overlapping length. The focus for the  $h/s$  ratio should cover different shear key distances in order to define limits for the compression strut failure for large grout thicknesses.

- In consequence of actual offshore load scenarios being composed of axial, torsional and bending loads, it is recommended to perform tests covering a **combined load scenario**, in order to determine the respective fatigue strength. With respect to torsional loading, tests are needed to assess the requirement for vertical shear keys. Despite the combined loading, an individual consideration of torsional loads is proposed, in order to quantify the torsional bearing capacity of grouted connections. As is not trivial to realise combined loading in tests, the individual large-scale test results for bending and for axial loading, performed at the Institute for Steel Construction, could be combined to evaluate the impact of combined loading effect by validated finite element simulations.
- With regard to the **load sequence effect**, experimental investigations are needed to confirm the numerical observed results. For that purpose, it is suggested to change the order of applied test load stages and to focus on extreme load scenarios for defining limits. Because offshore loads appear stochastically, probabilistic methods may support the evaluation of varied load sequences and their impact on the fatigue behaviour of grouted connections. Based on tests, the numerical calculation procedure could be enhanced.
- As the impact of **early age cyclic** movement is not sufficiently known at present, additional tests are required accounting for small movements during grout hardening. For one thing, a simplified test procedure being limited to the material influence is expedient. For another, a scaled grouted connection being exposed to a cyclic loading during grout hardening enables to determine the effect on the fatigue behaviour of the connection. Realistic load scenarios for the initial 24 hours need to be considered.
- Large-scale tests of **submerged grouted connections** need to be extended with respect to varied load conditions and test specimens. The occurrence of actual load cases needs to be taken into account to establish reasonable recommendations for the appropriate consideration of water effects.
- For improved correlation of **geometrical scale effects**, offshore measurements of relative displacements at the grouted connection, like the measuring box established at the Institute for Materials Sciences, are highly recommended. By referring documented relative displacements to test results, an improved transferability of experimental results would be achieved.

In addition to the construction related test proposal, following experimental investigations on the high strength grout material are required to improve current design approaches:

- Cyclic **triaxial tests of high strength grout materials** with varying compression-tension stress states are urgently needed to account appropriately for fatigue strength in respect of the confined grout layer in grouted connections. For this purpose, a large number of tests enabling a statistical validated design proposal for the fatigue strength is essential. Finally, the aim should be the implementation of multiaxial S-N curves for high strength concretes.

- In order to determine the impact of **submerged conditions** on the material specific fatigue behaviour, corresponding material tests are required ideally subjected to triaxial stress states.

In addition to experimental investigations, further numerical enhancements are proposed with respect to the fatigue behaviour of grouted connections:

- The presented numerical calculation approach could be improved by accounting for **triaxial S-N curves** for high strength grouts and validated by other similar grouted connection experiments to widen the applicability of the developed method. Moreover, by considering a discrete crack modelling and shear load transfer by the **crack surfaces** the increased interlocking impact could be covered.
- In addition, **probabilistic methods** could be used to consider the distribution and appearance of cracks in the grout layer. For this purpose, intensive numerical investigations are required being validated by crack occurrence at cyclic loaded grouted connections.
- As one of the crucial functions of grouted connections is to compensate for pile driving induced inclinations, it would be reasonable to perform extensive numerical investigations on possible **imperfections** like tilting and eccentricity enabling to quantify the impact and define limits for the installation procedure.

Finally, on the basis of further experimental and numerical investigations on grouted connections and high strength grouts, reasonable design recommendations can be derived leading to an optimised connection. In the end, these optimisations and associated cost reductions promote the expansion of offshore wind turbines and a sustainable development.

## 7 List of References

### 7.1 Standards, Codes of Practice and Laws

- BSH Instruction sheet (2011), *Instruction sheet for the approval in the individual case at the BSH for grouted connections - Verfahrenshinweise für die Zustimmung im Einzelfall (ZiE), beim BSH - Groutverbindungen*, Bundesamt für Seeschifffahrt und Hydrographie, Hamburg und Rostock, Germany (in German).
- BSH Standard (2007), *Standard - Konstruktive Ausführung von Offshore-Windenergieanlagen*, Bundesamt für Seeschifffahrt und Hydrographie, Hamburg und Rostock, Germany, BSH-Nr. 7005 (in German).
- BSH Standard (2015), *Standard Konstruktion - Mindestanforderungen an die konstruktive Ausführung von Offshore-Bauwerken in der ausschließlichen Wirtschaftszone (AWZ)*, Bundesamt für Seeschifffahrt und Hydrographie, Hamburg und Rostock, Germany, BSH-Nr. 7004 (in German).
- CEB-FIP (1993), *Model Code 1990*, Comité Euro-International du Béton, Thomas Telford Services Ltd, London, Great Britain.
- DAfStb Cast Concrete Guideline (2006), *Herstellung und Verwendung von zementgebundenem Vergussbeton und Vergussmörtel*, DAfStb Deutscher Ausschuss für Stahlbeton, Beuth Verlag GmbH, Berlin und Köln, Germany (in German).
- DIBt Bauregellisten (2015), *Bauregelliste A, Bauregelliste B und Liste C*, DIBt Mitteilungen, Ausgabe 2015/02, DIBt Deutsches Institut für Bautechnik, Beuth Verlag GmbH, Berlin, Germany (in German).
- DIBt Technische Baubestimmungen (2015), *Verzeichnis der eingeführten technischen Baubestimmungen*, DIBt Deutsches Institut für Bautechnik, Stand 21.08.2015, Berlin, Germany (in German).
- DIN EN 196-1 (2005), *Methods for testing cement - Part 1: Determination of strength*; DIN Deutsches Institut für Normung e.V., Beuth Verlag GmbH, Berlin, Germany, May 2005 (in German).
- DIN EN 197-1 (2011), *Cement - Part 1: Composition, specifications and conformity criteria for common cements*; DIN Deutsches Institut für Normung e.V., Beuth Verlag GmbH, Berlin, Germany, November 2011 (in German).
- DIN EN 206-1 (2001), *Concrete - Part 1: Specification, performance, production and conformity*, DIN Deutsches Institut für Normung e.V., Beuth Verlag GmbH, Berlin, Germany, July 2001 (in German).
- DIN EN 1992-1-1 (2011), *Eurocode 2 - Design of concrete structures - Part 1-1: General rules and rules for buildings*, DIN Deutsches Institut für Normung e.V., Beuth Verlag GmbH, Berlin, Germany, January 2011 (in German).

- DIN EN 1993-1-1 (2010), *Eurocode 3: Design of steel structures - Part 1-1: General rules and rules for buildings*, European Committee for Standardization, CEN/CENELEC, Brussel, Belgium, DIN Deutsches Institut für Normung e.V., Beuth Verlag GmbH, Berlin, Germany, December 2010 (in German).
- DIN EN 1993-1-6 (2010), *Eurocode 3: Design of steel structures - Part 1-6: Strength and stability of shell structures*, European Committee for Standardization, CEN/CENELEC, Brussel, Belgium, DIN Deutsches Institut für Normung e.V., Beuth Verlag GmbH, Berlin, Germany, December 2010 (in German).
- DIN EN 1993-1-9 (2010), *Eurocode 3: Design of steel structures - Part 1-9: Fatigue*, European Committee for Standardization, CEN/CENELEC, Brussel, Belgium, DIN Deutsches Institut für Normung e.V., Beuth Verlag GmbH, Berlin, Germany, December 2010 (in German).
- DIN EN 1993-2 (2010), *Eurocode 3: Design of steel structures - Part 2: Steel Bridges*, European Committee for Standardization, CEN/CENELEC, Brussel, Belgium, DIN Deutsches Institut für Normung e.V., Beuth Verlag GmbH, Berlin, Germany, December 2010 (in German).
- DIN EN 10025 (2011), *Hot rolled products of structural steels*, DIN Deutsches Institut für Normung e.V., Beuth Verlag GmbH, Berlin, Germany, April 2011 (in German).
- DIN EN 10025-4 (2005), *Hot rolled products of structural steels - Part 4: Technical delivery conditions for thermomechanical rolled weldable fine grain structural steels*, DIN Deutsches Institut für Normung e.V., Beuth Verlag GmbH, Berlin, Germany, April 2005 (in German).
- DIN EN 10210-2 (2006), *Hot finished structural hollow sections of non-alloy and fine grain structural steels - Part 2: Tolerances, dimensions and sectional properties*, DIN Deutsches Institut für Normung e.V., Beuth Verlag GmbH, Berlin, Germany, July 2006 (in German).
- DIN EN 10225 (2009), *Weldable structural steel for fixed offshore structures - Technical delivery conditions*, DIN Deutsches Institut für Normung e.V., Beuth Verlag GmbH, Berlin, Germany, October 2009 (in German).
- DIN EN 12495 (2000), *Cathodic protection for fixed steel offshore structures*, DIN Deutsches Institut für Normung e.V., Beuth Verlag GmbH, Berlin, Germany, April 2000.
- DIN EN 61400-1 (2011), *Wind turbines - Part 1: Design requirements*, DIN Deutsches Institut für Normung e.V., Beuth Verlag GmbH, Berlin, Germany, January 2011 (in German).
- DIN EN 61400-3 (2010), *Wind turbines - Part 3: Design requirements for offshore wind turbines*, DIN Deutsches Institut für Normung e.V., Beuth Verlag GmbH, Berlin, Germany, January 2010 (in German).



- DIN EN ISO 12944 (2008), *Paints and Vanishes - Corrosion protection of steel structures by protective paint systems*, DIN Deutsches Institut für Normung e.V., Beuth Verlag GmbH, Berlin, Germany, July 2008 (in German).
- DIN EN ISO 12944-4 (1998), *Paints and Vanishes - Corrosion protection of steel structures by protective paint systems - Part 4: Types of surfaces and surface preparation*, DIN Deutsches Institut für Normung e.V., Beuth Verlag GmbH, Berlin, Germany, July 1998 (in German).
- DIN EN ISO 19902 (2008), *Petroleum and natural gas industries - Fixed steel offshore structures*, DIN Deutsches Institut für Normung e.V., Beuth Verlag GmbH, Berlin, Germany, July 2008.
- DIN EN ISO 19902 (2014), *Petroleum and natural gas industries - Fixed steel offshore structures*, DIN Deutsches Institut für Normung e.V., Beuth Verlag GmbH, Berlin, Germany, January 2014.
- DIN EN ISO 4287 (2010), *Geometrical Product Specifications (GPS) - Surface texture: Profile method - Terms definitions and surface texture parameters*, DIN Deutsches Institut für Normung e.V., Beuth Verlag GmbH, Berlin, Germany, July 2010 (in German).
- DIN EN ISO 4288 (1998), *Geometrical Product Specifications (GPS) - Surface texture: Profile method - Rules and procedures for the assessment of surface texture*, DIN Deutsches Institut für Normung e.V., Beuth Verlag GmbH, Berlin, Germany, April 1998 (in German).
- DIN EN ISO 5817 (2003), *Welding - Fusion-welded joints in steel, nickel, titanium and their alloys (beam welding excluded)*, DIN Deutsches Institut für Normung e.V., Beuth Verlag GmbH, Berlin, Germany, December 2003 (in German).
- DIN EN ISO 6892-1 (2009), *Metallic materials - Tensile testing Part 1: Method of test at room temperature* DIN Deutsches Institut für Normung e.V., Beuth Verlag GmbH, Berlin, Germany, December 2009 (in German).
- DNV-OS-C101 (2011), *Design of Offshore Steel Structures - General (LRFD Method)*, Det Norske Veritas AS, Hørvik, Norway, April 2011.
- DNV-OS-C502 (2012), *Offshore Concrete Structures*, Det Norske Veritas AS, Hørvik, Norway, September 2012.
- DNV-OS-J101 (2004), *Design of Offshore Wind Turbines Structures*, Det Norske Veritas AS, Hørvik, Norway, June 2004.
- DNV-OS-J101 (2014), *Design of Offshore Wind Turbines Structures*, Det Norske Veritas AS, Hørvik, Norway, May 2014.
- E DIN 50100 (2015), *Load controlled fatigue testing - Execution and evaluation of cyclic tests at constant load amplitudes on metallic specimens and components*, DIN

- Deutsches Institut für Normung e.V., Beuth Verlag GmbH, Berlin, Germany, November 2015 (in German).
- EEG (2014), *Gesetz für den Ausbau erneuerbarer Energien - Erneuerbare Energien Gesetz 2014* (German Renewable Energy Source Act), Berlin, Germany (in German).
- GL Guideline (2012), *Guideline for the Certification of Offshore Wind Turbines*, GL Renewables Certification, Germanischer Lloyd Industrial Services GmbH, Hamburg, Germany, December 2012.
- GL Technical Note (2013), *Certification of Grouted Connections for Offshore Wind Turbines*, GL Renewables Certification, Germanischer Lloyd Industrial Services GmbH, Hamburg, Germany.
- Model Code 2010 (2012), *fib Model Code for Concrete Structures*, Final draft - Volume 1/Volume 2, fib Bulletin 65: CEB-FIP, International Federation for Structural Concrete (fib), Lausanne Switzerland, ISSN 1562-3610, ISBN 978-2-88394-105-2.
- Norsok Standard N-004 (2013), *Design of steel structures*, Rev. 3, Standards Norway, Lysaker, Norway.

## 7.2 Book, Articles and Handbooks

- Achmus, M. (2011), *Bemessung von Monopiles für die Gründung von Offshore-Windenergieanlagen - Konzepte und offene Fragen*, Bautechnik 88, Heft 9, pp. 602-616 (in German).
- Achmus, M., Kuo, Y.-S., Abdel-Rahman, K. (2009), *Behaviour of monopile foundations under cyclic lateral load*, Computers and Geotechnics, Vol. 36, pp. 725-735, Elsevier Ltd.
- Almar-Naess, A. (1985), *Fatigue Handbook - Offshore Steel Structures*, Tapir Publishers, Trondheim, Norway, ISBN 82-519-0662-8.
- Anders, S. (2007), *Betontechnologische Einflüsse auf das Tragverhalten von Grouted Joints*, Dissertation, Berichte aus dem Institut für Baustoffe, Heft 6, Leibniz Universität Hannover (in German).
- Andersen, M.S. & Petersen, P. (2004), *Structural Design of Grouted Connection in Offshore Steel Monopile Foundations*, Proceedings of the Global Windpower Conference 2004.
- Aritenang, W., Elnashai, A. S., Dowling, P. J. (1990), *Failure Mechanism of Weld-Beaded Grouted Pile/Sleeve Connections*, Marine Structures 3, pp. 391 - 417, Elsevier Science Publishers, United Kingdom, ISBN 0951-8339/90.
- Billington, C. J. (1978), *The Integrity of Jacket to Pile Connections*, Proceedings of the 4<sup>th</sup> International Conference for the Offshore Industries Oceanology International, pp. 79 - 88, Brighton, United Kingdom.
- Billington, C. J. & Lewis, G. H. G., (1978), *The Strength of Large Diameter Grouted Connections*, Proceedings of the 10<sup>th</sup> Annual International Offshore Technology Conference, OTC 3083, pp. 291 - 301, Houston, United States of America.
- Billington, C. J. & Tebbett, I. E. (1980), *The Basis for New Design Formulae for Grouted Jacket to Pile Connections*, Proceeding of the 12<sup>th</sup> Annual International Offshore Technology Conference, OTC 3788, pp. 449 - 458, Houston, United States of America.
- Billington, C. J. & Tebbett, I. E. (1982), *Fatigue Strength of Grouted Tubular Steel Connections for Offshore Structures*, Proceedings of the International Association for Bridge and Structural Engineering, pp. 625 - 632, IABSE Colloquium, Lausanne, Switzerland.
- Böker, C. (2009), *Load simulation and local dynamics of support structures of offshore wind turbines*, Schriftenreihe des Instituts für Stahlbau der Gottfried Wilhelm Leibniz Universität Hannover, Heft 26, Shaker-Verlag, ISBN 978-3-8322-8850-1.
- Boswell, L. F. & D'Mello, C. (1986), *The Fatigue Strength of Grouted Repaired Tubular Members*, Proceeding of the 18<sup>th</sup> Annual International Offshore Technology Conference, OTC 5307, pp. 147 - 152, Houston, United States of America.

- Cao, W., Liu, H.-C., Song, Y.-P. (2006), *Experimental investigation of plain concrete under triaxial tension-compression cyclic loading*, Magazine of Concrete Research, Vol. 58, No. 4, pp. 209 - 219, May 2006, Thomas Telford Ltd., ISSN 0024-9831.
- Chen, W. F. (1982), *Plasticity in Reinforced Concrete*, McGraw-Hill Book Company, New York, United States of America, ISBN 0-07-010687-8.
- Cheng, P. W., Jacquemin, J., Duffy, J., Passon, P., Kühn, M., Dahlberg, J.-A., Montgomerie, B., Thiringer, T., Bergström, H. (2005), *Research Program of the Utgrunden Demonstration Offshore Wind Farm - Executive Summary Report*, supported by Swedish Energy Agency, grant number STEM P11518-2, Sweden.
- Cornelissen, H. A. W. (1984), *Fatigue Failure of Concrete in Tension*, Heron, Vol. 29, No.4, Delft University of Technology, Delft, The Netherlands.
- Cornelissen, H. A. W. & Reinhardt, H. W. (1984), *Uniaxial tensile fatigue failure of concrete under constant-amplitude and programme loading*, Magazine of Concrete Research, Vol. 36, No. 129, pp. 216 - 226, December 1984.
- Dahl, K. K. B. (1992), *A Constitutive Model for Normal and High Strength Concrete*, Serie R, No 287, Technical University of Denmark, Denmark, ISBN 87-7740-107-7.
- DNV (1994), *Factors of Safety for Grouted Connection Phase I the Impact of Cyclic Load on Connections with high h/s Values*, Technical Report, Report No. 94-3243, Det Norske Veritas AS Industry AS, Hørvik, Norway.
- Domone, P. L. J. & Jefferis, S. A. (1994), *Structural Grouts*, Japman & Hall, Blackie Academic & Professional, Cambridge, United Kingdom, ISBN 07514 0097 1.
- Drucker, D.C., Prager, W. (1952), *Soil Mechanics and Plasticity Analysis of Limit Design*, Quarterly of Applied Mathematics, Vol. 10, No. 2, pp. 157 - 165.
- Elnashai, A. S., Carroll, B. C., Dowling, P. J. (1986), *Full-Scale Testing and Analysis of Prestressed Grouted Pile/Platform Connections*, Proceedings of the 18<sup>th</sup> Annual International Offshore Technology Conference, OTC 5325, pp. 301 - 311, Houston, United States of America.
- Elnashai, A. S. & Dowling, P. J. (1991), *Strength of composite tubular connections*, Proceedings Instn. Civ. Engrs., Part 2, Vol 91, Issue 3, Paper No. 9590, pp. 377 - 398, United Kingdom.
- Fehling, E., Leutbecher, T., Schmidt, M., Ismail, M. I. (2013), *Grouted connections for offshore wind turbines structures - Part 2: Structural modelling and design of grouted connections*, in Steel Construction 6, No. 3, pp. 216 - 228, Ernst & Sohn Verlag, Berlin, Germany.
- Forsyth, P. & Tebbett, I. E. (1988), *New Test Data on the Strength of Grouted Connections With Closely Spaced Weld Beads*, Proceedings of the 20<sup>th</sup> Annual International Offshore Technology Conference, OTC 5833, pp. 237 - 245, Houston, United States of America.

- Foster, C., Regueiro, R., Fossum, A., Borja, R. (2005), *Implicit numerical integration of a three invariant, isotropic/kinematic hardening cap plasticity model for geomaterials*, Computer Methods in Applied Mechanics and Engineering, Issue 194, pp. 5109-5138, Elsevier.
- Fossum, A. F. & Fredrich, J. T. (2000), *Cap plasticity models and compactive and dilatant pre-failure deformation*, Pacific Rocks 200: Rock around the Rim. Proceedings of the Fourth North American Rock Mechanics Symposium. Eds. Girard, J., Liebman, M., Breeds, C., Doe, T., Balkema, A.A., pp. 1169-1176, Rotterdam, The Netherlands.
- Gasch, R. & Twele, J. (2010), *Windkraftanlagen - Grundlagen, Entwurf, Planung und Betrieb*, 6. Auflage, Vieweg + Teubner Verlag, Wiesbaden, Germany, ISBN 978-3-8348-0693-2 (in German).
- Göhlmann, J. (2008), *Zur Schädigungsberechnung an Betonkonstruktionen für Windenergieanlagen unter mehrstufiger und mehraxialer Ermüdungsbeanspruchung*, Dissertation, Institut für Massivbau, Leibniz Universität Hannover, Hannover, Germany (in German).
- Grassl, P., Lundgren, K., Gylltoft, K. (2002), *Concrete in compression: a plasticity theory with a novel hardening law*, International Journal of Solids and Structures 39, Elsevier, pp. 5205 - 5223.
- Grünberg, J. & Oneschkow, N. (2011), *Gründung von Offshore-Windenergieanlagen aus filigranen Betonkonstruktionen unter besonderer Beachtung des Ermüdungsverhaltens von hochfesten Beton*, Abschlussbericht zum BMU-Verbundforschungsprojekt (Fkz. 0327673A), Institut für Massivbau, Leibniz Universität Hannover (in German).
- Grünberg, J. & Ertel, C. (2012), *A Triaxial Fatigue Failure Model for Ultra-High-Performance Concrete (UHPC)*, Proceeding of the 3<sup>rd</sup> International Symposium HiPerMat, . pp. 603 - 610, März 2012, Kassel, Germany.
- Grünberg, J., Göhlmann, J., Marx, S. (2014a), *Mechanische Modelle für mehraxiales Festigkeits- und Ermüdungsversagen von Stahlbeton*, Beton- und Stahlbetonbau 109, Heft 6, pp. 403 - 416, Ernst & Sohn Wiley Verlag, Berlin, Germany (in German).
- Grünberg, J., Lohaus, L., Ertel, C., Elsmeier, K. (2014b), *Fatigue Behaviour of UHPC due to Uni- and Multiaxial Loading - Experimental Investigations and Development of Mechanical Model*, Sustainable building with ultra-high performance concrete, Michael Schmidt (Editor), Kassel University Press, Germany, pp. 453 - 478, ISBN 978-3-86219-480-3.
- Hampel, T. (2006), *Experimentelle Analyse des Tragverhaltens von Hochleistungsbeton unter mehraxialer Beanspruchung*, Dissertation, Schriftenreihe Konstruktiver Ingenieurbau Dresden, Technische Universität Dresden, Heft 10, Germany, ISSN 1613-6934 , ISBN 3-86005-543-7 (in German).

- Harwood, R. G., Billington, C. J., Buitrago, J., Sele, A. B., Sharp, J. V. (1996), *Grouted Pile to Sleeves Connections: Design Provisions for the New ISO Standard for Offshore Structures*, Proceedings of the ASME 15<sup>th</sup> International Conference on Offshore Mechanics and Arctic Engineering OMAE, Vol. 3 Materials Engineering, pp. 1 - 12, Italy.
- Hilsdorf, H. & Kesler, C. E. (1960), *The Behaviour of Concrete in Flexure Under Varying Repeated Loads*, T. & A. M. Report No. 172, Department of Theoretical and Applied Mechanics University of Illinois, United States of America.
- Holmen, J. O. (1979), *Fatigue of Concrete by Constant and Variable Amplitude Loading*, Division of Concrete Structures, The Norwegian Institute of Technology, The University of Trondheim, Norway.
- Hooi, T. T. (2000), *Effects of passive confinement on fatigue properties of concrete*, Magazine of Concrete Research, Vol. 52 No 1, February 2000, Thomas Telford Ltd., pp. 7 - 15, ISSN 0024-9831.
- Hordyk, M. (1996), *The Static and Fatigue Strength of Grouted Pile-sleeve Connections*, Fatigue in Offshore Structures, Vol. 2, Oxford & IBH Publishers, London, United Kingdom.
- Ingebrigtsen, T., Løset, Ø., Nielsen, S. G. (1990), *Fatigue Design and Overall Safety of Grouted Pile Sleeve Connections*, Proceedings of the 22<sup>nd</sup> Annual International Offshore Technology Conference, OTC 6344, pp. 615 - 628, Houston, United States of America.
- Karsan, D. I. & Krahl, N. W. (1984), *New API Equation for Grouted Pile-to-Structure Connections*, Proceedings of the 16<sup>th</sup> Annual International Offshore Technology Conference, OTC 4715, pp. 49 - 56, Houston, United States of America.
- König, G. & Danielewicz, I. (1994), *Ermüdungsfestigkeit von Stahlbeton- und Spannbetonbauteilen mit Erläuterungen zu den Nachweisen gemäß CEB-FIP Model Code 1990*, Heft 439, Beuth Verlag, Berlin, Germany, ISSN 0171-7197, ISBN 3-410-65639-1 (in German).
- König, G., Tue, N. V., Zink, M. (2001), *Hochleistungsbeton - Bemessung, Herstellung und Anwendung*, Ernst & Sohn Wiley Verlag Berlin, Germany, ISBN 3-433-01738-7 (in German).
- Krahl, N. W. & Karsan, D. I. (1985), *Axial Strength of Grouted Pile-to-Sleeve Connections*, Journal of Structural Engineering, Vol. 111, No. 4, pp. 889 - 905, ISSN 0733-9445/85/0004-0889.
- Kühn, M. (2001), *Offshore Windpark Utgrunden - Projekterfahrungen mit einem Offshore-Windpark in Schweden*, Proceedings of the Offshore Congress Berlin, Section VI, pp. VI-7 - 10 Berlin, Germany (in German).

- Kupfer, H. (1973), *Das Verhalten des Betons unter mehrachsiger Kurzzeitbelastung unter besonderer Berücksichtigung zweiachsiger Beanspruchung*, DAfStb, Heft 229, Ernst & Sohn (in German).
- Lampton, W. B., Jirsa, J. O., Yura, J. A. (1986), *Grouted Pile-to-Sleeve Connection Tests*, Report on a Research Project, PMFSEL Report No. 86-7, Phil M. Ferguson Structural Engineering Laboratory, The University of Texas at Austin, Texas, United States of America.
- Lewis, G. H. G., Livett, I. G., Mead, K. C. (1980), *A Cost Saving Design for Pile to Structure Connections as Applied to BP Magnus*, Proceedings of the 12<sup>th</sup> Annual International Offshore Technology Conference, OTC 3789, pp. 495 - 466, Houston, United States of America.
- Lochte-Holtgreven, S. (2013), *Zum Trag- und Ermüdungsverhalten biegebeanspruchter Grouted Joints in Offshore-Windenergieanlagen*, Dissertation, Schriftenreihe des Instituts für Stahlbau der Gottfried Wilhelm Leibniz Universität Hannover, Heft 29, Shaker-Verlag, ISBN 978-3-8440-1987-2 (in German).
- Lochte-Holtgreven, S. & Bechtel, A. (2014), *Grout-Verbindungen in Monopile-Tragstrukturen von Offshore-Windenergieanlagen - Erkenntnisse und Entwicklungen*, Stahlbau 83, Heft 4, pp. 273 - 277, Ernst & Sohn Verlag, Berlin, Germany (in German).
- Lohaus, L., Wefer, M., Oneschkow, N. (2011), *Ermüdungsbemessungsmodell für normal-, hoch- und ultrahochfeste Betone*, Beton- und Stahlbetonbau 106, Heft 12, pp. 836 - 846, Ernst & Sohn Wiley Verlag, Berlin, Germany (in German).
- Lohaus, L., Lindschulte, N., Scholle, N., Werner, M. (2012), *Concrete technology for grouted joints - requirements for building materials and execution techniques*, Stahlbau 81, Heft 9, pp. 689 - 694, Ernst & Sohn Verlag, Berlin, ISSN 0038-9145 (in German).
- Lohaus, L., Schaumann, P., Lochte-Holtgreven, S., Bechtel, A., Griese, R., Lindschulte, N. (2013), *Approvals for grouted joints in offshore substructures*, Bautechnik 90, Heft 7, pp. 402 - 409, Ernst & Sohn Verlag, Berlin, Germany, ISSN 1437 0999, (in German).
- Lohaus, L., Cotardo, D., Werner, M. (2014), *A Test System to Simulate the Influence of Early Age Cycling on the Properties of Grout Material*, in Proceedings of the 24<sup>th</sup> International Offshore and Polar Engineering Conference (ISOPE), Busan, Korea, pp. 234 - 239, ISSN 1098-6189.
- Lohaus, L. & Griese, R. (2014), *Betontechnik meets Stahlbau - Erfahrungen mit Grouted Joints in der Offshore-Windenergie*, Festschrift gewidmet Prof. Dr.-Ing. Peter Schaumann zur Vollendung seines 60. Lebensjahres, Hrsg Peter Schaumann, S. 345 - 354, Hannover, Germany (in German).
- Lohaus, L. & Weicken, H. (2014), *Measures for autogenous shrinkage compensation and their influence on selected durability properties*, International RILEM Conference on Application of Superabsorbent Polymers and Other New Admixtures in Concrete Construction, in RILEM Proceedings PRO95, pp. 245 -56, Dresden, Germany.

- Lohaus, L., Schaumann, P., Cotardo, D., Kelma, S., Werner, M. (2015), *Experimental and Numerical Investigations on Grouted Joints in Monopiles Subjected to Early-age Cycling to Evaluate the Influence of Different Wave Loadings*, in Proceedings of the 25<sup>th</sup> International Offshore and Polar Engineering Conference (ISOPE), pp. 268 - 276, Hawaii, United States of America, ISSN 1098-6189.
- Lotsberg, I. (2011), *On the Capacity of Grouted Connections in Wind Turbines Structures*, Presentation at the Offshore Engineering Society London, on 2 June 2011, London, United Kingdom.
- Lotsberg, I., Bertnes, H., Cramer, E. (2011), *Joint Industry Project - Summary Report From the JIP on the Capacity of Grouted Connections in Offshore Wind Turbines Structures*, Technical Report No. 2010-1053, Revision No. 05, Det Norske Veritas, Høvik, Norway.
- Lotsberg, I. Lervik, A., Bertnes, H. (2013), *Capacity of Cylindrical Shaped Grouted Connections with Shear Keys*, Background Report No. 2011-1415 Rev. No. 09, Det Norske Veritas, Høvik, Norway.
- Lotsberg, I. & Solland, G. (2013), *Assessment of Capacity of Grouted Connections in Piled Jacket Structures*, Proceedings of the ASME 2013, 32<sup>nd</sup> International Conference on Ocean, Offshore and Arctic Engineering OMAE 2013, 9-14 June, Nantes, France.
- Meyer, L. (2007), *Zum Einfluss der Kontaktzone bei der Modellierung des Elastizitätsmoduls von Beton*, Dissertation, Herausgeber Institut für Bauforschung der RWTH Aachen, Rheinisch-Westfälischen Technischen Hochschule Aachen, Aachen, Germany (in German).
- Nelissen, L.J.M. (1972), *Biaxial testing of normal concrete*, HERON, Vol 18, No. 1.
- Oh, B. H. (1991), *Cumulative Damage Theory of Concrete under Variable-Amplitude Fatigue-Loadings*, Title no 88-M6, ACI Materials Journal, Vol. 88, No. 1, pp. 41 - 48, January-February 1991.
- OTH 86210 (1986), *The Strength of Grouted Pile-Sleeve Connections*, Offshore Technology Report, Department of Energy, Tests by Wimpey Laboratories Limited, Report by Wimpey Offshore Engineers & Constructors Limited, United Kingdom, ISBN 011 412860X.
- OTH 86230 (1987), *A Study of Length, Longitudinal Stiffening and Size Effects on Grouted Pile-Sleeve Connections*, Offshore Technology Report, Department of Energy, Tests by Wimpey Laboratories Limited, Report by Wimpey Offshore Engineers & Constructors Limited, United Kingdom, ISBN 011 412874X.
- Ottosen, N. S. (1977), *A Failure Criterion for Concrete*, Journal of the Engineering Mechanics Division, Vol. 103, No. 4, pp. 527 - 535, August 1977, American Society of Civil Engineers, ISSN 00447951.



- Petersen, C. (2013), *Stahlbau - Grundlagen der Berechnung und baulichen Ausbildung von Stahlbauten*, 4. Auflage, Springer Vieweg, München, Deutschland, ISBN 978-3-528-38837-9 (in German).
- Pfanner, D. (2003), *Zur Degradation von Stahlbetonbauteilen unter Ermüdungsbeanspruchung*, Dissertation, Fortschritt-Berichte VDI, Reihe 4, Nr. 189, Technisch-wissenschaftliche Mitteilungen, Institut für Konstruktiven Ingenieurbau, Ruhr-Universität Bochum, ISBN 3-18-318904-6 (in German).
- Pölling, R. (2000), *Eine praxisnahe, schädigungsorientierte Materialbeschreibung von Stahlbeton für Strukturanalysen*, Dissertation, Forschungsarbeit aus dem Sonderforschungsbereich 398 - Lebensdauerorientierte Entwurfskonzepte - Ruhr-Universität Bochum, ISBN 3-8311-1473-0 (in German).
- Rabbat B. G., & Russell, H. G. (1985), *Friction Coefficient of Steel on Concrete or Grout*, Journal of Structural Engineering, Vol. 111, No. 3, pp. 505 - 515, ASCE, ISSN 0733-9445/85/003-0505.
- Radaj, D. & Vormwald, M. (2007), *Ermüdungsfestigkeit - Grundlagen für Ingenieure*, Springer Verlag, Germany, ISBN 978-3-540-71458-3 (in German).
- Schaumann, P. & Wilke, F. (2006), *Fatigue of Grouted Joint Connections*, Proceedings of the 8<sup>th</sup> German Wind Energy Conference DEWEK 2006, Bremen, Germany.
- Schaumann, P., Böker, C., Rutkowski, T., Wilke, F. (2007), *Tragstrukturen für Windenergieanlagen*, Stahlbaukalender 2007, Kuhlmann, U. (ed.), Ernst & Sohn Verlag, pp. 569 - 645, Berlin, Germany, ISBN 978-3433018347 (in German).
- Schaumann, P. & Wilke, F. (2007), *Design of Large Diameter Hybrid Connections Grouted with High Performance Concrete*, Proceedings of the 17<sup>th</sup> International Offshore and Polar Engineering Conference ISOPE, Lisboa, Portugal.
- Schaumann, P., Wilke, F., Lochte-Holtgreven, S. (2008a), *Grouted Joint Connections of Monopile Support Structures - Structural and Fatigue Behaviour*, Stahlbau 77, Heft 9, pp. 647 - 658, Ernst & Sohn Verlag, Berlin, Germany, ISBN 978-3-936634-13-6 (in German).
- Schaumann, P., Wilke, F., Lochte-Holtgreven, S. (2008b), *Bending tests on Grouted Joints for Monopile Support Structures*, in Proceedings of the 10<sup>th</sup> German Wind Energy Conference DEWEK 2018, Bremen, Germany.
- Schaumann, P., Keindorf, C., Lochte-Holtgreven, S. (2009), *Static and dynamic axial compression tests on grouted tube-in-tube connections with various grout materials*, Bautechnik 86, Heft 11, pp. 719 - 728, Ernst & Sohn Verlag, Berlin, Germany (in German).

- Schaumann, P., Lochte-Holtgreven, S., Lohaus, L., Lindschulte, N. (2010a), *Sinking grouted joints in offshore wind turbines - Bearing behaviour, repair and optimisation*, Stahlbau 79, Heft 9, pp. 637 - 647, Ernst & Sohn Verlag, Berlin, Germany, ISSN 0038-9145 (in German).
- Schaumann, P., Bechtel, A., Lochte-Holtgreven, S. (2010b), *Fatigue Performance of Grouted Joints in Offshore Wind Energy Converters in Deeper Waters*, in Proceedings of the 20<sup>th</sup> International Ocean and Polar Engineering Conference ISOPE, pp. 672 - 679, Beijing, China, ISBN 978-1 880653-77-7.
- Schaumann, P. & Lochte-Holtgreven, S. (2011), *Damage Model for Hybrid Connections in Offshore Wind Turbines*, Stahlbau 80, Heft 4, pp. 226 - 232, Ernst & Sohn Verlag, Berlin, Germany (in German).
- Schaumann, P., Böker, C., Bechtel, A., Lochte-Holtgreven, S. (2011a), *Support Structures of Wind Energy Converters*, Environmental Wind Engineering and Design of Wind Energy Structures, C.C. Baniotopoulos et al. (eds.), pp. 191 - 253, CISM Courses and Lectures, Udine, Springer Vienna, ISBN 978-3-7-0953-3.
- Schaumann, P., Lochte-Holtgreven, S., Hausschildt, M., Klose, M., Hülsmann, N., Reisch, A., Schaaf, R., Kaiser, A. (2011b), *Experimental and numerical analysis of the load bearing behaviour of grouted structures for offshore wind turbines*, Final Report to the research project GROW Fkz. 0327585, Hannover, Germany (in German).
- Schaumann, P., Bechtel, A., Lochte-Holtgreven, S. (2012a), *Nachweisverfahren zur Tragfähigkeit überwiegend axial beanspruchter Grouted Joints in Offshore-Tragstrukturen*, Stahlbau 81, Heft 9, pp. 679-688, Ernst & Sohn Verlag, Berlin, Germany (in German).
- Schaumann, P., Bechtel, A., Lochte-Holtgreven, S. (2012b), *Grouted Connections with Large Annulus in Offshore Wind Turbines and Substations*, Proceedings of the 11<sup>th</sup> German Wind Energy Conference DEWEK 2012, Bremen, Germany.
- Schaumann, P., Bechtel, A., Lochte-Holtgreven, S. (2013a), *Grouted Joints for Offshore Wind Turbines Jackets under Full Reversal Axially Loading Conditions*, Proceedings of the 23<sup>rd</sup> International Ocean and Polar Engineering Conference ISOPE, pp. 173 - 180, Anchorage, United States of America, ISBN 978-1 880653-99-9.
- Schaumann, P., Bechtel, A., Lochte-Holtgreven, S., Lohaus, L., Lindschulte, N., Griese, R. (2013b), *Approvals for Grouted Joints in Offshore Structures in Germany*, Proceedings of the European Wind Energy Conference 2013, Vienna, Austria
- Schaumann, P., Bechtel, A., Raba, A. (2014a), *Effects of Attrition due to Water in Cyclically Loaded Grouted Joints*, Proceedings of the 33<sup>th</sup> International Conference on Ocean, Offshore and Arctic Engineering OMAE, San Francisco, United States of America.

- Schaumann, P., Bechtel, A., Lochte-Holtgreven, S. (2014b), *Grouted Joints in Monopiles - Analyses and Discussion of Earlier Design Approaches for Connections without Shear Keys*, Proceedings of the 24<sup>th</sup> International Ocean and Polar Engineering Conference ISOPE, pp. 47 - 53, Busan, Korea, ISBN 978-1 80653 91-3.
- Schaumann, P., Bechtel, A., Lochte-Holtgreven, S., Wilke, F. (2014c), *Analysis methods for grouted joints in offshore wind energy converters under predominant bending*, Stahlbau 83, Heft 8, pp. 509 - 515, Ernst & Sohn Verlag, Berlin, Germany (in German).
- Schaumann, P., Bechtel, A., Raba, A. (2016), *Impact of Water on the Fatigue Performance of Large-Scale Grouted Connection Tests*, Proceedings of the 35<sup>th</sup> International Conference on Ocean, Offshore and Arctic Engineering OMAE, June 2016, Busan, South Korea (accepted).
- Schlegel, R. (2006), *Materialmodelle für das Bauwesen und die Geotechnik in ANSYS*, 24<sup>th</sup> CAD-FEM User's Meeting International Congress on FEM Technology, Stuttgart, Germany (in German).
- Sele, A. B. & Kjeoy, H. (1989), *Background for the New Design Equations for Grouted Connections in the DnV Draft Rules for Fixed Offshore Structures*, Proceedings of the 21<sup>st</sup> Annual International Offshore Technology Conference, OTC 6163, pp. 463 - 474, Houston, United States of America.
- Sele, A., Skjølde, M., Moe, E. T. (1994), *Factors of Safety for Grouted Connection Phase II the Impact of Cyclic Load on Connections with High H/S Values*, Technical Report, Report No 94-3243, Det Norske Veritas, Høvik, Norway.
- Smith, B. L. & Tebbett, I. E. (1989), *New Data on Grouted Connections With Large Grout Dimensions*, Proceedings of the 21<sup>st</sup> Annual International Offshore Technology Conference, OTC 5910, pp. 291 - 298, Houston, United States of America.
- Sørensen, E. V. (2009), *Mechanical Properties of High Performance Cementitious Grout (II)*, DCE Contrast Report No. 66, Aalborg University, Department of Civil Engineering, Aalborg, Denmark.
- Speck, K. (2008), *Concrete under multiaxial loading conditions - A Constitutive Model for Short-Time Loading of High Performance Concretes*, Dissertation, Technische Universität Dresden (in German).
- Takhar, S. S., Jordaan, I.J., Gamble, B.R. (1974), *Fatigue of Concrete under Lateral Confining Pressure*, Abeles Symposium of Fatigue of Concrete, ACI Publication SP - 41, pp. 59 - 69.
- Tech-wise (2001), *Model tests of the grouted transition piece for the Horns Rev turbines*, Fredericia, Denmark (original in Danish, english translation by Tech-wise).

- 
- Wedel, F. (2013), *Numerical Investigations on the Influence of Geometrical Imperfections in Grouted Connections of Offshore Wind Turbines*, Bachelor Thesis at the Institute for Steel Construction supervised by Anne Bechtel, Examiner. Prof. Dr.-Ing. P. Schaumann and Dr.-Ing. S. Lochte-Holtgreven, Leibniz University Hannover, October 2013 (in German).
- Wefer, M. (2010), *Materialverhalten und Bemessungswerte von ultrahochfestem Beton unter einaxialer Ermüdungsbeanspruchung*, Dissertation, Berichte aus dem Institut für Baustoffe, Heft 7, ISBN 978-3-936634-06-8 (in German).
- Wilke, F. (2014), *Load bearing behaviour of grouted joints subjected to predominant bending*, Dissertation, Schriftenreihe des Instituts für Stahlbau der Gottfried Wilhelm Leibniz Universität Hannover, Heft 31, ISBN 978-3-8440-2481-4.
- Winkler, H. (2010), *Über mechanische Eigenschaften von normalfestem und hochfestem Beton unter besonderer Berücksichtigung des Elastizitätsmoduls*, Forschungsbericht 288, BAM Bundesanstalt für Materialforschung und -prüfung (Hrsg.), Berlin, Germany (in German).
- Yamasaki, T., Hara, M., Takahashi, C. (1980), *Static and Dynamic Tests on Cement-Grouted Pipe-to-Pipe Connections*, Proceedings of the 12<sup>th</sup> Annual International Offshore Technology Conference, OTC 3790, pp. 467 - 476, Houston, United States of America.
- Zilch, K. & Zehetmaier, G. (2010), *Bemessung im konstruktiven Betonbau - Nach DIN 1045-1 (Fassung 2008) und EN 1992-1-1 (Eurocode 2)*, 2. neu bearbeitete und erweiterte Auflage, Springer Verlag Berlin Heidelberg, ISBN 978-3-540-70637-3 (in German).

### 7.3 Product Information and Data Sources

- 4Coffshore-database (2015), *Global Offshore Wind Farm Database*, www.4coffshore.com, 4C Offshore Ltd, United Kingdom (Accessed 28 September 2015).
- Abaqus (2016), *Abaqus Documentation*, Dassault Systèmes Simulia Corp., Providence, RI, United States of America.
- alpha ventus (2012), *Fact sheet* by Christian Bartsch - Press Relations Officer, link: [http://www.alpha-ventus.de/fileadmin/user\\_upload/av\\_Factsheet\\_engl\\_Dec2012\\_2.pdf](http://www.alpha-ventus.de/fileadmin/user_upload/av_Factsheet_engl_Dec2012_2.pdf).
- ANSYS (2014), *ANSYS Academic Teaching Advanced*, Release 14.5, Ansys Inc., Canonsburg, United States of America
- ANSYS (2013), *Mechanical APDL Material Reference*, SAS, IP Inc. Canonsburg, United States of America.
- Atena (2016), *Program Documentation Part 1 - Theory*, [http://www.cervenka.cz/assets/files/atenapdf/ATENA\\_Theory.pdf](http://www.cervenka.cz/assets/files/atenapdf/ATENA_Theory.pdf) Cervenka, Consulting, Prag, Czech Republic (Accessed 23 March 2016).
- BASF Masterflow<sup>®</sup> (2011), *Technical Data Sheet Masterflow<sup>®</sup> 9500*, Augsburg, Germany.
- BASF Masterflow<sup>®</sup> (2015), *Technical Data Sheet Masterflow<sup>®</sup> 9800*, Augsburg, Germany.
- Densit Ducorit<sup>®</sup> (2013), *Product Data Sheet - ultra high performance grout*, ITW Densit ApS, Denmark.
- EEW (2011), *Inspection certificates*, Erndtebrücker Eisenwerke GmbH & CO KG.
- European Commission (2010), *Energy 2020 - A strategy for competitive, sustainable and secure energy*, Communication from the Commission to the European Parliament, the Council, the European Economic and Social Committee and the Committee of the Regions, SEC (2010) 1346, Brussel, Belgium.
- European Wind Energy Association (2016), *The European offshore wind industry - key trends and statistics 2015*, Editor: Ivan Pineda, February 2016.
- German government (2013), *Deutschlands Zukunft gestalten*, Coalition agreement between CDU, CSU, and SPD, 18<sup>th</sup> legislation period, Berlin, Germany (in German).
- German Windguard (2015), *Status des Offshore-Windenergieausbaus in Deutschland - Jahr 2015*, Deutsche Windguard GmbH, Varel, Germany (in German).
- MASA (2016), *Macroscopic Space Analysis*, Josko Ozbolt, [http://www.iwb.uni-stuttgart.de/fesimulation/masapdf/MASA\\_general.pdf](http://www.iwb.uni-stuttgart.de/fesimulation/masapdf/MASA_general.pdf), Institute of Construction Materials, University of Stuttgart (Accessed 23 March 2016).
- Pagel (2014), *Technisches Merkblatt 0214*, QS-Formblatt 09.14, Rev. 28, Pagel Spezial-Beton GmbH & Co KG, Essen, Germany.

## 8 Lists

### 8.1 List of Figures

Figure 1-1. Offshore wind energy turbines at the wind farm alpha ventus (photo: Bechtel).....	1
Figure 2-1. Grouted connections at offshore oil & gas platforms (left) and offshore wind turbines with monopile and jacket (right) based on Lamport (1988) and Schaumann et al. (2010b).....	6
Figure 2-2. Comparison of diameter to thickness ratios $D_g/t_g$ and water depths for varied grouted connections in accordance with 4coffshore-database (2015), Lochte-Holtgreven (2013), alpha ventus (2012), Ingebrigtsen et al. (1990), Sele & Kjoey (1989), Boswell & D'Mello (1986) and Elnashai et al. (1986).....	8
Figure 2-3. A jacket with a pre-piled grouted connection (left) and a tripod (right) with a post-piled grouted connection at offshore wind turbines adapted from Schaumann et al. (2012a).....	8
Figure 2-4. Geometric parameters and shear key geometry options: a) weld bead, b) square bar, c) round bar, for grouted connections referring to DIN EN ISO 19902 (2014).....	9
Figure 2-5. Stress ratio and cycles based on Almar-Naess (1985) and Radaj & Vormwald (2007).....	16
Figure 2-6. Load transfer at grouted connections with shear keys in steel-grout interface (left) acc. to Sele & Kjeoy (1989) and shear key interface (right) acc. to Karsan & Krahl (1984).....	20
Figure 2-7. Failure modes for axially loaded grouted connections with shear keys: a) grout crushing, b) compression strut failure, c) shear failure, d) shear key failure and e) local buckling according to Schaumann et al. (2012a).....	22
Figure 2-8. Relationship of bond strength and shear keys for experimental test results and resulting validity limit according to DIN EN ISO 19902 (2014).....	23
Figure 2-9. Relationship of bond strength parameter and radial stiffness for experimental test results and resulting validity limit according to DIN EN ISO 19902 (2014).....	25
Figure 2-10. Relationship of bond strength and uniaxial compressive cube strength of cementitious materials for tests and resulting validity limit acc. to DIN EN ISO 19902 (2014).....	26
Figure 2-11. S-N curves for unidirectional ( $R > 0$ ) and alternating loads ( $R = -1$ ) according to Ingebrigtsen et al. (1990) and tests results by Anders (2007) and by Schaumann et al. (2009).....	29
Figure 2-12. Comparison of calculated and measured bond strength according to DIN EN ISO 19902 (2014) and DNV-OS-J101 (2014) based on Schaumann et al. (2012a) with test results.....	34

---

Figure 2-13. Comparison of calculated and measured bond strength according to Schaumann et al. (2012a) (left) and compression strut model according to Lampion et al. (1986) (right).....	35
Figure 2-14. Proposed S-N curves for grouted connections with shear keys according to DNV-OS-J101 (2014), Billington & Chetwood (2012) and Harwood et al. (1996) and related fatigue test results, diagram based on Schaumann et al. (2012b).....	36
Figure 2-15. Flow chart for the fatigue design of grout layers in offshore wind turbines according to Schaumann & Wilke (2007) and Schaumann & Lochte-Holtgreven (2011). .....	40
Figure 2-16. Three-dimensional failure surface according to Ottosen (1977) and Drucker & Prager (1952) (left) and deviator plane (right).....	43
Figure 2-17. Schematic sketch of the cyclic strain development for normal strength concrete (NSC), high strength concrete (HSC) and ultra high strength concrete (UHPC) (left) and stiffness development (right) based on Holmen (1979) and Pfanner (2003).....	45
Figure 2-18. Fatigue test results for triaxial tested HPC and UHPC according to Grünberg & Oneschkow (2011) and Grünberg & Ertel (2012) (left) and S-N curves according to Model Code 2010 (2012) for uniaxial loaded HPC (right) based on Lochte-Holtgreven (2013).....	46
Figure 3-1. Overview of large-scale fatigue test specimens and their configuration.....	51
Figure 3-2. Sketch and table representing test specimen geometry and configuration.....	54
Figure 3-3. Test set-up: Large-scale grouted connection adapted to the test rig. ....	59
Figure 3-4. Applied main and short test load program and related load levels.....	60
Figure 3-5. Comparison of characteristic bearing capacity according to DIN EN ISO 19902 (2014) (left) and DNV-OS-J101 (2014) (right) for LS01 to LS08.....	61
Figure 3-6. Load spectrum for a reference grouted connection provided by industrial partners of GROWup (left) and comparison with its ultimate characteristic capacity according to DIN EN ISO 19902 (2014) and DNV-OS-J101 (2014) (right). ....	63
Figure 3-7. Cross-section of the test specimen depicting the location of lasers L (left), potentiometers P (left) and strain gauges S (right). ....	65
Figure 3-8. Overview of vertical displacements exemplarily displayed for TS01 at LS02. ....	67
Figure 3-9. Comparison of the measured global displacements by varied devices at TS01....	68
Figure 3-10. Global load-displacement behaviour at LS01 N = 1 at test specimens TS01 to TS04.....	69
Figure 3-11. Relative displacements at L1V for maximum tension (left) and compression (right) of the alternating load stage LS01 at test specimens TS01 to TS04.....	70
Figure 3-12. Relative displacements at L1V for maximum tension (left) and compression (right) of the alternating load stage LS02 at test specimens TS01 to TS04.....	72
Figure 3-13. Relative displacements at L1V for maximum tension (left) and compression (right) of the alternating load stage LS03 at test specimens TS01 to TS04.....	72

Figure 3-14. Relative displacements at L1V for unloading (left) and maximum compression load (right) of pulsating compression load stage LS06 at test specimens TS01, TS02 and TS04.....	74
Figure 3-15. Relative displacements at L1V for unloading (left) and maximum compression load (right) of LS08 at test specimen TS01, TS02 and TS04.....	75
Figure 3-16. Relative displacements at L1V for maximum tension (left) and compression (right) of the alternating load stage LS08 at test specimen TS02 and TS04. ....	76
Figure 3-17. Comparison of the relative displacements for LS03 and LS08 at test specimen TS02 (left) and TS04 (right). ....	77
Figure 3-18. Development of the stiffness $k_{L1}$ at the test specimens TS01 to TS04 for the alternating load stages LS01 (left) and LS02 (right). ....	78
Figure 3-19. Development of the stiffness $k_{L1}$ at the test specimens TS01 - TS04 during LS01 for the compression load -1 MN (left) and the tension load +1-MN (right).....	79
Figure 3-20. Related stiffness $k_{rel,L1V}$ at TS01 and TS04 for LS02 (top) and LS03 (bottom) separated for tension induced (left) and compression induced (right) values. ....	80
Figure 3-21. Stiffness development (left) and related stiffness development (right) for TS01, TS02 and TS04 in LS06.....	82
Figure 3-22. Comparison of the stiffness development for the test specimens TS01 to TS04 in consideration of the accumulated number of load cycles corresponding to LS01 to LS08.....	83
Figure 3-23. Longitudinal strains displayed by vertical level at TS02 for the maximum compression load (left) and tension load (right) at the beginning of LS01. ....	85
Figure 3-24. Longitudinal strains displayed by vertical level at TS01 for the maximum compression load (left) and tension load (right) in LS02. ....	86
Figure 3-25. Longitudinal strains at the sleeve displayed by vertical level at TS01 to TS04 for the maximum compression load (left) and tension load (right) at the beginning of LS03. ....	87
Figure 3-26. Longitudinal strains displayed by vertical level at TS04 for the maximum compression load (left) and tension load (right) at the end of LS03 and the beginning of LS08.....	88
Figure 3-27. Hoop strain development at S3H in LS02 at TS02 and TS04 (left) as well as TS01 and TS03 (right). ....	89
Figure 3-28. Hoop strain development at S4H in LS02 at TS02 and TS04 (left) as well as TS01 and TS03 (right). ....	90
Figure 3-29. Relative displacement range at TS03 for the alternating load stages LS01 to LS03.....	92
Figure 3-30. Evolution phases with regard to the relative displacement ranges appearing at TS03 in LS02 and LS03.....	93



---

Figure 3-31. Damage evolution phases based on the relative displacement range during LS01 (left) and LS02 (right) for the test specimens TS01 to TS04.....	94
Figure 3-32. Steel test plates from the sleeve (left) and shear key segment (right) for the surface roughness measurements after cyclic testing. ....	95
Figure 3-33. Surface roughness profile measured at TS03 before testing showing relevant surface roughness parameters and measuring lengths. ....	96
Figure 3-34. Radial cracks and grout powder at the grout surface of TS02 (left) and TS01 (right) after the alternating load stage LS02. ....	98
Figure 3-35. Grout wedge sticking to the sleeve and resulting cracks at TS01. ....	99
Figure 3-36. Fracture pattern at the test specimens TS01 to TS04 after testing. ....	100
Figure 3-37. Pile shear key and grout wedge exemplarily at test specimen TS04.....	101
Figure 3-38. Symptoms of inhomogeneous grout material behaviour at the test specimen TS04.....	102
Figure 3-39. Sketch of the derived compression strut cracks and angles for varied grout annulus.....	102
Figure 4-1. Three-dimensional numerical model of the grouted connection reflecting applied mesh and geometric parameters.....	107
Figure 4-2. Yield surface of the Extended Drucker-Prager Cap plasticity model in the meridional plane (left) and deviatoric plane (right) compared to Drucker-Prager criterion based on ANSYS (2014).....	110
Figure 4-3. Comparison of triaxial test results by Dahl (1990), Dahl (1992), Nielsen (1995) and Speck (2008) with the Ottosen failure criterion according to Model Code 2010 (2012).....	112
Figure 4-4. Comparison of experimental triaxial test results according to Speck (2008) and calibrated numerical results for triaxial cube tests.....	113
Figure 4-5. Comparison of different stress states for the grout layer being exposed to tension and compression force of 3 MN, coloured compression stresses and grey tension stresses. ....	115
Figure 4-6. Calculation procedure to cover the fatigue behaviour by the numerical model..	117
Figure 4-7. Comparison of experimental and numerical global load-displacement behaviour for the initial load cycle $N = 1$ of the first load stage LS01.....	119
Figure 4-8. Comparison of numerical and experimental derived relative displacements at L7V for LS01, $N = 1$ . ....	120
Figure 4-9. Comparison of numerical and experimental derived longitudinal strains for the peak compression load of $F_{c,max} = -1$ MN in LS01, $N = 1$ . ....	122
Figure 4-10. Achieved damage $D$ components depending on the stress state at TS01 for LS01, $N = 100'000$ . ....	123

- Figure 4-11. Comparison of numerical (FEM) and experimental (Exp) derived relative displacements at L7V for TS01 (left) and TS04 (right) for  $N = 1$  and  $N = 100'000$  in the load stages LS01 to LS03 including cyclic degradation effects. .... 124
- Figure 4-12. Comparison of numerical (FEM) and experimental (Exp) derived relative displacements at L7V for TS01 (left) and TS04 (right) for  $N = 1$  and  $N = 100'000$  in the load stages LS04 to LS06 including cyclic degradation effects. .... 127
- Figure 4-13. Comparison of numerical and experimental derived relative displacements at the end of LS03 and at the beginning of LS08 for TS04. .... 128
- Figure 4-14. Damage growth for the test specimen TS04 with small grout annulus at selected load stages LS01, LS03 and LS06. .... 129
- Figure 4-15. Adapted FE-model configurations based on validated models for the parametric studies ..... 130
- Figure 4-16. Impact of different grout thicknesses,  $t_g = 183.5$  mm at M01-A and  $t_g = 81.5$  mm at M02-A, to the cyclic relative displacements for two alternating load scenarios with  $F_{max} = +/- 1$  MN (left) and  $F_{max} = +/- 3$  MN (right) for  $N = 1$  and  $N = 100'000$  load cycles. .... 131
- Figure 4-17. Impact of two different materials A and B to the cyclic relative displacements for M01 (left) and M02 (right) depicted for  $N = 1$  and  $N = 100'000$  load cycles. .... 132
- Figure 4-18. Impact of varied friction coefficients (left) and varied shear key height to distance ratios  $h/s$  (right) to the relative displacements at M01-A and M02-A for  $F_t = 1$  MN and  $F_c = -1$  MN. .... 133
- Figure 4-19. Comparison of the relative displacement range at M01-A with and without cyclic degradation for the alternating load scenarios 1-2-3 (left) and 3-2-1 (right). .... 136
- Figure 4-20. Comparison of the accumulated displacement ranges (left) and the residual load-displacement behaviour (right) for the alternating load scenarios 1-2-3 and 3-2-1 at M01-A. .... 137
- Figure 5-1. Comparison of test results for TS01 to TS04 based on the ULS capacity according to DIN EN ISO 19902 (2014) with the Billington & Chetwood (2012) approach (left) and based on the ULS capacity according to DNV-OS-J101 (2014) with the S-N approach according to DNV-OS-J101 (2014) and corresponding test data according to Lotsberg et al. (2013). .... 147
- Figure 5-2. Tensile and compression loaded grouted connection (right) and compression strut model (left) based on Schaumann et al. (2012a). .... 149

## 8.2 List of Tables

Table 2-1. Cementitious materials and relevant properties for offshore applications.....	14
Table 2-2. Validity ranges for use of the empirical design equations according to DIN EN ISO 19902 (2014), DNV-OS-J101 (2014) and Norsok Standard N-004 (2013). .....	33
Table 3-1. Geometric dimensions of reference grouted connections and related test specimens. ....	53
Table 3-2. Comparison of validity ranges with reference connections and test specimens.....	55
Table 3-3. Steel material properties of the test specimens.....	56
Table 3-4 Grout material strength characteristics according to BASF Masterflow <sup>®</sup> (2011) and Densit Ducorit <sup>®</sup> (2013) and fatigue test accompanied material testing.....	57
Table 3-5. Fatigue design results for the test specimens TS01 to TS04 according to DIN EN ISO 19902 2014) and DNV-OS-J101 (2014). .....	62
Table 3-6. Characteristic ULS load and utilisation U for the reference grouted connection according to DIN EN ISO 19902 (2014) and DNV-OS-J101(2014).....	63
Table 3-7. Comparison of utilisation ratios U according to DIN EN ISO 19902 (2014) for the test specimen TS01 and the reference grouted connection at a jacket.....	64
Table 3-8. Percental stiffness variation at TS01 to TS04 for LS01 to LS03.....	81
Table 3-9. Percental stiffness variation at TS01 to TS04 for LS04 to LS07.....	83
Table 3-10. Surface roughness at the sleeves of TS03 and TS03 before and after testing. ....	97
Table 4-1. Numerical model configuration in terms of element types and contact parameter. ....	108
Table 4-2. Material parameters for finite element calculation. ....	109
Table 4-3. Material parameters according to experimental testing.....	109
Table 4-4. Calibrated input parameters for the EDP material model.....	113
Table 5-1. Equivalent number of load cycles for TS01 according to DNV-OS-J101 (2014).146	

## Appendix A. Properties of the test specimen

### A.1 Properties of the ordered steel tubes

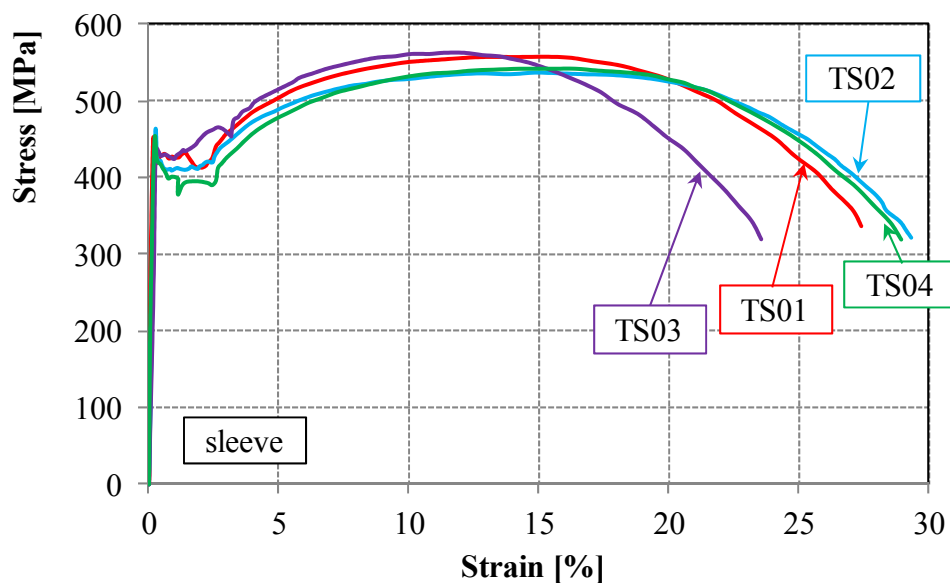
Table A-1 summarises the mean values for the steel tube characteristics according to the inspection certificates delivered with the steel tubes by Erndtebrücker Eisenwerke GmbH & CO KG.

**Table A-1. Summary of the ordered steel tube properties according to the inspection certificates**

Test specimen	Component [-]	Yield Point $R_{eh}$ [MPa]	Tensile strength $R_m$ [MPa]	Elongation A [%]
TS01	sleeve	423	565	26
	pile ( $D_p = 406.4$ mm)	360	450	29
TS02	sleeve	423	565	26
	pile ( $D_p = 610$ mm)	427	558	31
TS03	sleeve	454	561	26
	pile ( $D_p = 406.4$ mm)	360	495	29
TS04	sleeve	355	548	29
	pile ( $D_p = 610$ mm)	427	558	31

### A.2 Tensile test results of the sleeve steel tubes

Steel segments were cut out of the sleeve tubes after performed fatigue tests. The Institute of Materials (IW) at the Leibniz Universität Hannover prepared three tensile specimens for each sleeve segment and conducted the tensile tests according to DIN EN ISO 6892-1 (2009). The mean values of observed results are displayed in Figure A 1. Related steel properties are listed in Table 3-3.



**Figure A-1. Mean tensile test results for the sleeve segments of the test specimens TS01 to TS04.**

### A.3 Grout material properties

The grout material, which was filled in the grout annulus between sleeve and pile, was tested in the fresh and hardened condition to define the material properties. Table A-2 presents an overview of the material properties according to manufacturer' data and according to own tests of the fresh and hardened material.

**Table A-2. Grout material properties according to manufacturer's data and own material tests**

Test specimen				TS01	TS02	TS03	TS04
Material				BASF Masterflow® 9500		Densit Ducorit® S2	
data source	property	[unit]	grout-age				
Manufacturer's data	Mean compressive cube strength $f_{c,cube,75}$	[MPa]	28 days	140		90	
	Mean bending tensile strength $f_{ct,fl}$	[MPa]	28 days	18		-	
	Mean tension strength $f_t$	[MPa]	28 days	8		6	
	Mean Young's Modulus $E_{cm}$	[MPa]	28 days	50'000		40'000	
	Density $\rho$	[g/cm <sup>3</sup> ]	[-]	2.4		2.4	
	Poisson's ratio $\nu$	[-]	28 days	0.19		0.18	
	Consistence class acc. to DAfStb Vergussbeton-Richtlinie	[-]	-	n.a.*		a2	
	Compressive strength class according to EN 206-1	[-]	28 days	C100/115		C90/105	
	Shrinkage class (value) acc. to DAfStb Vergussbeton-Richtlinie	[%o]	91 days	SKVB 0 (0.46)		SKVB I (0.579)	
Own material tests conducted by the Institute of Building Materials Science	Mean slump-test results according to EN 12350-2	[mm]	[-]	93.5/93.0	85.5/85.0	80.0/80.0	82.0/83.0
	Mean density $\rho$	[g/cm <sup>3</sup> ]	[-]	2.4	2.4	1.8	2.2
	Mean air void content	[%]	[-]	-	2.1	3.7	3.8
	Mean compressive cube strength $f_{c,cube,75}$	[MPa]	1 day	78.67	85.33	-	14.82
			7 days	126.13	134.24	96.73	109.79
			28 days	143.13	143.44	123.35	131.26
	Mean compressive cylinder strength $f_{c,cyl}$	[MPa]	7 days	108.76	115.75	72.51	89.27
			28 days	144.37	124.01	99.77	110.88
	Mean compressive prism strength $f_{c,prism}$	[MPa]	1 day	77.31	77.48	46.94	19.26
			7 days	115.30	117.48	83.47	104.32
			28 days	128.52	130.38	104.04	125.18
	Mean bending tensile strength $f_{ct,fl}$	[MPa]	1 day	9.30	9.00	5.40	3.14
			7 days	13.52	13.95	10.09	13.31
28 days			15.11	17.59	12.46	15.07	
Mean Young's Modulus $E_{cm}$	[MPa]	28 days	47'033	44'250	43'700	45'433	
n.a.* → not available							

In addition to the grout properties during the initial 28 days, the characteristics at the starting point of the cyclic fatigue tests were determined by the Institute for Building Material Sciences. Table A-3 summarises the achieved test data with regard to the grout age.

**Table A-3. Grout properties of each test specimen at the beginning of the fatigue tests.**

Test specimen	Material	Date [dd.mm.yyyy]	Grout-age [dd]	Compressive strength		Tensile strength		Time effect $\beta_{cc}(t)$ [-]	Young's Modulus	
				$f_{c,cube,75}$ [MPa]	$f_{c,cyl}$ [MPa]	$f_{ct,fl}$ [MPa]	$f_{ct}$ [MPa]		$E_{cm}^*$ [MPa]	$E_c(t)$ [MPa]
TS01	BASF Masterflow® 9500	03.03.2014	98	152.75	143.95	18.29	8.0	1.10	47'033	49'274
TS02		11.06.2013	117	144.66	131.52	19.12	8.4	1.11	44'250	46'569
TS03	Densit Ducorit® S2	04.09.2014	63	128.35	106.11	14.97	6.6	1.07	43'700	45'181
TS04		02.06.2014	76	138.52	123.60	14.71	6.5	1.08	45'433	47'255
* according to 28 days testing										

#### A.4 Geometrical measurements

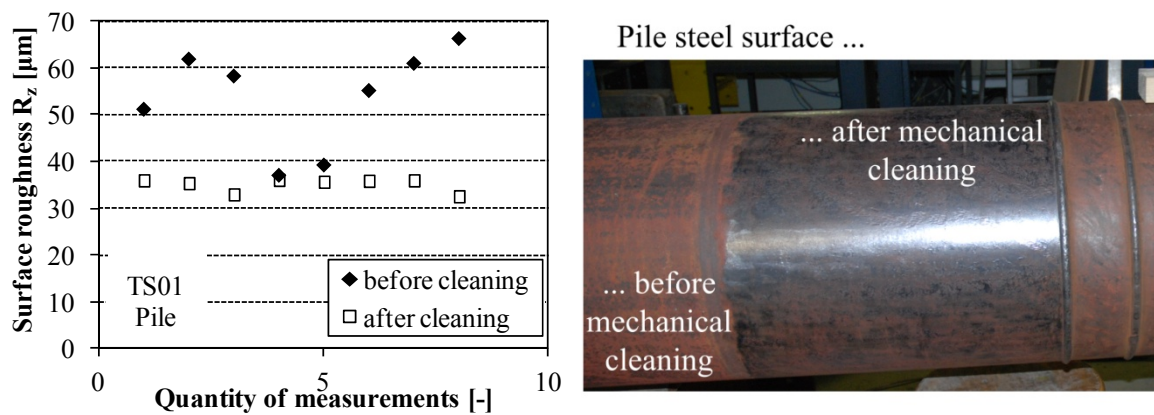
Prior to testing, the geometry of the test specimen components were measured to quantify the geometrical uncertainties. In Table A-3 are the measured values, the absolute deviation from the ideal geometry and the percentile deviation compiled.

**Table A-3. Geometrical values of the test specimen components reflecting the inaccuracies**

Test specimen	Component	Parameter	Ideal [mm]	Measured mean value [mm]	Absolute deviation [mm]	Percental deviation [%]
TS01	pile	diameter	406.4	405.25	-1.15	0.28
		thickness	25	25.54	0.54	2.17
		shear key height	6	4.99	-1.01	16.86
		shear key width	12	13.40	1.40	11.65
		shear key distance	100	99.50	-0.50	0.50
	sleeve	diameter	813	813.60	0.60	0.07
		thickness	20	20.12	0.12	0.61
		shear key height	6	5.87	-0.13	2.22
		shear key width	12	11.76	-0.24	1.99
		shear key distance	100	99.50	-0.50	0.50
TS02	pile	diameter	610	612.77	2.77	0.45
		thickness	25	25.53	0.53	2.13
		shear key height	6	4.89	-1.12	18.58
		shear key width	12	11.31	-0.69	5.74
		shear key distance	100	99.48	-0.52	0.52
	sleeve	diameter	813	813.73	0.73	0.09
		thickness	20	19.88	-0.12	0.62
		shear key height	6	6.07	0.07	1.22
		shear key width	12	11.91	-0.09	0.76
		shear key distance	100	100.17	0.17	0.17
TS03	pile	diameter	406.4	405.46	-0.94	0.23
		thickness	25	25.57	0.57	2.28
		shear key height	6	5.76	-0.24	4.07
		shear key width	12	12.54	0.54	4.53
		shear key distance	100	99.75	-0.25	0.25
	sleeve	diameter	813	813.62	0.62	0.08
		thickness	20	20.23	0.22	1.12
		shear key height	6	5.44	-0.56	9.39
		shear key width	12	12.19	0.19	1.58
		shear key distance	100	100.88	0.88	0.88
TS04	pile	diameter	610	612.69	2.69	0.44
		thickness	25	25.54	0.54	2.16
		shear key height	6	6.26	0.26	4.26
		shear key width	12	16.33	4.33	36.08
		shear key distance	100	100.38	0.38	0.38
	sleeve	diameter	813	813.76	0.76	0.09
		thickness	20	20.20	0.20	0.99
		shear key height	6	5.92	-0.08	1.35
		shear key width	12	11.66	-0.34	2.83
		shear key distance	100	99.88	-0.13	0.13

### A.5 Steel surface conditions

In order to have comparable steel surface conditions in the grouted connection of the test specimen, the steel surfaces were cleaned mechanically. By the mechanical cleaning process the surface in the overlapping area are cleaned from loose material, loose mill scale, corrosive particles and grease according to normative requirements, e.g. DIN EN ISO 19902 (2014). After the mechanical cleaning the steel surfaces had the standard purity degree St2 according to DIN EN ISO 12944-4 (1998). The surface texture of the test specimens was measured prior and after the mechanical cleaning in accordance to DIN EN ISO 4287 (2010) and DIN EN ISO 4288 (1998) by the profile method using the tactile measurement device Hommel Etamic T1000 waveline 20. Resultant values for the surface roughness parameter  $R_z$ , representing the mean of five values measured from the highest peak to the lowest valley, determined at the pile of test specimen TS01 are exemplarily shown in Figure A-2. The graphic illustrates the more even and smooth surface roughness after cleaning the surface of the pile.



**Figure A-2. Surface roughness  $R_z$  values before and after cleaning at the outer surface at the pile (left) and picture of cleaned and uncleaned inner surface at the sleeve (right)**



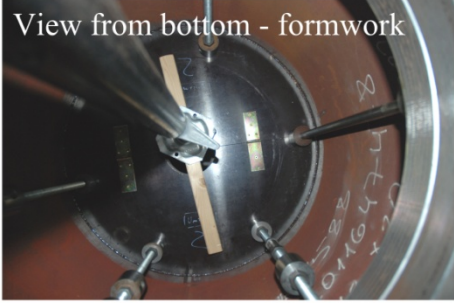

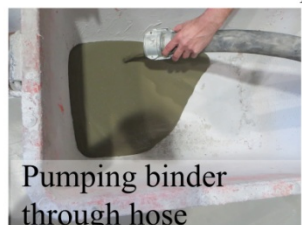
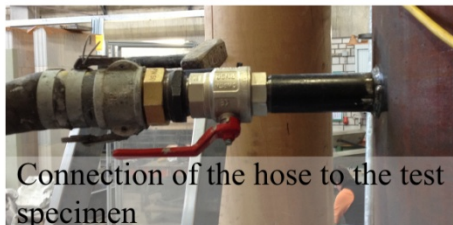






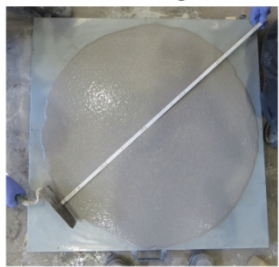
The surface roughness parameters of the different test specimens are compared by tactile measurement results, cf. Table A-4. With regard to an allowed scatter of the values of -20% to +30% it can be concluded that the surface conditions of the test specimens are comparable.

**Table A-4. Mean values of measured surface roughness parameters at the test specimens**

Test specimen	Component	Surface roughness	Arithmetic surface roughness	Max. roughness height	Root mean square roughness	Total waviness
		$R_z$ [ $\mu\text{m}$ ]	$R_a$ [ $\mu\text{m}$ ]	$R_t$ [ $\mu\text{m}$ ]	$R_q$ [ $\mu\text{m}$ ]	$W_t$ [ $\mu\text{m}$ ]
TS01	sleeve	44.60	7.36	59.56	9.22	-
	pile	30.73	4.93	48.15	6.70	-
TS02	sleeve	39.03	6.52	61.50	8.77	-
	pile	21.90	2.93	32.05	4.07	-
TS03	sleeve	54.77	9.70	70.33	12.20	26.14
	pile	36.33	5.72	53.97	7.62	32.47
TS04	sleeve	50.69	8.53	67.72	10.75	21.86
	pile	48.72	8.38	65.70	10.65	27.14



### A.6 Grout filling of the test specimens

<p>1. Installed and adjusted test specimen in testing rig</p>  <p>View from top into the empty grout annulus</p>  <p>View from bottom - formwork</p> 	
<p>2. Preparation and connection of the hose to the test specimen</p>  <p>Binder mixing</p>  <p>Pumping binder through hose</p>  <p>Connection of the hose to the test specimen</p>	
<p>3. Mixing and pumping technique</p> 	<p>5. Filling the test specimen and curing of the grout</p>    
<p>4. Testing of fresh and hardened grout</p>  	

### A.7 Position of measuring device

In Figure A-3 a drawing of an unrolled test specimen reflecting the positions of applied lasers and strain gauges at corresponding levels and axes is presented.

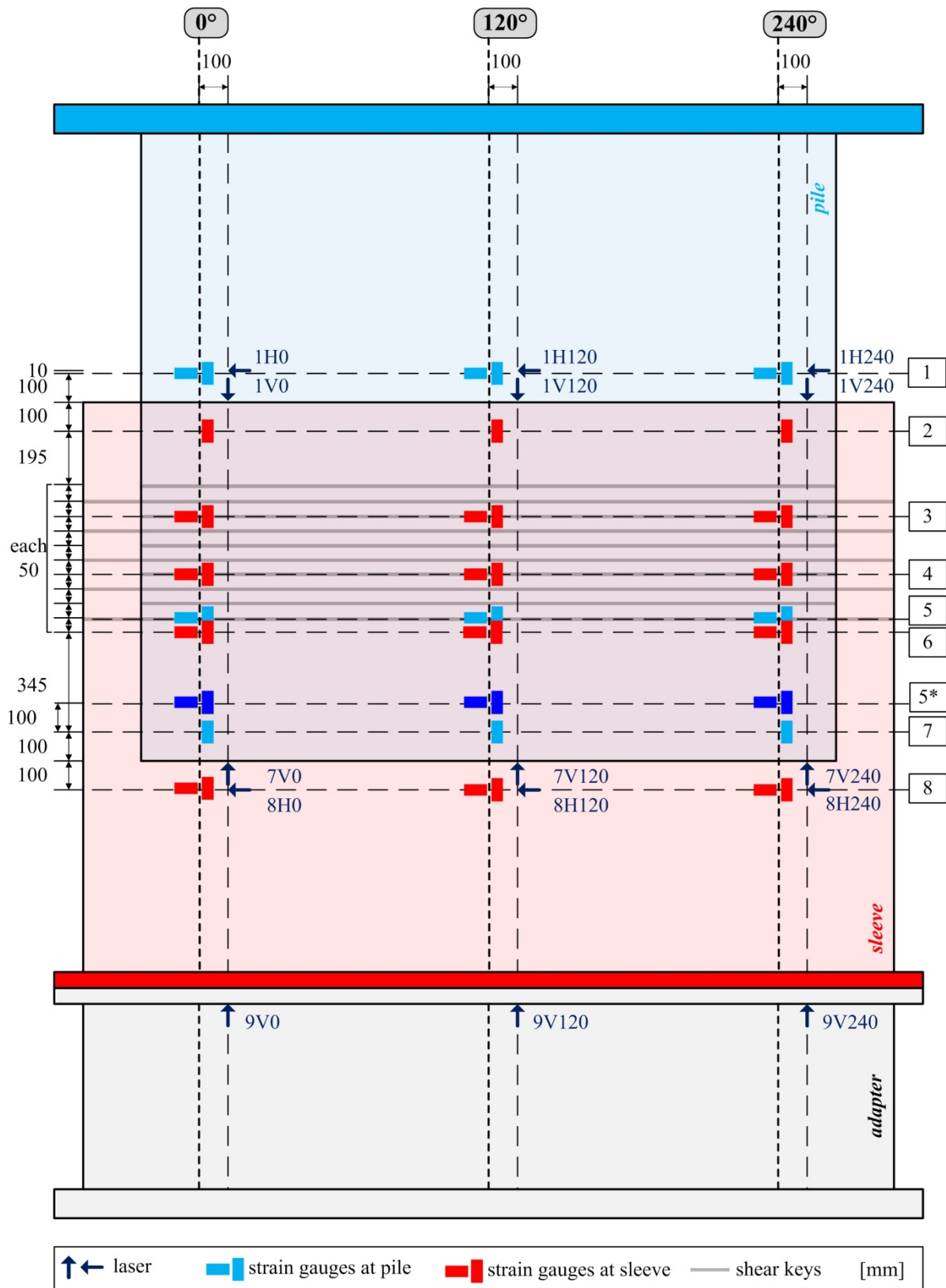


Figure A-3. Unrolled test specimen representing positions of the lasers and strain gauges at corresponding vertical and circumferential axes

### A.8 Overview of adjusted measuring devices at TS01

The subsequent Figure A-4 visualises the test specimens TS01 being installed in the test rig and applied measuring devices. A close-up of the individual measuring tools illustrates their position and adaptation.

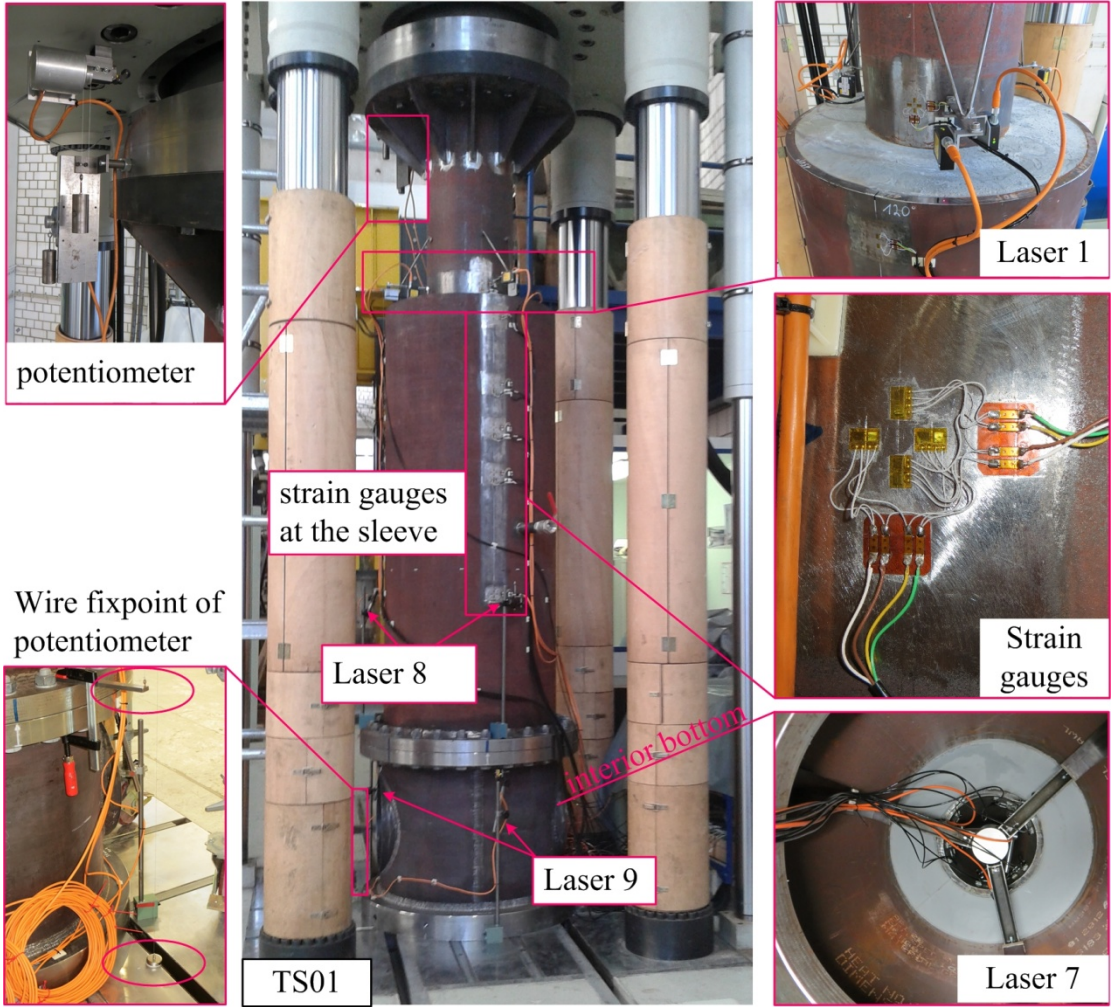


Figure A-4. Picture of test specimen TS 01 with close-ups of the applied measuring devices.

## Appendix B. Additional test results

### B.1 Relative displacement

Complementary to the relative displacements discussed at chapter 3.4.2 the relative displacements at the test specimens TS01 to TS04 are depicted by the subsequent illustrations, cf. Figure B-1.

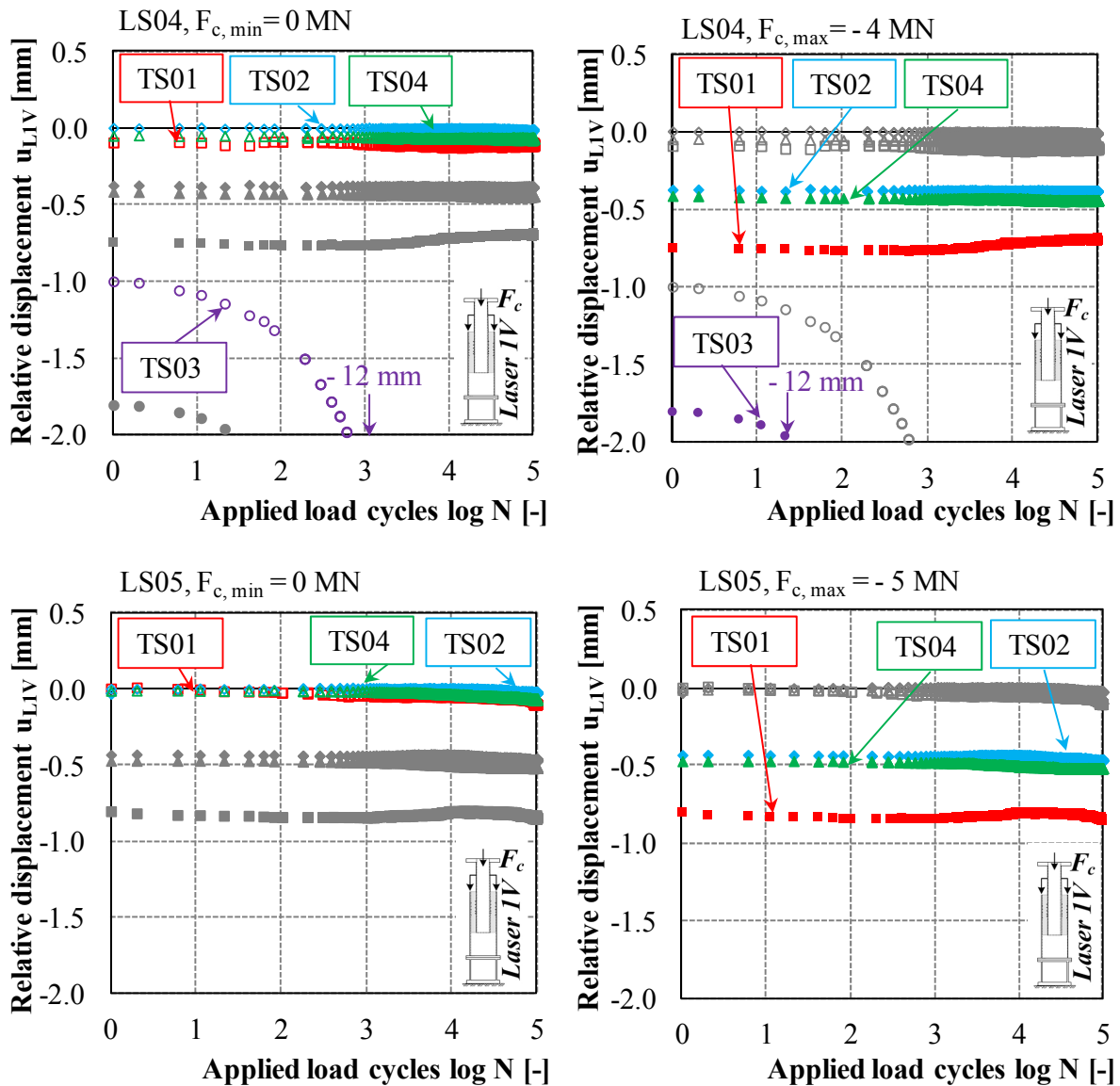


Figure B-1. Relative displacements appearing at LS04 (top) and LS05 (bottom) for the test specimens TS01 to TS04.

### B.2 Stiffness development

Figure B-2 summarises the stiffness development at TS01 to TS04 individually for each load stage LS03 to LS08 as additional completion to explanations and presentation of stiffness results for LS01 and LS02 in chapter 3.4.3.

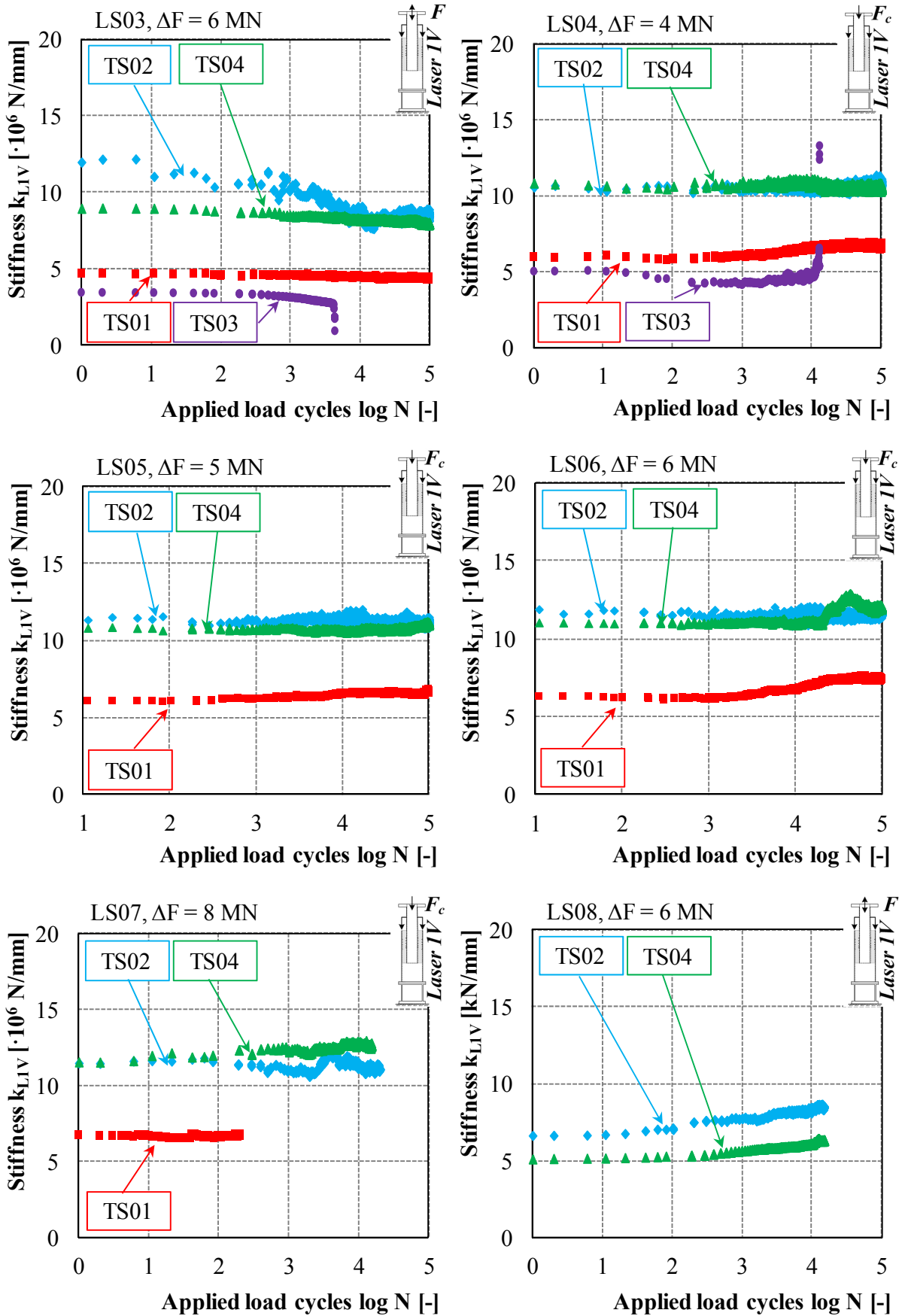
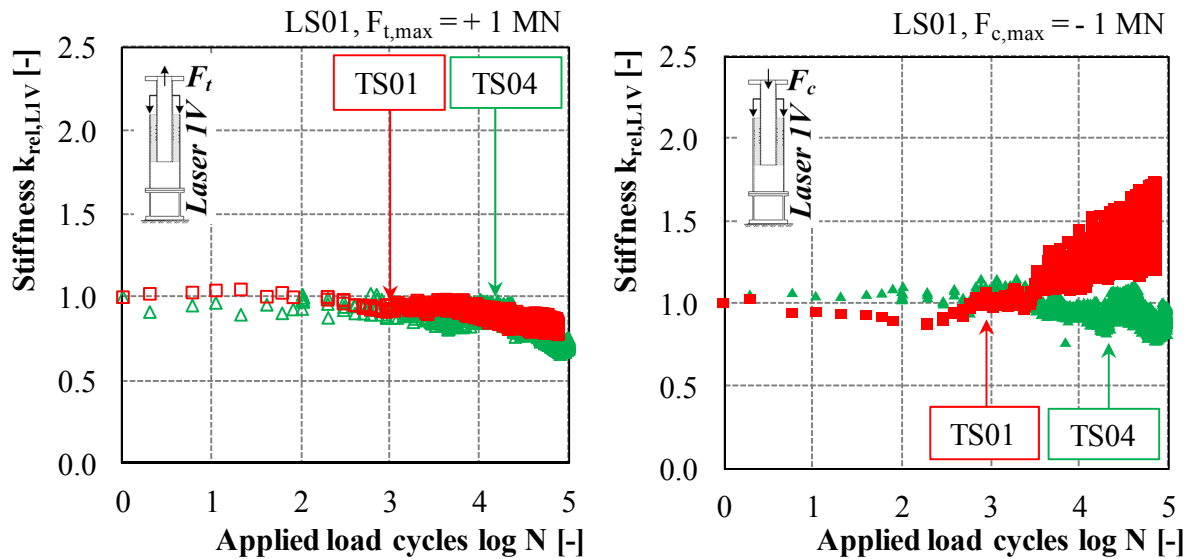


Figure B-2. Stiffness development at TS01 to TS04 for LS03 to LS08(f.l.t.r. and t.t.b.).

Supplementary to the presented related stiffness development and related descriptions and evaluation in chapter 3.4.3, Figure B-3 presents the stiffness development for the first load stage LS01 at TS01 (left) and for TS04 (right).



**Figure B-3. Relative stiffness development at load stage LS01 for TS01 and TS04.**

Complementary to the addressed stiffness reduction at TS01 and TS04 in chapter 3.4.3, the following Figure B-3 displays the tensile and compressive induced relative stiffness development for the load stages LS01 to LS03 (from top to bottom) at the test specimens TS03 (left) and TS02 (right).

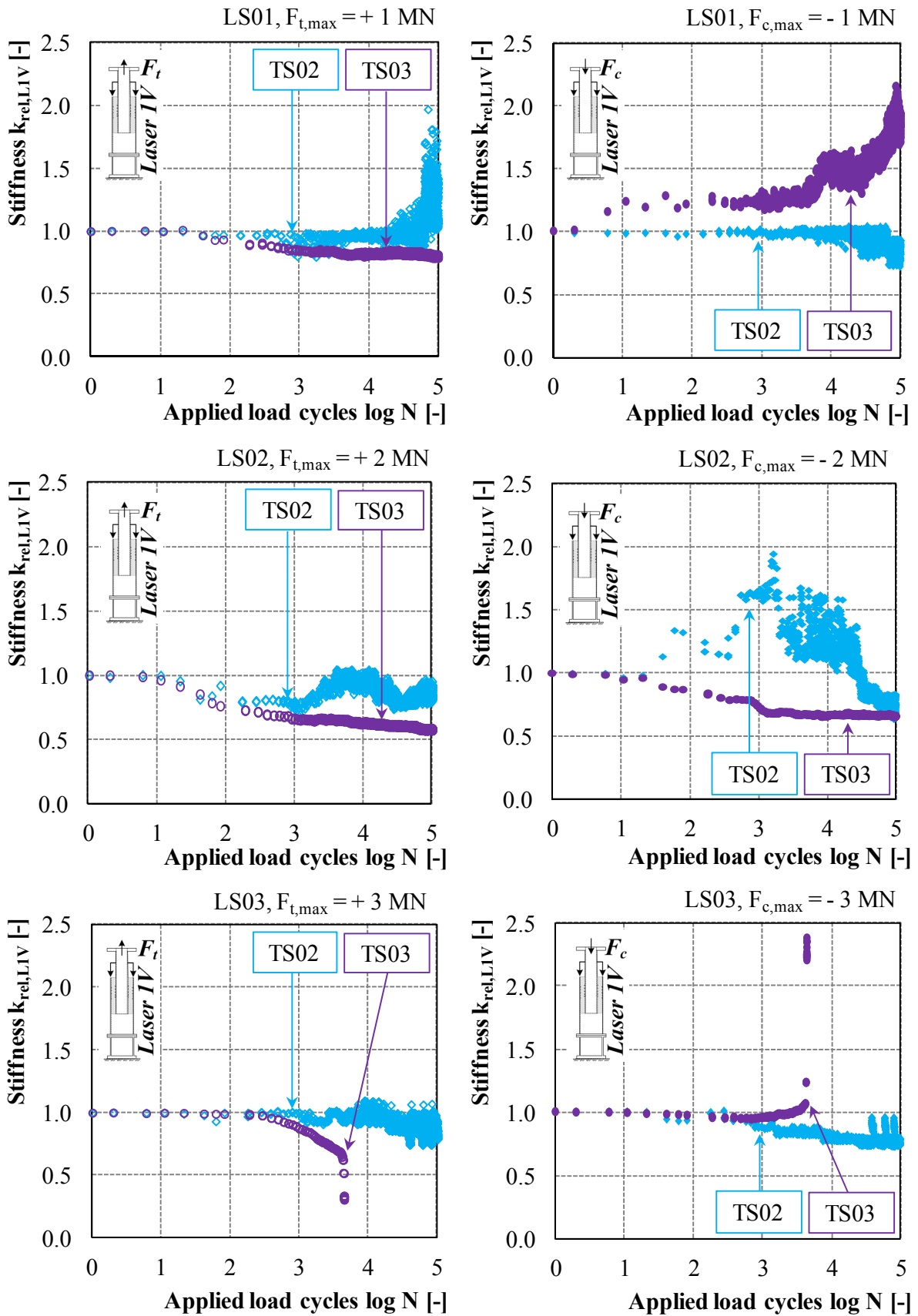


Figure B-3. Relative stiffness development at load stage LS01 to LS03 (top to bottom) for TS03 and TS02 for tensile (left) and compressive loading (right).

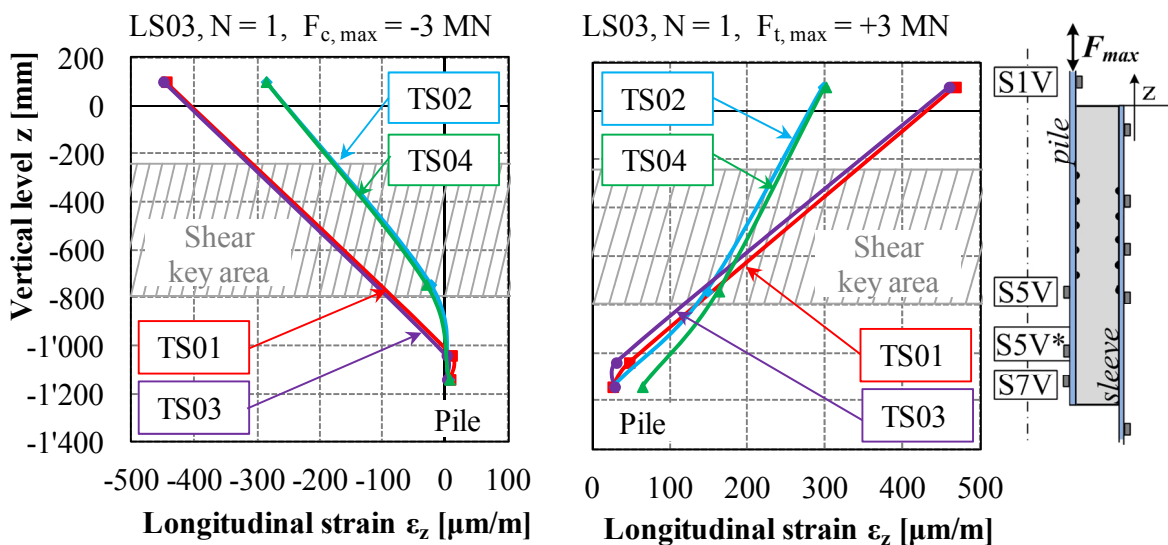
In addition to the percental stiffness increase and decrease for the LS01 to LS03 presented in chapter 3.4.3, Table B-1 summarises the load direction dependent stiffness increase or decrease for the test specimens TS01 to TS04.

**Table B-1. Percental stiffness increase and decrease related to the individual maximum forces during the alternating load stages LS01 to LS03.**

Load stage	Type of load reversal	Max. loading $F_{max}$ [MN]	Percental stiffness in-/decrease based on the related stiffness $k_{rel, L1}$			
			TS01	TS02	TS03	TS04
01	Alternating $R = -1$	-1	46%	-20%	78%	-10%
		1	-19%	30%	-21%	-29%
02		-2	-32%	-32%	-35%	33%
		2	-43%	-16%	-43%	-42%
03		-3	13%	-22%	-	-5%
		3	-20%	-20%	-	-13%

### B.3 Strain development

Figure B-4 reveals the vertically arising strains for the first load cycle in LS03 at the pile. It becomes apparent, that induced loading provokes due to the identical geometries for TS01 and TS03, and TS02 and TS04, nearly identical strain values. Related strains appearing at the sleeve are discussed and depicted in chapter 3.4.4.



**Figure B-4. Longitudinal strains at the pile displayed by vertical level at TS01 to TS04 for the maximum compression load (left) and tension load (right) in LS03, N = 1.**



#### B.4 Characteristics of the damage

Subsequent to the cyclic testing, the test specimens were opened by separating a sleeve segment from the test specimens. Resulting opened grout surfaces are depicted in Figure B-5.

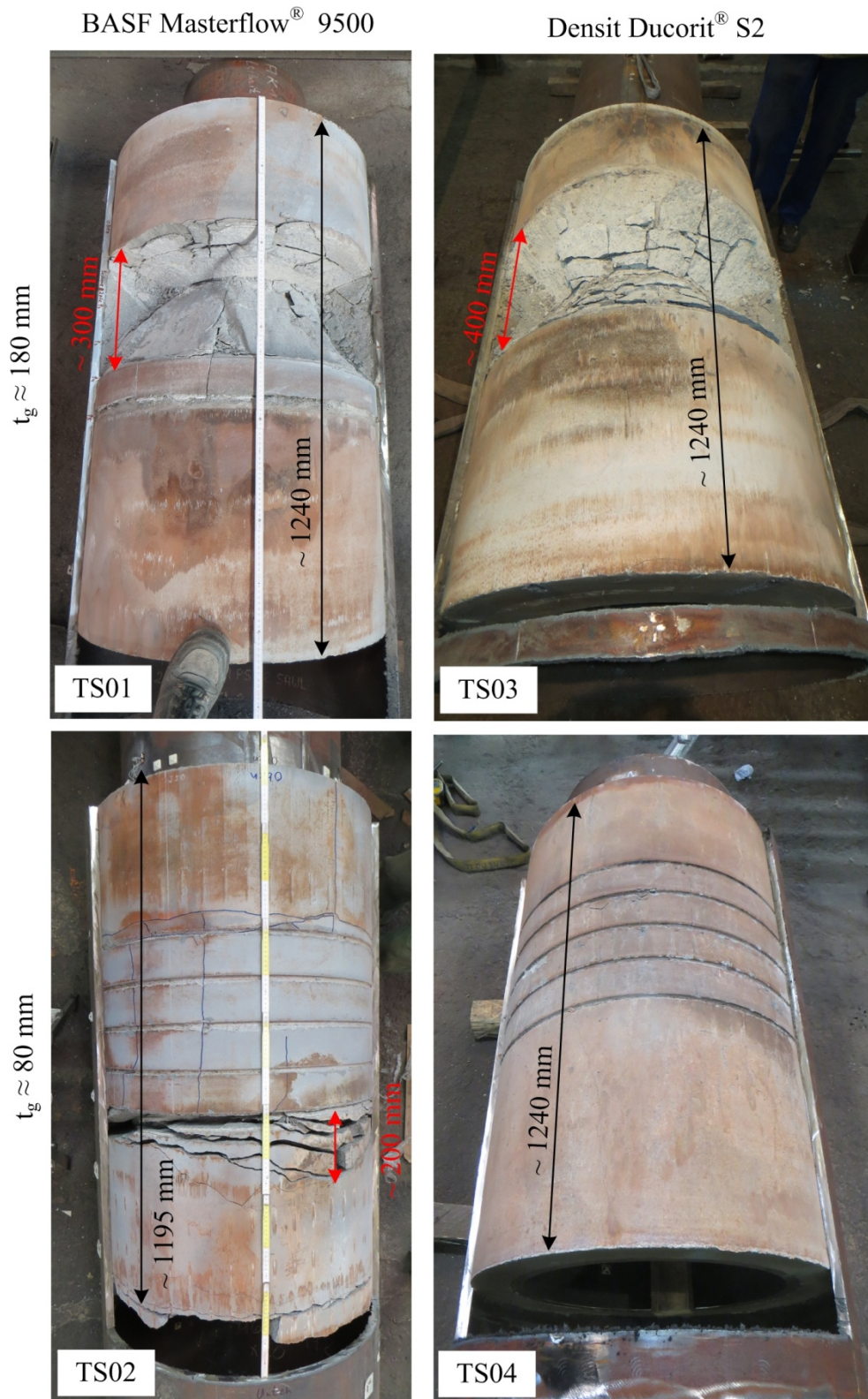
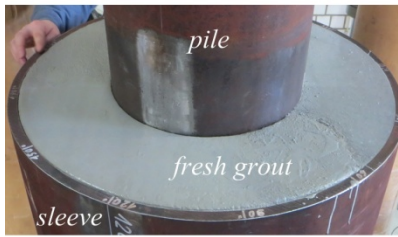
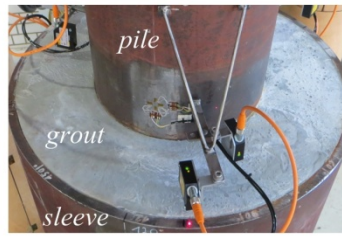


Figure B-5. Test specimens TS01 to TS04 revealing the damaged grout layer after cyclic testing and taking off a sleeve segment.

1. Grout surface before testing



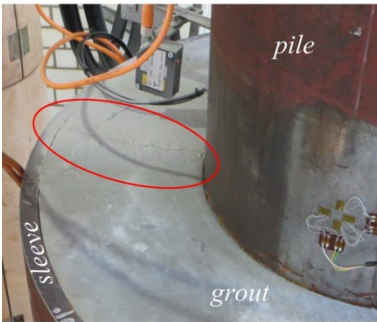
After grouting



Before testing: No visible cracks, conspicuous air bubbles arised during hardening process



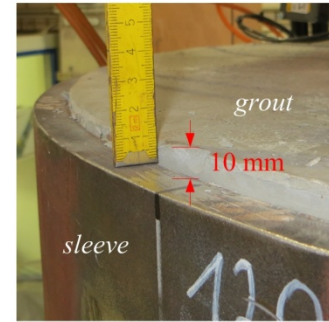
2. During testing



LS02: Radial crack



LS03: Powdery rust-coloured cementitious material



LS08: Grout layer pulled out

3. After testing

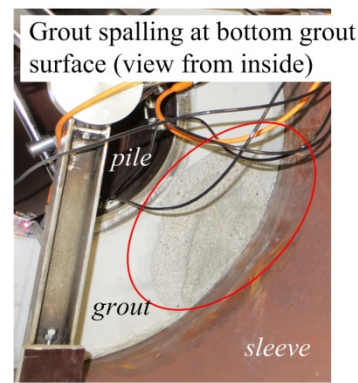
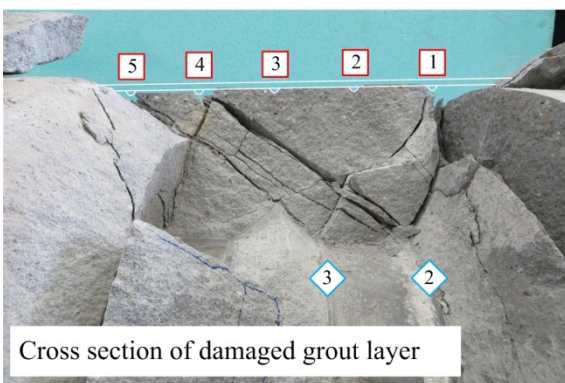
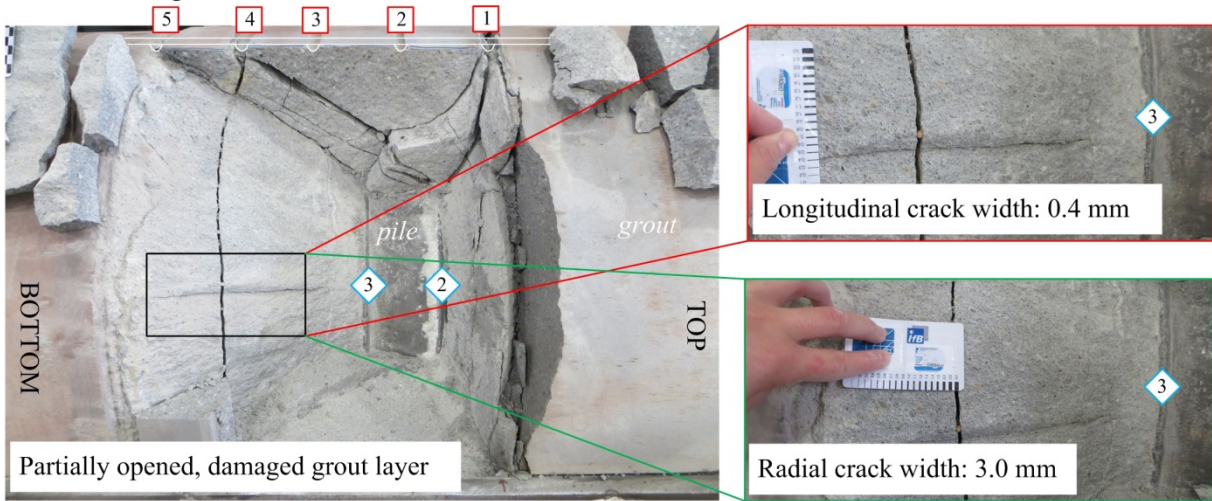
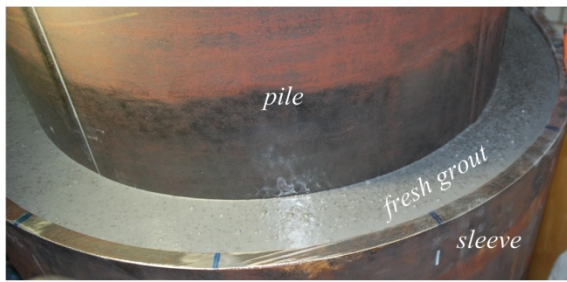


Figure B-6. Damage characteristics at the test specimen TS01 (BASF Masterflow® 9500,  $t_g = 183.5$  mm) prior to, during and after testing.

1. Grout surface before testing

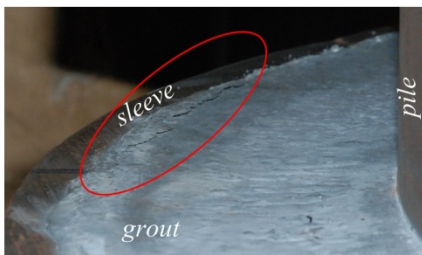


After grouting

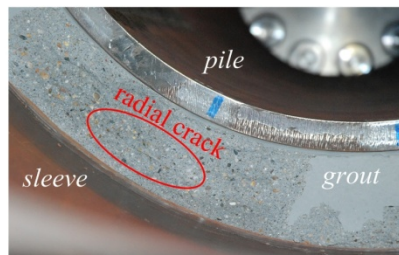


Before testing: No visible cracks

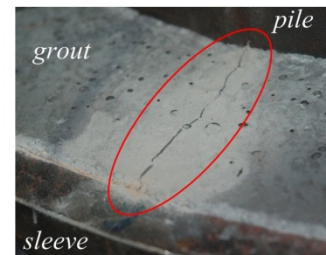
2. During testing



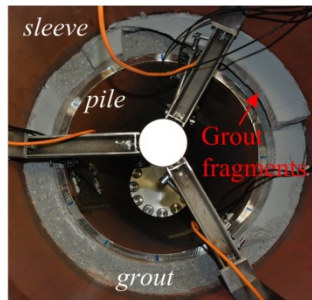
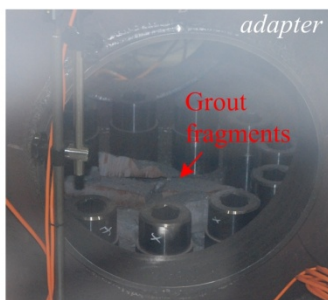
LS01: Initial loss of contact between grout and steel



LS03: Grout spalling (bottom view)

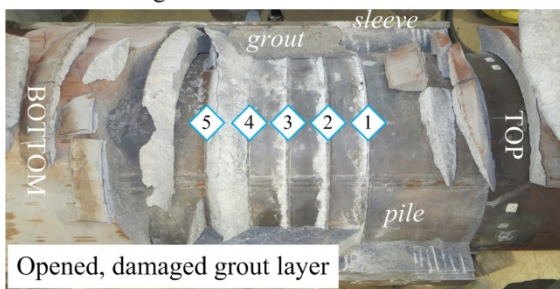


LS04: Crack and powdery material (top view)



LS08: Large fragments underneath test specimen (left), view from bottom (right)

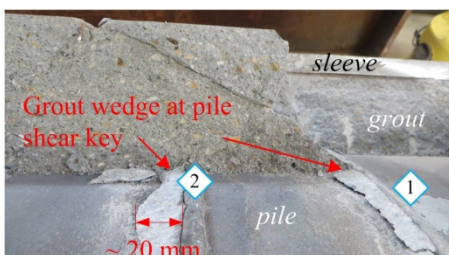
3. After testing



Opened, damaged grout layer

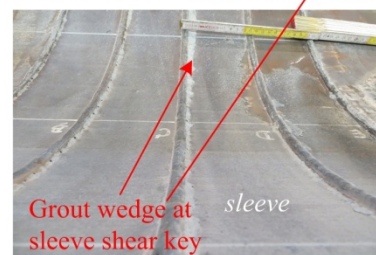


Grout surface being in contact with the sleeve



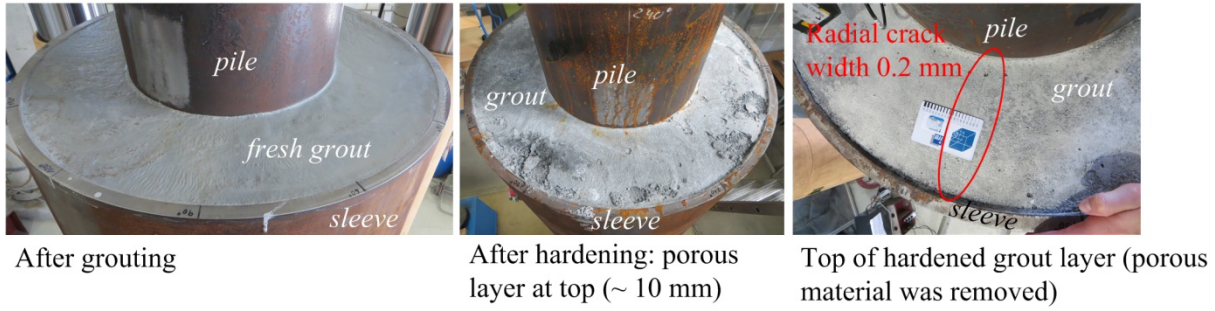
Grout wedge at pile shear key

~ 20 mm

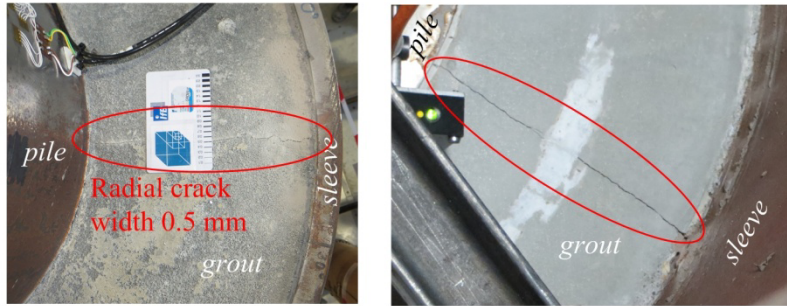


Grout wedge at sleeve shear key

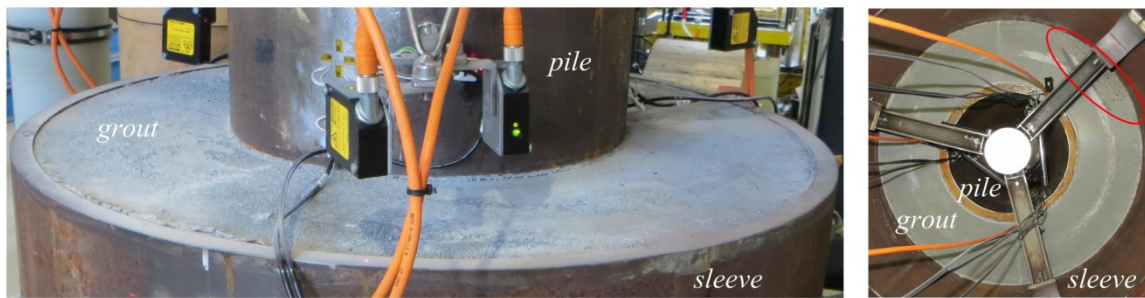
Figure B-7. Damage characteristics at the test specimen TS02 (BASF Masterflow<sup>®</sup> 9500,  $t_g = 81.5$  mm) prior to, during and after testing.



2. During testing



LS02: Radial crack at top (left) and at bottom (right)



LS03: Radial crack and powdery material at top (left) and grout spalling at bottom (right)

3. After testing

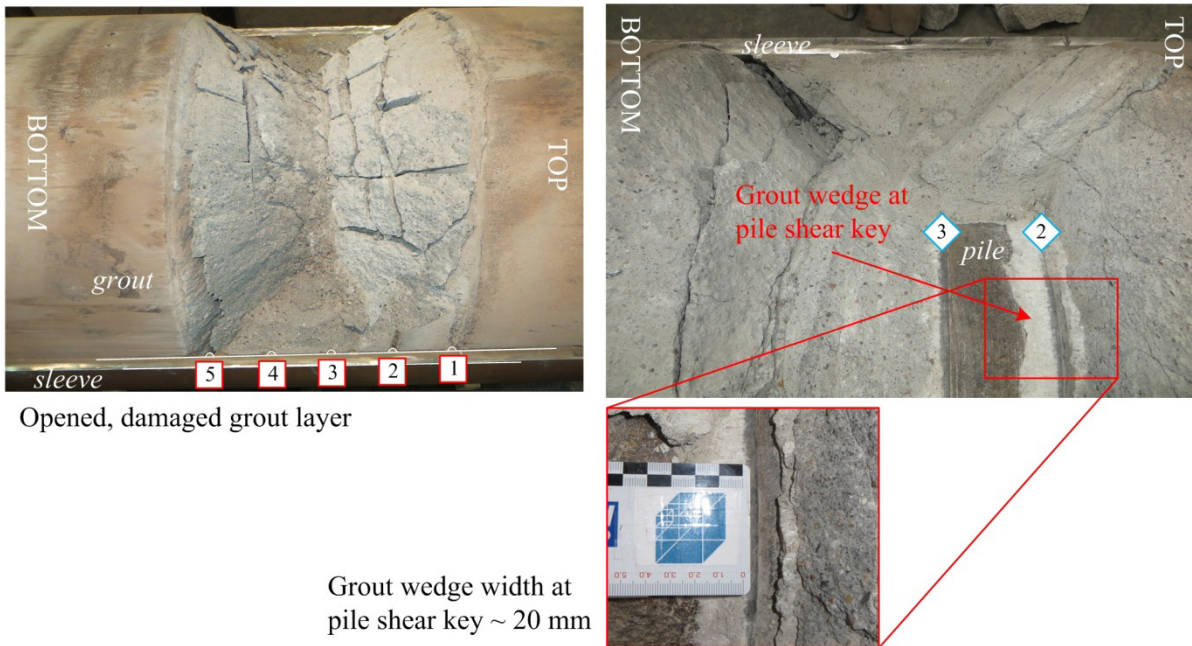
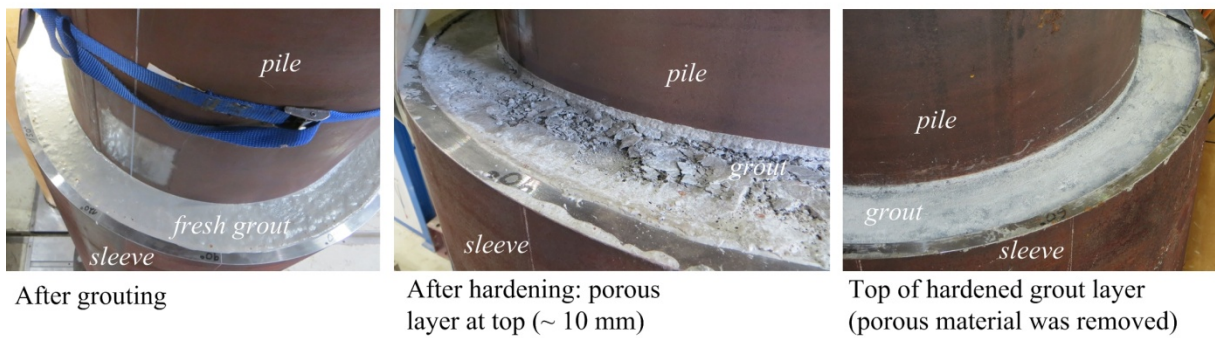
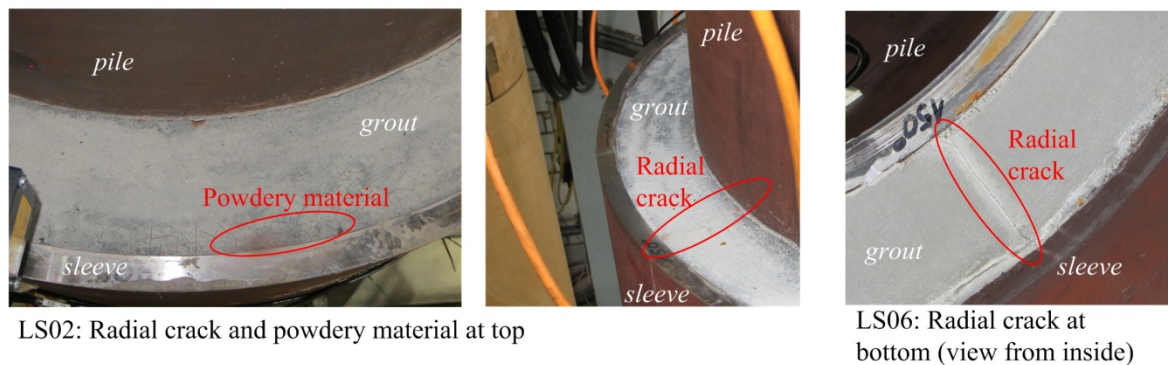


Figure B-8. Damage characteristics at the test specimen TS03 (Densit Ducorit<sup>®</sup> S2,  $t_g = 183.5$  mm) prior to, during and after testing.

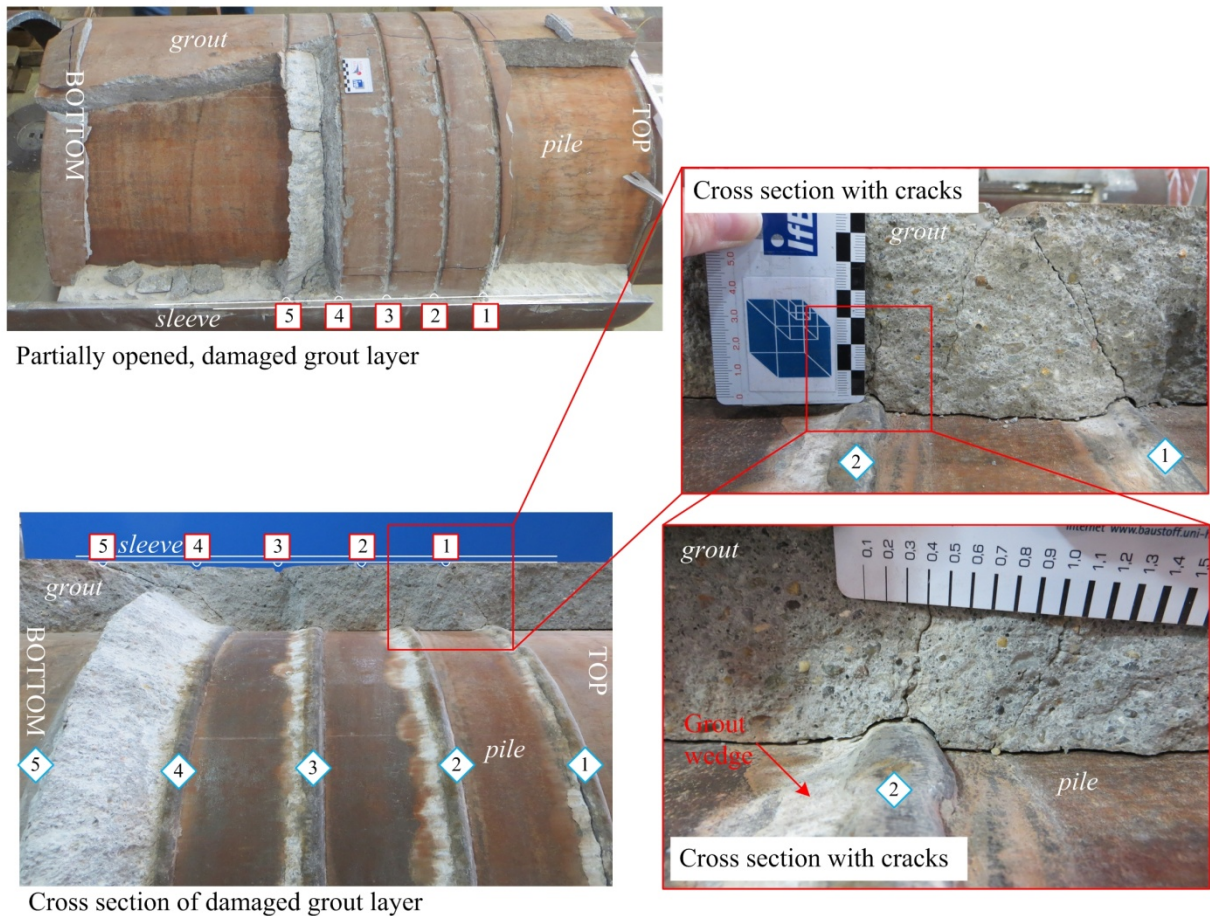
1. Grout surface before testing



2. During testing



3. After testing



**Figure B-8. Damage characteristics at the test specimen TS04 (Densit Ducorit<sup>®</sup> S2,  $t_g = 183.5$  mm) prior to, during and after testing.**

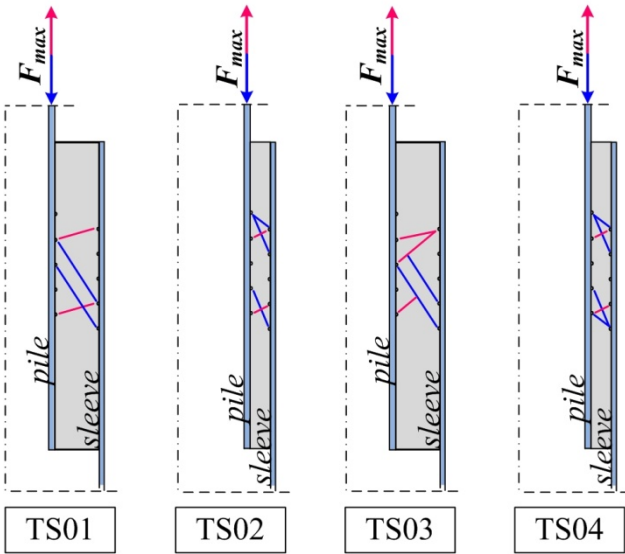


Figure B-10. Derived compression struts at TS01 to TS04.

## Appendix C. Mathematical description of the failure surface

### C.1 Principle stresses

With respect to the stress invariants  $I_1$  to  $I_3$  and the angle  $\theta$ , the principle stresses  $\sigma_1$  to  $\sigma_3$  result to:

$$\sigma_1 = \frac{I_1}{3} + \frac{2}{3} \left( \sqrt{I_1^2 - 3 \cdot I_2} \right) \cos \theta \quad \text{Eq. C-1}$$

$$\sigma_2 = \frac{I_1}{3} + \frac{2}{3} \left( \sqrt{I_1^2 - 3 \cdot I_2} \right) \cos \left( \theta + \frac{2\pi}{3} \right) \quad \text{Eq. C-2}$$

$$\sigma_3 = \frac{I_1}{3} + \frac{2}{3} \left( \sqrt{I_1^2 - 3 \cdot I_2} \right) \cos \left( \theta + \frac{4\pi}{3} \right) \quad \text{Eq. C-3}$$

### C.2 Stress invariants

The stress invariants  $I_1$  to  $I_3$ ,  $J_2$  and  $J_3$  can be described in the three-dimensional stress space in consideration of the Haigh-Westergaard coordinates  $\xi$  and  $\rho$  by the following equations:

$$I_1 = \sigma_1 + \sigma_2 + \sigma_3 = 3 \cdot \sigma_0 = \sqrt{3} \xi \quad \text{Eq. C-4}$$

$$I_2 = \sigma_{xx} \cdot \sigma_{yy} + \sigma_{yy} \cdot \sigma_{zz} + \sigma_{zz} \cdot \sigma_{xx} - \left( \tau_{xy}^2 + \tau_{yz}^2 + \tau_{zx}^2 \right) \quad \text{Eq. C-5}$$

$$I_3 = \sigma_{xx} \cdot \sigma_{yy} \cdot \sigma_{zz} + 2 \cdot \tau_{xy} \cdot \tau_{yz} \cdot \tau_{zx} - \sigma_{xx} \cdot \tau_{yz}^2 - \sigma_{yy} \cdot \tau_{xz}^2 - \sigma_{zz} \cdot \tau_{xy}^2 \quad \text{Eq. C-6}$$

$$J_2 = \frac{1}{6} \left[ (\sigma_1 - \sigma_2)^2 + (\sigma_2 - \sigma_3)^2 + (\sigma_3 - \sigma_1)^2 \right] = \frac{3}{2} \tau_0^2 = \frac{\rho^2}{2} \quad \text{Eq. C-7}$$

$$J_3 = (\sigma_1 - \sigma_m) \cdot (\sigma_2 - \sigma_m) \cdot (\sigma_3 - \sigma_m) \quad \text{Eq. C-8}$$

$$\sigma_m = \frac{1}{3} (\sigma_1 + \sigma_2 + \sigma_3) = \frac{1}{3} I_1 \quad \text{Eq. C-9}$$

### C.3 Haigh-Westergaard coordinates

The hydrostatic and deviatoric stresses in the High-Westergaard coordinates result to:

$$\xi = \sqrt{3} \cdot \sigma_0 = \frac{1}{\sqrt{3}} \cdot (\sigma_1 + \sigma_2 + \sigma_3) \quad \text{Eq. C-10}$$

$$\rho = \sqrt{3} \cdot \tau = \frac{1}{\sqrt{3}} \cdot \sqrt{(\sigma_1 - \sigma_2)^2 + (\sigma_2 - \sigma_3)^2 + (\sigma_3 - \sigma_1)^2} \quad \text{Eq. C-11}$$

### C.4 Drucker-Prager input parameters

According to numerical recommendations by Schlegel (2006) the input parameters  $\alpha$  and  $K$  for the Drucker-Prager criterion can be determined in consideration of the material strength parameters by the following equations:

$$\alpha = \alpha_c = \frac{\sqrt{3}(f_{cc} - f_c)}{2 \cdot f_{cc} - f_c}; \quad K = K_c = \frac{f_{cc} \cdot f_c}{\sqrt{3} \cdot (2 \cdot f_{cc} - f_c)} \quad \text{Eq. C-12}$$

$$\alpha = \alpha_t = \frac{\sqrt{3}(f_c - f_t)}{f_c + f_t}; \quad K = K_t = \frac{2 \cdot f_c \cdot f_t}{\sqrt{3} \cdot (f_c + f_t)} \quad \text{Eq. C-13}$$

Further modified parameter sets can be applied such as according to Chen (1982).

### C.5 Multiaxial failure surface according to Ottosen

According to Model Code 2010 (2012) the multiaxial stress state can be estimated in dependence of the material strength  $f_{cm}$  and the stress invariants by the failure criterion according to Ottosen as follows:

$$A \frac{J_2}{f_{cm}^2} + \lambda \frac{\sqrt{J_2}}{f_{cm}} + B \frac{I_1}{f_{cm}} - 1 = 0 \quad \text{Eq. C-14}$$

The input parameters A, B and  $\lambda$  can be determined in dependence of the uniaxial compressive strength  $f_c$ , biaxial compressive strength  $f_{cc}$  and the tensile strength  $f_{ct}$  and one additional point on the compressive meridian ( $\theta=60^\circ$ ) with  $\sigma_{com}$  and  $\tau_{com}$  by the following equations:

$$k = \frac{f_{ct}}{f_c}; f_{2c} = \frac{f_{cc}}{f_c}; x = \frac{\sigma_{com}}{f_c}; y = \frac{\tau_{com}}{f_c}; h = -\frac{\sqrt{2} \cdot x + y}{\frac{y}{\sqrt{2}} - \frac{1}{3}} \quad \text{Eq. C-15}$$

$$A = \frac{h \cdot B - \sqrt{2}}{y} \quad \text{Eq. C-16}$$

$$B = \frac{\sqrt{2} - \frac{3 \cdot y}{k \cdot f_{2c}}}{h - \frac{9 \cdot y}{f_{cc} - k}} \quad \text{Eq. C-17}$$

The parameter  $\lambda$  is described either by the tensile ( $\theta=0^\circ$ ) or the compressive ( $\theta=60^\circ$ ) meridian.

$$\lambda = \lambda_c(\theta = 60^\circ) = \left(1 - \frac{h}{3 \cdot y}\right) \cdot \sqrt{3} \cdot B + \sqrt{3} + \frac{\sqrt{2}}{\sqrt{3} \cdot y} \quad \text{Eq. C-18}$$

$$\lambda = \lambda_t(\theta = 0^\circ) = \left(2 \cdot \sqrt{3} - \frac{f_{2c} \cdot h}{\sqrt{3} \cdot y}\right) \cdot B + \frac{\sqrt{3}}{f_{2c}} + \frac{\sqrt{2} \cdot f_{2c}}{\sqrt{3} \cdot y} \quad \text{Eq. C-19}$$

$$K_1 = [2 \cdot \cos \theta - 1] \cdot \lambda_t + 4 \cdot [1 - \cos \theta] \cdot \lambda_c \quad \text{for } \frac{\lambda_c}{\lambda_t} \leq 0.5$$

$$K_2 = 1 \quad \text{Eq. C-20}$$



$$K_1 = \frac{\lambda_c}{\cos\left(\frac{\pi}{3} - \frac{1}{3} \cdot \arccos(K_2)\right)}$$

$$K_2 = \cos\left\{3 \cdot \arctan\left[\frac{\left(2 \cdot \frac{\lambda_c}{\lambda_t} - 1\right)}{\sqrt{3}}\right]\right\} \text{ for } \frac{\lambda_c}{\lambda_t} \geq 0.5$$

Eq. C-21

For additional information reference is made to Ottosen (1977) and Model Code 2010 (2012).

## Appendix D. Additional numerical results

### D.1 Relative displacements

In addition to the results presented in chapter 4.3.2, Figure D-1 depicts a comparison of the numerical and experimental load displacement behaviour based on measured relative displacements at L1V.

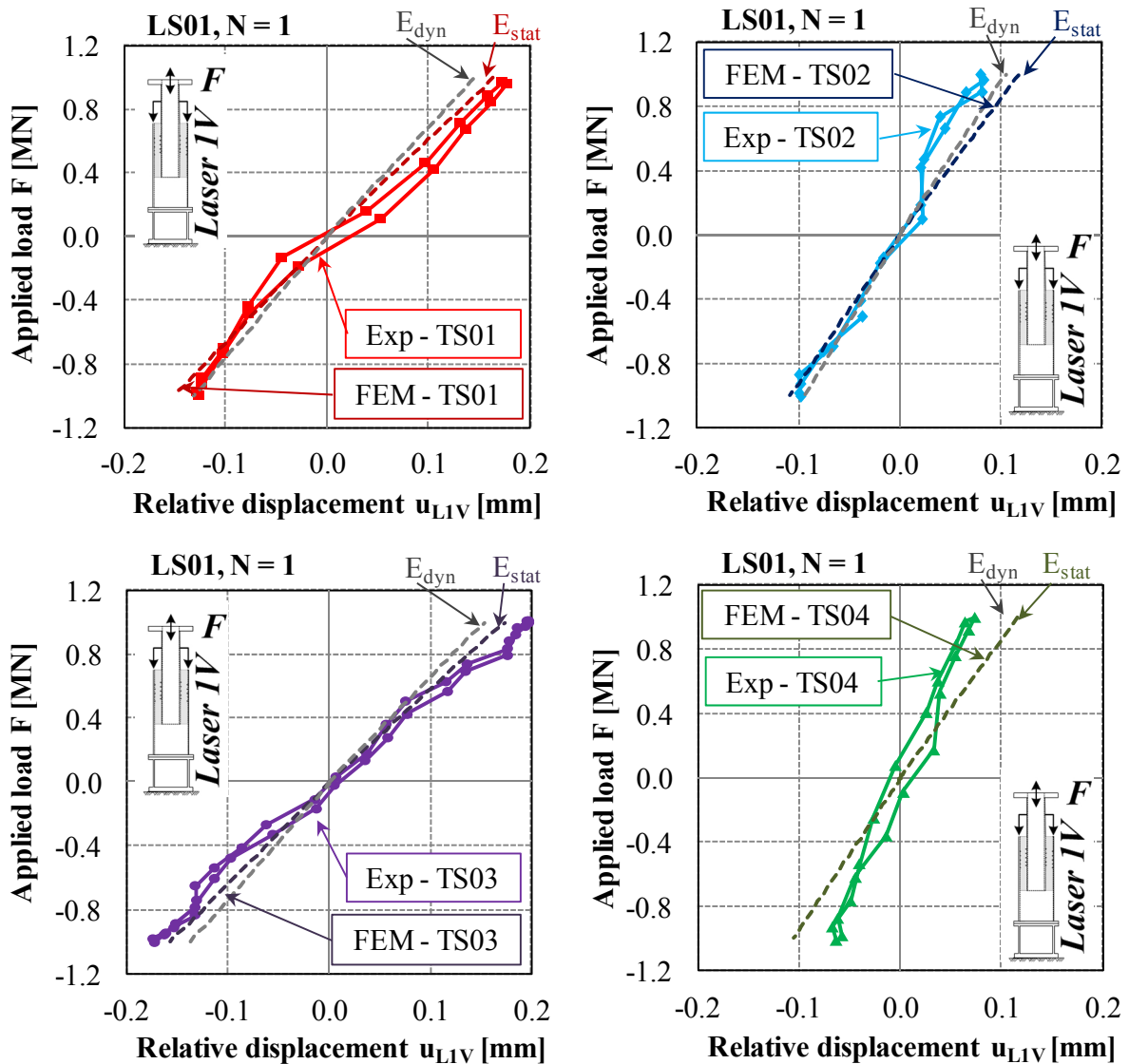


Figure D-1. Comparison of numerical and experimental derived relative displacements at L1V for LS01,  $N = 1$ .

### D.2 Strain development

Figure D-2 presents complementary to the discussed results in chapter 4.3.3, the longitudinal strains achieved by numerical and experimental investigations for the test specimens TS01 to TS04 for the maximum tension load of + 1 MN in LS01, N = 1.

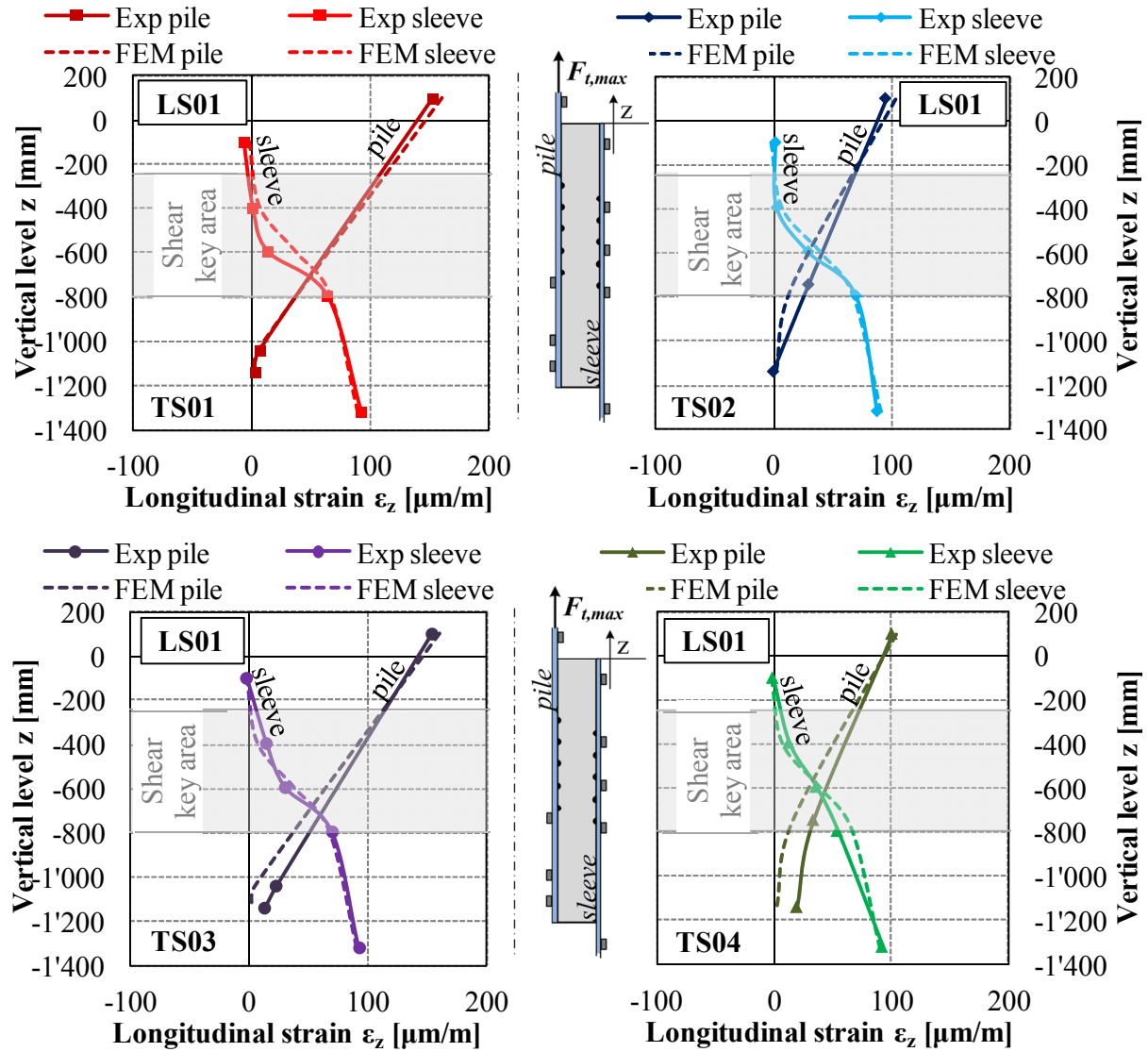


Figure D-2. Comparison of numerical end experimental derived longitudinal strains induced by the peak tension load of  $F_{t,max} = +1$  MN in LS01, N = 1.

## Appendix E. Additional results on the S-N curve comparison

### E.1 Equivalent number of load cycles for the test specimens TS01 to TS04

For each test specimen an equivalent number of load cycles was determined based on the design recommendations according to DNV-OS-J101 (2014) and according to the proposal according to Billington & Chetwood (2012) in combination with the ULS design according to DIN EN ISO 19902 (2014).

Table E-1 presents results for TS01 and TS02 with reference to DNV-OS-J101 (2014) being determined on the basis of applied load stages, corresponding load levels and load cycles.

**Table E-1. Equivalent number of load cycles for the test specimens TS01 and TS02.**

DNV							
TS01							
$F_{ULS,DNV}$	4'063	kN					
Load stage [-]	$F_{max}$ [kN]	$F_{max}/F_{ULS}$ [-]	$\log n_i$ [-]	$\log N_{failure}$ [-]	D [-]	$D_{eq}$ [-]	$\log N_{eq}$ [-]
LS01	1'000	0.25	5.00	3.77	16.99	0.000	9.38
LS02	2'000	0.49	5.00	1.46	3'451.25	0.009	7.07
LS03	3'000	0.74	5.00	0.00	100'000.00	0.248	5.61
LS04	4'000	0.98	5.00	0.00	100'000.00	0.248	5.61
LS05	5'000	1.23	5.00	0.00	100'000.00	0.248	5.61
LS06	6'000	1.48	5.00	0.00	100'000.00	0.248	5.61
LS07	8'000	1.97	2.38	0.00	240.00	0.001	5.61
LS08	3'000	0.74	-	0.00	-	-	-
$\Sigma$					403'708.24	1.000	

TS02							
$F_{ULS,DNV}$	6'105	kN					
Load stage [-]	$F_{max}$ [kN]	$F_{max}/F_{ULS}$ [-]	$\log n_i$ [-]	$\log N_{failure}$ [-]	D [-]	$D_{eq}$ [-]	$\log N_{eq}$ [-]
LS01	1'000	0.16	5.00	4.95	1.13	0.000	10.41
LS02	2'000	0.33	5.00	2.78	166.27	0.001	8.24
LS03	3'000	0.49	5.00	1.47	3'397.85	0.012	6.93
LS04	4'000	0.66	5.00	0.16	69'439.29	0.241	5.62
LS05	5'000	0.82	5.00	0.00	100'000.00	0.347	5.46
LS06	6'000	0.98	5.00	0.00	100'000.00	0.347	5.46
LS07	8'000	1.31	4.18	0.00	15'000.00	0.052	5.46
LS08	3'000	0.49	4.18	1.47	509.68	0.002	6.93
$\Sigma$					288'514.21	1.000	

Table E-2 presents results for TS03 and TS04 with reference to DNV-OS-J101 (2014) being determined on the basis of applied load stages, corresponding load levels and load cycles.

**Table E-2. Equivalent number of load cycles for the test specimens TS03 and TS04.**

<b>TS03</b>							
$F_{ULS,DNV}$	3'768	kN					
Load stage [-]	$F_{max}$ [kN]	$F_{max}/F_{ULS}$ [-]	$\log n_i$ [-]	$\log N_{failure}$ [-]	D [-]	$D_{eq}$ [-]	$\log N_{eq}$ [-]
LS01	1'000	0.27	5.00	3.49	32.02	0.001	7.88
LS02	2'000	0.53	5.00	1.15	7'019.15	0.289	5.54
<b>LS03</b>	<b>3'000</b>	<b>0.80</b>	<b>3.64</b>	<b>0.00</b>	<b>4'400.00</b>	<b>0.181</b>	<b>4.38</b>
LS04	4'000	1.06	4.11	0.00	12'800.00	0.528	4.38
LS05	5'000	1.33	-	0.00	-	-	-
LS06	6'000	1.59	-	0.00	-	-	-
LS07	8'000	2.12	-	0.00	-	-	-
LS08	3'000	0.80	-	0.00	-	-	-
$\Sigma$					24'251.17	1.000	

<b>TS04</b>							
$F_{ULS,DNV}$	5'843	kN					
Load stage [-]	$F_{max}$ [kN]	$F_{max}/F_{ULS}$ [-]	$\log n_i$ [-]	$\log N_{failure}$ [-]	D [-]	$D_{eq}$ [-]	$\log N_{eq}$ [-]
LS01	1'000	0.17	5.00	4.84	1.44	0.000	10.35
LS02	2'000	0.34	5.00	2.66	217.93	0.001	8.17
<b>LS03</b>	<b>3'000</b>	<b>0.51</b>	<b>5.00</b>	<b>1.29</b>	<b>5'098.93</b>	<b>0.016</b>	<b>6.80</b>
LS04	4'000	0.68	5.00	0.00	100'000.00	0.311	5.51
LS05	5'000	0.86	5.00	0.00	100'000.00	0.311	5.51
LS06	6'000	1.03	5.00	0.00	100'000.00	0.311	5.51
LS07	8'000	1.37	4.18	0.00	15'000.00	0.047	5.51
LS08	3'000	0.51	4.18	1.29	764.84	0.002	6.80
$\Sigma$					321'083.14	1.000	

Table E-3 presents results for TS01 and TS02 with reference to DIN EN ISO 19902 (2014) being determined on the basis of applied load stages, corresponding load levels and load cycles.

**Table E-3. Equivalent number of load cycles for the test specimens TS01 and TS02.**

ISO							
TS01							
$F_{ULS,ISO}$	8'868 kn						
Load stage [-]	$F_{max}$ [kN]	$F_{max}/F_{ULS}$ [-]	$\log n_i$ [-]	$\log N_{failure}$ [-]	D [-]	$D_{eq}$ [-]	$\log N_{eq}$ [-]
LS01	1'000	0.11	5.00	7.36	0.00	0.000	12.56
LS02	2'000	0.23	5.00	4.31	4.90	0.000	9.51
LS03	3'000	0.34	5.00	2.53	297.93	0.002	7.73
LS04	4'000	0.45	5.00	1.26	5'494.94	0.035	6.46
LS05	5'000	0.56	5.00	0.28	52'701.98	0.332	5.48
LS06	6'000	0.68	5.00	0.00	100'000.00	0.630	5.20
LS07	8'000	0.90	2.38	0.00	240.00	0.002	5.20
LS08	3'000	0.34	-	2.69	-	-	-
$\Sigma$					158'739.75	1.000	

TS02							
$F_{ULS,ISO}$	16'437 kN						
Load stage [-]	$F_{max}$ [kN]	$F_{max}/F_{ULS}$ [-]	$\log n_i$ [-]	$\log N_{failure}$ [-]	D [-]	$D_{eq}$ [-]	$\log N_{eq}$ [-]
LS01	1'000	0.06	5.00	10.08	0.00	0.000	13.48
LS02	2'000	0.12	5.00	7.03	0.01	0.000	10.43
LS03	3'000	0.18	5.00	5.24	0.57	0.000	8.65
LS04	4'000	0.24	5.00	3.98	10.59	0.004	7.38
LS05	5'000	0.30	5.00	2.99	101.52	0.040	6.40
LS06	6'000	0.37	5.00	2.19	643.87	0.254	5.60
LS07	8'000	0.49	4.18	0.93	1'781.30	0.702	4.33
LS08	3'000	0.18	4.18	5.24	0.09	0.00	8.65
$\Sigma$					2'537.95	1.000	

Table E-4 presents results for TS03 and TS04 with reference to DIN EN ISO 19902 (2014) being determined on the basis of applied load stages, corresponding load levels and load cycles.

**Table E-4. Equivalent number of load cycles for the test specimens TS03 and TS04.**

<b>TS03</b>							
$F_{ULS,ISO}$	8'224 kN						
Load stage [-]	$F_{max}$ [kN]	$F_{max}/F_{ULS}$ [-]	$\log n_i$ [-]	$\log N_{failure}$ [-]	D [-]	$D_{eq}$ [-]	$\log N_{eq}$ [-]
LS01	1'000	0.12	5.00	7.03	0.01	0.000	10.22
LS02	2'000	0.24	5.00	3.98	10.51	0.007	7.17
<b>LS03</b>	<b>3'000</b>	<b>0.36</b>	<b>3.64</b>	<b>2.19</b>	<b>28.14</b>	<b>0.018</b>	<b>5.38</b>
LS04	4'000	0.49	4.11	0.93	1'509.77	0.975	4.12
LS05	5'000	0.61	-	0.00	-	-	-
LS06	6'000	0.73	-	0.00	-	-	-
LS07	8'000	0.97	-	0.00	-	-	-
LS08	3'000	0.36	-	2.19	-	-	-
$\Sigma$					1'548.43	1.000	

<b>TS04</b>							
$F_{ULS,ISO}$	15'732 kN						
Load stage [-]	$F_{max}$ [kN]	$F_{max}/F_{ULS}$ [-]	$\log n_i$ [-]	$\log N_{failure}$ [-]	D [-]	$D_{eq}$ [-]	$\log N_{eq}$ [-]
LS01	1'000	0.06	5.00	9.88	0.00	0.000	13.48
LS02	2'000	0.13	5.00	6.83	0.01	0.000	10.43
<b>LS03</b>	<b>3'000</b>	<b>0.19</b>	<b>5.00</b>	<b>5.05</b>	<b>0.89</b>	<b>0.000</b>	<b>8.65</b>
LS04	4'000	0.25	5.00	3.78	16.50	0.004	7.38
LS05	5'000	0.32	5.00	2.80	158.29	0.040	6.40
LS06	6'000	0.38	5.00	2.00	1'003.91	0.254	5.60
LS07	8'000	0.51	4.18	0.73	2'777.34	0.702	4.33
LS08	3'000	0.19	4.18	5.05	0.13	0.00	8.65
$\Sigma$					3'957.09	1.000	

## Curriculum Vitae

Name: Anne Christine Bechtel  
Geburtstag/-ort: 01. November 1984 in Alsfeld, Deutschland  
Familienstand: ledig

### Ausbildung

2001 - 2004 Tellkampfschule Hannover, Deutschland  
2004 Abschluss: Hochschulreife (Abitur)  
2004 - 2009 Studium des Bauingenieurwesen an der Leibniz Universität Hannover, Vertiefungsrichtung: Konstruktiver Ingenieurbau  
2009 Abschluss: Diplomingenieurin (Dipl.-Ing.)

### Praktika und Auslandsaufenthalte

Jul 2005 Bayerische Hausbau GmbH in Budapest, Ungarn  
Aug - Sep 2007 PST Spezialtiefbau Nord GmbH, Wathlingen, Deutschland  
Feb - Mär 2008 E.ON Climate & Renewables, München, Deutschland  
Nov 2008 - Apr 2009 Studentische Hilfskraft am Institut für Stahlbau, Leibniz Universität Hannover  
Feb - Mai 2009 Diplomarbeit in Kooperation mit der TU Delft, Niederlande

### Berufstätigkeit

Okt 2009 - Dez 2015 Wissenschaftliche Mitarbeiterin am Institut für Stahlbau, Leibniz Universität Hannover, Deutschland

### Preise

Nov 2010 E.ON Future Award 2010  
Okt 2012 DAST Kolloquium Bestes Paper, Bester Vortrag Award 2012